Abstract

Title of Dissertation: Modeling Optically Thick Molecular Emission
                           Spectra of Comets Using
                           Asymmetric Spherical Coupled Escape Probability

                           Alan Michael Gersch, Doctor of Philosophy, 2014

Dissertation directed by: Professor Michael F. A'Hearn
                           Department of Astronomy

Comets are frozen remnants from the formation of the Solar System. As such, their chemical composition is of great significance to understanding the origin of the planets and the distribution of important molecules, including water and other volatiles, throughout the Solar System.

Recent observations, in particular those of the Deep Impact and EPOXI Missions, have provided better spectra of a cometary coma than were previously available. These observations include spectra with high spatial resolution very near to the nucleus.

The purpose of this research is to better understand the abundances, distributions and creation mechanisms of various volatiles observed in cometary comae, in particular those of comet 9P/Tempel 1, the target of the Deep Impact Mission, and 103P/Hartley 2, the subject of the EPOXI mission.

In order to do so, I have built a computer model of the spectrum of the comet's coma which includes the difficult and often ignored problem of accurately including radiative transfer to account for the potentially optically thick coma (or regions of the coma) near the nucleus.

I have adapted Coupled Escape Probability, a new exact method of solving radiative transfer problems, from its original plane-parallel formulation for use in asymmetrical spherical situations. My model is designed specifically for use in modeling optically thick cometary comae, although not limited to such use.

By providing for asymmetric geometry in the coma, the model is able to include the morphology of the near nucleus coma, as observed by the Deep Impact spacecraft for Tempel 1 and Hartley 2, and include this in the modeling of radiative transfer.

This method enables the accurate modeling of comets' spectra even in the potentially optically thick regions nearest the nucleus, such as those seen in Deep Impact observations of 9P/Tempel 1 and EPOXI observations of 103P/Hartley 2.

This model will facilitate analyzing the actual spectral data from the Deep Impact and EPOXI missions to better determine abundances of key volatile species, including CO, CO_2 and H_2O, as well as remote sensing data on active comets.

Modeling Optically Thick Molecular Emission Spectra of Comets Using Asymmetric Spherical Coupled Escape Probability

by

Alan Michael Gersch

Dissertation submitted to the Faculty of the Graduate School of the
University of Maryland at College Park in partial fulfillment
of the requirements for the degree of
Doctor of Philosophy
2014

Advisory Committee:

> Professor Michael F. A'Hearn, chair
> Professor Patrick Harrington
> Professor Derek C. Richardson
> Dr. Lori Feaga
> Dr. Ludmilla Kolokolova
> Dr. Neil DelloRusso
> Professor Robert Hudson

Preface

While none of this work has yet been published, we have presented much of the work as it was developed, primarily at AAS and DPS meetings.

Parts of Chapters 2 and 3 have been submitted for publication in the Astrophysical Journal.

The Garradd results in Chapter 3 have been included in Feaga et al. (2014), which has been submitted for publication in the Astronomical Journal.

הללו-י-ה
הללו את-יהו-ה מן-השמים   הללוהו במרומים
הללוהו כל-מלאכיו   הללוהו כל-צבאיו
הללוהו שמש וירח   הללוהו כל-כוכבי אור
הללוהו שמי השמים   והמים אשר מעל השמים
יהללו את-שם יהו-ה   כי הוא צוה ונבראו
ויעמידם לעד לעולם   חק-נתן ולא יעבור

תהילים פרק קמח

Hallelujah!

Praise the Lord from the heavens; praise Him on high.

Praise Him, all His messengers; praise Him, all His hosts.

Praise Him, sun and moon; praise Him, all stars of light.

Praise Him, heavens of heavens, and the water that is above the heavens.

Let them praise the name of the Lord;

    for He commanded, and they were created.

He established them forever and ever;

    He gave a law that will never be transgressed.

Psalms 148:1-6

To my parents, Charles and Marianna Gersch, without whom I would not be here; who sacrificed much to ensure that I had the best education possible and who always encouraged my love of science.

To Lili, who always had more confidence in me than I do in myself.

And to Jacob and Shaya for giving me inspiration when my own failed, and for putting up with Abba having to do his work all this long time.

Acknowledgements

Many people have given me much support of many kinds along the very long way to the completion of this degree. I will only name a few, but there are many more who deserve credit.

First and foremost, I must thank Mike A'Hearn who has taken (much) time from his very busy schedule (even after retirement) to share with with me, his lingering last student, his knowledge, wisdom, humor and, above all, patience.

I also thank all my other committee members, but especially Derek Richardson, without whom I would not know much about numerical methods, J. P. Harrington, who taught me more about radiative transfer than I ever thought I would want to know, and Lori Feaga, who has been incredibly helpful and encouraging, and without whom this work would have been impossible.

I would also like to thank Moshe Elitzur for his encouragement to pursue this study, which is, of course, heavily based on some of his own work.

To the UMD Astronomy Dept. faculty, staff and other students.

For endless encouragement and advice, I would like to thank all the other members of the UMD Comet Group and DI/EPOXI teams. Most especially, for being a mentor to me, even when he himself was still a student, and continually ever since, Matthew Knight.

In acknowledgement of the adage "it takes a village," I would also like to thank the many, many friends in the Washington area community, mostly at Kesher Israel and Rosh Pina, for always being supportive and encouraging. Of special mention, my gang of fellow scientists and the academics in other fields who were always there to commiserate and console me. And of even more special mention, the Kesher Morning Minyan and its senior physicists, Asher Namenson, Max Klein, and most of all, Phil Klein *Z"L*, whose wisdom and inspiration is sorely missed.

I must give the greatest thanks to my family, starting with my parents, without whom I would not be, and who sacrificed so much to ensure that I had the best education possible and who always encouraged my love of science.

Lastly to Lili, Jacob and Shaya for putting up with me all this long time.

Contents

List of Tables

List of Figures

Chapter 1

Introduction

1.1 History

Comets have been phenomena of fascination for humanity since the dawn of recorded history. Ancient records of comets show that they were thought to be significant, even though they were generally perceived as superstitious omens, not subjects of scientific fascinination and inquiry. An ancient Chinese book found in Mawangdui, China dating from the second century BCE shows that some ancients even attempted to categorize different types of comets, based on their appearances. This is the oldest known recorded taxonomy of comets. The classical Greek philosophers also thought about comets (and were the ones who named them $\kappa o\mu\eta\tau\eta\varsigma$, meaning "hairy one") in their studies of natural philosophy, with Aristotle (c. 330 BCE) deciding that they were in the sublunary sphere and part of the atmosphere. Aristotelian thought dominated science for well over 1500 years.

In the late sixteenth century, Tycho Brahe conducted precise methodical observations of comets and, based on parallax, concluded that they were in fact celestial bodies, i.e. beyond the Moon. With the Scientific Revolution of the seventeenth century, comets began to be understood scientifically, most notably by Edmund

Halley who, in the early eighteenth century, realized the periodic nature of their orbits around the Sun, and thus that the individual comets return for many apparitions. Thus their returns could be predicted, and plans and preparations to observe them made in advance. The ensuing observations of comets well into the nineteenth century mostly focused on the dynamics of comets.[1] Orbits were calculated based on observations, and different groups of comets were recognized. In particular, the "Jupiter family" of comets, possessed of low inclinations and aphelia close to Jupiter's orbit, was recognized as distinct from other comets having much longer orbits and greater aphelia. During the 1835 apparition of 1P/Halley, spatial structures within comets were observed by Herschel, Bessel, and Struve.

Meanwhile, in the mid- to late-eighteenth century, Immanuel Kant, although more well known for his contributions to metaphysics and philosophy, was the first to propose that the Solar System formed from the collapse of a giant cloud of gas and dust, called the "solar nebula," which formed a disk around the nascent Sun, from which the planets then formed. Over two-hundred years later, the scientific consensus today is that he was essentially right.

Also in the nineteenth century, with the advent of spectroscopy, observers began to investigate the chemical composition of comets. The first spectroscopic observations of the gas component of comets were made by Donati (1864) and Huggins (1868), who visually compared the spectra of Comets Tempel (C/1864 N1) and Tempel-Tuttle (55P/1865 Y1), respectively, with flame spectra. The bands recorded by Huggins, known as the carbon or Swan bands, were found in all subsequent observations of comets. The Swan bands so strongly dominated cometary spectra that

---

[1]The following several paragraphs of history are mostly excerpted and paraphrased from "A Brief Conceptual History of Cometary Science" by M. C. Festou, H. U. Keller, & H. A. Weaver in Comets II, 2004

carbon was immediately believed to be an important constituent of comets.

Schwarzschild and Kron (1911) studied the intensity distribution in 1P/Halley's straight tail during the 1910 passage and suggested that the emission could be explained by the effect of absorption of solar light, followed by its reemission, i.e., fluorescence.

Around 1950, Fred Whipple (see Whipple 1950, 1951 and Hamid and Whipple 1953) laid the foundations for the modern model of a solid nucleus. He proposed the "Icy Conglomerate" model (often colloquially referred to as the "Dirty Snowball" model) in order to explain non-gravitational forces experienced by comets. This idea states that comets' nuclei are composed of frozen volatiles (mostly water) and dust. As comets near the Sun, sublimation of the volatile components leads to the activity observed, with volatiles and dust being released from the nucleus and forming the coma and tails.

Also in 1950, Jan Oort (based on earlier work by Stromgren, 1914 & 1947, showing that comets were not coming from interstellar space and work by Sinding, 1937, and van Woerkom, 1948, showing that the original reciprocals of semi-major axes of long-period comets were $< 10^{-4}$ 1/AU) demonstrated the existence of a cloud of comets in the outermost reaches of the solar system ($10^{-5} < 1/a < 10^{-4}$ with a being semi-major axis in AU). This reservoir was populated by comets that formed near the orbits of the giant planets and were ejected from there due to those planets' gravity during the formation of the Solar System. (See Oort 1950)

Around the same time, Edgeworth (1949) and Kuiper (1951) argued that the protoplanetary disk from which planets formed would not have had a sharp cutoff at the position of Neptune's orbit, and thus a large population of what we now call planetesimals with a generally icy composition had to exist beyond Neptune's orbit. Kuiper (1951) claimed that such bodies could be identified with Whipple's cometary

nuclei. Thus two reservoir populations of comets were thought to exist, each having formed in its own primordial conditions, primarily governed by heliocentric distance.

In 1963, Whipple himself wrote that "an enormous, if not definitive, insight concerning these evolutionary problems could be gained by a space probe made to land on a cometary nucleus. Cores of the nucleus should be stratified like geological sedimentary strata and should give the oldest and least disturbed material record of ancient processes." (Whipple 1963)

The 1970s witnessed the development of systematic, quantitative observations of optical cometary emissions by means of photoelectric narrow-band filter photometry (by A'Hearn, Schleicher, Millis, and their collaborators) and CCD spectroscopy (by several groups led by Cochran, Newburn, and Fink).

During the same period, theoretical studies calculated the fluorescence efficiencies ("g-factors") of various coma species, which enable the calculation of column densities and gas production rates from observed surface brightnesses.

Over twenty years after Whipple wrote of a space mission to a comet, several were actually undertaken, although none actually tried to land. Several spacecraft have observed comets up close, begining in the 1980s. In 1985 the International Cometary Explorer (ICE) passed through the tail of Comet 21P/Giacobini-Zinner, about $\sim$8000 km from the nucleus. In the following year, ICE and five other spacecraft observed Comet 1P/Halley in situ. For the first time, a cometary nucleus was directly observed.

That apparition of Halley's Comet also featured important spectroscopic milestones. Although H and OH radicals had been observed, ordinary un-ionized water vapor itself had not been unambiguously *directly* detected until its strong IR ro-vibrational emissions were measured by Mumma et al. (1986) in the coma of 1P/Halley during observations from the Kuiper Airborne Observatory, and later

from the Vega flyby spacecraft (Combes et al. 1986; Moroz et al. 1987).

Since then, there have been more spacecraft missions to comets. Deep Space 1 flew past 19P/Borrelly. Stardust flew through the coma of 81P/Wild 2 and gathered and returned dust grains from the coma. The Deep Impact mission to 9P/Tempel 1 was a smashing success and its extended mission visited 103P/Hartley 2. Currently, the ESA-led Rosetta mission is on its way to a rendezvous with 67P/Churyumov-Gerasimenko.

During the intervening decades, ground-based spectroscopy has also proceeded apace and yielded a wealth of information about many molecules in many comets. A systematic survey of the principal optical emissions from 85 comets produced the first evidence for the existence of compositional families among the comets (A'Hearn et al. 1995).

In the twenty-first century, a new era of cometary studies is upon us. Which brings us to the topic at hand. The Deep Impact Mission, on July 4, 2005, succeeded in impacting and excavating a new crater on a cometary nucleus. This unique experiment fulfilled the goal of Whipple's envisioned space mission, although its impact cratering experiment might not be quite the "landing" he pictured.

1.2 Deep Impact Goals

The Deep Impact Mission is just what Whipple would have wanted. "The primary goal of Deep Impact is to understand the differences between the material at the surface of a cometary nucleus and the material in the interior in order to understand the evolutionary processes that have taken place in the surface layers."(A'Hearn et al. 2005b) More specific scientific objectives were to determine key properties of the nucleus (e.g. mass, density, porosity) and surface layers, the relation between the

surface and possibly pristine interior material, and the evolution of the nucleus.

The concept developed to achieve these scientific goals was to excavate a large crater on the comet's surface, using a high velocity impact that would reveal material from many meters beneath the surface. The mission was actually carried out by two spacecraft, the main flyby craft and the impactor, which separated from the flyby craft a bit more than a day before impact. While the impactor impacted the comet and created the crater, ejecting the subsurface material, the flyby spacecraft observed from a safe distance with scientific instruments performing visible imaging and infrared spectroscopy.

1.2.1 Deep Impact & EPOXI Ambient Coma Spectra

In addition to observing the impact cratering and ejecta, the Deep Impact mission observed Comet 9P/Tempel 1 for a period before and after the impact event itself. As the spacecraft approached the nucleus, spectral scans using the HRI-IR spectrometer produced unprecedented spectral data on a comet's coma. (See Feaga et al. 2007a)

These observations include spectra with high spatial resolution very near to the nucleus yielding an unprecedented combination of spatial and spectral resolutions. Feaga et al. (2007a) have produced brightness maps around the nucleus of relevant spectral bands, for H_2O and CO_2, with spatial resolution of less than a kilometer per pixel!

About five years later, the Deep Impact Extended Investigation (DIXI), which in conjunction with the EPOCh investigation was labeled "EPOXI", acquired similarly amazing quality spectral observations of Comet 103P/Hartley 2 in another successful flyby mission (this time, without an impact). (See A'Hearn et al. 2011)

1.2.2 Optical Depths

No previous observations had as much spatially well-resolved spectral data, and thus there had been little observationally driven need to pay special or close attention to the densest part of the coma. Ground-based observations could only see optically thick comae for the brightest and/or most active of comets. (e.g. Hale Bopp; see Disanti et al. 2001, 1999)

Therefore many earlier studies that modeled spectra of comae, in keeping with the available observations of the time, did not attempt to calculate optical depth effects on spectra. Optically thin comae were assumed, since the field of view in those observations being modeled would be dominated by the majority of the coma far from the nucleus, which is optically thin. (e.g. Chin and Weaver 1984; Crovisier and Le Bourlot 1983) However, with the proliferation of space missions to comets, as well as much better instruments for ground-based observations (see, e.g. Disanti et al. 1999), this is no longer a tenable approach.

Other space missions to comets in the near future, most imminent among them Rosetta, will hopefully reap even more detailed data from in-situ observations of comets.

In addition, more distant observations from Earth orbit (or other) space-based observatories, such as the *AKARI* satellite, are providing cometary spectra that are impossible to observe from the surface of the Earth due to atmospheric opacity. (See Ootsubo et al. 2012, 2010)

1.3 Scientific Importance

Comets are now understood to be frozen remnants from the formation of our solar system. As such, their chemical composition is of great significance to understanding the origin of the planets and the distribution of important molecules, including water, other volatiles and organic molecules throughout the solar system. Determining the chemical composition of comets was a major goal of the Deep Impact and EPOXI Missions, among others, as well as a goal of ground-based observations of comets.

1.3.1 Solar System Formation

Comets are leftover building blocks of the planets, in particular the giant planets which formed beyond the snow line in the proto-planetary disk. They also, by means of subsequent impacts, such as the "Late Heavy Bombardment" may have delivered water and other volatiles to the terrestrial planets after the initial formation of those planets interior to the snow line.

If we can determine the composition of comets in conjunction with dynamical knowledge of where they formed, comets can provide valuable information and constraints about the nature and details of the proto-planetary disk from which both comets and planets formed.

1.3.2 "Old" Ideas: Dynamical Families

Historically, comets were classified based on *observed* dynamic quantities. Comets with a period of less than ∼200 years were called "short period comets" and those with periods longer than 200 years "long period comets". Long period comets were categorized as "new" or "returning" based on their semi-major axis, with those having an original (before any perturbations by planets) $a_0 > 10,000$AU being "new" and vice versa. This roughly corresponded to the idea that "new" comets on their first passage through the inner Solar System were coming from distances typical of the Oort cloud. Short period comets were divided into "Jupiter Family Comets" (henceforth, JFCs) and "Halley Type Comets" (henceforth, HTCs). JFCs mostly had orbits close to (or inwards of) Jupiter's, and were dynamically dominated by that planet, hence the name. They also tend to have very low inclinations (mean $\sim 10°$) and are *all* in prograde orbits. These characteristics are not shared by HTCs.

The traditional understanding of short period comets was that they were originally from the Oort Cloud population of comets and were "captured" into their current short period orbits due to planetary gravitational interactions. They were presumed to have been ejected to the Oort cloud, from the region of the giant planets due to the gravity of the larger of those planets, during the latter stages of the formation of the Solar System. In the 1980s this view was generally supplanted by the idea, originally from Fernandez and Ip (1983), that their origin is from the Kuiper Belt and not the Oort Cloud, due to studies of numerical integration of orbits. (See e.g. Duncan et al. 1988; Quinn et al. 1990).

A new/alternative classification was suggested by Levison (1996), based on the much improved understanding of dynamical properties of comets' origins. His taxonomy divides comets into "Nearly-Isotropic" and "Ecliptic." The latter have very

low inclinations while the former, as their label implies, do not. "Ecliptic" comets include "JFCs" that cross Jupiter's orbit, and other comets whose orbits remain either interior or exterior to Jupiter. Dynamical considerations indicate that Ecliptic Comets all must have originated in a disk of low inclination, not the Oort Cloud. The "Nearly-Isotropic" comets include "new" and "returning" comets, with "returning" comets including HTCs and "External" (having semi-major axis $a > 40AU$).

Further dynamical studies continued to paint an even more complicated picture. The scattered disk, a higher inclination extension outwards of the Kuiper Belt, was needed to explain JFCs with higher inclinations (see Levison and Duncan 1997), and the inner Oort Cloud, with a less isotropic distribution, were needed to better explain the observed not quite isotropic distribution of some HTC inclinations (see Levison et al. 2001).

The "Nice model" (see Gomes 2003; Gomes et al. 2004; Levison et al. 2008; Tsiganis et al. 2005) and subsequent further dynamical studies using computational modeling trace the paths of comets from original starting locations in the early Solar System to explain the populations of the different comet reservoirs.

Many such studies have arrived at the idea that there has been much more movement and exchange between comet reservoirs than previously thought, and that current comet populations are somewhat dynamically mixed with respect to their original formation locations.

1.3.3 "New" Ideas: Chemical Composition "Families"

The above classification schemas for comets are all entirely based on dynamics. Simultaneously, through the advance of cometary spectroscopy of the past few decades, chemical compositions have also been used to attempt to formulate classifications of comet populations based on abundances of molecules. Over the course of time,

the results of these studies have also tended towards showing more heterogeneous populations than earlier simple classification schemes.

In A'Hearn et al. (1995), a landmark study of eighty-five comets, it was shown that most comets are fairly *similar* in chemical composition, as well as sharing other related properties. However, some (25-50%) comets from the Scattered Disk seem to be depleted in carbon-chain molecules relative to other comets. These compositional results were thought to be primordial rather than evolutionary, with the suggestion that mixing of primordial cometesimals from different formation areas could account for observed differences.

Similar studies of organic molecules in comets (e.g. Mumma et al. 2001) have also shown that composition with respect to abundances of different organics shows some comets that are depleted relative to others. Yet, these are not strongly correlated to the "old school" dynamical population divisions of Oort Cloud vs. Kuiper Belt. Mumma and Charnley (2011) suggest that improvements in the sensitivity of measurements of primary volatiles allow the creation of a taxonomy of comets based on chemical parameters, rather than merely dynamics, and that this effort is crucial to testing models of their origin in the protoplanetary disk.

A'Hearn et al. (2012) conducted a similar study based on relatively new data using comparisons of CO_2 (which can only be directly measured by space-based observations, such as those of the *AKARI* or Deep Impact spacecraft), CO, and H_2O. They find that there is fairly little correlation between the ratios of these volatiles based on traditional populations. They argue that there is indeed little compositional difference between JFCs on the one hand and long period comets and HTCs on the other, and what little difference is detected is the *reverse* of the "classical" picture: JFCs actually seem to have formed closer to the Sun than LPCs. This suggests that they may have formed in largely overlapping regions of the

proto-planetary disk, before reaching their current locations and "families". This study in particular illustrates the importance of space-based observations of primary volatiles, as without them CO_2 could not contribute these significant new insights to the understanding of comets' origins based on chemical composition.

1.4   Spectroscopy of Cometary Comae

As mentioned above, spectroscopy is the primary method for identifying and determining the abundances of volatile species in comets' comae. (Mass spectroscopy is also possible, but only for in-situ measurements.)

1.4.1   A Brief Review of Relevant Molecular Spectroscopy

In general, the basics of spectroscopy form a core pillar of modern scientific understanding of many subjects, well beyond astronomy. The Bohr model explaining the simplest example of spectral lines is a mainstay of introductory science classes in high schools and universities everywhere.

However, to understand cometary volatiles, a more in-depth understanding is necessary. In addition to electrons in atoms (as in the Bohr model) absorbing and emitting light (photons) of specific frequencies and by which the electrons gain or lose specific quantized amounts of energy, molecules as a whole may also similarly absorb and emit photons.

The total (internal) energy of a molecule $E_{tot} = E_{e^-} + E_{vib} + E_{rot}$, where E_{e^-} is the electronic energy, E_{vib} is the vibrational energy and E_{rot} is the rotational energy of a state. Molecular spectroscopy, in addition to electronic excitation, as in atoms, involves the addition or removal of energy to or from a molecule's rotational energy, and/or to or from the vibrational energy between atoms in the molecule,

or both. These processes are also quantized, and a molecule can only absorb or emit at specific frequencies, depending on the structure of the molecule. Generally, purely rotational transitions have wavelengths that fall into the "radio" regime of the electromagnetic spectrum, and vibrational and ro-vibrational frequencies usually are in the infrared portion of the spectrum. Electronic transitions usually involve visible to ultraviolet light.

Electronic states of molecular orbitals are indicated by Greek letters corresponding to the more familiar atomic orbitals: Σ, Π, Δ and Φ analogous to s, p, d and f, indicating the values of the quantum number $\Lambda = 0$, 1, 2, 3... (analogous to the atomic number l). The component of electron spin angular momentum along the internuclear axis is indicated by a quantum number labeled Σ (analogous to the atomic M_S), which can have $2S + 1$ values where S is the *total* electron spin angular momentum. The value of this multiplicity is prefixed as a superscript to the Greek letter. A preceding capital English letter is usually used to label the ground state, "X", or higher states of the same multiplicity: A, B, C... and lower case letters for states with multiplicity different from the ground state. Symmetry properties are indicated by adding to the Greek letter a "+" or "-" (super-scripted) indicating symmetry or anti-symmetry respectively to reflection across any plane through the internuclear axis, or "g" or "u" (sub-scripted) for symmetry or anti-symmetry to inversion through the center of the molecule. (See, e.g. Hollas 2004, Chapter 7)

However, we do not directly deal with electronic transitions in this study, primarily due to the fact that the transition rates due to solar radiative pumping for the ro-vibrational (IR) bands are about two orders of magnitude greater than the electronic bands. (See e.g. Crovisier and Le Bourlot 1983) Furthermore, the Deep Impact observations that motivated our modeling work presented here are of IR spectra. Thus, for example, all the CO transitions we deal with are in the $X^1\Sigma^+$

ground electronic state.

Integral quantum numbers referring to rotational states of a molecule are usually represented by "J," and in more complex molecules that are able to rotate around multiple axes (such as water) by expressions such as $J_{K_a K_b}$, where K_a and K_b are also integral rotational quantum numbers. Similarly, vibrational quantum numbers refer to the vibrational energy in each (stretching) bond between atoms in a molecule, and also to bending modes of vibrational energy. Thus, diatomic molecules have only one vibrational number (generally referred to as "v"), but polyatomic molecules have more, and they can be excited and de-excited independently, or in conjunction with one another. For polyatomic molecules, individual vibrational energy modes are usually designated with "ν_i" where i is an integer.

In a very simple quantum mechanical "rigid rotator" model of a molecule, the rotational energy of a level is expressed as $E_{rot} = \frac{h^2}{8\pi I} J(J + 1)$ where J is the aforementioned rotational quantum number, h is the Planck constant, and I is the moment of inertia of the molecule. (In a simple classical model of a diatomic molecule, $I = \frac{m_1 m_2}{m_1 + m_2} r^2$, where m_1 and m_2 are the masses of the two atoms in the molecule and r is the internuclear distance.) A transition between two energy levels has a change of $\Delta E = E_2 - E_1$, which emits or absorbs a photon of frequency $\nu = \Delta E / h$. (See, e.g. Herzberg 1950; Hollas 2004)

Using a similar simplification, treating a molecule as a harmonic oscillator, the vibrational energy of a state is $E_{vib} = \frac{h}{2\pi} \sqrt{\frac{k}{\mu}} (v + \frac{1}{2}) = h\nu_{osc}(v + \frac{1}{2})$ where $\nu_{osc} = \frac{1}{2\pi} \sqrt{\frac{k}{\mu}}$ refers to the classical vibration frequency, and its associated spring constant k for a molecule with reduced mass $\mu = \frac{m_1 m_2}{m_1 + m_2}$ (for a diatomic molecule, as above for rotation) and "v" is the integral vibrational quantum number. (See, e.g. Herzberg 1950; Hollas 2004) A vibrational transition involves a specific ΔE and ν, as above. Combined ro-vibrational transitions involve a change in both rotational and vibra-

tional quantum numbers simultaneously. These are the types of transitions to be dealt with in this work.

However, in order for a molecule to be able to absorb or emit due to rotation and/or vibration, it must have a dipole moment in which the incident light can induce a change in energy. Thus, homonuclear molecules, such as H_2, cannot fluoresce in frequencies arising from rotation and/or vibration. This leads to constraints based on symmetry properties of molecules. CO_2, for example, is linear and symmetric (in the ground vibrational state), so it has no permanent dipole moment, and cannot absorb/emit rotationally. But it can do so vibrationally, because stretching or bending of its bonds would cause it to have a dipole moment.

Thus, due to these and other quantum mechanical rules, constraints exist, which lead to certain "selection rules" allowing or forbidding specific rotational, vibrational or combined (ro-vibrational) transitions between states.

1.4.2   Einstein Coefficients and Radiative Transfer

The probabilities of a molecule emitting or absorbing a photon of an allowed transition's energy (and thereby moving up or down in corresponding energy states and quantum numbers) were discovered and described by Einstein using coefficients he labeled "A" for spontaneous emission, and "B" for both absorption and stimulated emission. For clarity, when dealing with a specific transition, subscripts are often used to indicate the quantum states involved. These constants are highly dependent on the characteristics of a given molecule and a given transition, and therefore vary greatly.

Einstein related the probabilities of absorption and emission, for a given transition, to each other using "detailed balance":

$$g_1 B_{12} = g_2 B_{21}$$

$$A_{21} = \frac{2h\nu^3}{c^2} B_{21}$$

where the upper level of the transition of frequency ν is denoted by 2 and the lower level by 1, g is the statistical weight of a level and c and h denote the usual physical constants. (See, e.g. Rybicki and Lightman 1986, Chapter 1.)

The radiative transfer equation describes the changes in the specific intensity along a ray of light propagating through some medium. We can use the Einstein coefficients to express this equation in a manner that relates its values to these microscopic expressions for emission and absorption:

$$\frac{dI_\nu}{ds} = -\frac{h\nu}{4\pi}(n_1 B_{12} - n_2 B_{21})\phi(\nu)I_\nu + \frac{h\nu}{4\pi}n_2 A_{21}\phi(\nu)$$

where I_ν is the specific intensity at frequency ν, $\phi(\nu)$ is a line shape function and n_i denotes the population of molecular level i. This can be expressed more succinctly as

$$\frac{dI_\nu}{d\tau_\nu} = -I_\nu + S_\nu$$

where the source function is

$$S_\nu = \frac{n_2 A_{21}}{n_1 B_{12} - n_2 B_{21}}$$

and the change in optical depth, is designated by

$$d\tau_\nu = ds\frac{h\nu}{4\pi}(n_1 B_{12} - n_2 B_{21})\phi(\nu)$$

A medium is called optically thin if $\tau < 1$ and optically thick if $\tau > 1$. (See, e.g. Rybicki and Lightman 1986, Chapter 1.)

Similar coefficients can be used for collisional excitation and de-excitation, in which molecules transfer energy to and from each other by collisions, which also change their states by some quantized amount of energy. When collisions are dominant, a gas will be in "thermodynamic equilibrium," at some temperature T. The

collisional excitation and de-excitation will also be governed by detailed balance between them:

$$C_{21}n_2 = C_{12}n_1$$

and thus

$$C_{21} = C_{12}\frac{g_1}{g_2}e^{\frac{h\nu}{kT}}$$

In any given gas, the molecules will occupy different quantum states, in some statistical distribution based on properties of the gas including temperature and density and their exposure to radiation of appropriate frequencies. The relative fractional population of the quantum states of a gas can often be determined using statistical equilibrium (except in cases where evolution over time matters).

1.4.3 Application to Comets' Comae

Observed light of specific wavelengths can be used to determine amazing amounts of information about the source. That's what astronomers do! Of particular importance for cometary studies, we can derive abundances of molecular species in cometary comae.

In simple situations - i.e. when a gas is optically thin and without optical depth effects - the number of photons emitted, and hence the intensity of the light, is directly proportional to the number of molecules in the given upper state for that transition. If one observes the emission along a given column of gas, then $\mathcal{I}_\nu = 4\pi g N$ where $\mathcal{I}_\nu$ is the intensity in photons per second per cm^2 per steradian of the relevant frequency, g is the g-factor (photons emitted per second per molecule, generally referenced with the value at 1 AU) and N is the column density (number of molecules per cm^2). If the flux is in ergs/s/cm^2 or in Watts/m^2 then conversion to photons by dividing the energy by $h\nu$ (or hc/λ or hc/ω using frequency, wavelength or wavenumber, respectively, of the given light). Thus the column density can

easily be derived from the intensity observed. However, when large optical depth is an issue, the relation is not linear but much more complex, as we will discuss at length below.

The g-factor is closely related to the Einstein A coefficient. For a given upper level and a given transition out of that level, $g = A_{ul}N_u$ where N_u is the number density of that upper level population. $N_u = n_u N_{tot}$ where n_u is the fractional population of state "u" and N_{tot} is the total number density of the molecules integrated along the line of sight. Of course, more information or assumptions (e.g. assuming LTE, or some theoretical model) are necessary to know the molecular levels' population distribution.

From this, it is possible to make a rough determination of the production rate, again by using a model, one that relates column density (at some projected distance from the nucleus) to the total production rate. In general, the Haser model is the simplest, most widely used model. (See e.g. Haser 1957; Swamy 1997) If we assume a constant and isotropic production rate Q (molecules per second) from the nucleus, and a constant expansion velocity, v_{exp}, then (neglecting photo-dissociation) $n(R) = \frac{Q}{4\pi v_{exp}R^2}$ is the number density at a distance R from the center. At a projected distance (or impact parameter) ρ from the center (as seen in the plane of the sky for an observation) the column density will then be $N(\rho) = \frac{Q}{4v_{exp}\rho}$. Inverting this equation makes it possible to calculate production rates of a comet based on column density observed at some radial distance: $Q = N(\rho)4v_{exp}\rho$.

This is an extreme simplification, which we nonetheless use in this work. A slightly better model would multiply the above expression for $n(R)$ by e^{-R/R_d} where $R_d = v_{exp}\tau$ where τ is the photodissociation lifetime of the molecule. Even this is quite a simple model. Better treatments are possible that could account for both creation and dissociation of parent and daughter molecules, acceleration of the coma

18

gas, and excess energy released on dissociation. (See e.g. Combi 1989, 1996)

1.5 Motivation for This Study

Our goal is to better understand the abundances, distributions and creation mechanisms of various gases observed in comae.

This research is particularly motivated by observations of comet 9P/Tempel 1, the target of the Deep Impact Mission, and 103P/Hartley 2, the subject of the EPOXI mission. Those missions succeeded in providing a wealth of new spectral information on those comets, with an unprecedented combination of spatial and spectral resolutions. (A'Hearn et al. 2011; Feaga et al. 2007a)

In order to do so, I have built a computer model of the spectra of the comet's coma that includes the difficult and often ignored problem of accurately including radiative transfer to account for the potentially optically thick coma (or regions of the coma) near the nucleus. The model includes radiative transfer calculations using our spherical adaptation of the Coupled Escape Probability method (hereafter, "CEP"; see Elitzur and Asensio Ramos 2006, hereafter, "CEP06") to more correctly model optically thick (or potentially thick) regions of cometary comae.

My model will facilitate analyzing the actual spectral data from the Deep Impact and EPOXI missions to better determine abundances of key species, including CO, CO_2 and H_2O, as well as remote sensing data on active comets.

1.5.1 Outline

In the following chapter (Chapter 2) of this work, I first describe the method I have crafted for our model. Then, in Chapter 3, I present and discuss results of modeling spherical comae (i.e. with no morphological features) for general, hypothetical, comets of varying production rates and for Comet C/2009 P1 Garradd, which was observed distantly and without morphology. Finally, in Chapter 4, I present results including observed near nucleus morphology for comets 9P/Tempel 1 and 103P/Hartley 2, the targets of the Deep Impact and EPOXI missions.

Chapter 2

The Modeling Method

2.1 Overview of the Model

We begin our modeling of IR ro-vibrational spectra of a coma by initially following the method used by Chin and Weaver (1984), Crovisier (1987), and others for optically thin cases, with some minor improvements (see Sec. 2.3).

Our major improvement is the inclusion of radiative transfer calculations using our own spherical adaptation of the Coupled Escape Probability method (see Elitzur and Asensio Ramos 2006) to more correctly model optically thick (or potentially thick) regions of cometary comae. This is described in detail below, and is the main part of the research work done here. We use the coma integration results to provide the "initial guess" values for populations used in the subsequent radiative transfer calculations using CEP.

For the purposes of the initial coma model, we treat the comet as spherically symmetric, and as having a uniform and constant gas production rate over its entire surface.

Additionally, we can include coma morphological features. Such features, as seen in the Deep Impact and EPOXI encounters, are a main motivation for creating this model to better understand possible optical depth effects in the near-nucleus regions of the coma. (See e.g. A'Hearn et al. 2011; Feaga et al. 2007a) These are done using a separate integration, with different parameters, which is then included in the radiative transfer model for a specified cone-shaped feature.

2.2   The Coma Model: The Initial Step

The first step of our model is similar to earlier ones (e.g. Chin and Weaver 1984; Crovisier 1987) but more developed. Like those models, we numerically integrate over time the linear differential equations defined by the rate constants.

$$\frac{dn_k}{dt} = \sum_i (A_{ik}n_i + J_{\nu_{ik}}(B_{ik}n_i - B_{ki}n_k)) + \tag{2.1}$$

$$- \sum_l (A_{kl}n_k + J_{\nu_{kl}}(B_{kl}n_k - B_{lk}n_l)) +$$

$$\sum_j C_{jk}(n_k - n_j e^{-E_{jk}/k_B T})$$

Here i, j, k and l indicate energy levels of a molecule with the n's with those indices being the corresponding level populations. A_{xy} and B_{xy} are the Einstein coefficients between levels x and y, C is a similar collisional coefficient, $J_{\nu_{xy}}$ is the mean intensity of radiation at the frequency corresponding to the transition between x and y, E_{xy} is the energy difference between levels x and y, and k_B and T have their usual meanings. The summations are over all levels i, l or j which have a transition into or out of level k. For collisional coefficients, $C = n_{H_2O}\sigma\bar{v}$ where n_{H_2O} is the number density of H_2O (assumed to be the dominant collisional partner), σ is the collisional cross section for a given transition, and $\bar{v}$ is the mean (thermal) molecular speed.

This formulation (Eqn. (2.1)) is equivalent to that used by Chin & Weaver for the specific case of CO, which can be expressed as in their formulation:

$$\frac{dn_J^v}{dt} = A_{J-1,J}^{v+1,v}n_{J-1}^{v+1} + A_{J+1,J}^{v+1,v}n_{J+1}^{v+1} + \tag{2.2}$$

$$A_{J+1,J}^{v,v}n_{J+1}^v + B_{J+1,J}^{v-1,v}\rho n_{J+1}^{v-1} +$$

$$B_{J-1,J}^{v-1,v}\rho n_{J-1}^{v-1} + \sum_{k=0}^{J_{max}} C_{k,J}n_k^v -$$

$$\left[A_{J,J-1}^{v,v-1} + A_{J,J+1}^{v,v-1} + A_{J,J-1}^{v,v} + \right.$$

$$\left. B_{J,J+1}^{v,v+1}\rho + B_{J,J-1}^{v,v+1}\rho + \sum_{k=0}^{J_{max}} C_{J,k} \right] n_J^v$$

Where n_J^v is the fractional population of the energy state with vibrational number v and rotational number J. dn_J^v/dt is the rate of change of the fractional population of that energy level. The A's and B's are the Einstein coefficients for spontaneous emission and stimulated emission/absorption respectively. ρ is the solar photon density (a function of solar distance, here taken to be 1 AU, and in the relevant frequencies.) The C values are collisional rate coefficients. The first subscript or superscript attached to a constant represents the initial level of a transition and the second subscript or superscript is the final level of a transition. Thus, Eq. (2.1) implicitly incorporates (via its sub- and super-scripts) the selection rules for rotational and ro-vibrational transitions ($\Delta J = \pm 1$ and $\Delta v = \pm 1$). As per Chin and Weaver (1984), we do not consider electronic transitions. They assumed that those would require higher energies than are expected in a typical cometary coma (except in comets nearer than $\sim$1 AU when high solar pumping may happen).

As in most earlier models, we assume a constant expansion velocity, thus linearly relating any radial distance to a specific time since a "parcel" of gas was released from the surface of the nucleus. Therefore we can numerically integrate over time the linear differential equations defined by the Einstein coefficients and collisional rate coefficients to get fractional molecular energy level populations for each distance from the nucleus, from which we could calculate emission spectra, as in those earlier models. However, instead of ignoring optical depth and immediately calculating emission spectra, we use these values as the initial basis for our coma model before including the subsequent radiative transfer calculations. This manner of coma integration allows us to include a time-variable production rate.

We ignore the photodestruction of CO in our coma model, due to its long lifetime (see Crovisier 1994). The lifetime at 1 AU is $> 10^7$ s, and we are integrating out to 10^5 km with a typical expansion velocity of $0.5 \sim 0.8$ km/s. (Note that others, e.g. Morgenthaler et al., 2011, find a shorter lifetime, but still $\gtrsim 4 \times 10^5$ s, which is large enough that it can be neglected in our modeling out to 10^5 km.)

The expansion speed of the coma gas is also assumed to be constant, as per Chin and Weaver (1984), who used a value of 0.8 km/s. (Later we can vary this value.) Note that this is not physically accurate (see Combi 1989) but the variation over distance is relatively small. These approximations make integration of Eqn. (2.1) or (2.2) over time equivalent to calculating these values over increasing distances from the comet nucleus for a "shell" of gas expanding outwards from the nucleus.

We have improved on earlier CO models by adding the capability of including an arbitrary number of different rotational and ro-vibrational energy levels. In our initial CO simulations, we still use the same number of levels as Chin and Weaver (1984); two vibrational ($v = 0, 1$) and 21 rotational levels ($J = 0..20$) for a total of 42 levels. Our model is also enhanced to include changing the temperature, gas velocity and production rates.

For CO, we calculate the Einstein coefficients based on Chin and Weaver's (1984) equations, but have (re)calculated the transition frequencies used based on first principles (as per Herzberg 1971) and constants supplied by (Krupenie 1966). This is necessary to add extra energy levels not included by Chin and Weaver (1984). For other molecules (so far, only H_2O and CO_2) we take the necessary energy values from the HITRAN database. (Rothman et al. 1998) Similar to the case for CO, we can use a variable number of levels for models of other molecules simply by using a selected subset of data from the database.

2.2.1 Collisional Excitation

The varying temperature and density conditions are significant in the calculations of collisional rates, which are the only coefficients in Eqn. (2.1) to vary over time. The collisional rate coefficients used are also based on Chin and Weaver (1984). They are expressed here using CO as an example, but are adapted to other species using a similar treatment.

We have adopted an extremely simplified treatment of collisional excitation and de-excitation.

The coefficients for CO-H_2O collisions (H_2O is normally assumed to be the dominant volatile and thus the dominant source of collisional excitation of CO, albeit with exceptions such as Comet Garradd, at 2 AU) are as per Chin and Weaver (1984): only rotational excitation and de-excitation are considered. (Vibrational cross sections are about 5 orders of magnitude smaller. See Weaver and Mumma, 1984, Table 2.)

$$C_{J,J'} = \sigma_{J,J'} n_{H_2O} \bar{v} \tag{2.3}$$

where $C_{J,J'}$ is the probability of a collisionally induced transition from level J to J', n_{H_2O} is the number density of H_2O (cm^{-3}) and $\bar{v}$ is the average relative speed of the molecules (cm s^{-1}) of CO and H_2O. $\sigma_{J,J'}$ is the collisional cross-section and is based on a de-excitation total cross section of $\sigma_{tot} = 1.32 \times 10^{-14}$ cm^2, which is apportioned between $\Delta J's$ up to 6 as per Chin and Weaver's (1984) Table 1, which we reproduce here in our Table 2.1.

We also use detailed balance to get the corresponding excitation cross sections as per Goldsmith (1972) (also e.g. Swamy 1997):

$$\sigma_{l \to u} = \sigma_{u \to l} \frac{g_u}{g_l} exp \left[-\frac{E_u - E_l}{kT_{kin}} \right] \tag{2.4}$$

Table 2.1: Reproduction of Chin & Weaver's Table of CO-H_2O Collisional Cross Section Information.

Δ J = J$_{upper}$ - J$_{lower}$	Fraction of Total De-Excitation
1	0.34
2	0.25
3	0.20
4	0.10
5	0.07
6	0.05
>6	0

Total cross section is always $\sigma_{rot} = 1.32 \times 10^{-14}\ cm^2$.
Excitation is derived from de-excitation using
detailed balance.

where subscripts l and u denote the values for the lower and upper levels, respectively, for cross-sections (σ), energies (E) and statistical weights (g), k is the Boltzmann constant and T_{kin} the (kinetic) temperature. More detailed calculations of the contributing average relative velocities of molecules, used in deriving the collisional coefficients, are found in Swamy (1997):

$$\bar{v} = \left(\frac{8kT}{\pi} \left[\frac{1}{m_{H_2O}} + \frac{1}{m_{CO}} \right] \right)^{1/2} \tag{2.5}$$

where, once again, k is the Boltzmann constant and T the temperature and the m's denote the molecular masses of H_2O and CO (or some other species being integrated).

For other molecules we have modeled, the collisional cross section for H_2O-H_2O collisions for de-excitation is taken from Weaver and Mumma's (1984) Table 2 to be $2.5 \times 10^{-15}\ cm^2$. For CO_2-H_2O collisions a total collisional cross section for de-excitation taken from Weaver and Mumma's (1984) Table 2 to be $3.6 \times 10^{-15}\ cm^2$.

Using these values, the coefficients for H_2O-H_2O or CO_2-H_2O collisions can then be calculated as per Chin and Weaver (1984): only rotational excitation and de-excitation are considered. Since the simple rotational energy level structure of CO

27

is *not* found in H_2O or CO_2, we adapted the method to use an energy level ordered index number instead of ΔJ.

After initially using the above method for all three molecules, it became clear, especially for CO_2, that it was an imprecise treatment that led to poor model fitting of the DI data. We subsequently modified the apportioning of σ_{tot} between $\Delta J's$ for CO_2 and tested multiple methods suggested by Goldsmith (1972). We found his first option, using σ_{tot} as the cross-section for all downward $\Delta J's$ (not only up to $\Delta J=6$) to be a better choice for us to produce results that matched our available CO_2 data. Note that this approach effectively increases σ for all transitions to σ_{tot}, i.e. equal to the former total value in the approach used by Chin and Weaver (1984). However the exponential and statistical weights in Eq. 2.4 still cause the populations to maintain a similar distribution, while increasing the strength of collisional vs. radiative excitation. Also note that Goldsmith (as well as Chin & Weaver) suggest both that little is truly known about accurate calculation of these collision rates and that there is little difference between these approaches, at least for CO. (Even less seems to be known for CO_2.) Thus what may seem like arbitrary ad hoc modifications can be justified by the fact that the initial method was also somewhat arbitrary, and certainly not intended for molecules other than CO.

2.2.2 Integration Technique and Software

We solve for the initial conditions in the same manner as Chin and Weaver (1984) and Schleicher (1983). We set all the $dn_J^v/dt = 0$ at the surface of the comet nucleus and replace one of the equations of the above system (Eq. (2.1)) with

$$\sum_v \sum_J n_J^v = 1. \tag{2.6}$$

The fact that all fractional populations must sum to equal one (i.e. together all energy levels contain the total amount of the given species) is the source of this

normalization condition.

These linear equations (Eq. (2.1) and (2.6)) are then solved for n_J^v with LU decomposition with back substitution, using the **ludcmp** and **lubksb** routines from Press et al. (1992).

The numerical integration of Eq. (2.1) is done using methods from Press et al. (1992) which are able to solve "stiff" systems of equations (where the orders of magnitude of coefficients differ greatly, as is the case here where rate constants even for the ambient coma conditions range from $\sim 10^2 s^{-1}$ to $\sim 10^{-8} s^{-1}$). See Appendix A-C for further details of the computer algorithms and code.

The values of the integration, all the n_J^v's of Eq. (2.1) for each step of the integration passing an integral number of seconds, are saved in an output file.

2.2.3 The Temperature Model

In their coma integration, Chin and Weaver (1984) use a kinetic temperature profile based on Marconi and Mendis (1982). This profile starts at the nucleus with a temperature of ~ 187 K and cools rapidly to a minimum of T ~ 5 K at a distance ~ 50 km from the nucleus. Beyond ~ 100 km, photolytic heating gradually heats the gas up again. They derived a polynomial fit to model Marconi and Mendis's (1982) Fig. 1. However, there remains some question as to their fit at large distances. Marconi and Mendis integrated their profile only out to $r = 2.5 \times 10^4$ km, while Chin and Weaver's integration (and presumably their polynomial fit) goes out to 10^5 km. Chin and Weaver do not explain what they used beyond that radius. Based on their Fig. 5, they seem to have simply extended it past 10^4 km with a constant temperature of 500 K. Marconi and Mendis state that their (original) integration took the temperature up to 520 K at $r = 10^4$ km and 810 K at $r = 2.5 \times 10^4$ km. I initially attempted to use the same profile as Chin and Weaver (see Fig. 2.1) in our

29
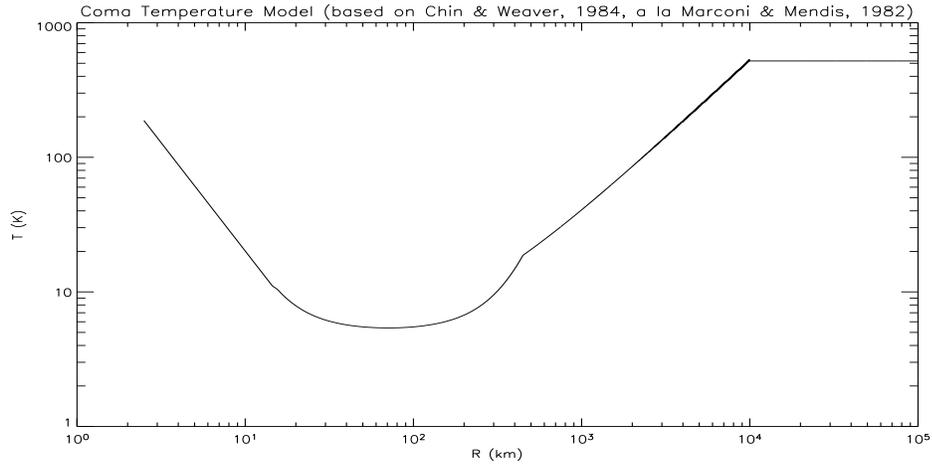
Figure 2.1: Temperature profile of cometary atmosphere used by Chin & Weaver (1984; approximate.) Based on Marconi and Mendis (1982).

testing phase, in order to duplicate their results, albeit without precisely duplicating their polynomial fit. We estimate the maximum temperature from Chin and Weaver (1984) Fig. 5 to be about 500 K, and use that value, even though it is certainly not the result of the Marconi and Mendis (1982) integration.

It should be noted that Marconi and Mendis (1983) calculated an improved model and that the model used by Chin and Weaver (1984) is no longer considered to be accurate. Combi (1989) subsequently also improved the temperature profile (see below), although the difference between Marconi & Mendis' improved model (1983) and Combi's is much less than the difference between Marconi and Mendis' original (1982) model and either of the later ones. The more recent models have a maximum temperature $\sim 10^2$ K or less at larger distances, a significant difference from the model used by Chin and Weaver (1984).

2.2.4 Model Verification Results

We tested our model to verify its validity by comparing results with Chin and Weaver (1984). For this stage, we used the same physical parameters of a "typical" comet as they did, most notably the temperature profile (see above). Other "inputs" included a nucleus of radius 2.5 km and production rates of $Q_{H_2O} = 2 \times 10^{29}$ and $Q_{CO} = 2 \times 10^{28}$ molecules per second (at a heliocentric distance of 1 AU.) Radial outflow velocity is taken to be a constant 0.8 km s^{-1}. Solar flux (in the relevant bands) is also assumed to be a constant, 2.5×10^{13} photons $\cdot$ cm^{-2}s^{-1}/cm^{-1} (also a 1 AU value.) As in Chin and Weaver (1984) Fig. 1, we encapsulate the relative population levels resulting from our integration in contour plots (Figs. 2.2 & 2.3). Each contour line represents a certain value of a fractional population (generally in powers of 10) and the points at which a contour intersects a given level (x axis values) indicates the population of that level, at a given radius from the center of the comet (y axis values). Our results are quite similar to those of Chin and Weaver (1984). Some of the (minor) discrepancies can be explained due to the resolution of the integration (which has varying step sizes, which can get quite large) and the different plotting methods. (Their curves appear smoother than ours, an effect which we believe was produced due to our using IDL's contour function along with the granularity of our data.) More significant differences are most likely due to the difficulties mentioned above in the precise duplication of their temperature profile.

For comparison with Chin and Weaver (1984), we also produced spectral plots of the IR(1,0) band. In general, ours were integrated along a line-of-sight column (which approximates the much higher spatial resolution of the Deep Impact Flyby Spacecraft) as opposed to the 1' and 4" fields of view used by Chin and Weaver (1984) to simulate Earth-based observations. We created an average spectrum of

31
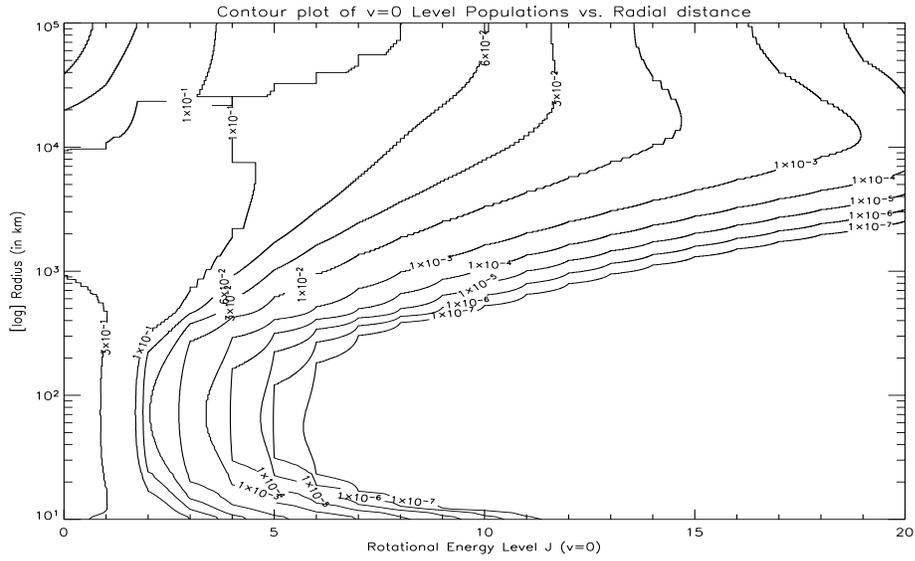
Figure 2.2: Contour plot of relative populations of rotational levels in v=0 vibrational level. Plot for the ambient coma based on Chin & Weaver's (1984; Marconi & Mendis, 1982) temperature model.
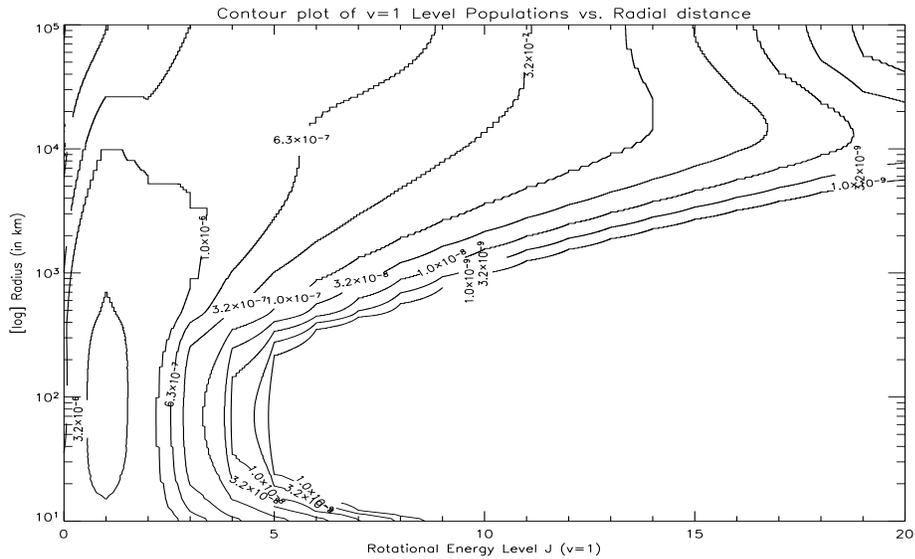
Figure 2.3: Contour plot of relative populations of rotational levels in v=1 vibrational level. Plot for the ambient coma based on Chin & Weaver's (1984; Marconi & Mendis, 1982) temperature model.
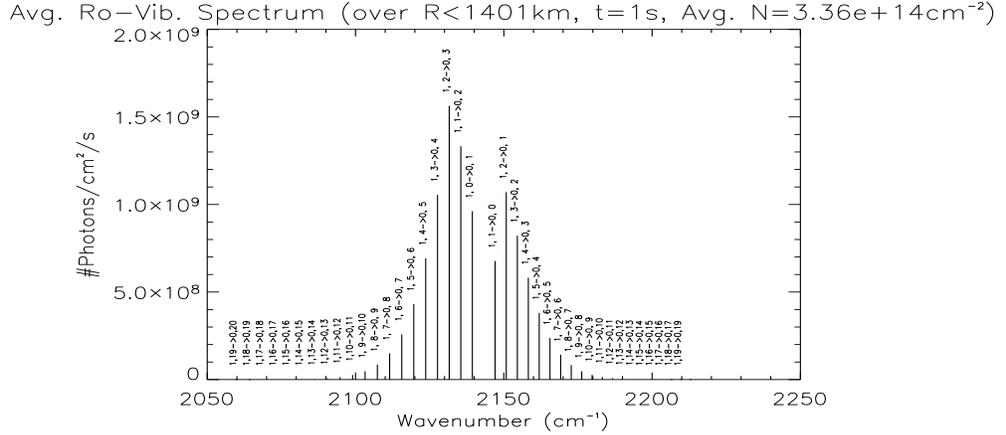
Figure 2.4: Our IR(1,0) Rotational-Vibrational Spectra averaged over the center of the comet out to 1400 km (to approximate Chin and Weaver's (1984) 4" FOV).

the comet, which approximates their 4" FOV. (See Fig. 2.4 and Fig. 2.5 for a plot of the 4" FOV intensity data from their Table 2. Note that their Table 2 does not include as many lines as our spectra, thus explaining the absence of the lines near the fringes in our plot of their data.) This yields an average column density close to $\sim 10^{15}$ cm^{-2}, about the same as Chin and Weaver's (1984) 4" FOV. Note that our results are plotted in different units than Chin and Weaver's for historical reasons; the numbers calculated from their table are *per steradian* whereas ours are averaged over the 4" FOV discussed (approximately). The conversion factor is $4'' \times (1\text{sr}/4.25 \times 10^{10}'')$. The IR(1,0) band spectra resulting from our simulation depicted in Fig. 2.4 could also be *loosely* compared with Chin and Weaver's (1984) Fig. 10 with respect to *general shape only*. (Their plot of *g*-factors differs from our plot of photons/cm^2/s but should represent the same relative level populations.)
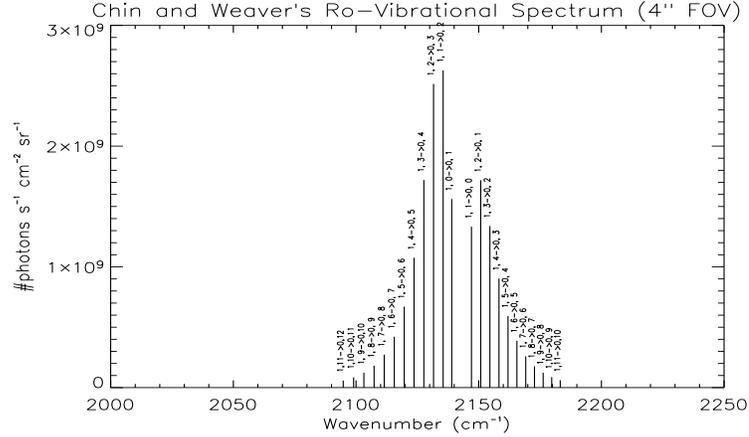
Figure 2.5: Chin and Weaver's (1984) IR(1,0) Rotational-Vibrational Spectra averaged over a 4" FOV (plot of values from their Table 2, in converted units).

2.3 Improvements to the Model

2.3.1 The Temperature Model

As mentioned above, Marconi and Mendis's (1982) temperature model used by Chin and Weaver (1984) has been superseded. Therefore, to improve the accuracy of our model we use Combi's (1989) temperature profile.

We have also expanded on the capabilities of the model to create a profile for any desired temperature at the comet's surface, based on Combi's profile. From the given initial surface temperature, the model cools down with increasing radius to the same minimum temperature as the original Combi profile (in an equal cooling *time*, as opposed to *distance*) and then continues to behave in the original manner. Figs. 2.6, 2.7 and 2.8 are log-log plots of our modified Combi profile, for a surface temperature of 200 K, 500 K and 2000 K, respectively.

One feature to note from these, most notably Fig. 2.8, is that even when the surface temperature is so much higher than the ambient case, the cooling curve is
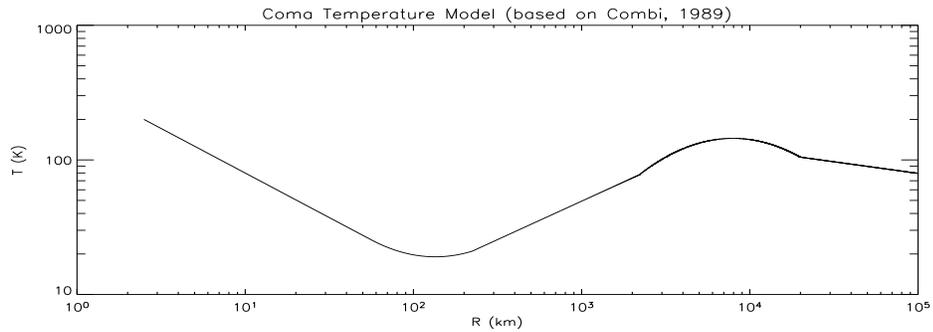
Figure 2.6: Temperature profile of cometary atmosphere based on Combi (1989) for ambient coma conditions: surface temperature of 200 K and radial gas velocity of 0.8 km/s.
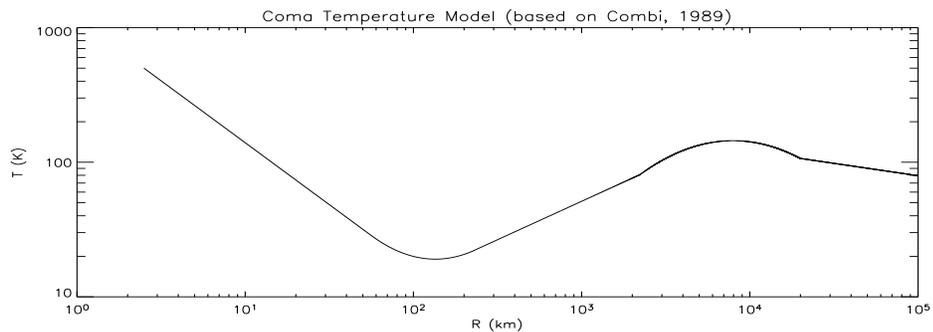
Figure 2.7: Temperature profile of cometary atmosphere with surface temperature of 500 K and radial gas velocity of 0.8 km/s, based on Combi (1989).

still quite steep, and within 10–20 km of the nucleus the temperature is already about the level of the ambient surface, and the cooling reaches its minimum at a distance of only slightly more than 100 km.
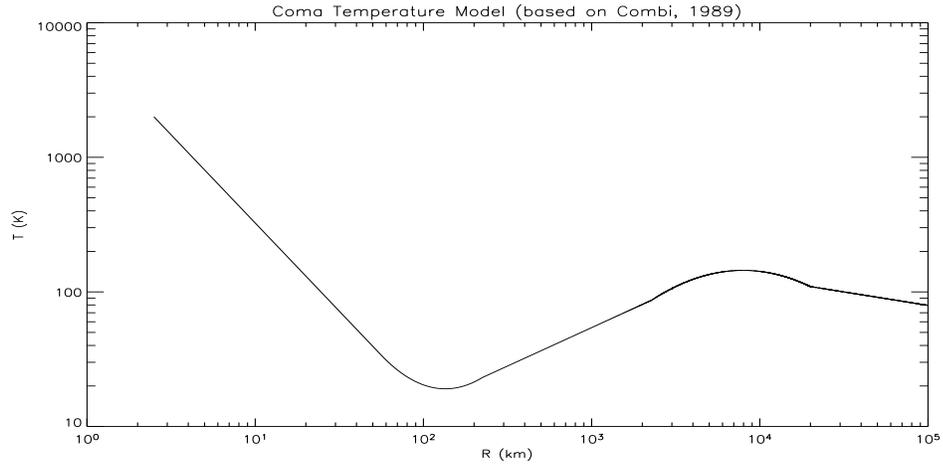
Figure 2.8: Temperature profile of cometary atmosphere with surface temperature of 2000 K and radial gas velocity of 0.8 km/s, based on Combi (1989).

2.3.2   Other Parameters

Our code also can take as input parameters different comet radii, production rates and gas outflow velocities. In addition, we can specify various parameters of the numerical integration and can choose a "fluorescence only" or a "collisional only" (thermally dominated) integration scenario. This is useful for testing against earlier models that used a more simple treatment of excitation (e.g. Crovisier 1987; Weaver and Mumma 1984). In addition, the code can also be switched between Combi and Chin and Weaver (1984)/Marconi and Mendis (1982) temperature profiles.
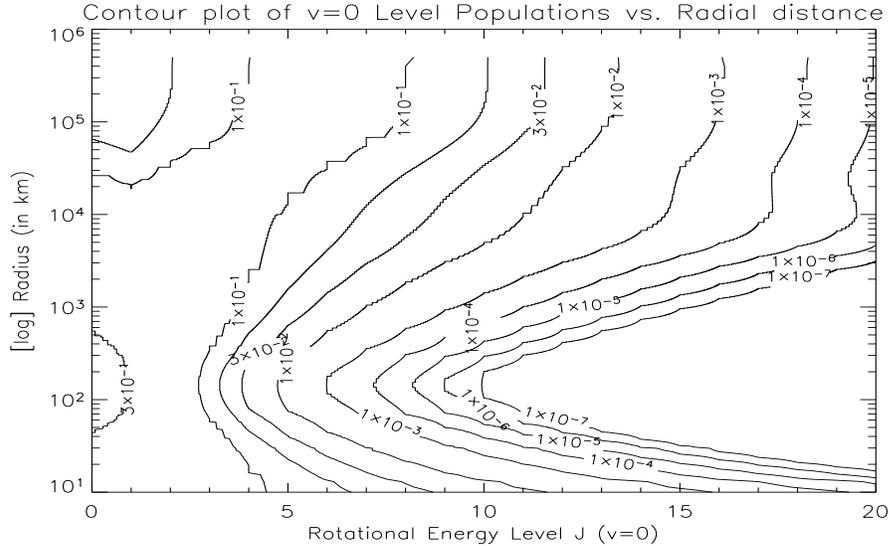
Figure 2.9: Contour plot of relative populations of rotational levels in v=0 vibrational level. Plot for the ambient coma based on Combi temperature model.

2.4 Improved Model Results for the Simple Coma

The most noticeable difference in the results obtained with our new improved model using Combi's temperature profile relate to the thermal conditions of the coma. The population levels vary in an approximately similar manner to the old model (compare Figs. 2.9 and 2.10 with Figs. 2.2 & 2.3). Especially for smaller radii ($r < 10^3$ km), where temperatures are mostly cool, the lower J states contain most of the population, and result in a "peak" near the center of the spectra (near 2140 cm^{-1}). Very far out in the coma ($r > 2 \times 10^5$ km) the rotational distribution is more spread out, as conditions reach fluorescent equilibrium, close to the typical distribution of the population when only radiative excitation is considered.

However, it is in the "transition region" discussed by Chin and Weaver (1984) that our model is most different from theirs. This is not surprising, as this is also the region where the temperature profiles diverge most dramatically, but are still

37
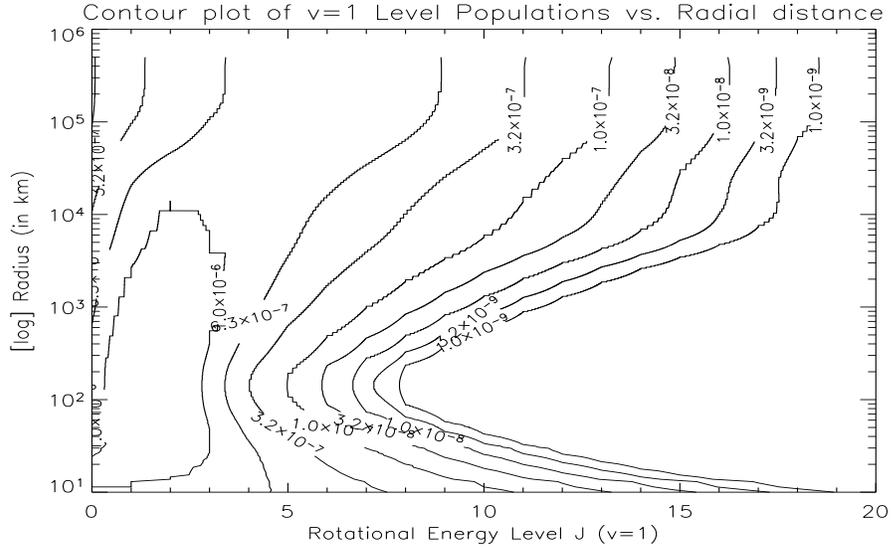
Figure 2.10: Contour plot of relative populations of rotational levels in v=1 vibrational level. Plot for the ambient coma based on Combi temperature model.

very significant before the fluorescent regime has been reached.

Chin and Weaver (1984) discuss the "relaxation" their DGEAR model requires to transition from the inner collisionally dominated region to the outer fluorescence-dominated regime. Our model transitions between the two regimes more smoothly than theirs. Notice the sharper bends in the contour lines of their Fig. 1 near $r \sim 10^4$, and the "lobes" of 10% population value which reach towards each other across the 10^4 "boundary." (These are more clearly visible in their original plots than in our reproduction of their data.) Also recall that in their modified Marconi and Mendis (1982) temperature profile, we believe $r \sim 10^4$ km to be the final turning point after which the temperature remains constant (see above discussion and especially Fig. 2.1). In our model's contour plots, these features are reduced or nonexistent due to our smoother regime change. Judging from our reproductions of their results, it would seem that the different temperature profiles are not the only reason for a smoother transition, but that our software has produced a (marginally) smoother

transition even with the same temperature profile (Figs. 2.2 and 2.3).

Overall, these results seem to primarily indicate that energy level populations in the cometary coma, especially at greater distances, vary more smoothly than Chin and Weaver's (1984) earlier results would indicate. Since this model uses a less dramatically varying temperature profile, that is to be expected. It should be noted that Chin and Weaver (1984) themselves found similar smoother variation for their DGEAR simulation when using an isothermal temperature profile (T = 200 K), which is more similar to the Combi profile we have used.

2.5 Our Method: CEP Adapted for an Asymmetric Spherical Case

This section describes our adaption of the Coupled Escape Probability radiative transfer technique to spherical cases in which the plane parallel approximation is not appropriate, including most cometary problems. (Note that Yun et al., 2009, previously adapted CEP for *purely symmetric* spherical cases.) We have developed this model specifically for use in studying cometary comae, but it could be applied to many other astrophysical phenomena as well (e.g. planetary atmospheres, molecular clouds, etc.).

The CEP method (see CEP06) divides up a plane-parallel "slab" into "zones" (each of which has uniform properties) and calculates the net radiative bracket ("p") that is multiplied by the Einstein A coefficient in the equations of statistical equilibrium (see Eqn. 2.1) for each radiative transition for each zone. (Note that the "p" term effectively combines the "B" terms into the "A" term. See CEP06 for more detail.) The innovation of CEP is that the net radiative brackets for each zone can accurately represent the contributions of *all* zones' emission and absorption to/from other zones. This is in distinction to "plain" Escape Probability where a similar factor added to the statistical equilibrium equations is only a *local* approximation of a photon's likelihood of escaping the entire slab. (See Bockelee-Morvan 1987; Litvak and Kuiper 1982; Zakharov et al. 2007) The statistical equilibrium equations for all zones, with the inclusion of the net radiative bracket, form a single non-linear matrix. This matrix can be solved using an algorithm for non-linear matrix solving such as Newton's Method. We use functions from Numerical Recipes in C (Press et al. 1992) for the Newton based matrix solver, as well as other calculations such as numerical integration. This solution yields the fractional populations of

molecular energy levels for each zone. From these, the flux emitted by the slab can be calculated. See CEP06 for more details and the derivations of the original plane-parallel equations to which we make reference below.

A brief explanatory note is in order here. The solution of the CEP matrix is effectively calculating (coupled) equilibrium solutions for the populations of all Zones (or Regions). Despite the fact that the method uses the Chin and Weaver (1984) integration results as the initial guess, the CEP solution does not necessarily maintain the "non-equilibrium quality" of that integration. This is *not* to say that the solutions are for either the LTE or fluoresence equilibrium conditions, but often for some balance between those two extremes (as in the "transition region" of the Chin and Weaver, 1984 results), with a full treatment of radiative transfer included to arrive at these calculated populations. Furthermore, in most cases the physical size of the Zones/Regions is large enough that at typical expansion velocities and for typical transition rates (of the molecules/bands we have studied here) the expanding gas *would* have sufficient time to relax to equilibrium within a Zone/Region.

We derive expressions analogous to the relevant CEP06 equations, adapted from the plane parallel situation to spherically symmetric cases. Then we include asymmetries of two different types: radiation from an outside source (here, the Sun) and non-uniform conditions due to morphology.

2.5.1 Net Radiative Bracket: Theoretical/Analytical Expressions

In CEP06 equation 7, Elitzur & Asensio Ramos derive a purely analytical expression for the net radiative bracket in a plane parallel slab, based on the formal solution of the radiative transfer equation and the definition of the net radiative bracket:

$$p(\tau) =$$

$$1 - \frac{1}{2S(\tau)} \int_0^{\tau_t} S(t)dt \int_{-\infty}^{\infty} \Phi^2(x)dx \int_0^1 e^{-|\tau - t|\Phi(x)/\mu} \frac{d\mu}{\mu} \qquad (2.7)$$

where τ and t refer to optical depths, with τ_t being the overall optical thickness of the slab, $S(\tau)$ or $S(t)$ to the source function for a given line, $(S_{\nu_{21}} = \frac{A_{21}n_2}{B_{12}n_1 - B_{21}n_2})$ $\Phi(x)$ is a dimensionless line profile, and $\mu = \cos\theta$, where θ is the angle of a given ray measured from the normal to the plane.

We use a spherical analog to this theoretical expression (i.e. as opposed to the discrete expression they introduce later involving a number of "zones") for the net radiative bracket:

$$p(\tau(r, \theta, \phi)) =$$

$$1 - \int_{4\pi} \left[\frac{1}{2S(\tau(r, \theta, \phi, \Omega))} \int_0^{\tau(r,\theta,\phi,\Omega)} S(t(r, \theta, \phi, \Omega)) \right.$$

$$\left. \times \int_{-\infty}^{\infty} \Phi^2(x) \left(e^{-|\tau(r,\theta,\phi,\Omega) - t(r,\theta,\phi,\Omega)|\Phi(x)|} \right) dx \, dt \right] d\Omega \qquad (2.8)$$

where $p(\tau(r, \theta, \phi))$ refers to the net radiative bracket at any point labeled by the coordinates (r, θ, ϕ) in spherical coordinates with the origin at the center of some sphere of interest. (In our study, the sphere is centered on the comet nucleus; it could be the center of any spherical astronomical object for any given case.)

As in CEP06, $\Phi(x) = (\pi \Delta\nu_D)^{-1/2} e^{-x^2}$ is a dimensionless line profile, normalized so that $\int \Phi(x)dx = 1$, where $x = (\nu - \nu_0)/\Delta\nu_D$ is the dimensionless line shift from line center ν_0 and $\Delta\nu_D$ is the doppler line width, $\nu_0/c(2kT/m)^{1/2}$. In the present work, we extend the CEP06 treatment of line profiles (which for the sake of presentation of a simple example used a $\Phi(x)$ that was the same throughout). We have included variations in line width (due to temperature) and doppler shifts

42

between different regions of the coma. The latter have been calculated for all three relevant aspects of the model with differing line of sight velocities: incident solar radiation, emergent flux along the observers' line of sight and the calculation of the net radiative bracket between regions in the coma.
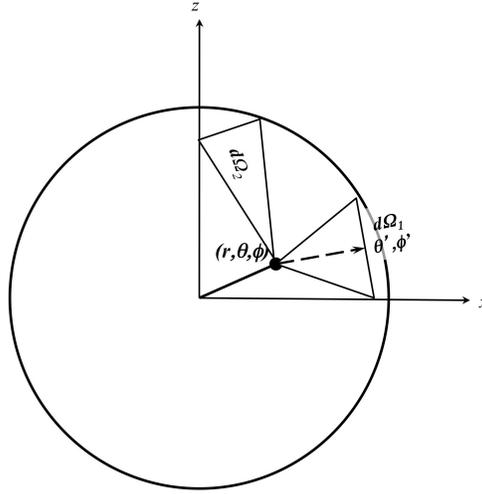
Figure 2.11: Sphere showing a point (r, θ, ϕ) and two solid angle elements $d\Omega_1$ and $d\Omega_2$. (Viewed from the $-y$ direction.)

Both $\tau(r, \theta, \phi, d\Omega)$ and $t(r, \theta, \phi, d\Omega)$ refer to optical depths and $S(\tau(r, \theta, \phi, d\Omega))$ to the source function *as viewed from the coordinates* (r, θ, ϕ) along a "pencil" of solid angle $d\Omega$.

The optical depth along a "pencil" (or cone) of solid angle $d\Omega$ is, of course, highly dependent on the particular direction of a given solid angle element $d\Omega$, i.e. dependent on θ', ϕ', the direction of a vector centered on (r, θ, ϕ) pointing along the centerline of $d\Omega$. (See Fig. 2.11.)

2.5.2 Discrete Expressions for p

The above CEP06 expression for $p(\tau)$ (2.7) is turned into a discrete expression by dividing the slab into multiple "zones" (labeled with index i or j). This yields CEP06 equation 14:

$$p^i = 1 - \frac{1}{2\tau^{i,i-1}S^i} \sum_{j=1}^{z} S^j \times \int_{\tau^{i-1}}^{\tau^i} d\tau \int_{\tau^{j-1}}^{\tau^j} dt$$

$$\times \int_{-\infty}^{\infty} \Phi^2(x)dx \int_0^1 e^{-|\tau-t|\Phi(x)/\mu} \frac{d\mu}{\mu}$$

(2.9)

This expression for p can be calculated for each zone (and each wavenumber/frequency) and the resultant p's included in the equations of statistical equilibrium, which are then solved. (See also CEP06 equations 32-36, and accompanying CEP06 text, for a more complete discussion.)

Similar to CEP06 Eqn. 14, for the purposes of our integration of a discrete p^i the sphere is divided into spherical shells (analogous to the plane-parallel zones of the original CEP) where i (or j) is a shell index. (See Fig. 2.12.) The integration is broken down into a sum of integrals along different "cones" of solid angle (the aforementioned $d\Omega$'s). Note that although $d\Omega$ may seem somewhat conceptually analogous to $d\mu$ in the plane-parallel case, we cannot use the convenient exponential integrals as in the plane-parallel situation, but instead must integrate along each $d\Omega$ separately.

$$p^i = 1 - \int_{4\pi} \left[\frac{1}{2\tau^{i,i-1}(\Omega)S^i} \sum_{j=1}^{z} S^j \int_{\tau^{i-1}(\Omega)}^{\tau^i(\Omega)} d\tau \int_{\tau^{j-1}(\Omega)}^{\tau^j(\Omega)} dt \right.$$

$$\left. \times \int_{-\infty}^{\infty} \Phi^2(x)dx \left(e^{-|\tau(\Omega)-t(\Omega)|\Phi(x)} \right) \right] d\Omega$$

(2.10)
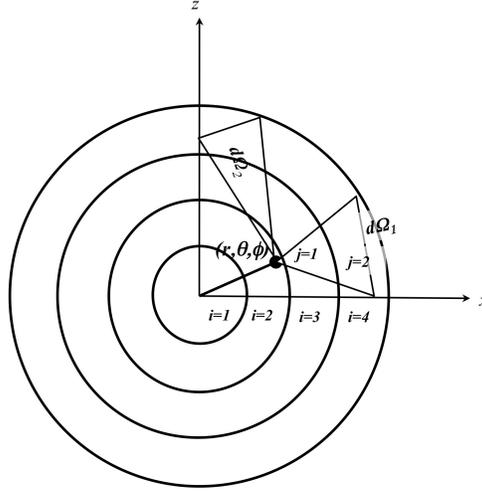
Figure 2.12: Example sphere showing division into 4 shells, $i = 1..4$ and solid angle $d\Omega_1$ for which $z = 2$ with indices $j = 1, 2$, as per Eqn. 2.10 (Viewed from the $-y$ direction.)

Here we have dropped the coordinate subscripts r, θ, ϕ for clarity/simplicity and use shell indices instead (where some shell i contains the point defined by r, θ, ϕ). Note that the "z" in the summation, the maximum number of shells along a given $d\Omega$, will be different for each $d\Omega$. For each "cone" of solid angle we will sum $S^j(\Omega)e^{-|\tau-t|}$ from "z" (the outermost shell) to $i + 1$, where $i + 1$ is the shell adjacent to shell i.

2.5.3 Further steps towards implementation

In actual practice (i.e. computer implementation), the integration of the source function of $d\Omega$ over 4π steradians will also be done by a discrete summation.

Along any particular element of $d\Omega$ originating in shell i, this sum will be:

$$\sum_{j=1}^{z} S^j(d\Omega)(1 - e^{-\tau^{j,j-1}(d\Omega)})e^{-\tau^{j-1,i}(d\Omega)}$$

$$= \sum_{j=1}^{z} S^j(d\Omega)(1 - e^{-\tau^{j,j-1}(d\Omega)}) \prod_{j'=j-1}^{i} e^{-\tau^{j'}(d\Omega)} \tag{2.11}$$

Note that, unlike the plane-parallel case, each $d\tau$ must be calculated explicitly

from the geometry and local molecular energy level populations for each shell along the "pencil":

$$d\tau^j(d\Omega) = \alpha^j(d\Omega) \times ds^j(d\Omega),$$

where $\alpha^j(d\Omega)$ is the absorption coefficient in region j and $ds^j(d\Omega)$ is the distance through that region. Note that this distance may vary over the width of a given $d\Omega$ but we can either approximate using the centerline of $d\Omega$ or derive a θ'-dependent expression and calculate a proper integration to get a mean value over the region. (In our implementation we use the former option, for the sake of simplicity.)

This integration over solid angle is more tedious than in the plane-parallel case (which was able to use exponential integrals over a zone's $d\tau$) and more computationally costly, but straightforward enough to be feasible.

Turning this all into a fully discrete expression for p^i (for shell "i") we get

$$p^i = 1 - \sum_{\omega=1}^{Z} \left[\frac{1}{2\tau_\omega^{i,i-1} S_\omega^i} \sum_{j=1}^{z} S_\omega^j (1 - e^{-(\alpha_\omega^j \times \Delta s_\omega^{j;j-1})}) \right.$$
$$\left. \times \prod_{j'=j-1}^{i} e^{-(\alpha_\omega^{j'} \times \Delta s_\omega^{j',j'-1})} \times \Delta\Omega_\omega \right] \qquad (2.12)$$

Where Z is the maximum numbered spherical shell and all the quantities indicated by the subscript ω are dependent on a particular direction viewed from a given point (or shell i, in a spherically symmetric case).

2.5.4   Asymmetric case: Incident Radiation

Our motivating interest in this study is comets' comae, which are *not* spherically symmetric cases.

To adapt CEP to this asymmetry we divide each shell further into "regions." In the case of comets, one source of asymmetry is incident solar radiation coming from

one direction (outside the outermost shell). Therefore, the natural way to further divide shells into regions is along lines parallel to the direction of solar radiation (i.e. the center-of-comet-to-center-of-Sun line, which we will arbitrarily label as the z-axis.) Thus we superimpose a set of co-axial cylinders (with radii equal to corresponding shell radii, for the sake of simplicity) on the shells to divide the coma into regions bounded by two cylinders and two spherical shells. (Note that some regions, specifically those along the $z = 0$ plane perpendicular to the solar radiation, are only bounded by an inner cylinder and outer sphere. See Figs. 2.13 & 2.14.)
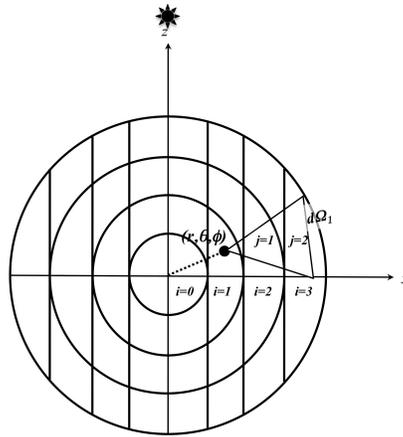
Figure 2.13: 2-D cross section of sphere on $y = 0$ plane, viewed from the $-y$ direction, showing division into 4 shells, *with* superimposed cylinders along solar ($\hat{z}$) direction.

These regions form annuli or rings of unusual, but easily envisioned, cross-sections. (See Fig. 2.14.)
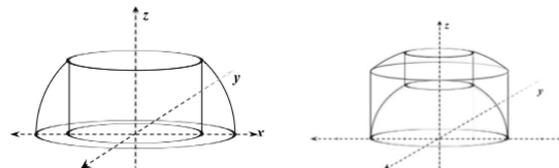
Figure 2.14: Two examples of different possible shapes of 3D annuli formed by intersecting spheres and cylinders.

Incident solar radiation is parallel to the z-axis (due to our choice of the z direction). Hence each ray of sunlight travels along the axial direction of a specific cylinder. For each region, the solar radiation absorbed is calculated based on the relevant optical depths along that direction ($d\tau$'s) of those regions in the same cylinder that are closer to the Sun than the given region. This is similar to the case of external radiation described in CEP06 Appendix A, equations A3 and A4, where we set $\mu_0 = 1$, due to the above constraint of cylinders being co-axial with the incident solar radiation:

$$\bar{J}_e^i = J_e \frac{1}{\tau^{i,i-1}} \left[\gamma(\tau^i) - \gamma(\tau^{i-1}) \right] \qquad (2.13)$$

$$where$$

$$\gamma(\tau) = \int_{-\infty}^{\infty} [1 - e^{-\tau \Phi(x)}] dx$$

where $\bar{J}_e^i$ is the average over a region i of J_e^i, the contribution of external radiation, J_e, to the mean intensity of the region, which is to be included in the equations of statistical equilibrium (Eqn. 2.1) by addition to the "B" term.

From a purely radiative standpoint, assuming that within each region there exists uniform density, temperature and other physical conditions, the radiative excitation of molecules (hence, the emission and absorption) in each region/annulus should be equal throughout the region. In our expanded CEP implementation, these regions are analogous to zones in the plane-parallel CEP. Each region's radiative effect or contribution to each other region, i.e. the net radiative bracket, must be calculated. Note that self-irradiation from around an annulus must also be taken into account, as well as irradiation from other regions. Once this calculation is done, the entire

region will be equal with respect to radiative processes (i.e. there is symmetry around the z-axis).

2.5.5 Further Asymmetry: Coma Morphology

If models of distantly observed comets were all we needed, this might be sufficient. But we are motivated by the desire to better understand spectral observations of Deep Impact & EPOXI that have very high spatial resolution around the comets' nuclei. (See e.g. Feaga et al. 2007a, 2011) Therefore the above radiative treatment alone is insufficiently asymmetric to *fully* model a cometary coma, when coma morphology is included in the model. The inclusion of the morphological variation of outgassing undoes the aforementioned symmetry around the z-axis within each annulus/region. These observations are one of the primary motives for this study, and therefore these morphological asymmetries must also be dealt with appropriately in this model.

To model morphological features, we use a cone shape superimposed over the aforementioned divisions into regions. (Other geometric shapes could also have been used. We chose to implement a cone due to its similarity in shape to many observed coma features.) A cone of arbitrary orientation and size with its vertex at the center of the sphere creates intersections with the above-described regions. Each of these is then added as a sub-region, which may have different properties from the surrounding (or subsumed/replaced) region.

Each sub-region can possess different initial conditions from the surrounding region. Thus morphological features, which by their nature tend not to be axisymmetric around our z-axis, can be included in the model. It should be noted that these sub-regions are only included as necessary. Thus for those annuli that *do* have constant axisymmetric conditions (i.e. no interesting morphological features

49

impinging on them), we can save time and memory computationally by leaving them undivided, as they would have been originally.

2.5.6 Implementation: Our Algorithm Described

Given the above geometric divisions, we have implemented Asymmetric Spherical CEP as follows. For each region (or sub-region, as applicable) we take representative population values from the coma integration and use these as the basis of an "initial guess". We then make an immediate improvement to the initial guess values by recalculating each region's populations (individually) taking into account the attenuation of incident solar radiation by intervening regions in the solar direction (as per Eqn. 2.13). These recalculated populations are the values we then use as the initial guess (required by the implementation of Newton's method in Press et al., 1992) for CEP calculations. (Note that the recalculation step described is *not* essential; it merely accelerates the calculation by starting with a closer initial guess.) Based on these populations, we calculate the necessary source functions, delta-taus and net radiative brackets "p," as above, for each wavenumber (or line, transition, etc.) Following the above discrete equation (2.12) for each region, which in this context we will call the "recipient" region, we iterate over all other regions to calculate their contribution to the recipient's p. Each other region's contribution is essentially its own source function attenuated over the optical depth of all intervening regions along the line of sight between itself and the recipient region, integrated over (or, to simplify, multiplied by) the solid angle subtended by one region from the other. This is then divided by the recipient region's source function and optical depth (along the given line of sight).

To implement this in a practical algorithm of manageable complexity, we make several simplifying approximations.

Due to the z-axis symmetry that exists (before adding sub-regions), we can *partially* simplify to a two-dimensional diagram in which a region is represented by the cross-section of the annulus in the (arbitrarily chosen) $y = 0$ plane. We calculate a region's "centroid", i.e. the centroid of its 2-D projected area in this plane which (in our approximation) corresponds to a point (r, θ, ϕ) in spherical coordinates.

For (cone shaped) sub-regions, which in general do not have their centerline on the $y = 0$ (X-Z) plane, we must use a different centroid. We use the midpoint along the cone's centerline (within region boundaries).

We also choose a series of points distributed evenly along circles parallel to the X-Y plane around each region, which will be the "starting points" for calculation of lines of sight (which will terminate at the centroids). These are chosen by rotating a region's centroid around the z-axis by multiples of some angle that depends on the size (radius) of the region. The choice of angle is such that the larger a region's size, the more starting points it will have, and thus the region will be divided into more elements of solid angle.

We use the line of sight between the "centroids" of regions and this series of starting points to calculate the contributions of every other region (or the region to itself) to a given recipient region's p. We calculate the optical depth of each intervening region, along the line of sight, based on the molecular population levels of the intervening regions. (See Fig. 2.15.) These "integration lines" encapsulate the main part (within the square brackets in Eqn. 2.12) of the calculation of p. These line of sight calculations use a simple approach to radial velocities and doppler shifts between regions. Each region's velocity component along the integration line is calculated. The integration of intensity along the line is spread over bins in wavenumber increments, $\Delta\nu$, and the line center is shifted according to the region's radial velocity. A simple "rectangle function" of width $\Delta\nu_D$, the doppler line width,

is used to approximate the line shape, thus intensity is equally spread across all bins within $\Delta\nu_D/2$ of the shifted line center. (Based on results, this approximation seems to be only slightly inaccurate; it produces $\lesssim 5\%$ error in optically thin cases.)
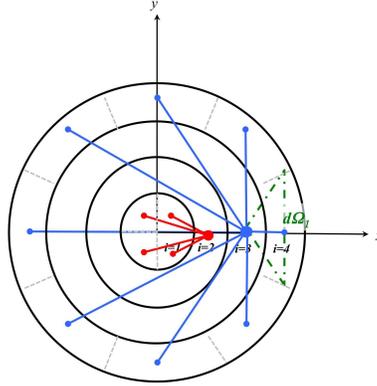
Figure 2.15: A two-dimensional view from above (i.e. the $+z$ direction) of examples of integration lines in the $X - Y$ plane. Four lines originating in the $i = 1$ region and ending at the centroid of the $i = 2$ region are shown in red, with corresponding division of the $i = 1$ circle (shown by dashed grey lines). Eight lines originating in the $i = 4$ region and ending at the centroid of the $i = 3$ region are shown in blue, with corresponding division of the $i = 4$ annulus (also shown by dashed grey lines). One example of a corresponding $d\Omega$ is also shown in green. Note that this 2-D diagram only shows horizontal cross-sections of regions, and so regions and shells/annuli are essentially indistinguishable in this diagram.

We approximate the solid angle subtended by the integration lines from another region's centroid by integrating $d\Omega = d\phi \, \sin\theta d\theta$ from zero up to the mean value ($\bar{\theta}$) of the angles between the starting point of that region, the centroid of the recipient region and the multiple "corners" of that region around the starting point. Effectively, this gives a solid angle between regions of $2\pi(1- \cos \bar{\theta})$. (See Fig. 2.16.) Note that we also, in the course of development, tried other approximations for the solid angle, but none were dramatically better.

Note that due to these approximations, the sum of solid angles over all integration lines between a region and all regions in a given shell exterior to the region is *not* necessarily constrained to exactly equal 4π, as it should be in reality. Therefore, in

calculating a "p" value, we sum the solid angles involved and average over that sum instead of 4π steradians (as Eqns. 2.8 & 2.10 dictate we should do).
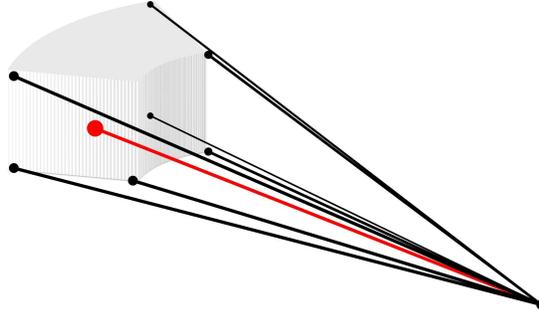
Figure 2.16: Calculation of mean angle. Lines originating from an angular slice of a region's "corners" and terminating at another region's centroid are shown in black. The line between the centroid of the "recipient" region and a "start point" of the other region, which corresponds to the relevant integration line, is in red. The integration line and each of the other eight lines define the angles that are averaged together to get the mean angle θ_{mean} used to calculate the solid angle subtended by one region as viewed from the other's centroid. Note that not all regions will have eight "corner points."

In the limit of arbitrarily small (and numerous) regions, these approximations *would* approach a physical situation of arbitrarily precise accuracy. Thus we maintain the "exactness" of the CEP method.

Unlike the plane-parallel situation, the flux exiting the surface of the coma (or other sphere of interest) is not simply a single value (per wavenumber) that has been integrated over angle. In the spherical situation, the resultant intensities form a two-dimensional mapping (in a plane perpendicular to the observer's line of sight. See Fig. 2.17.)

In our implementation, this plane is specified by rotation angles, θ, ϕ and ψ with the comet's center at the origin, and is assumed to be at a distance $\geq R_{coma}$, the maximum radius of the comet's coma. We can also specify the density of and interval between points on this plane for which the output intensities will be calculated. Each
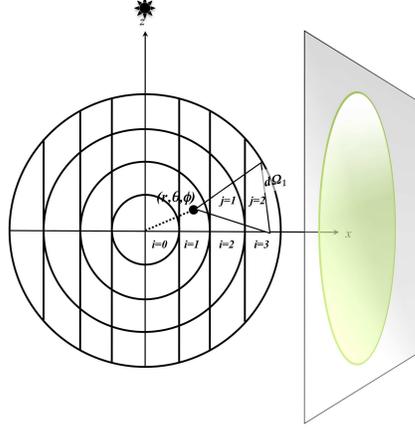
Figure 2.17: As per Fig. 2.13 above, with observer plane also shown, aligned perpendicular to X-axis.

point in this planar mapping shows the intensity (or surface brightness) integrated along a specific line of sight, perpendicular to the plane, through the coma from one side to the other (again, for each wavenumber).

$$I_{surf} = \sum_{i=1}^{z} \left(S_i \Delta \nu_i (1 - e^{-\tau^i}) \prod_{j=i-1}^{j=1} e^{-\tau^j} \right) \qquad (2.14)$$

Where S_i is the source function of a region i, $\Delta\nu_i$ is the line width of wavenumber/frequency ν in region i, and τ^i, or τ^j, represents the optical depth of wavenumber ν in region i or j along the relevant line of sight. Indices i and j run from 1 to z, where z equals the number of regions along a given line of sight.

Thus the spherical CEP algorithm produces results that could be described as a four-dimensional data "hypercube": for each point in the above 2-D spatial mapping, there is a complete (flux vs. wavenumber) spectrum. This data can then be presented in multiple formats. Several forms of data presentation for simulating observations are described in the following section.

This is also precisely the output needed to compare with the Deep Impact and EPOXI observations that have been displayed as two-dimensional brightness maps for specific wavelengths or bands.

2.6 Next Steps

Further work, not yet implemented, will include several planned improvements to our model. A more accurate treatment of radial velocities and doppler shifts in lines due to them is a highly desirable improvement. We have, so far, implemented doppler shifts along integration lines (including those for emergent flux) using a very simple "rectangle" function, where the width of the rectangle is the doppler line width, $\nu_0/c(2kT/m)^{1/2}$. This rectangle is doppler shifted using the component of radial velocity projected along the integration line. A more realistic treatment of line shape is a planned improvement. However, we do not expect the more accurate line shape to have a very large effect. It should be noted that the relative velocities involved in this problem ($O(\sim 1\ km\ s^{-1})$) are of a similar order of magnitude to the typical thermal velocities in the problem. (However, a thermal/gaussian doppler profile *is* used for calculating absorption of solar radiation. This is solely due to the different parts of the code being developed separately.)

However, we are also making a gross simplfication with respect to the radial velocity itself. We take it to be a constant value (which is a model parameter) throughout the coma. (This simplification follows the example of many other coma models. See e.g. Chin and Weaver, 1984, Crovisier, 1987.) This neglects acceleration, which should be significant near the nucleus, or at distances where dissociation or sublimation from icy grains may increase velocities. In addition to more accurate radial velocities, more flexible radial temperature and density profiles are planned, so as to be able to model deviations from a very simple Haser model. For example, it would be ideal to include volatiles produced from icy grains or large chunks and not solely from the nucleus' surface. (See A'Hearn et al. 2011)

Including thermal radiation from grains and/or dust in the calculation would also

be a useful improvement. This could be accomplished in a similar manner to that used by Sahai and Wannier (1985) with the addition of another term to the equations of statistical equilibrium (Eqn. 2.1) that represents the thermal contribution by dust.

Computational limits are currently a limiting factor in how optically thick and how refined (in terms of gradation of conditions, which requires more regions) the modeled cases can be. As of now, the maximum production rates we can deal with are on the order of $Q = 10^{28} s^{-1}$, and somewhat less for molecules requiring inclusion of more lines/levels (CO_2) than the other molecules. We are planning to address these concerns with algorithmic improvements, such as adapting the code to make use of parallel processors. Running the code on faster and more powerful computers is also a possibility.

We have coded the algorithm described above in the C++ language, using numerous functions from Press et al. (1992). See Appendices A-C for more details.

Although designed specifically with comets in mind, our model and code is versatile enough to be used in other spherical radiative transfer problems as well. Parameters that define a specific comet model or other problem, including molecule of interest, size of nucleus and radial shells, production rate, morphology (if any), incident radiation, etc., are all fairly flexible.

Chapter 3

Model Results: Spherical Comae

3.1 Some Preliminary Results: Observables for Distant Comets

In this chapter, we present examples of model results for three different production rates of three molecules (CO, H_2O & CO_2) which could be potentially useful for distant (e.g. ground based or orbital telescope) observations of comets. These are modeled using a spherical coma, without any morphological features but including optical depth effects both with respect to incident solar radiation within the coma and with respect to emergent "observed" radiation.

The output data from the CEP model can be presented graphically in various ways. Here, we show an example of a band total brightness map (analogous to Feaga et al., 2007a, but for the entire coma), radial profiles of brightness, column density, and g-factors for various azimuthal angles. (These could also be produced for individual spectral lines, but in the interests of space and avoiding complexity we have not presented such results here.) We also present spectra integrated and averaged over different "aperture" sizes. The band total brightness is more likely to be similar to actual observations, but high resolution spectra are possible, even from ground based telescopes (see e.g. Disanti et al. 2001, 1999), in particular for comets close to Earth, which might more closely resemble the latter form of model results.

3.2 Carbon Monoxide

Carbon monoxide was the first molecule we modeled, and much of the model was developed using it as the sample molecule. It is the one for which we have done the most extensive study of the various results and the best understood. Here we present a sample of results in the forms described above.

We also demonstrate the potential usefulness to observers of the ratio of the total brightness of the P branch to that of the R branch of CO to determine whether observations include significant optical depth effects. This may be measurable even with relatively poor spectral resolution.

Many of the model "input values" (see Table 3.1) have been chosen so as to facilitate comparisons (of our optically thin cases) with other earlier models. Model parameters that are the same for all the following hypothetical examples are: Solar distance = 1 AU. Solar flux (over the CO band) is $2.5 \times 10^{13} \, photons \, cm^{-2} s^{-1} (cm^{-1})^{-1}$, as per Labs and Neckel (1968) (and as used by both Chin and Weaver, 1984 and Weaver and Mumma, 1984). The code is able to read a flux input file and could use a more detailed and accurate solar spectrum (e.g. including Fraunhofer lines). The simplification of a constant incident solar flux does not represent an inherent limitation of the model. Also note that for comet Garradd, which we have modeled here (see Sec. 3.6) the heliocentric velocity at the time of observations was 14.5 km s^{-1}, well above a value likely to cause significant Swings effects (e.g. ± 5 km s^{-1}, see Kim, 1996). Gas expansion speed is a constant 0.8 km s^{-1} and the initial gas temperature at the surface is 200 K. $Q_{H_2O} = 10 \times Q_{CO}$, as in Chin and Weaver (1984). As mentioned above, the radial temperature profile closely follows Combi's (1989) model (see Fig. 2.6) but scaled to the initial gas temperature at the surface, T$_{surface}$.

Varying heliocentric distance (and solar flux along with it) will change solar pumping rates (as r^{-2}). However, due to the orders of magnitude difference between ro-vibrational and collisional or rotational transition rates *for these molecules*, the model results scale linearly with the solar flux (at least for typically observed heliocentric distances, e.g. from 0.5 to >2 AU).

The coefficients for CO-H_2O collisions (assumed to be the dominant source of collisional excitation of CO) are as per Chin and Weaver (1984): only rotational excitation and de-excitation are considered. (Vibrational cross sections for collisional excitation are about 5 orders of magnitude smaller. See Weaver and Mumma, 1984, Table 2.) $C = n_{H2O}\, \sigma\, \bar{v}$, where $\bar{v}$ is the average relative speed of the molecules (cm s^{-1}), n_{H_2O} is the number density of H_2O (cm^{-3}) and σ is the collisional cross section of a given transition of CO (cm^2). The last value is based on a total cross section of $\sigma_{tot} = 1.32 \times 10^{-14}\ cm^2$, which is apportioned between $\Delta J's$ up to 6 as per Chin and Weaver's Table 1, which we reproduce here in our Table 2.1.

3.2.1 Brightness Maps

We present here one example of a brightness map of a modeled coma (see Fig. 3.1). This format of output presentation is most similar to the radiance maps of Feaga et al. (2007a) and A'Hearn et al. (2011). For a spherical coma with no morphological features, it is rather uninteresting. It is nevertheless included here as a demonstration and used to illustrate the azimuthal angles of the radial profiles presented below with the addition of overlaid lines. Note that for the $Q_{CO} = 10^{28}$ s^{-1} case, there is some difference in brightness noticeable to the eye between the sunward side (azimuthal angles nearer to zero) and the anti-sunward side, especially in the near-nucleus portion of the image. This is due to the optical depth along the solar direction reducing the excitation and emission from the anti-sunward hemisphere.

Hypothetical Comets Model Parameters	
Heliocentric Distance	1 AU
Mean Nuclear Radius	3 km
$T_{surface}$	200 K
Expansion speed V_{exp}	0.8 km/s
CO	
Q	$10^{26} - 10^{28} s^{-1}$
$Q_{H_2O} = 10 \times Q_{CO}$ Band Center Wavenumber	2149 cm^{-1}
Band Center Einstein A	33 s^{-1}
Highest Rot. Level, J_{max}	20
Solar flux	$2.5 \times 10^{13} \, photons \, cm^{-2} s^{-1}/cm^{-1}$
Collisional Cross-section, σ_{rot}	$3.2 \times 10^{-15} \, cm^2$
H_2O	
Q	$10^{26} - 10^{28} s^{-1}$
Ortho:Para Ratio	3:1
Ortho Band Head Wavenumber	3732.13 cm^{-1}
Ortho Band Head Einstein $A_{1,1_{0,0}-0,1_{0,1}}$	89.6 s^{-1}
Para Band Head Wavenumber	3779.49 cm^{-1}
Para Band Head Einstein $A_{1,1_{0,1}-0,0_{0,0}}$	28.6 s^{-1}
Highest Rot. Level, J_{max}	7
Solar flux	$3.9 \times 10^{13} \, photons \, cm^{-2} s^{-1}/cm^{-1}$
Collisional Cross-section, σ_{rot}	$2.5 \times 10^{-15} \, cm^2$
CO_2	
Q	$10^{26} - 10^{28} s^{-1}$
$Q_{H_2O} = 10 \times Q_{CO_2}$ Band Center Wavenumber	2349.9 cm^{-1}
Band Center Einstein A	140.3 s^{-1}
Band *Mean* Einstein A	206.097 s^{-1}
Highest Rot. Level, J_{max}	70 - 50
Solar flux	$2.8 \times 10^{13} \, photons \, cm^{-2} s^{-1}/cm^{-1}$
Collisional Cross-section, σ_{rot}	$3.6 \times 10^{-15} \, cm^2$

Table 3.1: Model input parameters for models of H_2O, CO_2 and CO in hypothetical comets.
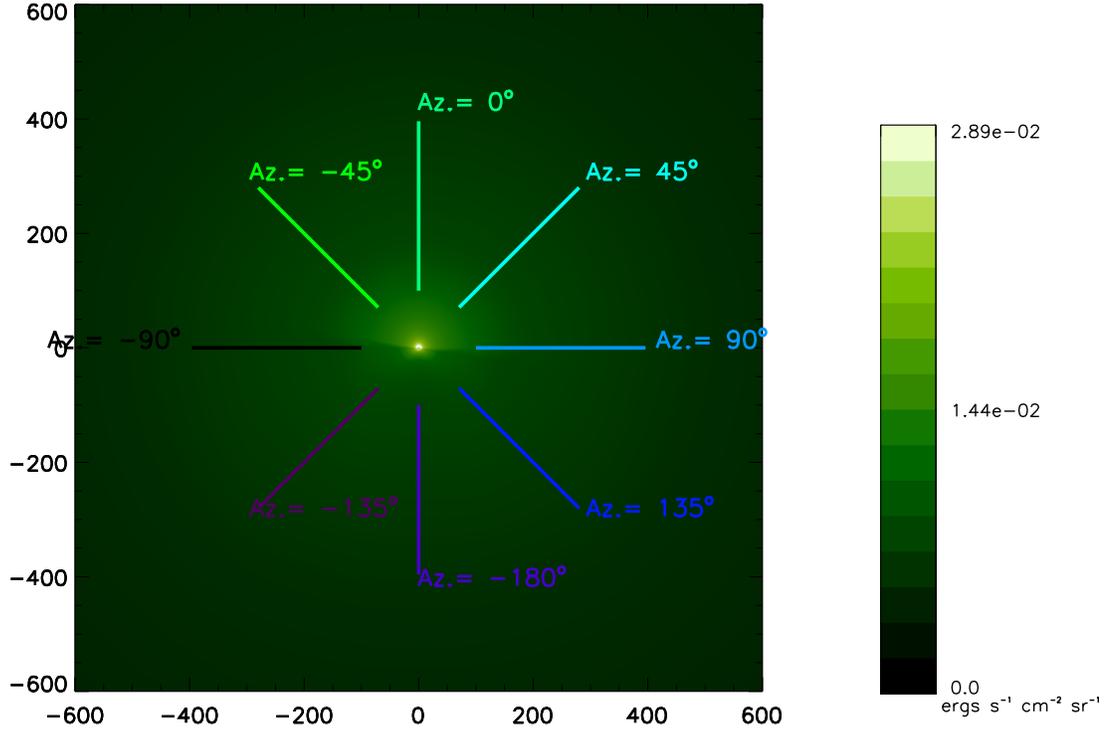
Figure 3.1: Example of a band total brightness map for the CO 1-0 band, for the inner ± 600 km near the nucleus of a hypothetical comet with $Q_{CO} = 10^{28} s^{-1}$, viewed from phase angle $= 90°$. Overlaid radial lines indicate the orientation of azimuthal angles in radial profiles below. The sunward direction is up, i.e. azimuthal angle $= 0°$. Note that within the ± 600 km field of view, the brightness never reaches zero (even where it appears to be totally dark). The colors of the azimuthal angles correspond to those in subsequent radial profiles.

3.2.2 Radial Profiles: Brightness, Column Density and g-factors

Abundances of cometary species are frequently calculated from observed fluxes using fluorescence efficiencies, or g-factors. In an optically thin case, the brightness of a given line or band is directly proportional to the column density of the relevant molecule. In such cases $B_{band} = g_{band} \times N$ and $g_{band} = \sum_{band} A_{ul} \times n_u$ where B_{band} is the band total brightness, g_{band} the band g-factor, N the total column density, A_{ul}

the Einstein A coefficient for the relevant transition originating in upper level "u" and n_u is the column density of the population of a specific upper level "u" (which in our model is numerically approximated as the sum over all regions along a line of sight of the fractional population of level "u" times each region's column density).

However, large optical depths will spoil this simple linear relation between column density and brightness. With radiative transfer modeling, it is possible to get a calculated g-factor ($g_{band} = \sum_{band} A_{ul} \times n_u$) from the model and the "effective g-factor", $g_{eff} = B_{band}/N$, which is the actual ratio of brightness to column density.

In Figs. 3.2, 3.3, and 3.4 we present all these values together as radial profiles, for hypothetical comets of three different production rates, $Q_{CO} = 10^{26}, 10^{27}$, and $10^{28} s^{-1}$. (All observed at 1 AU, at a phase angle of $90°$ and multiple azimuthal angles. In all cases $Q_{H_2O} = 10 \times Q_{CO}$.)

In our results, we typically see that g_{eff} does tend towards the calculated g-factor values at larger impact parameters, where optical depth effects are negligible, as would be expected. (The actual numerical values of the "asymptotic" band g-factors produced by our model, $2.4 \times 10^{-4} s^{-1}$ per molecule for CO at 1 AU, also agree well with other published values such as those calculated by Chin and Weaver, 1984, Crovisier and Le Bourlot, 1983, and Weaver and Mumma, 1984.) The actual radii at which this convergence occurs depends primarily on the production rate of a comet. We can use the distance at which $g_{eff} = 0.9\, g_{thin}$ as a very rough measure of the point where a coma can be considered to transition from optically thick to thin. For the "thin" and "intermediate" coma models ($Q_{CO} = 10^{26}$ and $Q_{CO} = 10^{27}\, s^{-1}$) the convergence is fairly close to the nucleus, within $\sim$100-200 km. But for the "thick" model ($Q_{CO} = 10^{28} s^{-1}$) with its high production rate, the "optically thick regime" can extend as far as $O(10^3)$ km, which can be spatially resolved even in some remote observations. Note that at radial distances very near the nucleus, worrying

about optical depth effects may be relevant even for lower production rates.
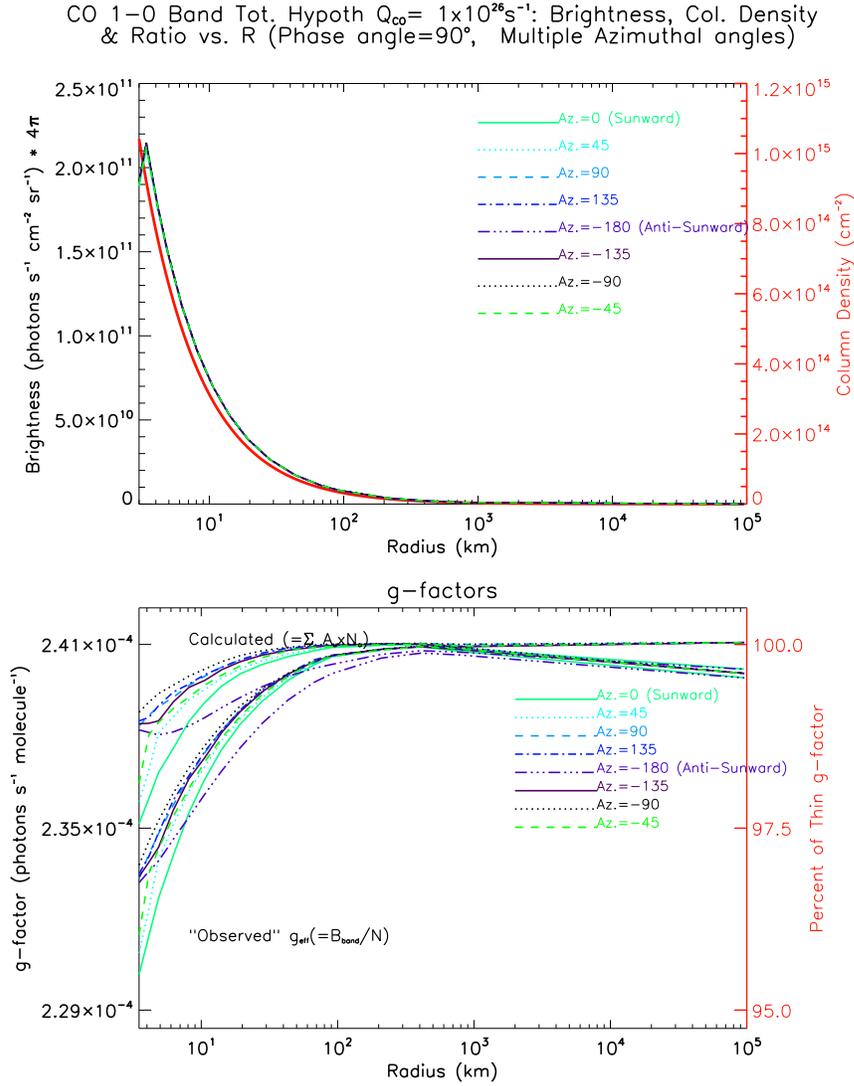
Figure 3.2: For $Q_{CO} = 10^{26}s^{-1}$. Upper frame: Radial profile of band total Brightness vs. R (impact parameter) for Phase angle $= 90°$ and for multiple Azimuthal angles. Profiles of azimuthal angles (indicated by color coding) show no variation for this case and overlap, appearing indistinguishable. Column density is included as the bold solid red line using a different y-axis scale. Lower frame: g-factors. Both the calculated g-factor (the higher group of lines) and g_{eff}, the observed brightness over column density, plotted with matching styles and colors for each azimuthal angle which also match those in the upper frame. Profiles for $0°$, $\pm 45°$, and $90°$ overlap each other almost entirely. (The apparent decrease of the profiles at large radii is an artifact of the code/plotting, not an actual decrease in g-factor.)
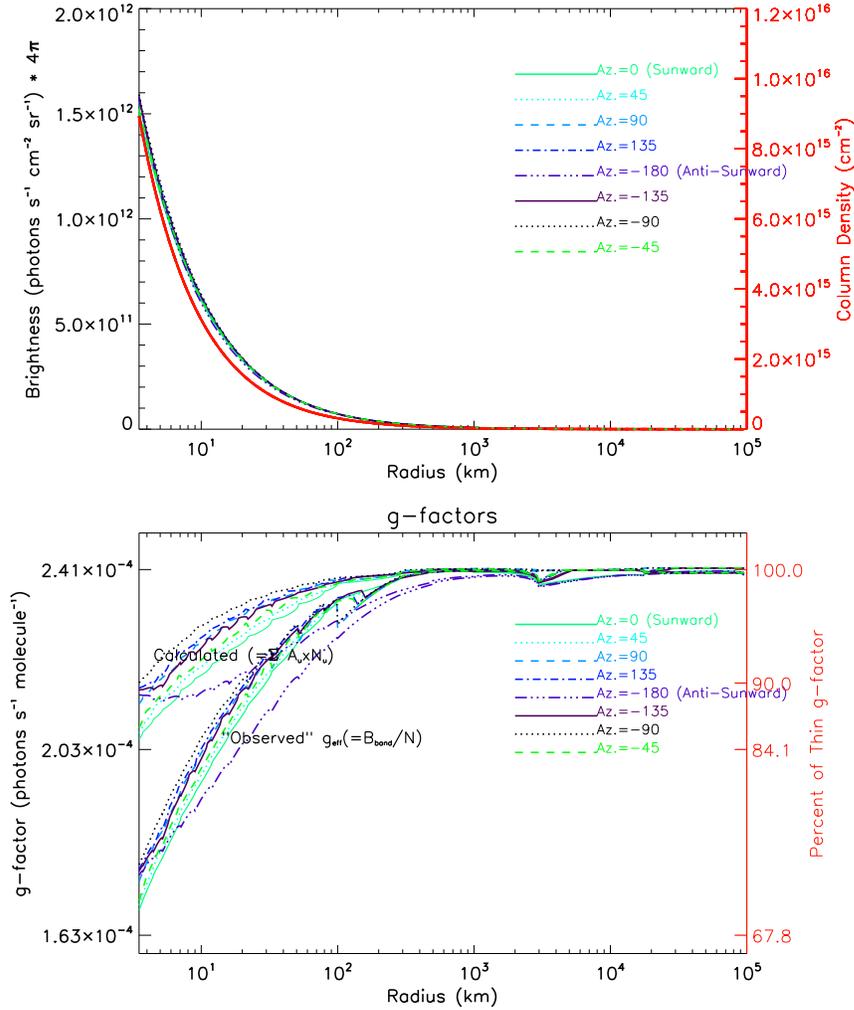
Figure 3.3: For $Q_{CO} = 10^{27} s^{-1}$. Upper frame: Radial profile of band total Brightness vs. R (impact parameter) for Phase angle = 90° and for multiple Azimuthal angles. Profiles of azimuthal angles (indicated by color coding) for 0°, ±45°, and 90° overlap each other almost entirely and other brightness profiles are almost indistinguishable. Column density is included as the bold solid red line using a different y-axis scale. Lower frame: g-factors. Both the calculated g-factor (the higher group of lines) and g_{eff}, the observed brightness over column density, plotted with matching styles and colors for each azimuthal angle which also match those in the upper frame. Profiles of azimuthal angles 0°, ±45°, and 90° overlap each other almost entirely and are almost indistinguishable. ("Jaggedness" of the profiles is due to the division into discrete regions in the model.)
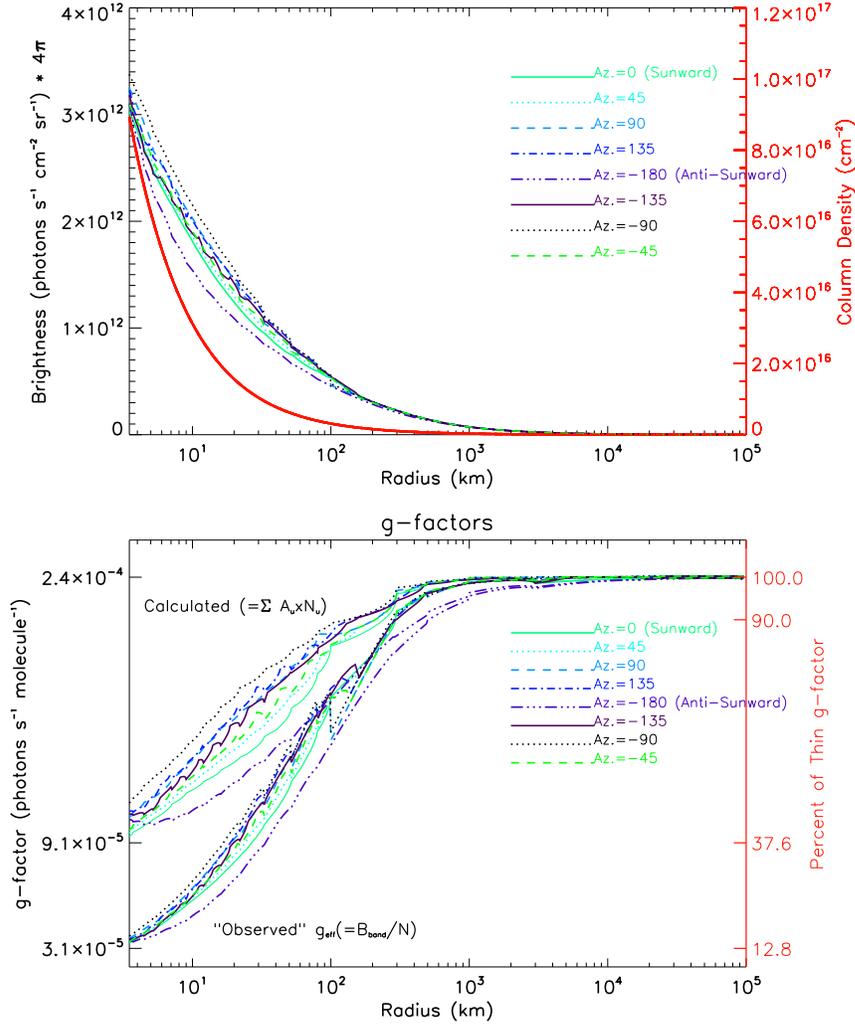
Figure 3.4: For $Q_{CO} = 10^{28} s^{-1}$. Upper frame: Radial profile of band total Brightness vs. R (impact parameter) for Phase angle = 90° and for multiple Azimuthal angles. Profiles of azimuthal angles (indicated by color coding) for 0°, ±45°, and 90° overlap each other almost entirely. Column density is included as the bold solid red line using a different y-axis scale. Lower frame: g-factors. Both the calculated g-factor (the higher group of lines) and g_{eff}, the observed brightness over column density, plotted with matching styles and colors for each azimuthal angle which also match those in the upper frame. ("Jaggedness" of the profiles is due to the division into discrete regions in the model.)

66

3.2.3 Radial Profiles: Phase and Azimuthal Angular Variations

Another optical depth effect is variation of brightness (and corresponding g-factor) with varying angles, both phase angle (of observer) and azimuthal angle within any given observation.

The radial profiles in Figs. 3.2-3.4 demonstrate the azimuthal variation for a single phase (observing) angle. It may seem somewhat surprising and counter-intuitive that the radial profile lines in the sunward direction are not the brightest (nor those closer to sunward on either side). However, when velocities and doppler shifts are accounted for this is readily explained. Along the sunward (or anti-sunward) direction there is no change in the sunward component of the expansion velocity, and thus no relative doppler shifting of the line-center frequencies, all along that direction. This causes greater effective optical depths and less solar excitation in that direction. Conversely, the profiles of directions perpendicular to sunward show greater excitation. However, the degree to which the actual g-factor varies is of note. Even for the only moderately thick case of $Q_{CO} = 10^{27}s^{-1}$ for radii ≤ 100 km, there is a difference of as much as $\sim$5-10% between sunward and anti-sunward directions, and even slightly greater differences between some other profiles. The effect is even more pronounced for the thicker case of $Q_{CO} = 10^{28}s^{-1}$.

In Figs. 3.4-3.8 we present profiles of brightness (and column density) for model results observed from different phase angles, ranging from 0° to 180° , for the optically thicker case of $Q_{CO} = 10^{28}s^{-1}$. Each plot includes multiple azimuthal angles, which would all be visible simultaneously in a wide field observation (i.e. including the entire coma) from each given phase angle. (The above plot for 90° phase angle for $Q_{CO} = 10^{28}s^{-1}$, Fig. 3.4, should be considered part of this series as well.)

Observations with a slit spectrometer with sufficient spatial resolution (see e.g. Disanti et al. 1999) might observe along one specific azimuthal angle and thus see possible variations along the slit with sufficiently high spatial resolution.
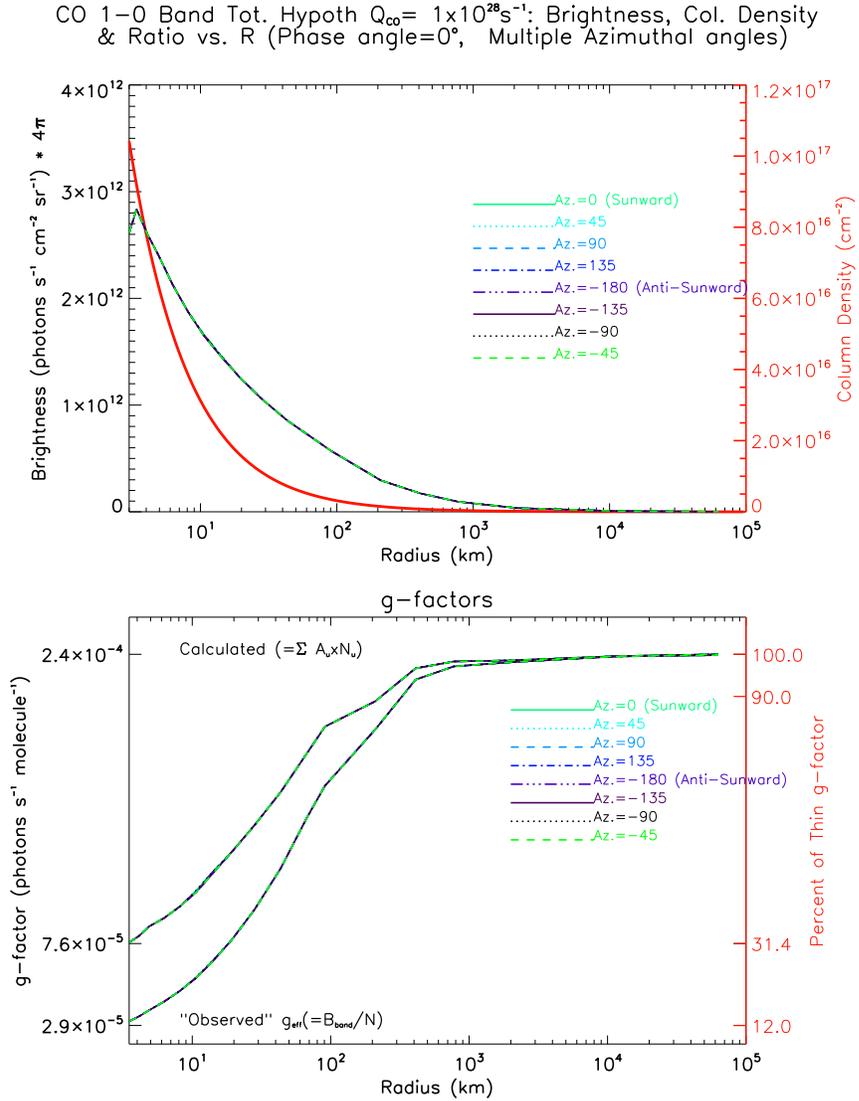

Figure 3.5: For Phase angle $= 0°$, $Q_{CO} = 10^{28} s^{-1}$. Upper frame: Radial profile of band total Brightness vs. R (impact parameter) for Phase angle $= 90°$ for multiple Azimuthal angles. Profiles of azimuthal angles (indicated by color coding) show no variation for this case (as should be expected) and overlap, appearing indistinguishable. Column density is included as the bold solid red line using a different y-axis scale. Lower frame: g-factors. Both the calculated g-factor (the higher group of lines) and g_{eff}, the observed brightness over column density, plotted with matching styles and colors for each azimuthal angle (which also match those in the upper frame).

Figure 3.6: For Phase angle $= 45°$, $Q_{CO} = 10^{28}s^{-1}$. Upper frame: Radial profile of band total Brightness vs. R (impact parameter) for Phase angle $= 90°$ for multiple Azimuthal angles. Profiles of azimuthal angles (indicated by color coding) are slightly displaced for viewing purposes. Column density is included as the bold solid red line using a different y-axis scale. Lower frame: g-factors. Both the calculated g-factor (the higher group of lines) and g_{eff}, the observed brightness over column density, plotted with matching styles and colors for each azimuthal angle (which also match those in the upper frame).

The most obvious effect seen at a glance in these figures is the spread among azimuthal angles for a given phase angle. As would be expected, the 0° and 180° phase angles (sunward and anti-sunward) have no real azimuthal variation. From phase
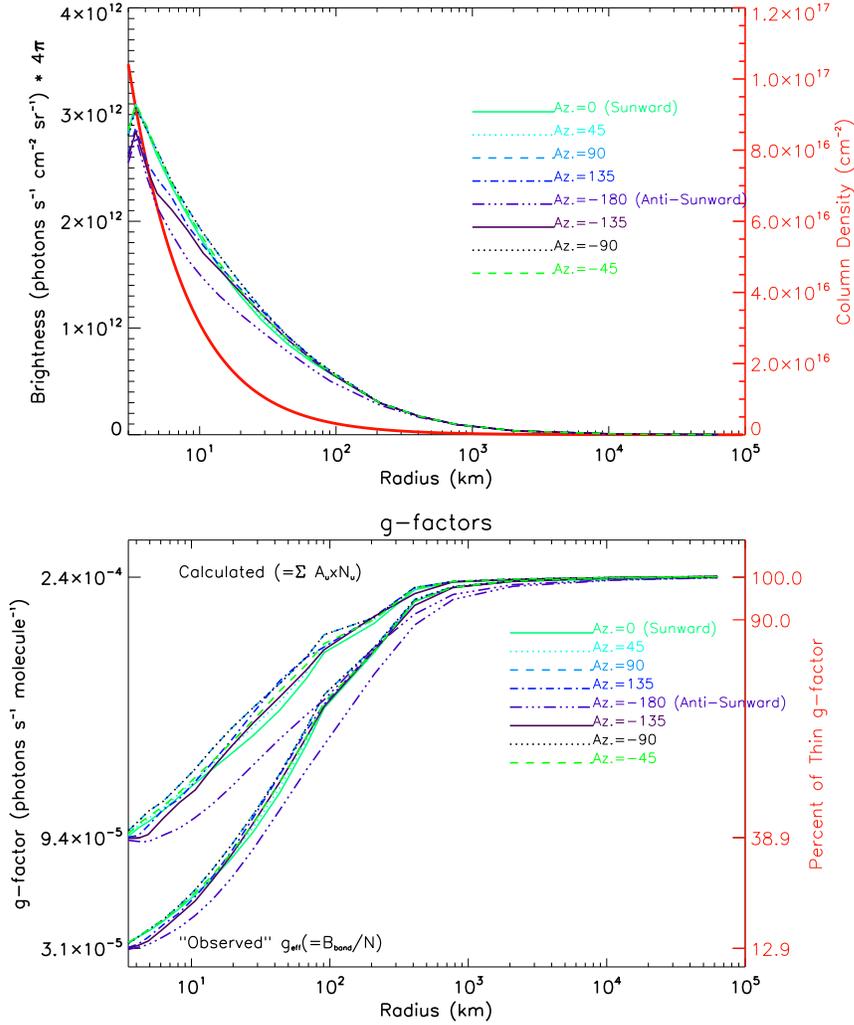
Figure 3.7: For Phase angle $= 135°$, $Q_{CO} = 10^{28} s^{-1}$. Upper frame: Radial profile of band total Brightness vs. R (impact parameter) for Phase angle $= 135°$ for multiple Azimuthal angles. Profiles of azimuthal angles (indicated by color coding) are slightly displaced for viewing purposes. Column density is included as the bold solid red line using a different y-axis scale. Lower frame: g-factors. Both the calculated g-factor (the higher group of lines) and g_{eff}, the observed brightness over column density, plotted with matching styles and colors for each azimuthal angle (which also match those in the upper frame).

angle $45°$ to $90°$ to $135°$ there is a progression: the azimuthal lines get spread out farther from each other, as well as noticeably dropping in brightness for those radii in the anti-sunward hemisphere.
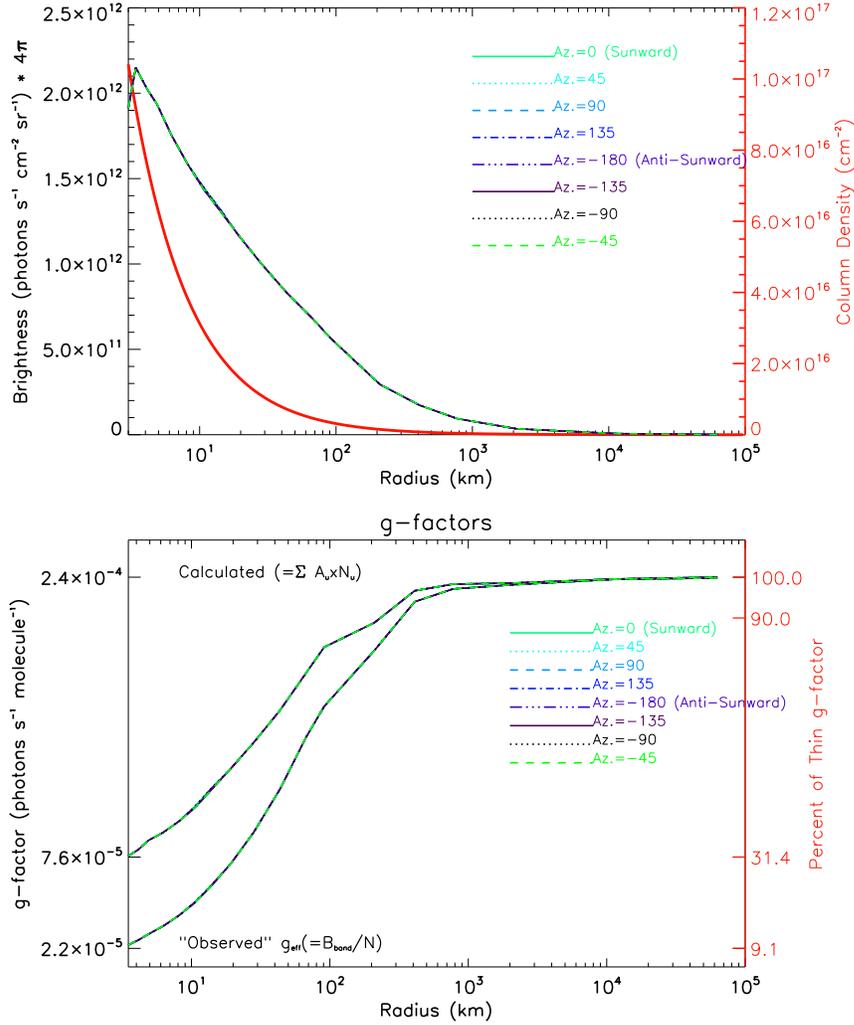
Figure 3.8: For Phase angle $= 180°$, $Q_{CO} = 10^{28}s^{-1}$. Upper frame: Radial profile of band total Brightness vs. R (impact parameter) for Phase angle $= 180°$ for multiple Azimuthal angles. Profiles of azimuthal angles (indicated by color coding) show no variation for this case (as should be expected) and overlap, appearing indistinguishable. Column density is included as the bold solid red line using a different y-axis scale. Lower frame: g-factors. Both the calculated g-factor (the higher group of lines) and g_{eff}, the observed brightness over column density, plotted with matching styles and colors for each azimuthal angle (which also match those in the upper frame).

With respect to total brightness, the phase angles 0°, 45°, 90°, and 135° produce roughly equal peak brightness for their *strongest* azimuthal profiles (the more sun-

ward directions, at the nucleus grazing radius) of about $\sim 3 \times 10^{12}$ photons s^{-1} cm^2 sr^{-1}. Most significantly, for the 180° phase angle, the peak values are about $\sim 2 \times 10^{12}$ - significantly less bright than at other phase angles.

With respect to "effective" (or "observed") g-factors, the minimum values in the most optically thick regions (again, at the nucleus-grazing radii) also show a trend from sunward to anti-sunward. For the 0° through 135° phase angles, the minimum values of the ratio of the band total flux over the column density are roughly 3×10^{-5} photons s^{-1} molecule^{-1} while for 180° the value decreases to a minimum of about 2×10^{-5}. This trend is due to a combination of two optical depth effects. The first is attenuation of incident solar light from the sunward to anti-sunward sides of the coma, leading to less fluorescent pumping, and thus less emission, by the anti-sunward hemisphere. Second, whatever emission there is is more likely to "escape" the coma along lines of sight along the azimuthal angles closer to where it is emitted, experiencing less total optical depth on its path out of the coma. Thus the already greater emission of the sunward regions is also more likely to be observed along azimuthal directions closer to sunward.

However, the similarly located values for "actual" calculated g-factors do *not* follow a similar simple monotonic trend. The greatest values for a given phase angle rise from 0° through 45° and peak for phase angle 90°. From 90°, through 135° down to 180° they fall through the same values, creating a symmetric peak around 90°. This symmetrical and non-monotonic pattern of the calculated values is less intuitive than the trend of g_{eff} over angles in the same cases. Yet it is clearly understood in light of the fact that these values are based only on the actual population distributions in different regions and do *not* include optical depth effects on the *emergent* radiation. Thus observing from phase angles 0° and 180° are sampling exactly the same lines of sight and regions' populations, including the darkest (i.e. least excited

populations) of the anti-sunward side of the coma. The same is essentially true for 45° and 135° (due to symmetry around the z-axis) but they do not sample the darkest parts of the anti-sunward directions (and the differences in populations are less between outermost regions on the sunward side among azimuthal angles between ±45 – they are all experiencing direct solar illumination). For 90° the higher azimuthal profiles are sampling from more excited and higher emission populations than the profiles with lower values, and consistently so all the way along their lines of sight (which is not true for 45° and 135°). Thus the more sunward lines for 90° is the brightest seen, and the anti-sunward values fall between values of the 0° or 180° and the 45° or 135° lines.

Lastly, the profiles for $Q_{CO} = 10^{28} s^{-1}$ have a deviation from linear slopes in their in brightness in the vicinity of $\sim 100 \sim 1000$ km, most easily visible for the 180° plot, but also present for the other phase angles (and growing in size from 0° up to 180°). This is mostly due to the temperature profile reaching its minimal values at these radii in conjunction with the higher density of the $Q_{CO} = 10^{28} s^{-1}$ case. The higher density leads to this still being a collisionally dominated regime, and the low temperatures lead to the lowest population levels being most highly populated. These levels also have the highest Einstein A values, thus leading to a higher overall number of photons emitted for the same number of molecules. The effect is greatest for the 180° view due to a cumulative effect – the lines of sight all sample the most dense and cold regions at these radii. The same extreme effect is not seen for the 0° phase angle due to the overall greater fluorescent excitation of the sunward regions dominating it. (Note that the difference in total brightness between the two azimuthal angles at these radii is about a factor of two.)

3.2.4 Aperture Averaged Spectra

If one is observing with high spectral resolution but low spatial resolution, the spectra observed will be the sum of as much of the coma as fills the field of view. To model this, we have simulated "aperture averaged" spectra, where the "aperture" controls the area of the coma sampled. Our apertures are square boxes and are all centered exactly on the center of the comet, and sample a nucleus centered area equal to the square of the "aperture size" over which we average the brightness. We present a series of apertures from 2×10^1 km (very near the nucleus) through 2×10^5 km (the whole coma) for each of the three production rates. (All these example spectra are modeled at a heliocentric distance of 1 AU and phase angle $90°$, with $Q_{H_2O} = 10 \times Q_{CO}$, as in Chin and Weaver, 1984.)

The spectra have been shown with an outline around them indicating the spectra as they would be if observed with the DI HRI spectrometer, with a convolution using appropriate resolving power ($\lambda/\delta\lambda = 200$ for H_2O and 330 for the other two molecules; see Hampton et al., 2005) and pixel binning as per the instrument's detector. This is not an intrinsic part of the modeling and could be varied for other situations or observations, or skipped entirely. (It is added in IDL "post-processing" when the spectra are plotted.)

Band shape for apertures including the outer coma (approximately $10^4 < R_{ap} < 10^5$ km) does not change significantly for different production rates. The total brightness for this regime increases approximately in linear proportion to production rate. This is due to spectra with such large aperture sizes being dominated by the fluorescence-dominated optically thin outer coma with optical depth effects playing a minimal role. (But not entirely non-existent: note the small, $\lesssim 6\%$ reduction in g-factor with higher production rate for $R_{ap} = 2 \times 10^4$ km.)
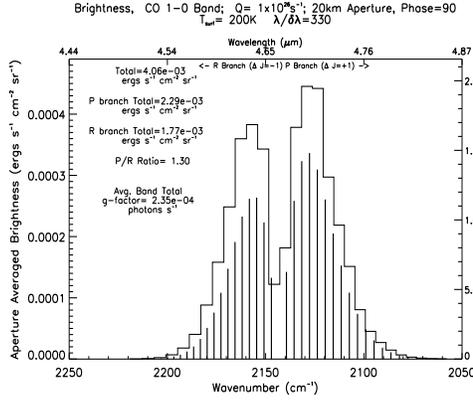
(a) Aperture = 20km.
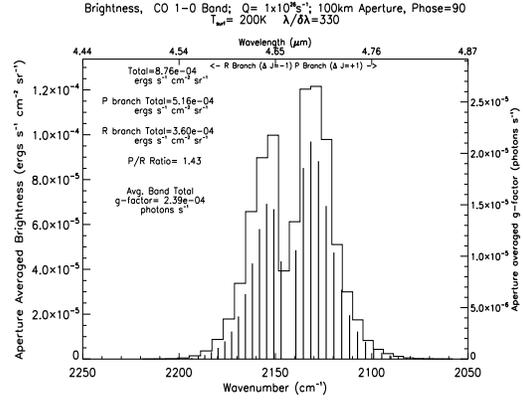
(b) Aperture = 100km.
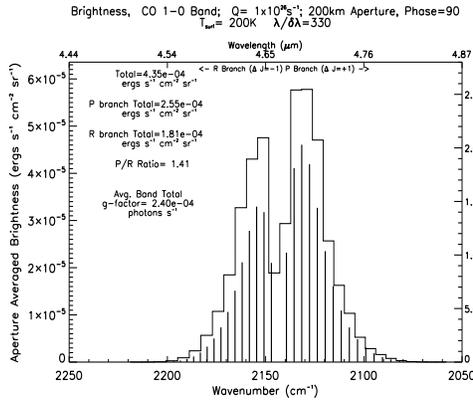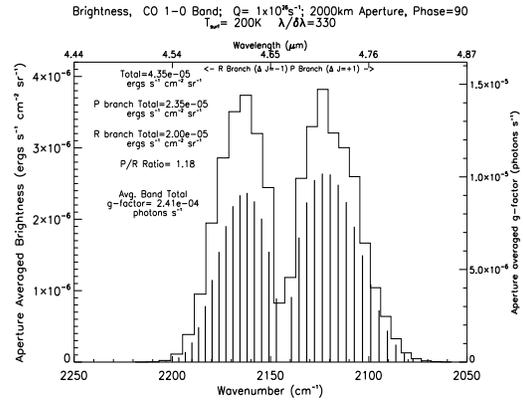
(c) Aperture = 200km.
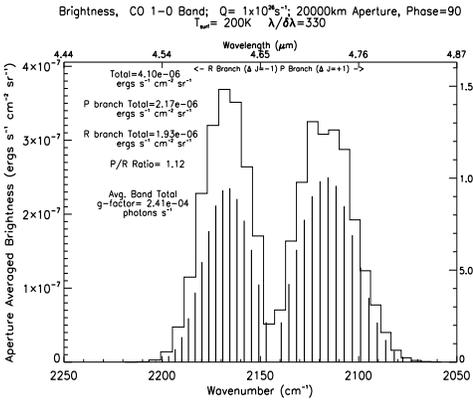
(d) Aperture = 2,000km.
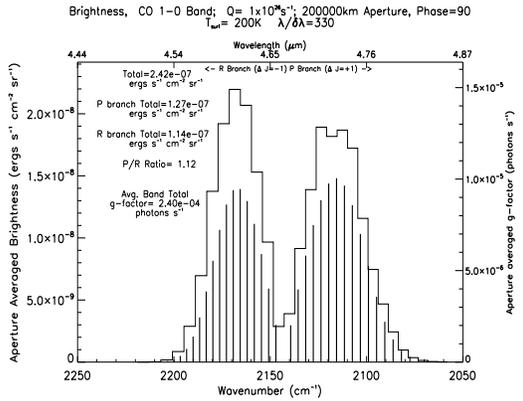
(e) Aperture = 20,000km.

(f) Aperture = 200,000km.

Figure 3.9: Aperture averaged spectra for $Q_{CO} = 10^{26}$ s^{-1}. Left side y-axis is aperture averaged brightness. Right y-axis is effective (line) g-factor (brightness/column density). Totals are indicated on each graph. The continuous line is the spectrum after convolution and pixel binning simulating the Deep Impact HRI instrument.
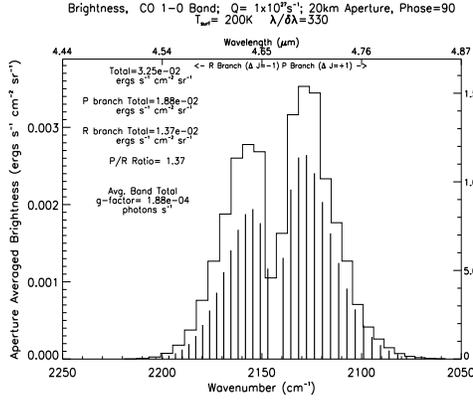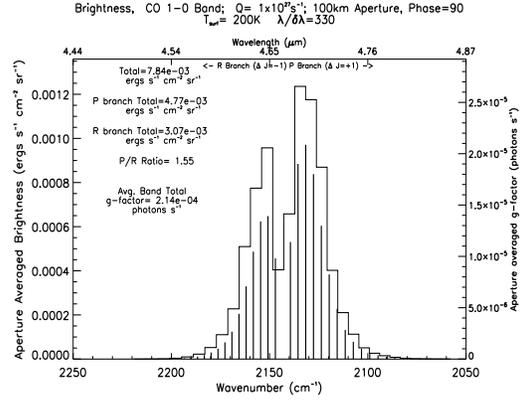
(a) Aperture = 20km.

(b) Aperture = 100km.
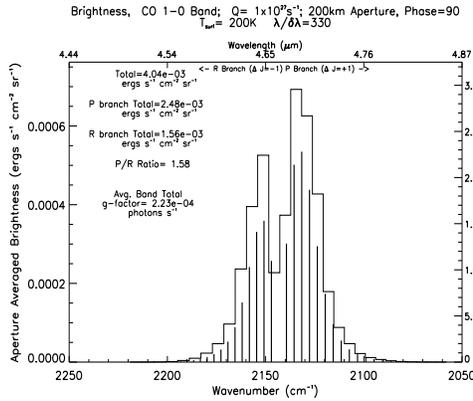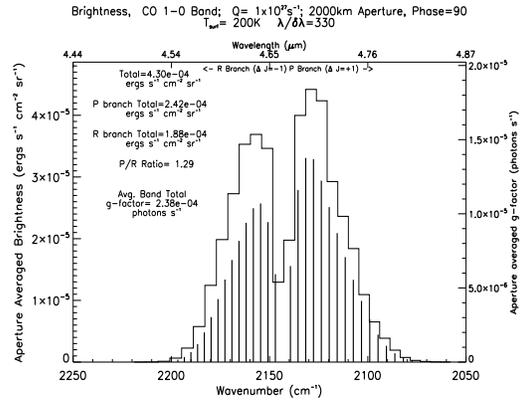
(c) Aperture = 200km.
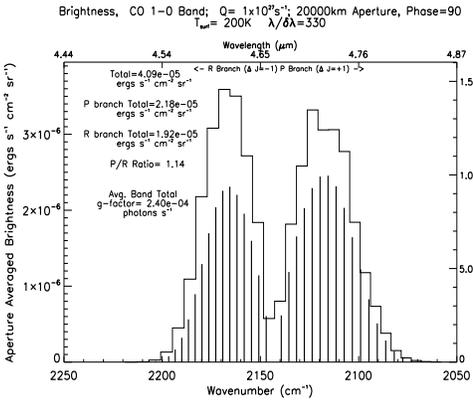
(d) Aperture = 2,000km.
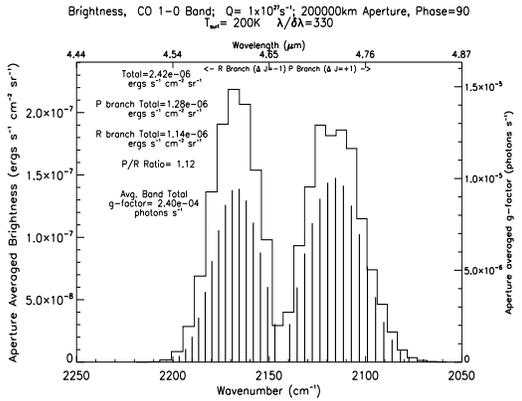
(e) Aperture = 20,000km.

(f) Aperture = 200,000km.

Figure 3.10: Aperture averaged spectra for $Q_{CO} = 10^{27}$ s^{-1}. Left side y-axis is aperture averaged brightness. Right y-axis is effective (line) g-factor (brightness/column density). Totals are indicated on each graph. The continuous line is the spectrum after convolution and pixel binning simulating the Deep Impact HRI instrument.

(a) Aperture = 20km.

(b) Aperture = 100km.

(c) Aperture = 200km.

(d) Aperture = 2,000km.

(e) Aperture = 20,000km.

(f) Aperture = 200,000km.
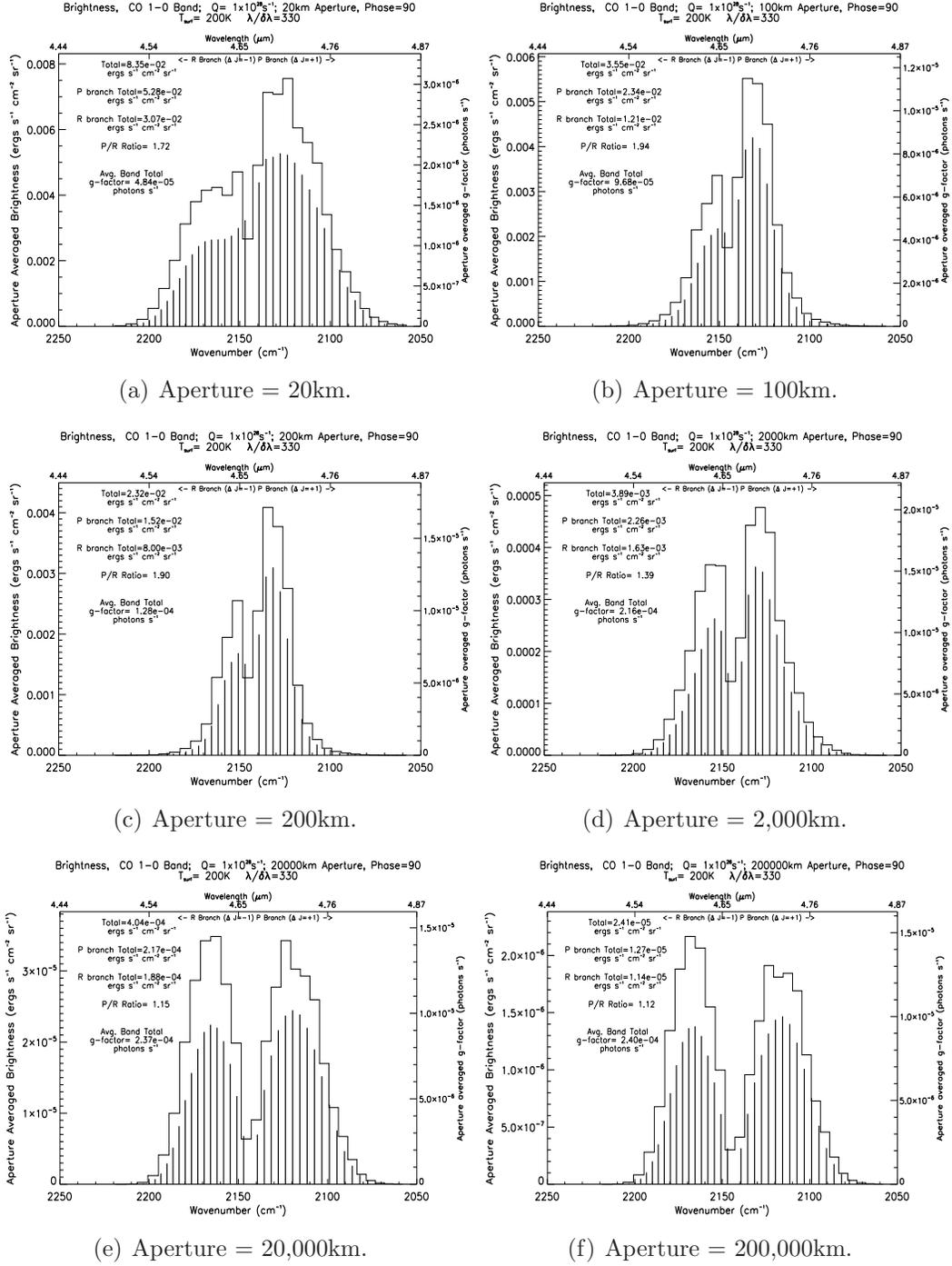
Figure 3.11: Aperture averaged spectra for $Q_{CO} = 10^{28}$ s^{-1}. Left side y-axis is aperture averaged brightness. Right y-axis is effective (line) g-factor (brightness/column density). Totals are indicated on each graph. The continuous line is the spectrum after convolution and pixel binning simulating the Deep Impact HRI instrument.

77

In the inner coma, however, optical depth effects can be quite striking. The "thickest" spectra (for higher production rates and smaller R_{ap}) have remarkably altered band shapes from the optically thin spectra.

First, however, a word about changes that are *not* specifically caused by optical depth effects. It is clear that there is much variation, even within a given production rate, from large to small aperture sizes. Not all of this is due to optical depth effects. Even in our optically thin case, the band shape changes noticeably in breadth. This occurs primarily due to the temperature profile and the relative importance of collisional vs. radiative pumping. We have used a fairly simplified profile, which can be scaled to a surface temperature parameter, but does not vary much otherwise between different model cases. This provides a straightforward "control" for this aspect of spectral change with aperture size.

In the innermost coma near the nucleus, the temperature is quite warm ($\sim$100 - 200K), which leads to a broader band in the 10 km spectrum. The coma gas cools to a minimum ($\sim$20K) around 100-200 km out from the nucleus, which produces a much narrowed band. Since the Einstein A coefficient for the lowest J lines is higher than for the lines in the "wings" of the band, the cold temperature also increases the g-factor, even in optically thick regions. At larger radii, the temperature rises again, but becomes less significant since the coma gets less dense and tends towards fluorescent equilibrium. Between these regimes, in a "transition region," there are still optical depth effects, which can be more easily isolated since g-factors are less temperature controlled.

Temperature is also a factor in determining doppler broadening and line width, which is proportional to $T^{1/2}$, so the ratio between line widths for the coldest and the warmest regions of the coma are about 2-3, for a given wavenumber. This may lead to temperature playing a significant role in the optical thickness of the coma

to incident solar radiation.

Temperature effects notwithstanding, the spectra from the denser near-nucleus regions of a coma show optical depth effects in several aspects. In addition to the total brightness no longer increasing linearly with production rate (and a corresponding reduction of g-factors), energy is also dramatically shifted between lines within the band.

The notable shifting of flux from R branch to P branch (evident in many of the optically thicker spectra), and to lower wavenumbers in both branches (as is most evident in the R_{ap} =100 & 200 km spectra for $Q = 10^{28}$ s^{-1}), are very noticeable optical depth effects. (See Sahai and Wannier, 1985, for an analytical discussion of similar effects.)

This effect appears due to the branching ratio of a given pair of P and R branch lines originating in the same upper level, which generally (slightly) favors emission in the P branch line. In optically thick cases, repeated absorption and emission of photons leads to a cumulative effect which favors the P branch over the R branch much more than in optically thin conditions (where it is probable that any emitted photon will not be re-absorbed before escaping the coma).

Similarly, flux is "pushed" outwards in the branches, and more so in the P branch due to combination with the above effect. This is due to the lines closer to the center of the band becoming optically thick before those in the wings (both due to their higher Einstein coefficients and generally being more populated.) Flux initially emitted in lines that are optically thick will through repeated absorption and emission be forced out into lines that are less thick.

3.2.5 The P/R Ratio: A Useful Heuristic of Optical Depth

As seen above, the P branch total brightness and the R branch total brightness vary with respect to each other over different optical depths (as well as other factors, such as temperature distribution.) The ratio of the sums of P/R branches' brightnesses can be useful to alert an observer (or anyone analyzing observations) that they must in a given case beware of, and if possible account for, optical depth effects.

This alone, would not be sufficient, as temperatures along a given line of sight are also a significant factor in controlling the P/R ratio, in the collisionally dominated inner coma. Colder population distributions will emit more in the lower lines (in both branches) for which the ratio of P/R for each pair of lines originating in the same upper state is greater. Also, the values of τ and $d\tau$ in Eqns. 2.7 - 2.14 will effectively vary inversely with linewidth, other factors being equal.

Use of a model like ours can show where the P/R ratio is large due to temperature and where (its excess beyond that value is) due to optical depth. In our optically thin, $Q_{CO} = 10^{26}$ s^{-1}, model the P/R ratio does not exceed ~1.4, even for aperture sizes dominated by the coldest portion of the coma. (Note, however, that this is an aperture *averaged* value. In Fig. 3.12 below, the peak value is slightly higher, ~1.5.) However, the ratio for corresponding aperture sizes in the $Q_{CO} = 10^{27}$ s^{-1} and $Q_{CO} = 10^{28}$ s^{-1} cases is ~1.6 and ~1.9, respectively. Furthermore, in the thickest case modeled, even the spectrum with aperture size of 2000 km has a ratio of ~1.4. Note that in all cases the 2×10^{5} km aperture, which is dominated by the outer coma in fluorescent equilibrium, has a ratio of ~1.12. All of this indicates that a P/R ratio in excess of ~1.4~1.5 is a warning sign that optical depth effects are involved.

3.2.6 Further Discussion

While it would be ideal to be able to derive a simple correction factor from the P/R ratio in such cases, alas, it is not exactly possible. However, a rough estimate of the degree of optical depth effects can be derived.
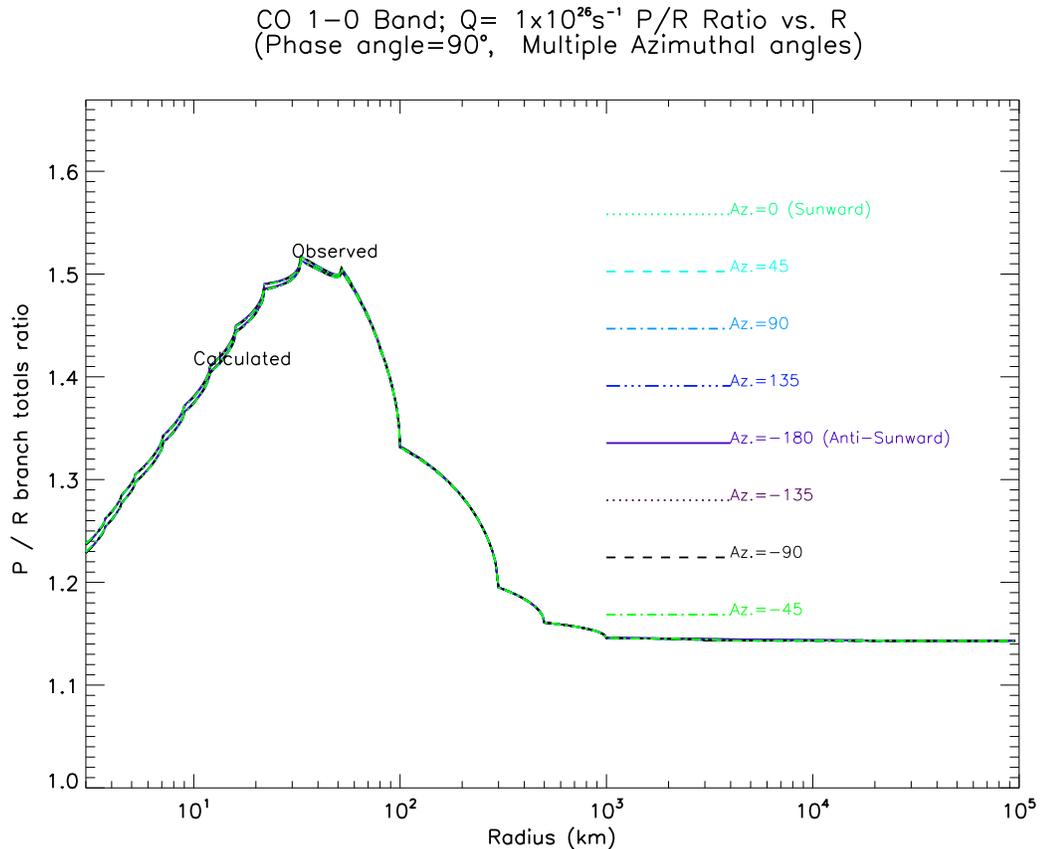
Figure 3.12: For $Q_{CO} = 10^{26} s^{-1}$. Ratio of P branch vs. R branch total Brightness (in $photons\, s^{-1} cm^{-2} sr^{-1}$) vs. R (impact parameter) for Phase angle $= 90°$ and for multiple azimuthal angles. Profiles of azimuthal angles show negligible variation for this case and overlap, appearing indistinguishable. ("Sawtoothed" appearance of the profiles is a plotting artifact due to the division into discrete regions in the model.)

To do so, we create radial profiles of the P/R ratio, for both the observed emergent flux/brightness and the calculated value based on underlying populations without attenuation of emergent light, as shown in Figs. 3.12, 3.13, and 3.14. By
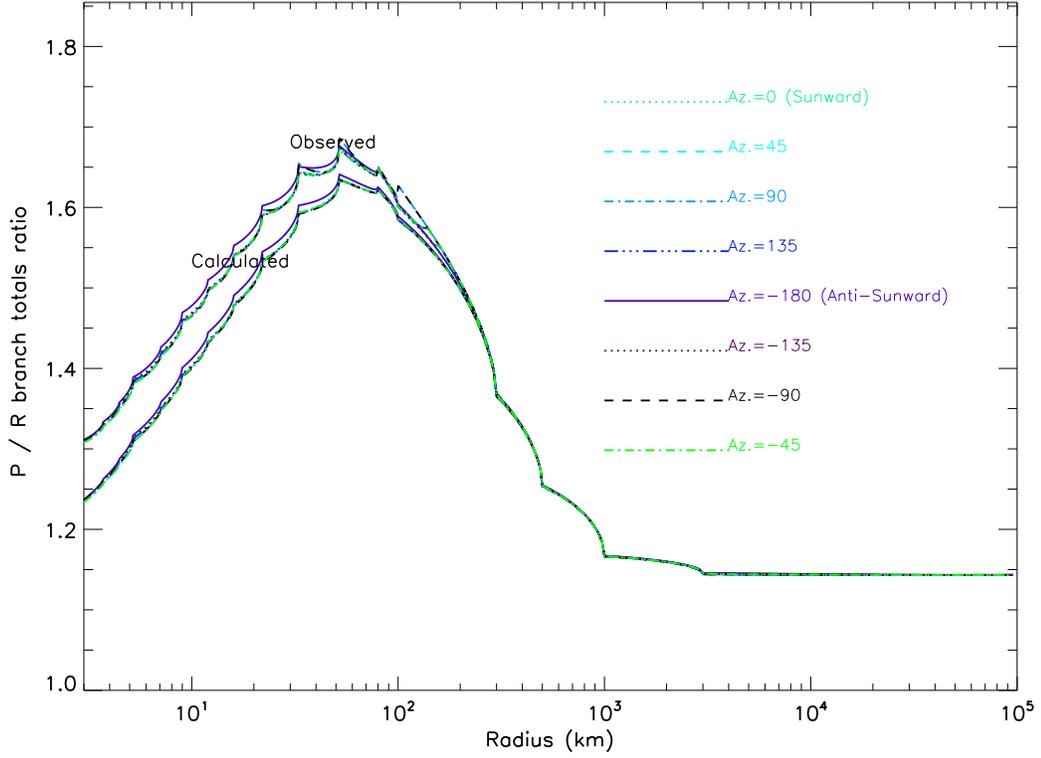
Figure 3.13: For $Q_{CO} = 10^{27}s^{-1}$. Ratio of P branch vs. R branch total Brightness (in $photons\,s^{-1}cm^{-2}sr^{-1}$) vs. R (impact parameter) for Phase angle = 90° and for multiple azimuthal angles. Profiles of azimuthal angles show minimal variation for this case and overlap, appearing *nearly* indistinguishable, except inwards of ~40-50 km. ("Sawtoothed" appearance of the profiles is a plotting artifact due to the division into discrete regions in the model.)

cross-referencing the observed P/R ratio for a given radial distance with the corresponding g-factor in Figs. 3.2, 3.3, and 3.4 one can ascertain the "real" g-factor to use to calculate a correct column density from the observed flux. (Note that the different P/R ratio values for large radii are slightly different than those appearing in the corresponding aperture averaged spectra of Figs. 3.9, 3.10 & 3.11 due to the difference in flux units used: $photons\,s^{-1}cm^{-2}sr^{-1}$ in Figs. 3.12, 3.13 & 3.14 and $ergs\,s^{-1}cm^{-2}sr^{-1}$ in Figs. 3.9, 3.10 & 3.11.)

This heuristic is, of course, limited in use to the carbon monoxide $X^1\Sigma^+$ band.
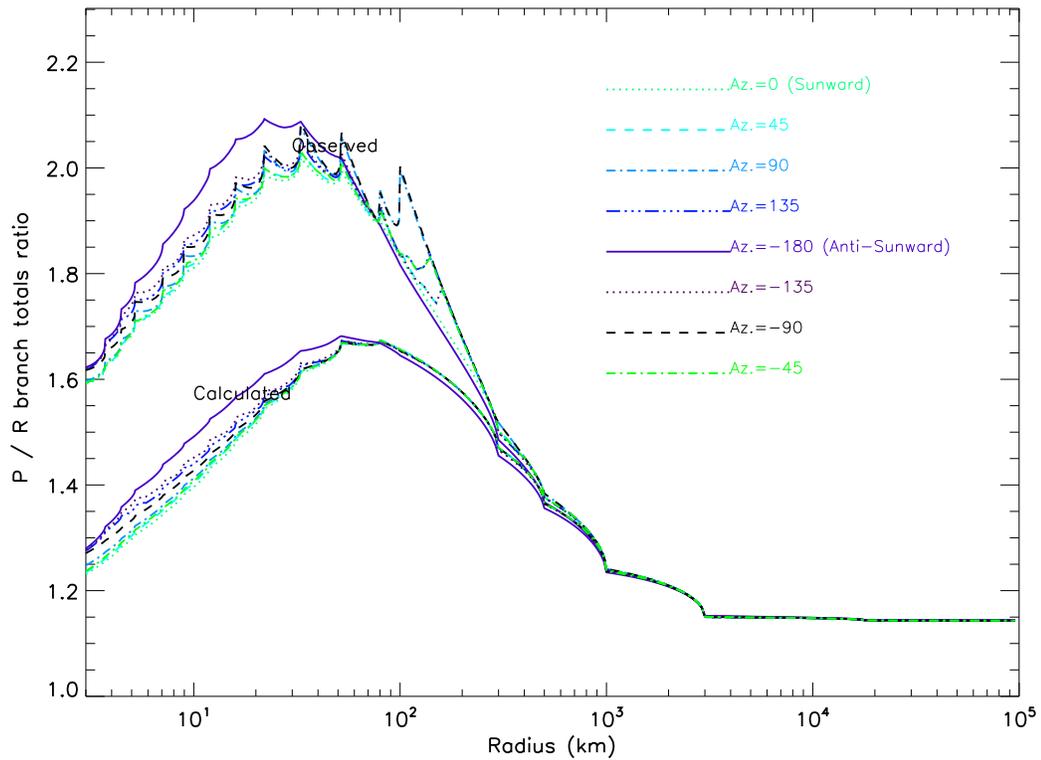
Figure 3.14: For $Q_{CO} = 10^{28}s^{-1}$. Ratio of P branch vs. R branch total Brightness (in $photonss^{-1}cm^{-2}sr^{-1}$) vs. R (impact parameter) for Phase angle $= 90°$ and for multiple azimuthal angles. Profiles of azimuthal angles show some variation in this case, but those for $0°$, $\pm45°$, and $90°$ overlap each other entirely in the calculated profiles and almost entirely in the observed. ("Sawtoothed" appearance of the profiles is a plotting artifact due to the division into discrete regions in the model.)

Other spectra with P and R branches will have their own ratios, which can be derived by similar modeling. More complicated spectra may also, but such ratios would be more complicated to find than for cases with a simple two-branch structure.

3.3 Water

3.3.1 Model Details for Water

We have modeled the 1-0 ν_3 ro-vibrational band of water.

Molecular Levels and Einstein Coefficients

Our model includes transitions that occur between rotational levels up to and including J=7 in the ν_3 1 and 0 vibrational levels. Earlier models (e.g. Bockelee-Morvan 1987; Weaver and Mumma 1984) and our results show that this is more than enough levels and lines for most comets' comae. In general, throughout most of the coma, a small handful of strong lines are dominant by orders of magnitude. This is due to the very high Einstein coefficients of those transitions as compared to collisional coefficients. Only in the inner coma, where collisional transition rates are significant compared to radiative rates (and LTE is approached) are there many other strong lines visible. However, we are particularly concerned with the inner coma, and so have included many more levels and transitions. Our results confirm *a posteriori* that many of these levels remain extremely underpopulated and could have been left out. (In some particular cases with large production rates, such as for comet C/2009 P1 Garradd, we actually do leave out the J=6 and 7 levels to make the problem more computationally tractable. Tests show that even within a few kilometers of the center, this only reduces the total flux by less than $\sim$5%.)

The necessary energies and transition rates for these levels and transitions are taken from the HITRAN database (see Rothman et al. 1998).

Collisional Excitation

A literature search (see, e.g. Bockelee-Morvan and Crovisier 1987a; Combi 1996; Crovisier 1987; Crovisier and Encrenaz 1983; Weaver and Mumma 1984, etc.) will reveal that there is little consensus on the matter of collisional excitation models and values for collisional cross-sections, other than the agreement that truly accurate values remain elusive. With respect to the latter, for H_2O-H_2O collisions, values range from $2.5 \times 10^{-15}\ cm^2$ in Weaver and Mumma (1984) to as high as $5 \times 10^{-14}\ cm^2$ in Bockelee-Morvan and Crovisier (1987a).

We have adopted a fairly simplified treatment of collisional excitation and de-excitation, similar to the one used for CO (see Sec. 2.2.1). The collisional cross section for de-excitation is taken from Table 2 of Weaver and Mumma (1984) to be $2.5 \times 10^{-15}\ cm^2$. Detailed balance is used to calculate the excitation values. Using these values, the coefficients for H_2O-H_2O collisions (assumed to be the dominant source of collisional excitation) are then calculated as per Chin and Weaver (1984): only rotational excitation and de-excitation are considered. $C = n_{H_2O}\ \sigma\ \bar{v}$, where $\bar{v}$ is the average relative speed of the molecules (cm/s), n_{H_2O} is the number density of H_2O (cm^{-3}) and σ is the collisional cross section of a given transition. The last value is based on the above total cross section, which is apportioned between J levels in a manner similar to Chin and Weaver (1984) Table 1. Since rotational levels which are "adjacent" in the quantum number J (or K_a and K_c) are not necessarily adjacent in energies, we use an energy ordered array of levels, and use Δi, where i is the array index, in place of the actual ΔJ as in Chin and Weaver's treatment of CO.

Ortho and Para Water

Since transitions between ortho and para states of water are strongly forbidden, ortho and para water are treated as two separate species in our model; all calculations from coma integration through radiative transfer are done separately. They interact only through collisions, as we use the total density of water as the dominant collision partner for every species in our model. We then merge the results from the ortho and para calculations into one spectrum in IDL code as it is plotted. The ortho to para ratio is a model parameter that can be adjusted, for both parts of this process. As a default, we use 3:1 in all of the following modeled spectra. We *did* test some models with somewhat varied (by ~10-15%) O:P ratio, but the change in resulting spectra was negligible.

Model Parameters

Other model parameters (see Table 3.1) have been chosen for simplicity in the modeling of theoretical comets: Solar distance = 1 AU. Solar flux (over the H_2O band) is $3.9 \times 10^{13} \, photons \, cm^{-2} s^{-1}/cm^{-1}$, (Labs and Neckel 1968; and as used by Weaver and Mumma 1984). Note that these are changed below when we model comet Garradd, which was observed at a heliocentric distance $\gtrsim 2$ AU. Gas expansion speed is a constant 0.8 km/s and surface temperature 200 K.

The radial temperature profile closely follows the model of Combi (1989) (see Fig. 2.6).

3.3.2 Results for Water: Hypothetical Example Comets

There have been numerous previous efforts to model H_2O in comets, including Weaver and Mumma (1984), Crovisier (1984a) and Bockelee-Morvan (1987) among others. Our model improves on earlier ones in its treatment of optical depth effects and also in its geometry. To test our model (along with other tests) we have compared results for optically thin cases with these and found reasonably close agreement (for similar model inputs and parameters).

In this section we present model results for H_2O for hypothetical comets with three different (total; ortho + para) production rates, $Q_{H_2O} = 10^{26}$, 10^{27} and 10^{28} s^{-1}.

3.3.3 Radial Profiles: Brightness, Column Density and g-factors

We again present radial profiles of the values for B_{band}, g_{band}, g_{eff} and N, as we did above for CO. Again, we typically see that g_{eff} does tend towards the calculated g-factor values at larger impact parameters (i.e. farther away from the nucleus), where optical depth effects are negligible, as would be expected. Figs. 3.15, 3.16 & 3.17 show radial profiles in which we present all these values together, for hypothetical comets of three different production rates, $Q = 10^{26}, 10^{27}$, and $10^{28} s^{-1}$. (All observed at 1 AU, at a phase angle of 90° and multiple azimuthal angles.)

The actual numerical values of the "asymptotic" band g-factors produced by our model, $3.1 \times 10^{-4} s^{-1}$ per molecule at 1 AU, are not in obvious agreement with other published values such as those calculated by Crovisier (1984a) and Weaver and Mumma (1984), who both have a lower value of $\sim 2.7 \times 10^{-4} s^{-1}$. However, their model omitted one strong line, as Crovisier (1984b) pointed out in an

erratum regarding his own model of the ν_3 spectrum (and the same is true for Weaver and Mumma).

The actual radii at which this convergence occurs depends primarily on the production rate of a comet. We can again use the distance at which $g_{eff} = 0.9\,g_{real}$ as a very rough measure of the point where a coma can be considered to transition from thick to thin.

For the low-Q ("thin") coma model ($Q = 10^{26}\ s^{-1}$) this is immediate; right down to the nucleus this "90%" measure is surpassed.

For the "intermediate" coma model ($Q = 10^{27}\ s^{-1}$) the convergence is fairly close to the nucleus, within tens of kilometers. But for the high-Q ("thick") model ($Q = 10^{28}s^{-1}$) it is relatively far out, at near 10^3 km or more!

For our highest modeled production rate, the "optically thick regime" can extend as far as $O(10^3)$km, which can be spatially resolved even in some remote observations. Note that at radial distances near the nucleus, worrying about optical depth effects may be relevant even for lower production rates.

3.3.4   Aperture Averaged Spectra

We have modeled spectra averaged over apertures in order to model spectra observed remotely with high spectral resolving power. Our "apertures" are simply squares centered on the nucleus, which correspond to equivalent slit widths and distances to the target that include that size of the coma in the observed spectra.

We present a series of aperture averaged spectra (Figs. 3.18, 3.19 & 3.20) from 2×10^1 km (very near the nucleus) through 2×10^5 km (the whole coma) for each of 3 production rates. (All these example spectra are modeled at a heliocentric distance of 1 AU and phase angle $90°$.)

A brief analysis shows that for all but the thickest cases (the 20 km apertures for
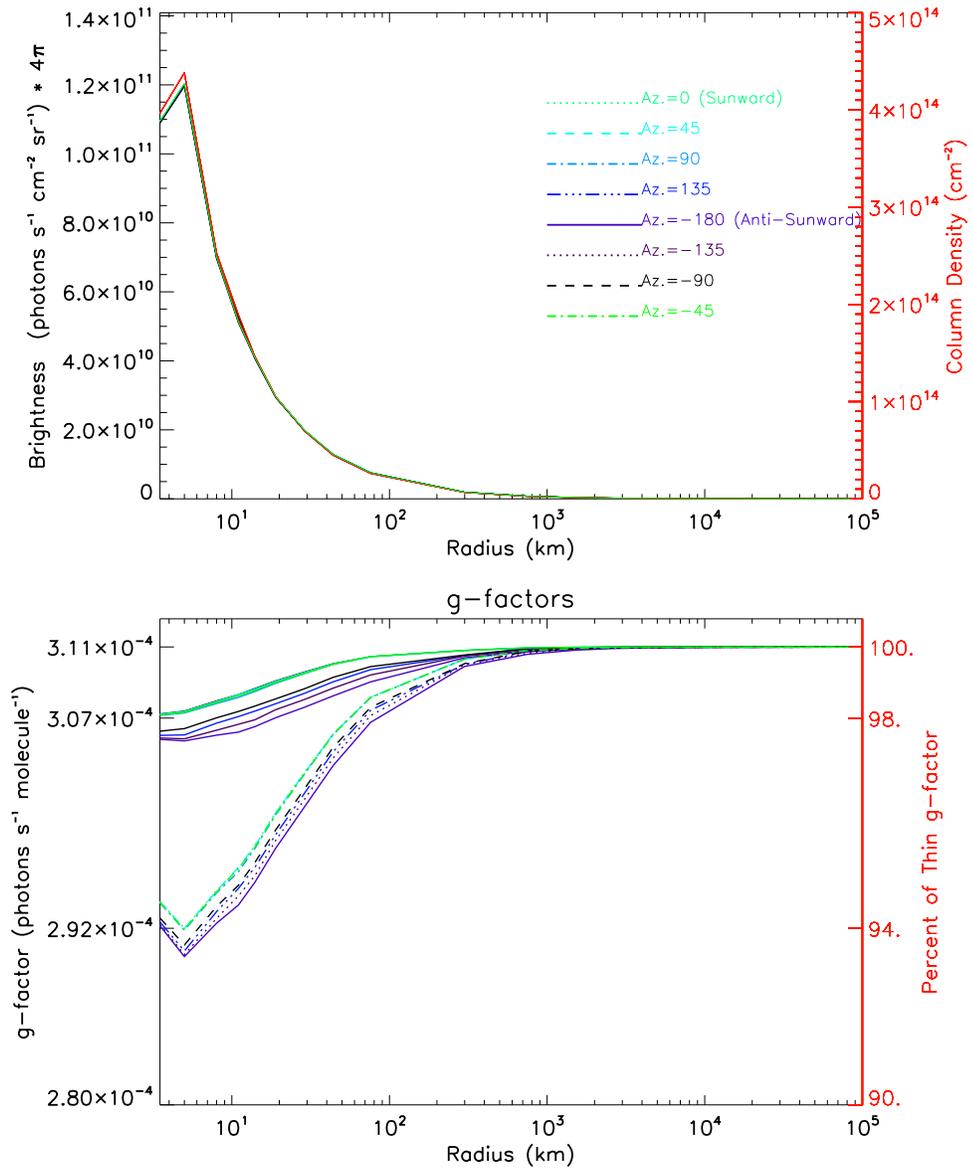
Figure 3.15: For H$_2$O $Q = 10^{26}s^{-1}$. Upper frame: Radial profile of band total Brightness vs. R (impact paramater) for Phase angle $= 90°$ and for multiple Azimuthal angles. Various azimuthal angles are indicated by color coding and their lines slightly vertically displaced for viewing purposes. Column density is included in red (on a different y-axis scale). Lower frame: g-factors. The calculated g-factor (solid lines) and g_{eff}, Brightness over Column density (dashed lines), again plotted with matching colors to indicate azimuthal angle.

Figure 3.16: For H$_2$O $Q = 10^{27}s^{-1}$. Upper frame: Radial profile of band total Brightness vs. R (impact paramater) for Phase angle = 90° and for multiple Azimuthal angles. Various azimuthal angles are indicated by color coding and their lines slightly vertically displaced for viewing purposes. Column density is included in red (on a different y-axis scale). Lower frame: g-factors. The calculated g-factor (solid lines) and g_{eff}, Brightness over Column density (dashed lines), again plotted with matching colors to indicate azimuthal angle.

Figure 3.17: For H_2O $Q = 10^{28}s^{-1}$. Upper frame: Radial profile of band total Brightness vs. R (impact paramater) for Phase angle $= 90°$ and for multiple Azimuthal angles. Various azimuthal angles are indicated by color coding and their lines slightly vertically displaced for viewing purposes. Column density is included in red (on a different y-axis scale). Lower frame: g-factors. The calculated g-factor (solid lines) and g_{eff}, Brightness over Column density (dashed lines), again plotted with matching colors to indicate azimuthal angle.

all three production rates, and the 100 km aperture in the $Q = 10^{28}s^{-1}$ model) the band shape is dominated by the prominent five lines that are associated with the

(a) Aperture = 20 km.

(b) Aperture = 100 km.

(c) Aperture = 200 km.

(d) Aperture = 2,000 km.

(e) Aperture = 20,000 km.

(f) Aperture = 200,000 km.
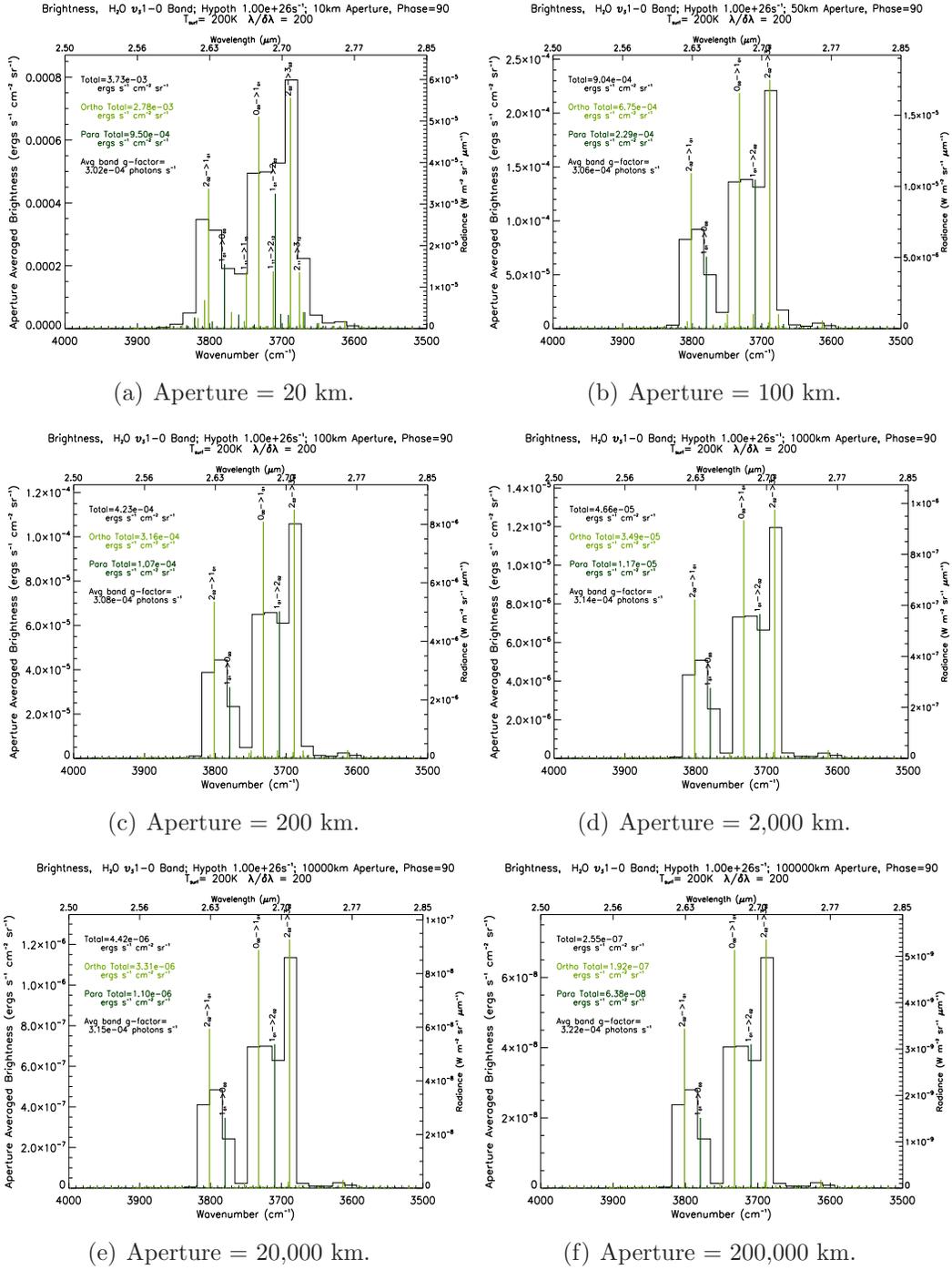
Figure 3.18: Aperture averaged spectra for H_2O for $Q = 10^{26}s^{-1}$. Left side y-axis is total brightness. Right y-axis is Radiance. Totals are indicated on each graph. The continuous line is the spectrum after convolution and pixel binning simulating the Deep Impact HRI instrument.
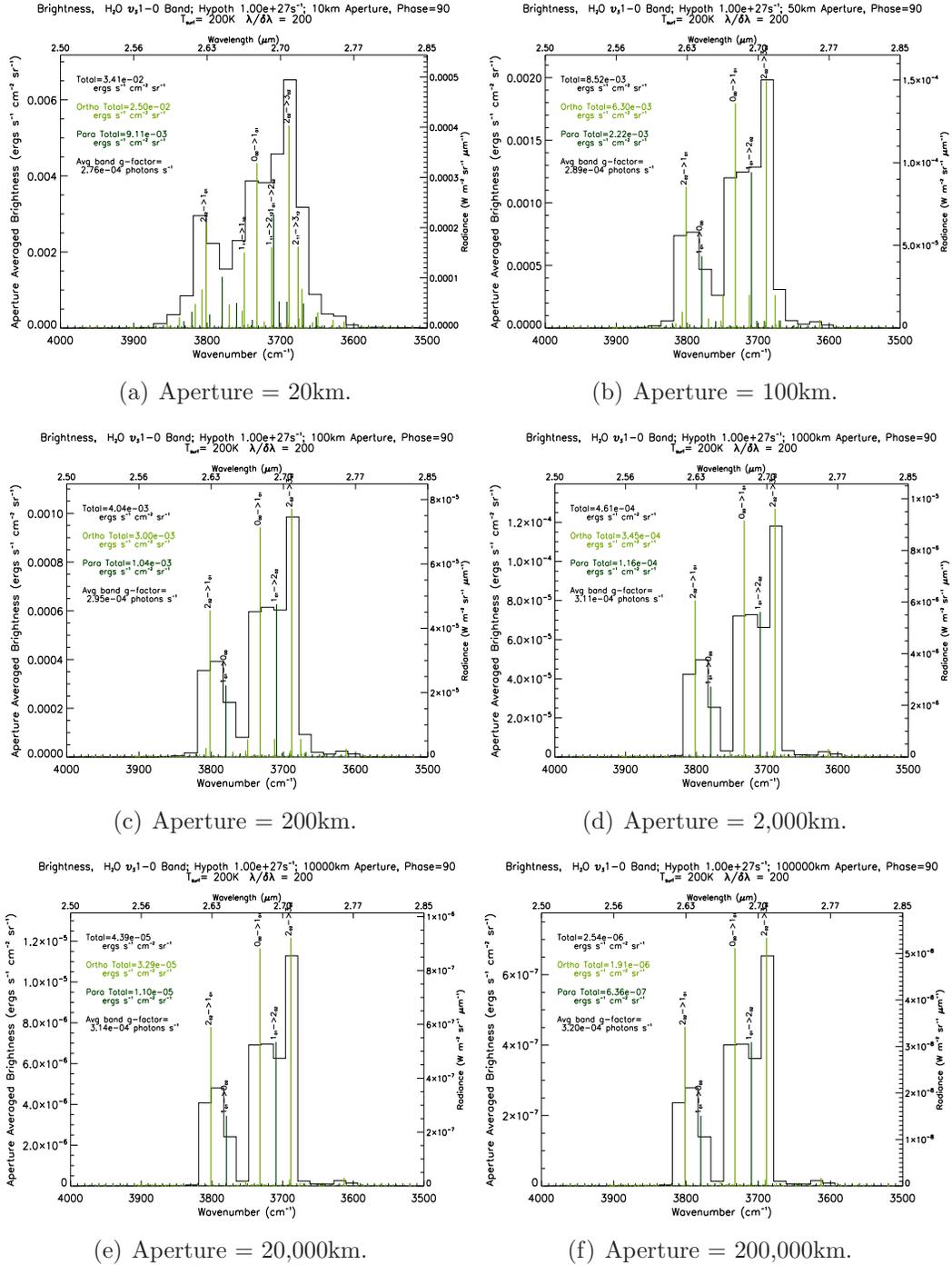
Figure 3.19: Aperture averaged spectra for H_2O for $Q = 10^{27} s^{-1}$. Left side y-axis is total brightness. Right y-axis is Radiance. Totals are indicated on each graph. The continuous line is the spectrum after convolution and pixel binning simulating the Deep Impact HRI instrument.

93

(a) Aperture = 20km.

(b) Aperture = 100km.

(c) Aperture = 200km.

(d) Aperture = 2,000km.

(e) Aperture = 20,000km.

(f) Aperture = 200,000km.
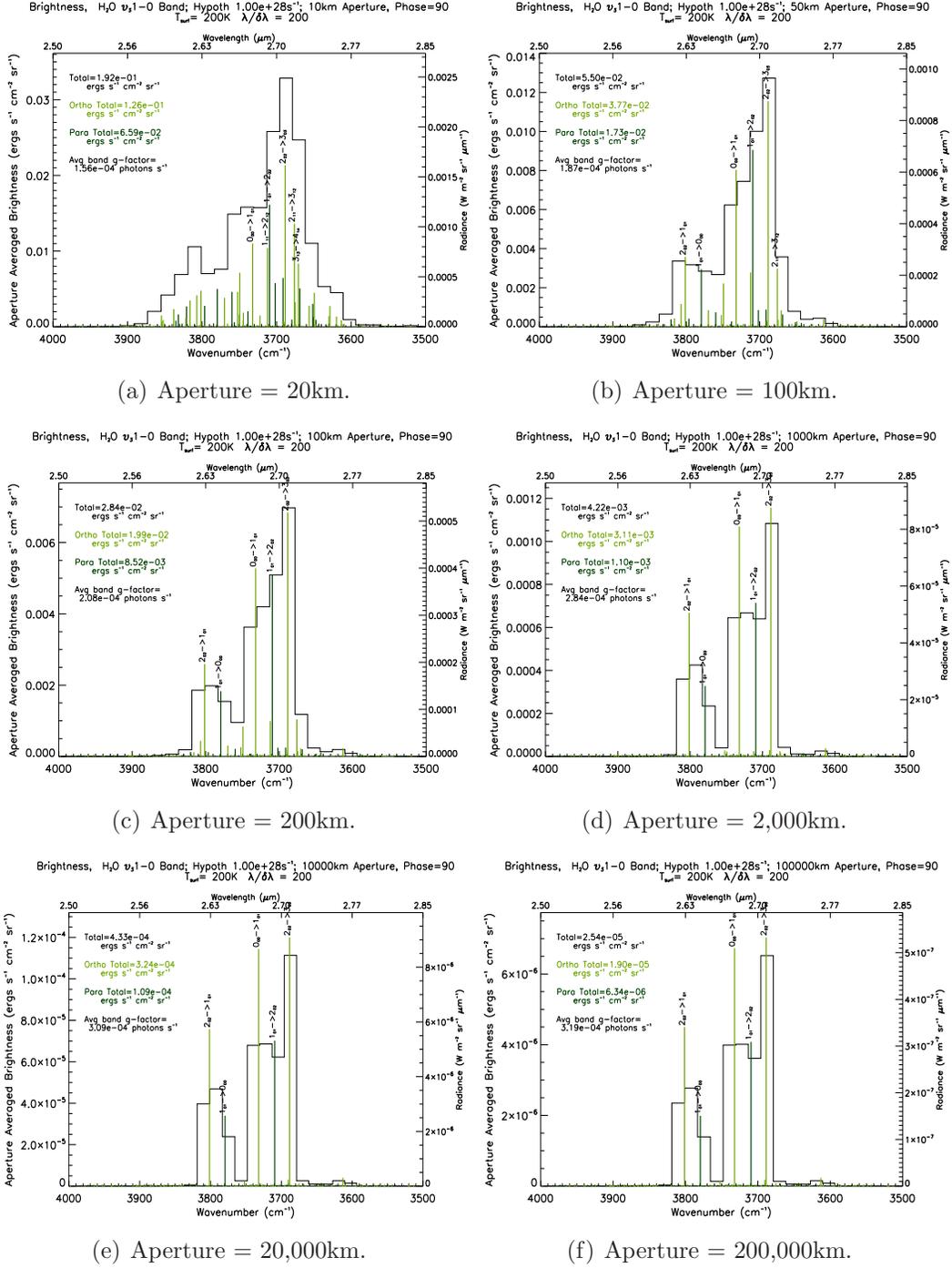
Figure 3.20: Aperture averaged spectra for H_2O for $Q = 10^{28}s^{-1}$. Left side y-axis is total brightness. Right y-axis is Radiance. Totals are indicated on each graph. The continuous line is the spectrum after convolution and pixel binning simulating the Deep Impact HRI instrument.

lowest rotational levels. The prominence of these lines in fluorescence dominated regimes of water spectra has been shown (see Weaver and Mumma 1984). Our models show that there is some shifting of flux between these lines, even when they dominate the spectra, and this is due to optical depth effects: Energy from optically thick lines is being forced into other lines on its path out of the coma. The optically thicker, many-lined spectra in the inner coma apertures are collisionally dominated due to the higher density and are significantly influenced by temperature. (See, e.g. Bockelee-Morvan 1987; Bockelee-Morvan and Crovisier 1987a)

3.4 Carbon Dioxide

Carbon dioxide has recently been considered much more important in understanding cometary volatiles than was previously realized. (See, among others, A'Hearn et al. 2012; Mumma and Charnley 2011; Ootsubo et al. 2012)

The earlier situation was, to a great extent, due to the infrared bands of CO_2 having not been directly observed in many comets at all until quite recently. (See Ootsubo, 2010, for a historical list.) This is due to telluric absorption rendering Earth's atmosphere opaque in those bands of CO_2. In very recent years, the Deep Impact spacecraft (see A'Hearn et al. 2011; Feaga et al. 2014, 2007a) and the *AKARI* satellite (see Ootsubo et al. 2012, 2010) have dramatically increased the number of comets in which the CO_2 4.2 μm IR band have been observed.

Unlike water, presumably owing to the difficulty of observing it, there has been little modeling attention lavished on CO_2 in comets. Previous efforts include those by Weaver and Mumma (1984) and by Crovisier (1987). Both neglect a thorough treatment of radiative transfer and optical depth effects (as well as, particularly the former, having relied on other simplifications).

We have modeled the 1-0 ν_3 rovibrational band of CO_2, with a more thorough treatment.

3.4.1   Model Details for CO_2

For CO_2 our model includes transitions up to rotational levels J=50 at a minimum, and up to a possible maximum of J=100, (see Crovisier 1987) in the ν_3 1 and 0 vibrational levels. This much greater maximum for J levels (than either H_2O, above, or CO, as per Chin and Weaver, 1984) is primarily due to two factors: the very high values of CO_2 Einstein coefficients for vibrational transitions (approximately an order of magnitude higher than for CO or H_2O) and the lack of purely rotational lines to allow rapid relaxation from higher J states (since CO_2 is a linear symmetric molecule, it has no purely rotational dipole moment). Also, due to symmetry rules, only even or odd J levels exist for a given vibrational level. (Thus with respect to computational complexity, for our modeled levels, J=50 is roughly analogous to J=25 for carbon monoxide.)

However, collisional transitions between rotational levels within the same vibrational level are allowed, but are only effective in relaxing populations between J levels in the higher density inner coma, where conditions approach LTE. In the outer coma, where flourescence dominates, populations are pumped up to much higher J levels. (In fact, using only levels up to J=70 leaves an abrupt cutoff appearance in spectra instead of typical smoothly descending wings, and may be insufficient for a true picture of such spectra. However, computational considerations have, in general, prevented us from using a much higher limit.)

As with H_2O, the necessary energies and transition rates for these levels and transitions are taken from the HITRAN database (see Rothman et al. 1998).

Initially, we used a treatment of collisional excitation and de-excitation that was

essentially the same as above for H_2O, with a total collisional cross section for de-excitation taken from Weaver and Mumma's (1984) Table 2 to be 3.6×10^{-15} cm^2. The cross section for individual transitions was, again, apportioned between J levels in a manner similar to Chin and Weaver's (1984) Table 1. As with water, we again use an energy ordered array of levels, and use Δi, where i is the array index, in place of the actual ΔJ as in Chin and Weaver (since the J levels have alternating quantum numbers).

Subsequently, after our early attempts to fit actual CO_2 observations with our adaptation of Chin and Weaver's method resulted in poor fits, we attempted to model CO_2 collisions using the approach taken from Goldsmith (1972), as described above, in place of that taken from Chin and Weaver (1984), which we had adapted to CO_2.

The solar flux (over the CO_2 ν_3 band) is 2.8×10^{13} $photons\,cm^{-2}s^{-1}/cm^{-1}$ (Labs and Neckel 1968; and as used by Weaver and Mumma 1984). Other model parameters are as above for H_2O, with $Q_{H_2O} = 10 \times Q_{CO_2}$.

3.4.2 Comparison with Earlier Models

To verify our model we ran test cases for comparison with Crovisier (1987), one of the few similar models published for CO_2.

We have produced three models using input parameters corresponding to those of Crovisier (1987). For all three cases, $Q_{CO_2} = 2 \times 10^{26} s^{-1}$ and other parameters are listed in Table 3.2. The resulting spectra are shown in Figs. 3.21, 3.22 & 3.23.

While not a perfect match, our results are qualitatively similar to those of Crovisier (1987). The relatively minor differences are readily attributed to several inherent differences between that model and ours, most notably the temperature profile and the different treatment of collisional excitation and coefficients. (In ad-

CO$_2$ Test Model Parameters Corresponding to Crovisier (1987)			
	A	B	C
Q_{H_2O}	$1 \times 10^{30} s^{-1}$	$2 \times 10^{29} s^{-1}$	$2 \times 10^{28} s^{-1}$
Heliocentric Distance	0.8 AU	1.0	1.6
Observing Distance	10^4 km	1.0 AU	10^3 km
Radius of Angular Field of View	30'	0.1'	4.5'
Radial Aperture Size	87.3 km	4000 km	1.3 km
Q_{CO_2}	$2 \times 10^{26} s^{-1}$		
Mean Nucleus Radius	3 km		
Surface T	250 K		
Expansion speed V$_{exp}$	0.8 km/s		
σ_{rot}	1×10^{-14} cm^2		

Table 3.2: Test Model input parameters, for CO$_2$.

dition, Crovisier (1987) used a much higher collisional cross section than we have generally used. However, *only* for this comparison, we used the higher value for these test cases.) These factors all cause Crovisier's model to favor collisional excitation more strongly than ours.

This leads to the most noticeable difference between our spectra and Crovisier's occurring in the case with the largest aperture. This includes portions of the coma where our model is already begining to tend towards being fluorescence dominated (hence the greater flux in the wings of the band) whereas Crovisier's is still solidly collisionally dominated. (Note also, that he mentions that fluorescent equilibrium is *never* reached in his model, whereas in ours it certainly is. See below, Figs. 3.27 - 3.29.) We have also included a 2000 km aperture spectrum from the same model ("B"), which considerably more closely resembles Crovisier's corresponding model spectrum. This closer matching at smaller radii follows logically from the aforementioned divergence at larger radii due to the greater range of collisional dominance of Crovisier's model.

Furthermore, our model includes optical depth effects, whereas Crovisier's does

(a) Model "A": For radial Aperture ∼87 km. Left side y-axis is aperture averaged brightness. Right y-axis is effective (line) g-factor (brightness/column density). Totals are indicated on graph.

(b) Crovisier's Spectrum at 0.8 AU. $\theta = 30'$.

Figure 3.21: Aperture integrated spectrum for $Q_{CO_2} = 2 \times 10^{26} s^{-1}$ and $Q_{H_2O} = 1 \times 10^{30} s^{-1}$ at 0.8 AU, and corresponding spectrum taken from Crovisier (1987). Note that the x axis in our plot (a) is reversed from Crovisier's (b). (We maintained this orientation so that ours matches other spectra we model throughout this work.)

Brightness, CO₂ v_3 1-0 Band; Q= 2x10²⁶s⁻¹; 8000km Aperture, Phase=90
T_{surf}= 250K

Total=1.30e-04
ergs s⁻¹ cm⁻² sr⁻¹

P branch Total=6.51e-05
ergs s⁻¹ cm⁻² sr⁻¹

R branch Total=6.52e-05
ergs s⁻¹ cm⁻² sr⁻¹

P/R Ratio= 1.00

Avg. Band Total
g-factor= 2.80e-03
photons s⁻¹

Brightness, CO₂ v_3 1-0 Band; Q= 2x10²⁶s⁻¹; 4000km Aperture, Phase=90
T_{surf}= 250K

Total=2.55e-04
ergs s⁻¹ cm⁻² sr⁻¹

P branch Total=1.29e-04
ergs s⁻¹ cm⁻² sr⁻¹

R branch Total=1.26e-04
ergs s⁻¹ cm⁻² sr⁻¹

P/R Ratio= 1.03

Avg. Band Total
g-factor= 2.79e-03
photons s⁻¹

(a) Model "B": For radial Aperture ∼4000 km.

(b) Model "B": For radial Aperture ∼2000 km.
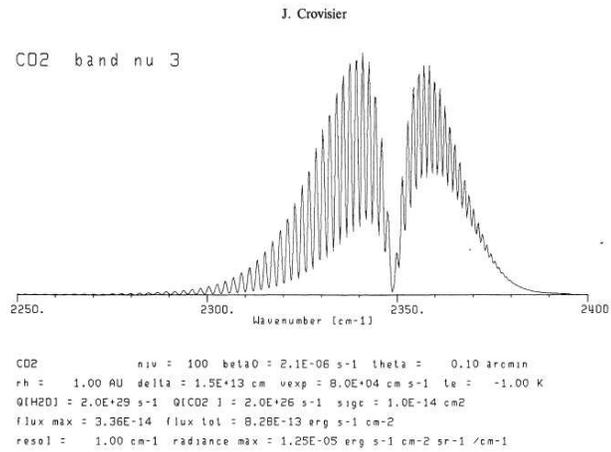
(c) Crovisier's Spectrum at 1.0 AU. $\theta = 30'$.

Figure 3.22: Aperture integrated spectra for $Q_{CO_2} = 2 \times 10^{26} s^{-1}$ and $Q_{H_2O} = 2 \times 10^{29} s^{-1}$ at 1.0 AU, and corresponding spectrum taken from Crovisier (1987). In our plots, (a & b) the left side y-axis is aperture averaged brightness. Right y-axis is effective (line) g-factor (brightness/column density). Totals are indicated on each graph. Note that the x axis in our plots is reversed from Crovisier's.

not. This would be relevant only near the nucleus for the low production rate of $Q_{CO_2} = 2 \times 10^{26} s^{-1}$ that we are modeling here, but two of the three sample cases are spectra of small aperture sizes (Models A & C) where optical depth effects should be expected even for a low production rate. However, the differences for these models

Brightness, CO_2 v_3 1−0 Band; Q= $2 \times 10^{26} s^{-1}$; 2km Aperture, Phase=90
T_{surf} = 250K

Total=7.42e−03
ergs s⁻¹ cm⁻² sr⁻¹

P branch Total=3.98e−03
ergs s⁻¹ cm⁻² sr⁻¹

R branch Total=3.44e−03
ergs s⁻¹ cm⁻² sr⁻¹

P/R Ratio= 1.16

Avg. Band Total
g−factor(@1.6AU)= 6.94e−04
photons s⁻¹
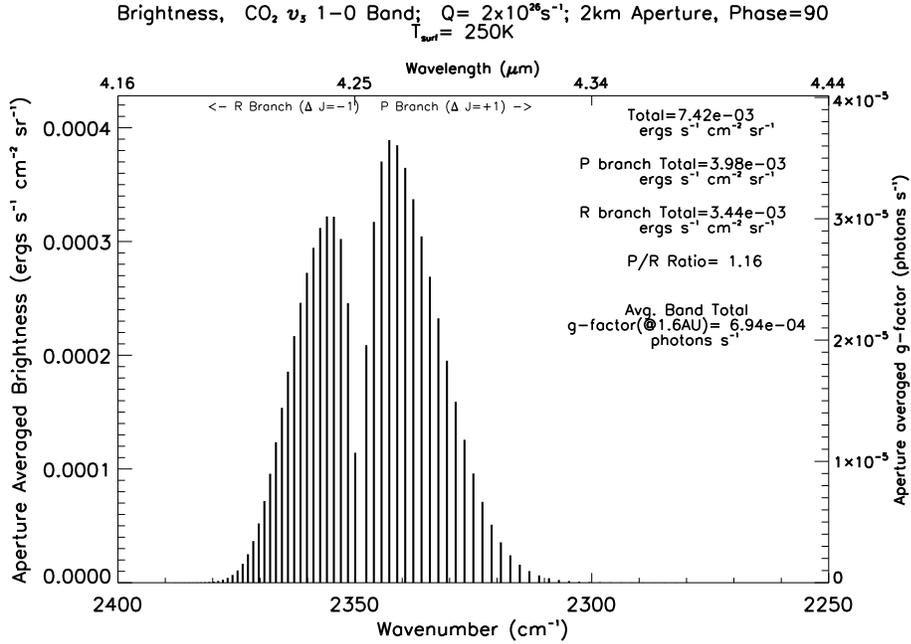
(a) Model "C": For Radial Aperture ~1.3 km. Left side y-axis is aperture averaged brightness. Right y-axis is effective (line) g-factor (brightness/column density). Totals are indicated on graph.

CO2 band nu 3

CO2   niv = 100 beta0 = 2.1E-06 s-1 theta =   4.50 arcmin
rh =   1.60 AU delta = 1.0E+08 cm vexp = 8.0E+04 cm s-1 te =   -1.00 K
Q[H2O] = 2.0E+28 s-1 Q[CO2] = 2.0E+26 s-1 sigc = 1.0E-14 cm2
flux max = 8.14E-08 flux tot = 1.34E-06 erg s-1 cm-2
resol =   1.00 cm-1 radiance max = 1.51E-02 erg s-1 cm-2 sr-1 /cm-1
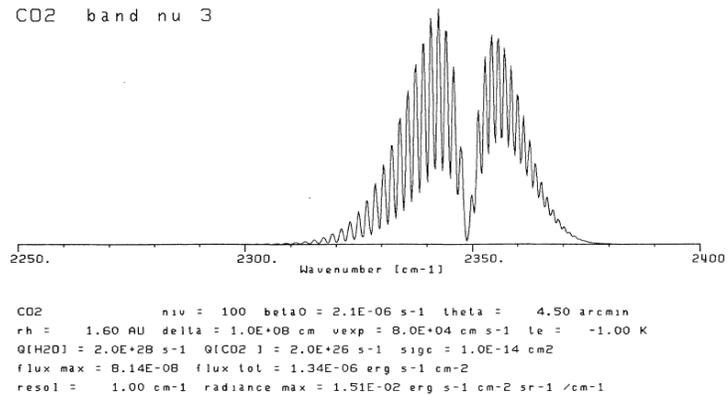
FIGURE 6(b)

FIGURE 6. — (a-m) Synthetic vibrational bands of the various molecules, for the population distributions of figure 3, and for a space instrument at 1000 km from the comet with a 9′ diameter field of view.

(b) Crovisier's Spectrum for $Q_{CO_2} = 2 \times 10^{26} s^{-1}$ and $Q_{H_2O} = 2 \times 10^{28} s^{-1}$ at 1.6 AU. $\theta = 30'$.

Figure 3.23: Aperture integrated spectrum for $Q_{CO_2} = 2 \times 10^{26} s^{-1}$ and $Q_{H_2O} = 2 \times 10^{28} s^{-1}$ at 1.6 AU, and corresponding spectrum taken from Crovisier (1987). Note that the x axis in our plot (a) is reversed from Crovisier's.

are smaller than for the larger aperture case ("B"). This is presumed to be due to the band shape being more affected by the differences in collisional treatment and

temperature model than optical depth effects for production rates of this magnitude. (See the band shapes in Fig. 3.27.)

3.4.3 Results for CO_2: Hypothetical Example Comets

As with the previous two molecules, in this section we present model results for the CO_2 ν_3 band for hypothetical comets with three different production rates, $Q_{CO_2} = 10^{26}$, 10^{27} and 10^{28} s^{-1}. (For all three, $Q_{H_2O} = 10 \times Q_{CO_2}$.)

3.4.4 Radial Profiles: Brightness, Column Density and g-factors

We now present radial profiles of brightness, column density and g-factors for the three different production rates we have modeled in Figs. 3.24, 3.25 & 3.26.

The most striking feature in the CO_2 profiles is the extremely protracted "flat shoulder" region in the $Q = 10^{28}s^{-1}$ model, and the similar but shorter one in the $Q = 10^{27}s^{-1}$ case. This feature begs some explanation.

The much higher optical depth of CO_2, as compared to CO or H_2O, is certainly the main contributing factor. Note that in the analogous optically thick case ($Q = 10^{28}s^{-1}$) of CO that we modeled there is a somewhat similar feature. There we see a "bump" in the vicinity of ~ 100 - 1000 km (most noticeable in the profile viewed from an anti-sunward phase angle). We attributed this primarily to high optical depths (with temperature also playing some role) on both the emergent flux and the incident solar radiation. The attenuation of the latter was the reason for it being most visible in the anti-sunward direction. The same is true here, except that due to the extremely high optical depth of CO_2, the effect is even seen from angles that are not anti-sunward, such as the profiles shown here (all for phase angle $= 90°$).
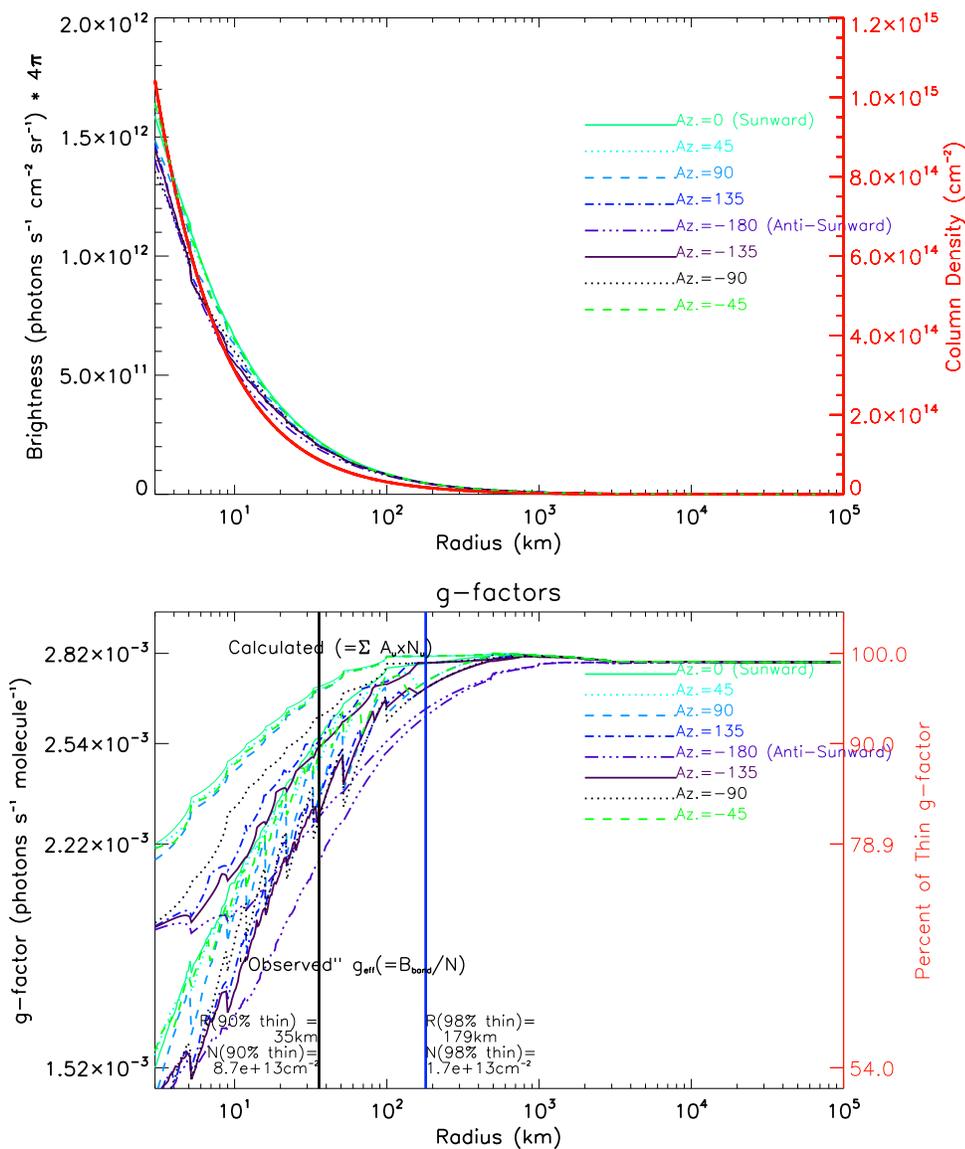
Figure 3.24: For $Q = 10^{26}s^{-1}$. Upper frame: Radial profile of band total Brightness vs. R (impact paramater) for Phase angle = 90° and for multiple Azimuthal angles. Various azimuthal angles are indicated by color coding. Column density is included in red (on a different y-axis scale). Lower frame: g-factors. The calculated g-factor (solid lines) and g_{eff}, Brightness over Column density (dashed lines), again plotted with matching colors to indicate azimuthal angle.

The relative "flatness" of the feature is due to the lesser dependence of the CO_2 band shape on temperature (compared with CO). Throughout most of the
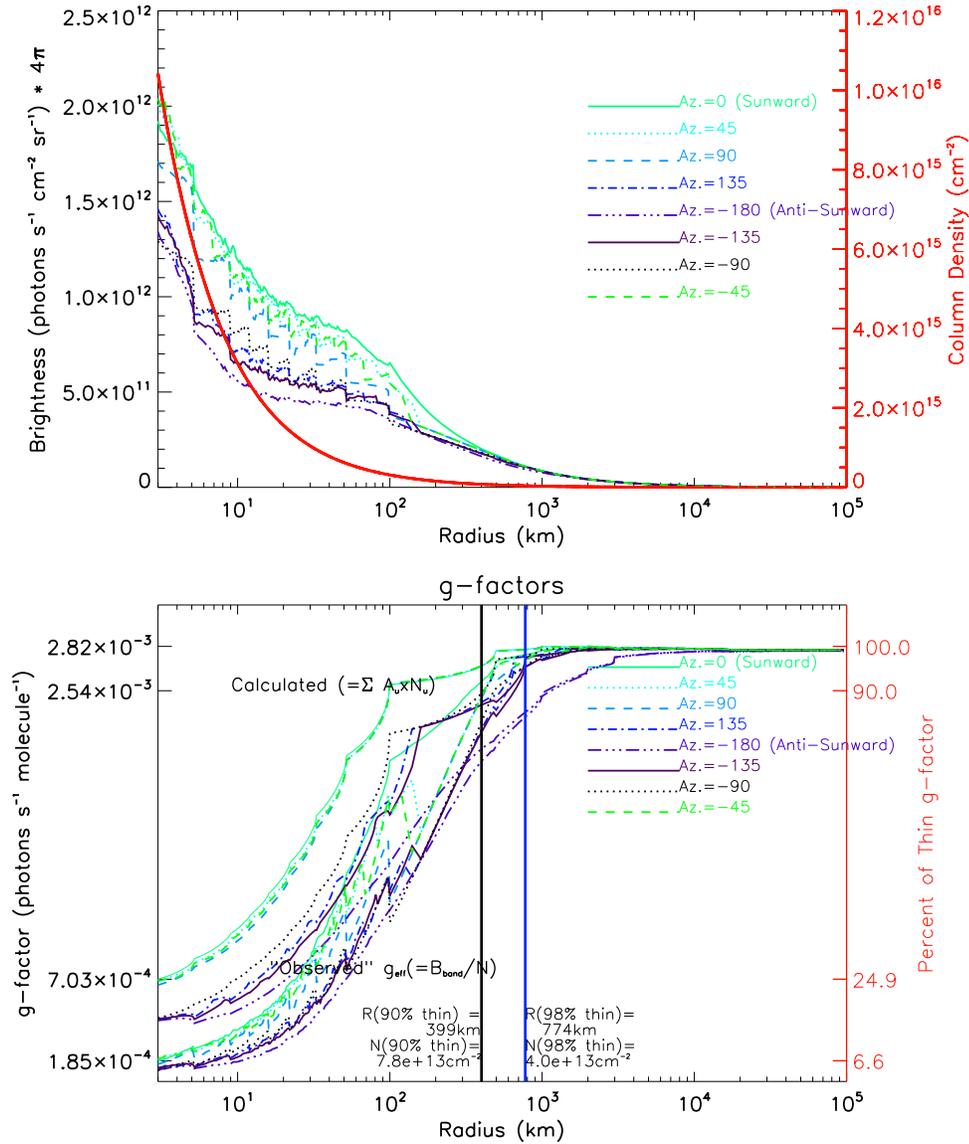
Figure 3.25: For $Q = 10^{27} s^{-1}$. Upper frame: Radial profile of band total Brightness vs. R (impact paramater) for Phase angle $= 90°$ and for multiple Azimuthal angles. Various azimuthal angles are indicated by color coding. Column density is included in red (on a different y-axis scale). Lower frame: g-factors. The calculated g-factor (solid lines) and g_{eff}, Brightness over Column density (dashed lines), again plotted with matching colors to indicate azimuthal angle.

inner coma (from $\sim 100 \sim 1000$ km; see Figs. 3.29(b) - 3.29(d) above), where the spectra are not fluorescence dominated, the peak and width of the band remains
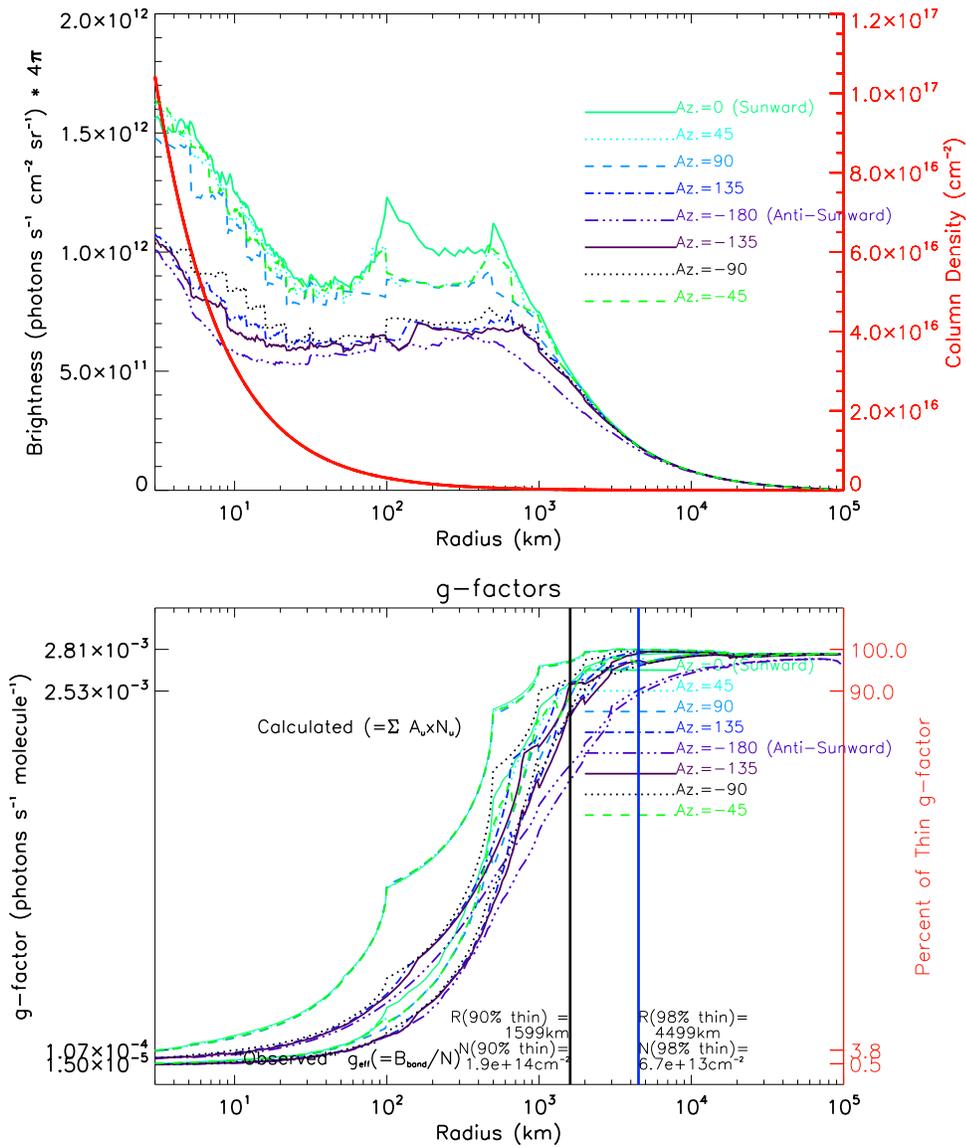
Figure 3.26: For $Q = 10^{28}s^{-1}$. Upper frame: Radial profile of band total Brightness vs. R (impact paramater) for Phase angle $= 90°$ and for multiple Azimuthal angles. Various azimuthal angles are indicated by color coding. Column density is included in red (on a different y-axis scale). Lower frame: g-factors. The calculated g-factor (solid lines) and g_{eff}, Brightness over Column density (dashed lines), again plotted with matching colors to indicate azimuthal angle. (Note: The sharp discontinuities in slope that appear in some lines are an artifact of the granularity and plotting, not an actual feature of the data.)

approximately the same.

3.4.5 Aperture Averaged Spectra

Figs. 3.27, 3.28 & 3.29 show our aperture averaged CO_2 spectra.

One notable feature of these CO_2 spectra is that the shape of the band in the radiatively dominated regime changes very little. Furthermore, the transition from collisionally dominated to fluorescence dominated happens quite abruptly. This is due to the extremely high Einstein A coefficients of the band. As soon as collisions cease to be the dominating mechanism, the spectra shift to their radiatively dominated shape, with hardly any transition zone in between.

One of the most striking features of the CO_2 spectra here is their breadth (for the larger "apertures", i.e. those including greater nucleocentric distances). When compared to CO, a molecule with a seemingly similar band shape and structure (P and R branches) it seems hard to believe, at first glance, that so many lines could be excited (under equivalent conditions). However, this excitation is supported by several factors. It is reasonable in light of the lack of relaxation by rotational radiative transitions. In the outer coma where density is low and collisional de-excitation negligible, solar radiation pumps the molecule up to higher J levels through rovibrational transitions, and its only relaxation is through those same transitions, so it reaches a high "rotational" temperature. A comparison with Crovisier (1987) shows a similarly broad band and large number of lines.

It is however interesting to note that for the relatively few comets in which CO_2 has been (directly) observed, the bands often appear fairly narrow. (See e.g. A'Hearn et al. 2011; Feaga et al. 2007a, and supporting online material, or Chapter 4 below) This is presumably due to these observations being primarily of the collisionally dominated regime (close to the nucleus) and of relatively low tempera-
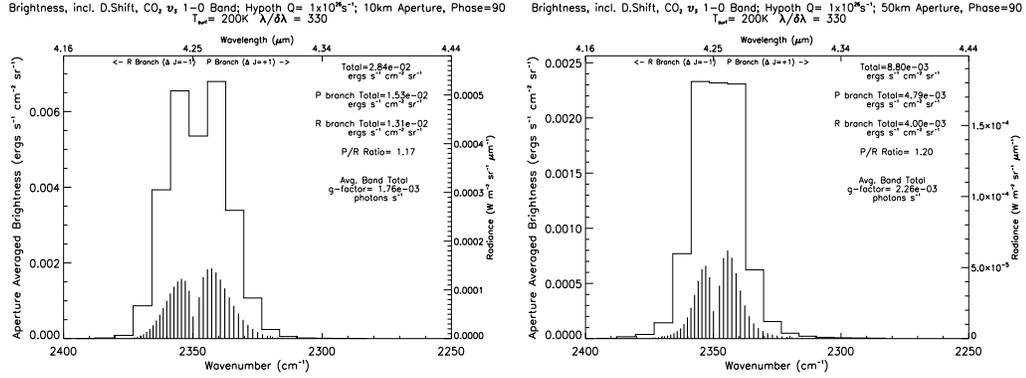
(a) Aperture = 20 km.

(b) Aperture = 100km.
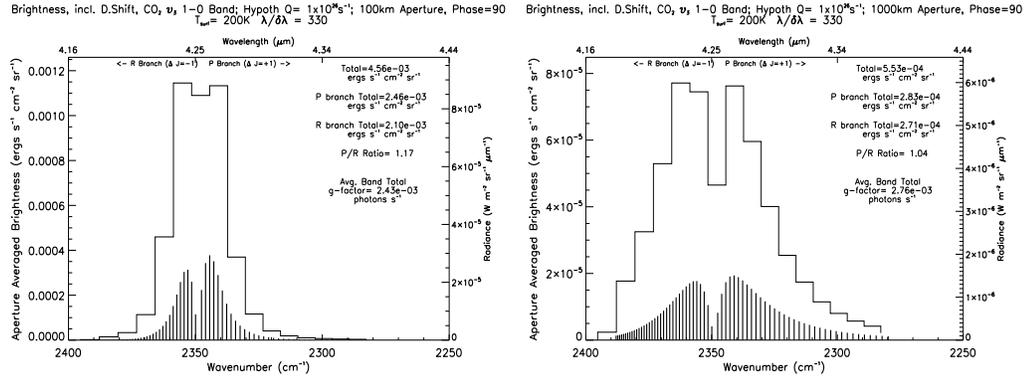
(c) Aperture = 200 km.
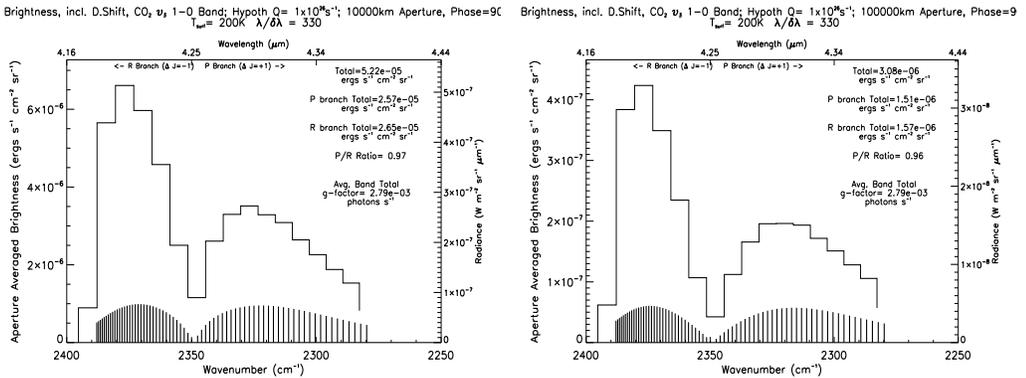
(d) Aperture = 2,000 km.

(e) Aperture = 20,000 km.

(f) Aperture = 200,000 km.

Figure 3.27: Aperture averaged spectra for CO_2 for $Q = 10^{26} s^{-1}$. Left side y-axis is aperture averaged brightness. Right y-axis is Radiance. Totals are indicated on each graph. The continuous line is the spectrum after convolution and pixel binning simulating the Deep Impact HRI instrument.

tures.

On the other hand, many of the *AKARI* spectra (see Ootsubo et al. 2012) show

(a) Aperture = 20 km.

(b) Aperture = 100km.

(c) Aperture = 200 km.

(d) Aperture = 2,000 km.

(e) Aperture = 20,000 km.

(f) Aperture = 200,000 km.

Figure 3.28: Aperture averaged spectra for CO_2 for $Q = 10^{27}s^{-1}$. Left side y-axis is aperture averaged brightness. Right y-axis is Radiance. Totals are indicated on each graph. The continuous line is the spectrum after convolution and pixel binning simulating the Deep Impact HRI instrument.

this band of CO_2 spanning from approximately 4 to 4.5 μm, a band width similar to, or even greater than, our spectra. Although their band shapes do not for the most
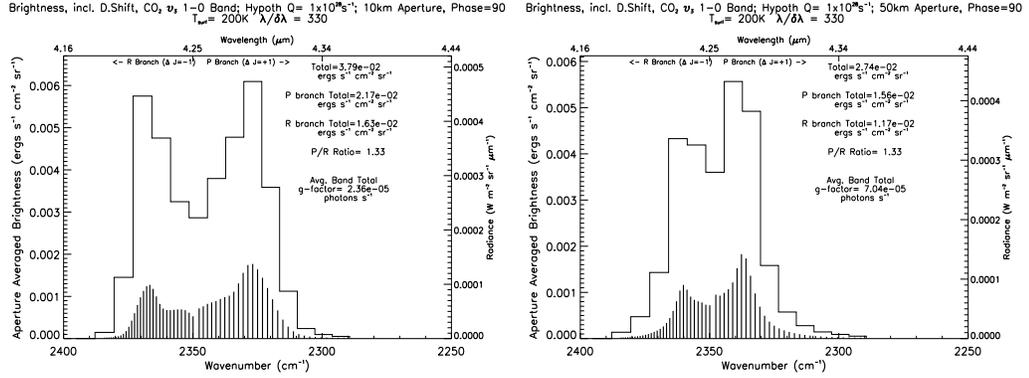
(a) Aperture = 20 km.

(b) Aperture = 100km.
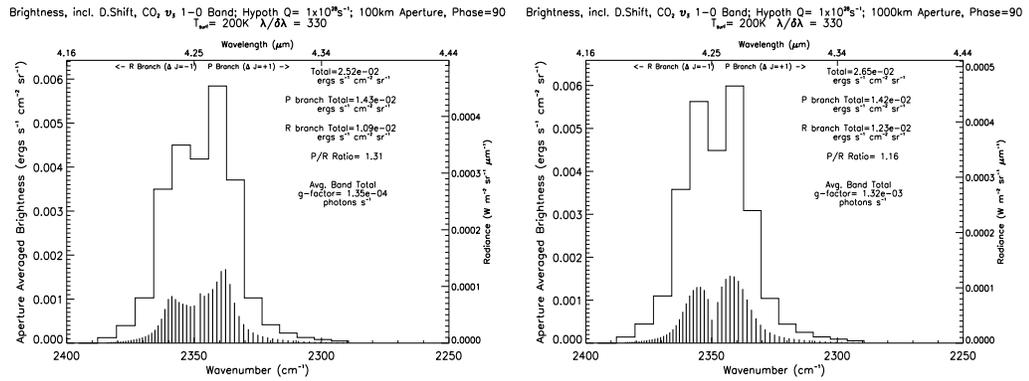
(c) Aperture = 200 km.
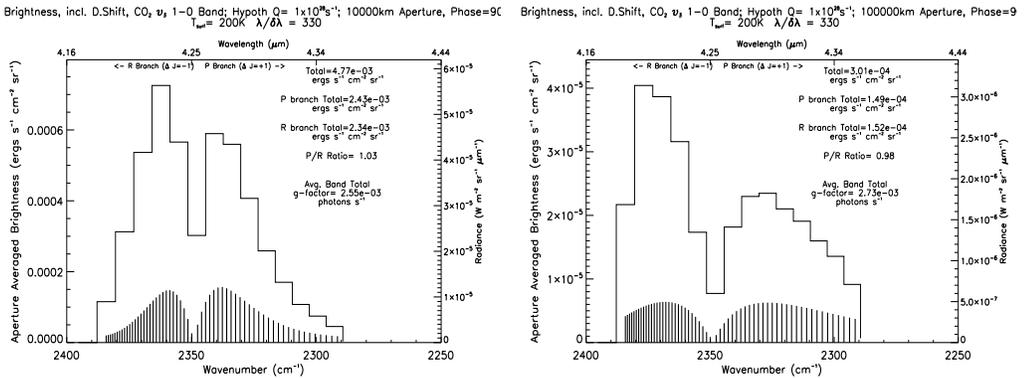
(d) Aperture = 2,000 km.

(e) Aperture = 20,000 km.

(f) Aperture = 200,000 km.

Figure 3.29: Aperture averaged spectra for CO_2 for $Q = 10^{28} s^{-1}$. Left side y-axis is aperture averaged brightness. Right y-axis is Radiance. Totals are indicated on each graph. The continuous line is the spectrum after convolution and pixel binning simulating the Deep Impact HRI instrument.

part resemble ours (e.g. most do not show two branches) this can be accounted for if our spectra are convolved using a resolving power similar to those they cite.
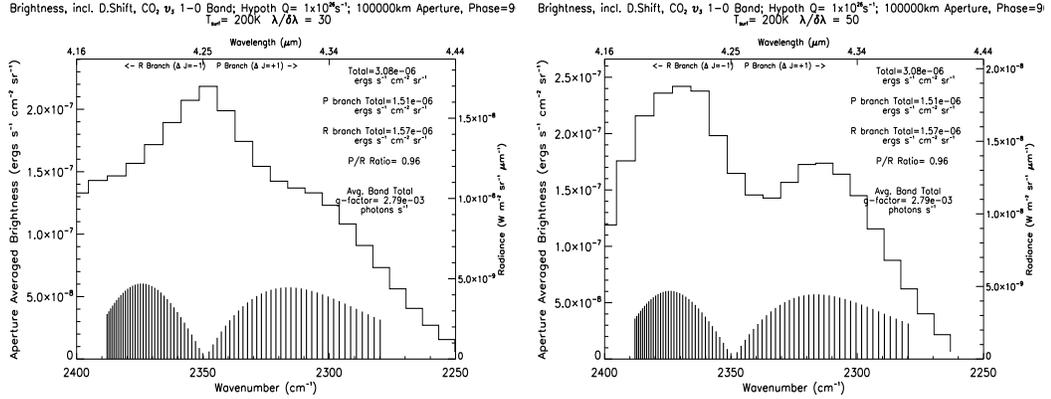
(a) For $\lambda/\delta\lambda = 30$. Aperture = 200,000 km. (b) For $\lambda/\delta\lambda = 50$. Aperture = 200,000 km.
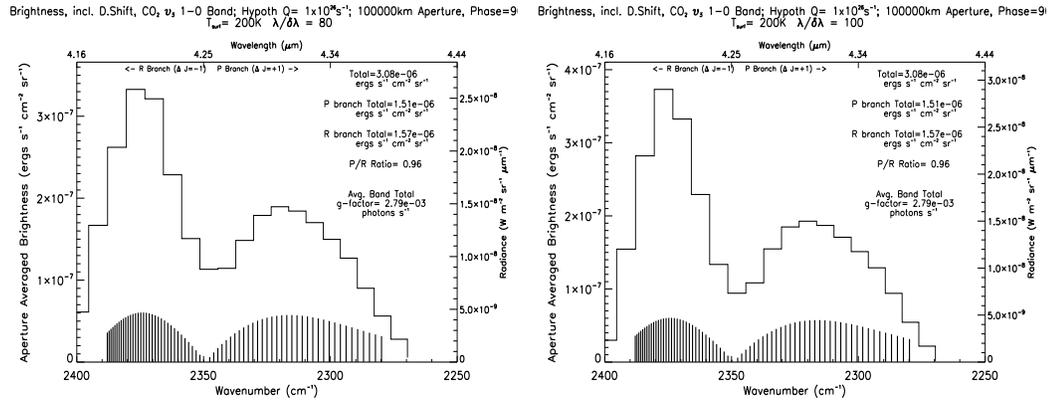
(c) For $\lambda/\delta\lambda = 80$. Aperture = 200,000 km. (d) For $\lambda/\delta\lambda = 100$. Aperture = 200,000 km.

Figure 3.30: Aperture averaged spectra for CO_2 for $Q = 10^{26}s^{-1}$ and Aperture = 200,000 km. Left side y-axis is aperture averaged brightness. Right side y-axis is Radiance. Totals are indicated on each graph. The continuous line is the spectrum after convolution and pixel binning simulating the Deep Impact HRI instrument. Panels a through d correspond to resolving powers, $\lambda/\delta\lambda$, of 30, 50, 80 and 100.

As examples of the extreme role that varying resolving power can play, we present the same 2×10^5 km aperture spectra as in Fig. 3.27(f), convolved with lower spectral resolutions, in Fig. 3.30. Comparing these with the band shapes of some of the *AKARI* spectra in Ootsubo et al. (2012), should, at a glance, make this clear.

3.5 Analysis

Both for water and carbon dioxide, the ν_3 band shape and breadth undergo a dramatic change from the collisionally dominated inner coma to the fluorescence dominated outer coma. This shape change is much more dramatic than the analogous shift for CO. However, the change seen for H_2O and CO_2 is more or less opposite in sense; for H_2O the number of (strongly) visible lines is greatly reduced while for CO_2 it is dramatically increased. To a first order approximation, this shape shift is not significantly changed by optical depth. (However, it does occur increasingly farther from the nucleus with increasing production rate.) Essentially, this results from CO_2 having no radiative rotational relaxation mechanism and H_2O having a highly efficient one. So collisions narrow the band for CO_2 but expand it (or increase the number of lines visible) for H_2O. For CO, in the absence of high optical depths (and also of extremely high temperatures, by cometary standards) the 1-0 band does not change quite so dramatically when going from collisionally to radiatively dominated regimes.

Nevertheless, for H_2O increasing optical depths *do* cause a shift of energy from line to line within the band; from thicker to thinner lines (i.e. from ones having more populated lower levels - thus higher optical depths - to ones with lower populations) originating in the same upper level. This is analogous to the effect of higher optical depths for CO.

On the other hand, CO_2 might be expected to show similar optical depths effects to CO, since their band shapes are somewhat similar. Yet it does not exhibit effects similar to those our model has shown for CO. The lack of significant flux shifting from R to P branch can be ascribed to the much smaller differences between the Einstein coefficients of pairs of lines with the same upper level (i.e. the branching

ratios are very close to one), which is a primary cause of this effect for CO.

3.6 Results for C/2009 P1 Garradd: CO, H_2O and CO_2

Comet C/2009 P1 Garradd (hereafter just "Garradd") was observed by the Deep Impact spacecraft with both the MRI and HRI instruments at a distance of 1.4 AU when the comet was at a heliocentric distance of 2 AU post-perihelion. All three of the volatile species we have modeled were observed simultaneously. (See Feaga et al. 2014) The H_2O ν_3 1-0 band is visible around 2.6 - 2.8 μm, the CO_2 ν_3 1-0 band around 4.2 - 4.4 μm, and the CO 1-0 band around 4.6 - 4.7 μm (with peaks for both P and R branches visible for CO).

These observations provide an excellent test case for our model. Unlike the Tempel 1 and Hartley 2 observations, the CO band is very clearly detected in the spectra, and the observed spectra are from large apertures similar to the model results presented above (see Secs. 3.2.4, 3.3.4 and 3.4.5). Furthermore, since imaging observations showed minimal morphology in the coma (see Farnham et al. 2012; Feaga et al. 2014) this seemed an appropriate case in which to apply a spherically symmetric coma model.

3.6.1 Garradd DI HRI Observations

The DI-HRI observations of Garradd had sufficient S/N ratio to detect the coma signal above the background and extract spectra from the data in a 5×9 pixel aperture centered on the unresolved nucleus. (Note that the pixels are rectangular, not square.) Smaller apertures of 3×5 pixels and 1 pixel were also extracted from the data. We began modeling efforts while the data was still in a preliminary form.

These aperture sizes were approximated by square boxes that circumscribed circles of 9500, 5000 and 1000 km radii, respectively. These preliminary spectra are shown in Figs. 3.31-3.32.

Over the course of several months, these data were recalibrated and produced improved spectra with the aperture sizes more precisely labeled as corresponding to 21050×18945 km^2, 12630×10525 km^2 and $4,210 \times 2,105$ km^2 respectively, shown in Figs. 3.42-3.43.

A visual comparison of the final calibrated spectra in Figs. 3.42-3.43 with the preliminary spectra in Figs. 3.31-3.32 shows that the final spectra appear to show more noise, such as single-pixel-wide spikes and troughs (especially in the CO and CO_2 bands). However, this is in fact due to the initial spectra being smoothed (with a 3 pixel boxcar function). Also noteworthy is that the final calibration produced a factor of 2 increase in the absolute scale in the final spectra over the preliminary ones.

The S/N ratio for the integrated CO band is $\sim$3 in the largest aperture and as low as $\sim$2 in the smallest. For H_2O the S/N ratio is $\sim$10 for the large aperture and $\sim$5 for the small aperture and for CO_2 $\sim$5 and $\sim$2 respectively. The middle sized aperture has S/N close to that of the large aperture. Thus noise in the spectra (see Figs. 3.42-3.43) is significant.

In our modeling, we used a convolution and pixel binning simulating that of the Deep Impact HRI instrument, with $\lambda/\delta\lambda \sim 200 - 330$.

For further details of the Garradd observations, see Feaga et al. (2014).
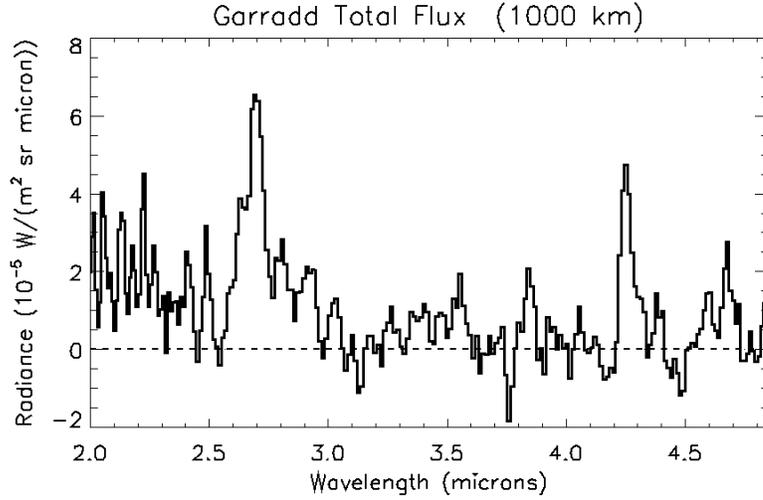
Figure 3.31: *Preliminary* (i.e. before final calibration) 1000 km nucleus centered square aperture averaged spectrum of comet Garradd observed with the Deep Impact HRI instrument at 2 AU. (Figure from Feaga et al. 2012)
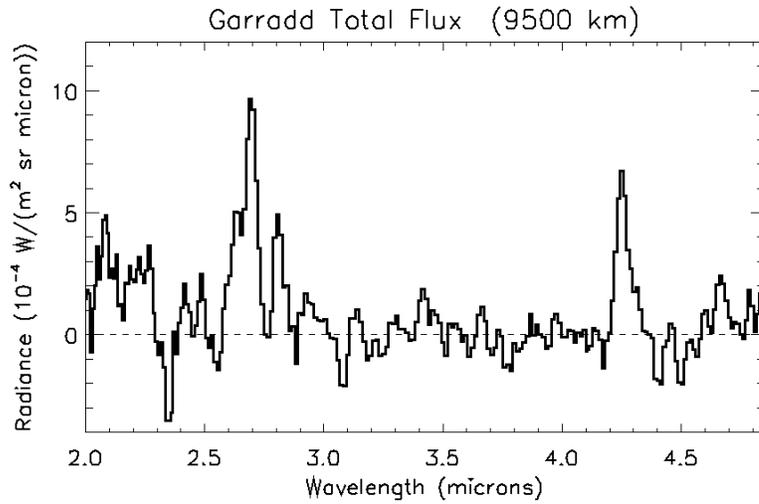
Figure 3.32: *Preliminary* (i.e. before final calibration) 9500 km nucleus centered square aperture averaged spectrum of comet Garradd observed with the Deep Impact HRI instrument at 2 AU. (Figure from Feaga et al. 2012)

3.6.2 Initial Garradd Modeling: Temperature and Morphology

During those months before and while the data were being calibrated, we attempted initial modeling efforts to match the preliminary data. Of course, once the final calibrated data was available we attempted to fit the improved data and abandoned our earlier, preliminary models. However, we will briefly describe some relevant aspects of those early modeling efforts here.

Initial spherical models, without any coma morphology, were a poor fit in both band shape and overall brightness to the preliminary data, especially for CO_2, which seemed to have only a single narrow peak in the observed spectra. Comparison with our hypothetical models (see Secs. 3.2.4, 3.3.4 and 3.4.5) implies that the observations are dominated by cold and collisionally dominated regions of the coma. One obvious problem with our preliminary spherical models was that the emission from the fluorescence-dominated regime of the coma (which for CO_2 produces very broad spectral branches) was overwhelming the emission from the collisionally dominated inner coma, where a low temperature could lead to narrower peaks in spectra.

After testing a range of fairly cold temperature profiles with surface temperatures up to 100 K, we concluded that using a constant temperature throughout the coma would produce a better fit than our general temperature profile (which produced a warmer coma, and hence a broader band shape than observed, at cometocentric distances interior to the apertures dealt with here). This is a gross but not unreasonable approximation. It is in rough agreement with Villanueva et al. (2012b), who measured a rotational temperature around 40 ± 7 K (1σ) for Garradd at 2 AU for several species (within $\sim$3000 km of the center of the comet, judging from the spatial profiles in their Fig. 2). Furthermore, our initial temperature profile has a fairly

broad trough around its minimum of ~20K that extends out to several hundred kilometers distance from the nucleus. Since the subsequent warming of the coma after the minimum is primarily due to photo-dissociation of H_2O and the kinetic energy it produces, the warming at 2 AU should be considerably slower/farther out than at 1 AU, and probably stretches out the low temperature zone discussed to somewhere between 1500-2000 km, or perhaps even farther. It should also be noted that the outer coma, where fluorescence dominates, is mostly unaffected by this approximation, so use of a constant temperature model effectively altered the model to a constantly colder inner coma with the outer coma unchanged.

In order to further increase the dominance of the thermally controlled (cold) regime in the inner ~10,000 km observed, without increasing the overall production rate, we also tested models that included a morphological "cone" feature. This effectively increased the density of the majority of the gas, without changing the total, thus extending the collisionally dominated regime by as much as a factor of 10. (Note that Farnham et al., 2012 have detected some spiral morphology in Garradd observations of reflected continuum. However none is known to exist in the emission bands of three volatiles we are modeling.)

The spectral bands produced by these models were much narrower, due to increased collisional domination, and the gap between branches almost entirely "filled in." A constant T=20 K model in conjunction with a cone that concentrates 90% of the CO_2 produced a pretty good fit to the observations.

We followed a similar approach to fit the CO portion of the observed spectra. The P and R branches in the initial HRI Garradd CO spectra seemed to be distinguishable and not merged like the CO_2 peaks. However, the peak in the P branch at around 4.675 μm is nevertheless a very narrow one, seeming to indicate a cold temperature. Also, the peak of the P branch is much greater than the peak of the R

116

branch. In addition to considerations of temperature similar to those of CO_2, this large P/R branch ratio of fluxes also indicated that significant optical thickness was involved (as per Fig. 3.11 above.)

As was the case for CO_2, we found that the T=20 K model in conjunction with a cone that concentrated 90% of the CO produced a pretty good fit to the observations. The agreement of temperatures between molecules lent some credence to the models' results.

Nevertheless, after our modeling efforts using a cone, we subsequently modeled CO_2 collisions using the approach to collisional cross-sections taken from Goldsmith (1972), (see Secs. 2.2.1 and 3.4.1) in place of that taken from Chin and Weaver (1984). This change obviated the need for the (rather *ad hoc*) inclusion of cones, since it enabled the model to produce collisionally-dominated spectra that fit the data better than the previous iterations while using only a simple spherical coma.

However, this exploration of models with cones for Garradd illustrates a relevant point even though the models produced were ultimately abandoned. The effectively increased collisional cross-section resulting from the use of the Goldsmith model and the higher density due to the inclusion of a cone both serve essentially the same function: they increase the radial extent of the collisionally dominated zone of the coma. This, in conjunction with low temperatures, produces models that can successfully match the narrow peaks observed, thus showing that collisions still control the population distributions even at fairly large cometocentric distances. It also implies that model parameters to fit the shape of spectra of distant comets may not be uniquely determined.

Model Parameters used for C/2009 P1 Garradd	
Mean Nucleus Radius	3 km
Heliocentric Distance	2 AU
Heliocentric Speed	14.5 km/s
T (const.)	40 K (*tested* 20 K - 100 K)
Expansion speed V_{exp}	0.5 km/s
H_2O	
Ortho:Para Ratio	3:1
Ortho Band Head Wavenumber	3732.13 cm^{-1}
Ortho Band Head Einstein $A_{1,1_{0,0}-0,1_{0,1}}$	89.6 s^{-1}
Para Band Head Wavenumber	3779.49 cm^{-1}
Para Band Head Einstein $A_{1,1_{0,1}-0,0_{0,0}}$	28.6 s^{-1}
Highest Rot. Level, J_{max}	5
Solar flux	9.75×10^{12} $photons\,cm^{-2}s^{-1}/cm^{-1}$
σ_{rot}	2.5×10^{-15} cm^2
CO_2	
Band Center Wavenumber	2349.9 cm^{-1}
Band Center Einstein A	140.3 s^{-1}
Band *Mean* Einstein A	206.097 s^{-1}
Solar flux	7×10^{12} $photons\,cm^{-2}s^{-1}/cm^{-1}$
σ_{rot}	3.6×10^{-15} cm^2
Highest Rot. Level, J_{max}	50
CO	
Band Center Wavenumber	2149 cm^{-1}
Band Center Einstein A	33 s^{-1}
Highest Rot. Level, J_{max}	20
Solar flux	6.25×10^{12} $photons\,cm^{-2}s^{-1}/cm^{-1}$
σ_{rot}	3.2×10^{-15} cm^2

Table 3.3: Model input parameters for modeling of actual observations of comet Garradd, for H_2O, CO_2 and CO.

3.6.3 Final Garradd Modeling: Improved Data and Improved Model

The final calibrated spectra included three different sized apertures (see Figs. 3.42-3.43), for which we attempted to fit our models. These spectra *do* show some features

that resemble the usually expected double branched spectra for CO and CO_2, although not very clearly, and the apparent gap between branches could possibly be noise.

Due to noise considerations, the aperture averaged band total brightness was deemed the most important measure of quality of model fitting, followed by peak values and band shape. See Table 3.4 for these brightness values and calculated column densities and production rates derived from them assuming negligible optical depth. (See Feaga et al., 2014 for further details.) Corresponding model results are shown in Table 3.5.

Recalibrated Brightness & Derived Values for C/2009 P1 Garradd

	Aperture Sizes (km^2)		
Species	4210×2105	12630×10525	21050×18945
Integrated avg. Surface Brightness of Bands (ergs/cm^2/s/sr)			
H_2O	6.2×10^{-3}	2.9×10^{-3}	1.6×10^{-3}
CO_2	2.9×10^{-3}	1.5×10^{-3}	8×10^{-4}
CO	2.4×10^{-3}	8×10^{-4}	5×10^{-4}
Integrated average Flux of Bands (ergs/cm^2/s)			
H_2O	1.2×10^{-12}	5.8×10^{-13}	3.2×10^{-13}
CO_2	5.8×10^{-13}	3×10^{-13}	1.6×10^{-13}
CO	4.8×10^{-13}	1.6×10^{-13}	1×10^{-13}
Average Column Densities (cm^{-2})			
H_2O	1.4×10^{15}	6.4×10^{14}	3.5×10^{14}
CO_2	1.1×10^{14}	5.8×10^{13}	3.1×10^{13}
CO	1.2×10^{15}	3.9×10^{14}	2.5×10^{14}
Average Production Rates (s^{-1})			
H_2O	2.4×10^{28}	4.2×10^{28}	3.9×10^{28}
CO_2	1.9×10^{27}	3.8×10^{27}	3.5×10^{27}
CO	2.0×10^{28}	2.5×10^{28}	2.8×10^{28}

Table 3.4: Brightness and derived values (assuming negligible optical depth) from observations of comet Garradd, for H_2O, CO_2 and CO. See Feaga et al. (2014) for further details.

Adjusting Parameters and Fitting the CO_2 Observations

We explored a variety of temperatures within the range of the 40±7 K measurements of Villanueva et al. (2012b), and even some below the lower end of their 1σ range of 33 K. We found that these changes in temperature made some small differences in the resulting spectra but the model with a constant temperature of 40 K fit best.

Our "best-fit model" for CO_2 (with the caveat that any "best fit" is limited by noise in the data) used a production rate of $Q_{CO_2} = 4.1 \times 10^{27} s^{-1}$. This value is slightly greater than the value that would be calculated from the largest aperture values using the optically thin g-factor of $g_{CO_2} = 2.8 \times 10^{-3} s^{-1}$, which yields $Q_{CO_2} \sim 3.7 \times 10^{27} s^{-1}$ (for which a model was tried, but it produced a less close match to the data). Thus some effects of optical depth are still indicated for CO_2, even in the largest aperture size. We present our model results in Figs. 3.33, 3.34 and 3.35, as well as the model overplotted on the actual data in Figs. 3.42 and 3.43.

Adjusting Parameters and Fitting the CO Observations

The final calibrated spectra in Figs. 3.42 and 3.43 actually seemed to have more noise in the CO features than the preliminary spectra; the expected P and R branches, were not very clearly discernable, and for some aperture sizes the most obvious features could possibly be noise. (e.g. The single pixel wide "peaks" on the edges of the CO band's wavelengths.)

We tested colder temperatures within the range of the 40±7 K measurements of Villanueva et al. (2012b), both 40 K and 33 K. We found that these changes in temperature made very slight differences in the resulting spectra, but, as with CO_2, that 40 K seemed to produce the closest fit.

Our "best-fit model" for CO used a production rate of $Q_{CO} = 3.2 \times 10^{28} s^{-1}$. This value is again greater than the value that would be calculated (from the largest

Model ("best-fit") Values for C/2009 P1 Garradd	
Species	**Production Rate (s^{-1})**
H_2O	4.6×10^{28}
CO_2	4.1×10^{27}
CO	3.2×10^{28}

	Aperture Sizes (km^2)		
	4,210×2,105	12630×10525	21050×18945
Aperture Avg. Band Total Surface Brightness (ergs/cm^2/s/sr)			
H_2O	7.9×10^{-3}	2.6×10^{-3}	1.6×10^{-3}
CO_2	4.2×10^{-3}	1.4×10^{-3}	8.3×10^{-3}
CO	2.7×10^{-3}	8.4×10^{-4}	5.1×10^{-3}
Band Total g-factor *at 2 AU* (s^{-1})			
H_2O	5.2×10^{-5}	6.6×10^{-5}	6.9×10^{-5}
CO_2	4.9×10^{-4}	6.2×10^{-4}	6.5×10^{-4}
CO	4.4×10^{-5}	5.4×10^{-5}	5.6×10^{-5}
Band Total g-factor *at 1 AU* (s^{-1})			
H_2O	2.1×10^{-4}	2.6×10^{-4}	2.8×10^{-4}
CO_2	2.0×10^{-3}	2.5×10^{-3}	2.6×10^{-3}
CO	1.8×10^{-4}	2.1×10^{-4}	2.2×10^{-4}
Percentage of Optically Thin g-factor (listed in parentheses)			
H_2O (3.1×10^{-4})	68%	84%	90%
CO_2 (2.8×10^{-3})	71%	89%	93%
CO (2.4×10^{-4})	75%	88%	90%

Table 3.5: Brightness and effective g-factor from our model of comet Garradd, for H_2O, CO_2 and CO. Note: "Standard" g-factors are usually referred to with respect to comets' assumed heliocentric distance as 1 AU. We have presented both for the sake of clarity. (The 1 AU values are simply 4 times the 2 AU values.)

aperture) using the optically thin g-factor of $g_{CO} = 2.4 \times 10^{-4} s^{-1}$, which yields $Q_{CO} \sim 2.7 \times 10^{28} s^{-1}$ (for which a model was tried, but it produced a less close match to the data). Thus some effects of optical depth are still indicated for CO, even in the largest aperture size.

We present our model results in Figs. 3.36, 3.37 and 3.38, as well as the model overplotted on the actual data in Figs. 3.42 and 3.43. Also see the values shown above in Table 3.5 (and compare with observational data in Table 3.4).
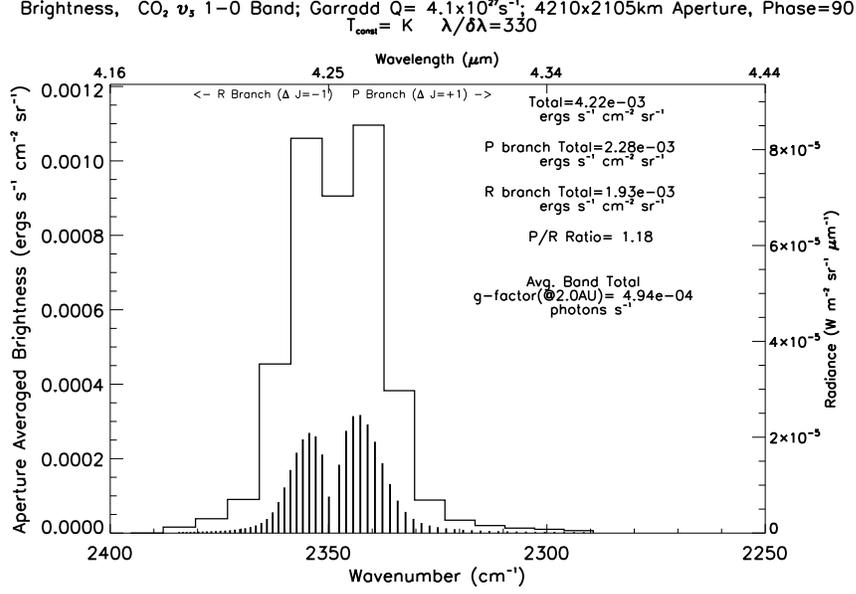
Figure 3.33: 4,210 km $\times$ 2,105 km aperture averaged spectrum for $Q_{CO_2} = 4.1 \times 10^{27}$ s^{-1}. Left side y-axis is aperture averaged brightness in erg s^{-1} cm^{-2} sr^{-1}. Right y-axis is Radiance in W m^{-2} sr$^{-1}\mu^{-1}$. Vertical lines are individual line brightnesses. Continuous line is simulated HRI instrument spectrum. Totals are indicated on each graph.

Adjusting Parameters and Fitting the H$_2$O Observations

Modeling the spectra of the ν_3 band of water for Garradd was a somewhat more straightforward process than modeling the other two molecules. Initial models without the use of any cone were much closer to the data than initial models for CO or CO$_2$ thus we did not attempt to use any morphology in the water model but simply a spherical coma.

The model that most closely fit the final calibrated data was for Q$_{H_2O}$ = 4.6$\times 10^{28}$ s^{-1} and T = 40 K. The spectra for the three aperture sizes are shown in Figs. 3.39, 3.40 and 3.41 and the relevant values are listed in Table 3.5.
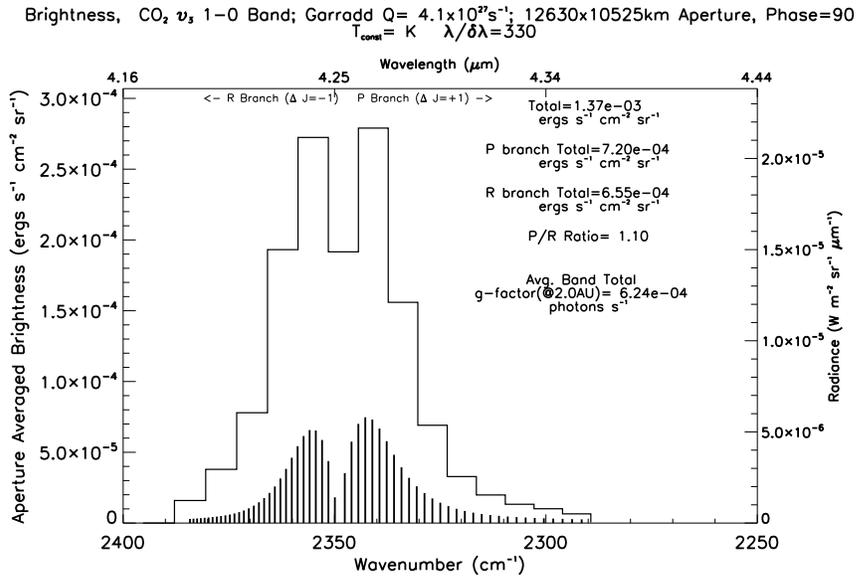
Figure 3.34: 12630 km × 10525 km aperture averaged spectrum for $Q_{CO_2} = 4.1 \times 10^{27}$ s^{-1}. Left side y-axis is aperture averaged brightness in erg s^{-1} cm^{-2} sr^{-1}. Right y-axis is Radiance in W m^{-2} sr$^{-1}\mu^{-1}$. Vertical lines are individual line brightnesses. Continuous line is simulated HRI instrument spectrum. Totals are indicated on each graph.

3.6.4 Conclusions

The DI HRI Garradd spectra show optical depth effects, even for the largest apertures, which include approximately a 10000 km radius from the center of the comet.

Figs. 3.44, 3.45 and 3.46 show radial profiles for the three molecules' for our "best-fit" models. The locations of the vertical lines, indicating where the effective g-factor is 90% and 98% of the optically thin g-factor along the (less bright) anti-sunward profile, demonstrate that none of the spectra observed out to a radius of approximately 10000 km are entirely free from optical depth effects. Furthermore, although these effects are relatively small in a 10000 km aperture, they are considerably greater for smaller apertures.

Numerically, these effects are also shown in 3.5, in the section showing percentage of optically thin g-factors; the values for the smallest aperture are about 50-60% of
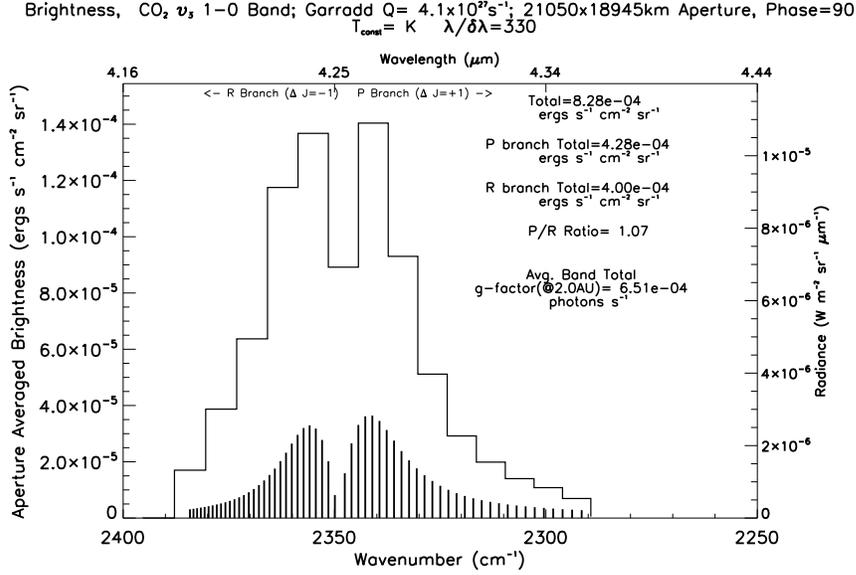
Figure 3.35: 21050 km × 18945 km aperture averaged spectrum for $Q_{CO_2} = 4.1 \times 10^{27}$ s^{-1}. Left side y-axis is aperture averaged brightness in erg s^{-1} cm^{-2} sr^{-1}. Right y-axis is Radiance in W m^{-2} sr$^{-1}\mu^{-1}$. Vertical lines are individual line brightnesses. Continuous line is simulated HRI instrument spectrum. Totals are indicated on each graph.

the thin values. Thus, were one to naively use the optically thin g-factor to calculate production rates based on brightness values from the coma up to about 1000-2000 km radius, the resulting production rates would be incorrect by almost a factor of two!

Our models have fit the final calibrated data quite well in band total brightness, and fairly closely in peak values and band shape. The differences between the models and the data are at levels comparable to the noise and uncertainty of the observations themselves, particularly with respect to band shapes. The production rates used in these models are somewhat higher, but not dramatically so, than those that would be derived from the data based on the largest aperture assuming that the data was optically thin.

Temperature also proved important in modeling band shape, to the noise-limited extent that shape fitting was possible. Our best-fit models use a fairly low temperature of 40 K throughout the inner coma, which at first may seem quite low at 2 AU,

124
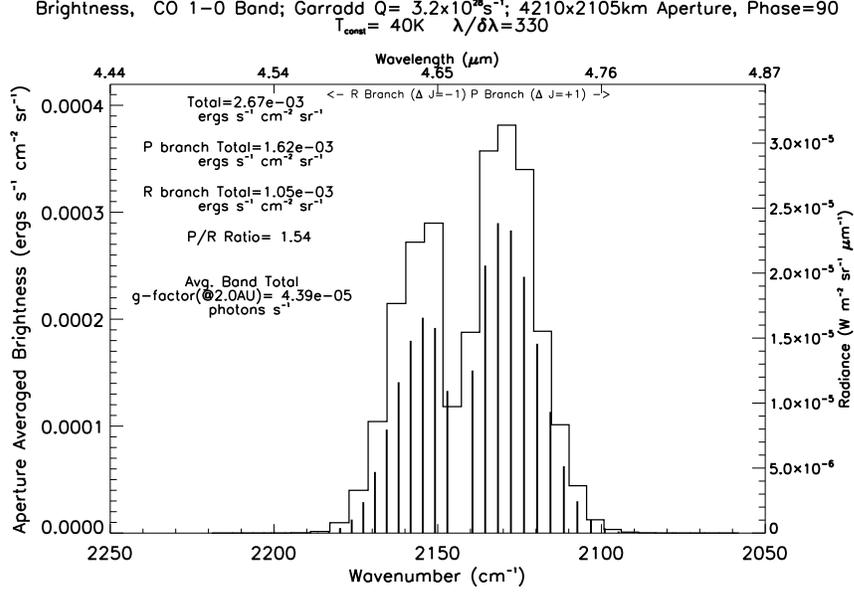
Figure 3.36: 4,210 km × 2,105 km aperture averaged spectrum for $Q_{CO} = 3.2 \times 10^{28}$ s^{-1}. Left side y-axis is aperture averaged brightness in erg s^{-1} cm^{-2} sr^{-1}. Right y-axis is Radiance in W m^{-2} sr$^{-1}\mu^{-1}$. Vertical lines are individual line brightnesses. Continuous line is simulated HRI instrument spectrum. Totals are indicated on each graph.

but it is in agreement with other observations (Villanueva et al. 2012b). This low temperature, in the collisionally dominated inner coma, works to fit the relatively narrow band shapes observed in particular for CO_2, but also for the other molecules as well. We also note that the collisionally dominated part of the coma extends to quite large distances from the nucleus, dominating even the largest aperture spectrum.
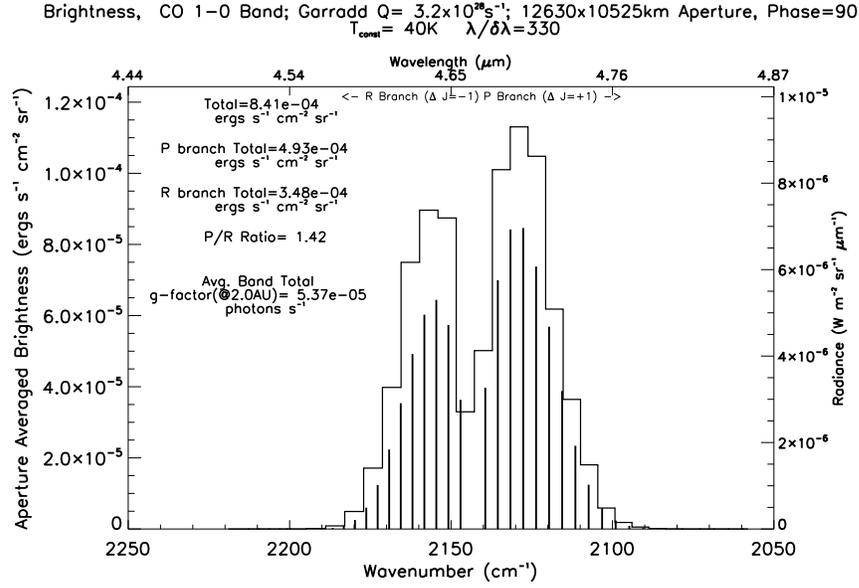
Figure 3.37: 12630 km × 10525 km aperture averaged spectrum for $Q_{CO} = 3.2 \times 10^{28}$ s^{-1}. Left side y-axis is aperture averaged brightness in erg s^{-1} cm^{-2} sr^{-1}. Right y-axis is Radiance in W m^{-2} sr$^{-1}\mu^{-1}$. Vertical lines are individual line brightnesses. Continuous line is simulated HRI instrument spectrum. Totals are indicated on each graph.
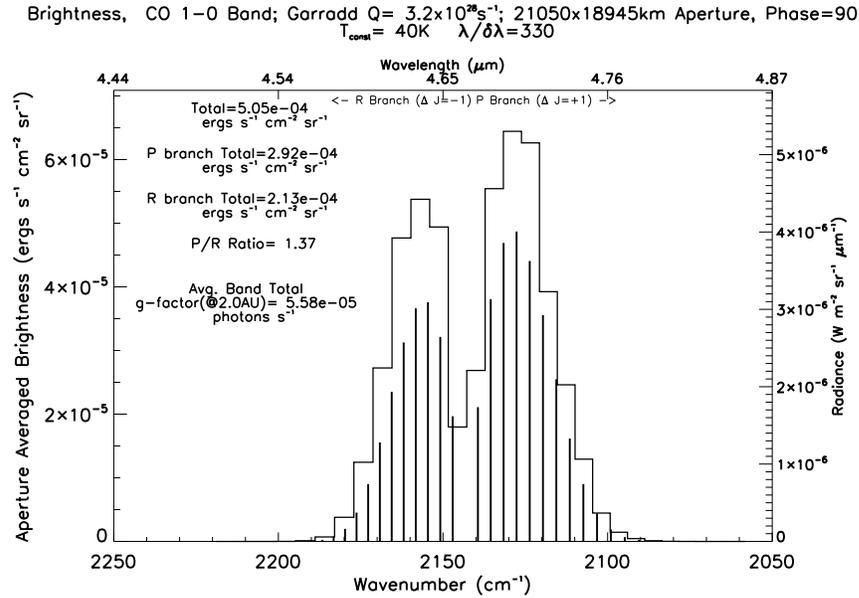
Figure 3.38: 20000 km × 20000 km (very close to 21050 km × 18945 km) aperture averaged spectrum for $Q_{CO} = 3.2 \times 10^{28}$ s^{-1}. Left side y-axis is aperture averaged brightness in erg s^{-1} cm^{-2} sr^{-1}. Right y-axis is Radiance in W m^{-2} sr$^{-1}\mu^{-1}$. Vertical lines are individual line brightnesses. Continuous line is simulated HRI instrument spectrum. Totals are indicated on each graph.

126
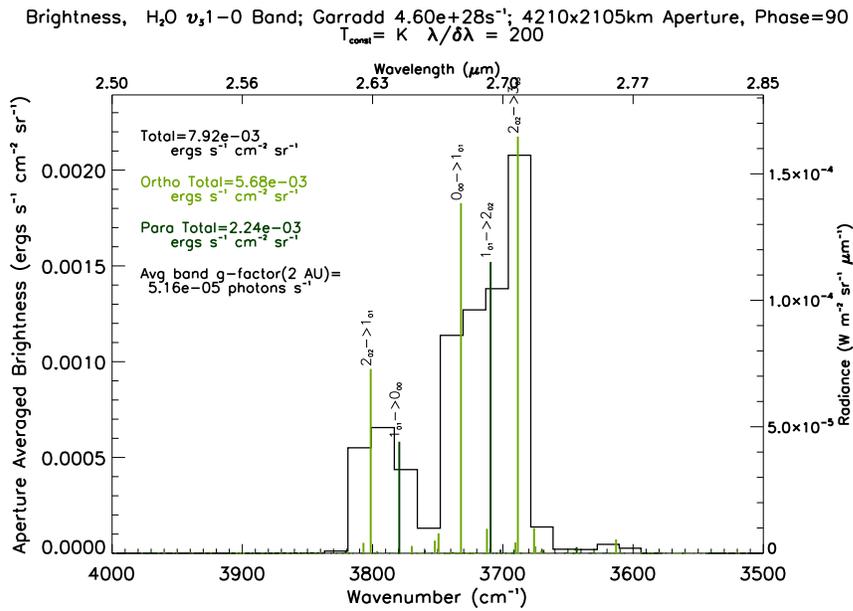
Figure 3.39: 4,210 km × 2,105 km aperture averaged spectrum for $Q_{H_2O} = 4.6 \times 10^{28}$ s^{-1}. Left side y-axis is aperture averaged brightness in erg s^{-1} cm^{-2} sr^{-1}. Right y-axis is Radiance in W m^{-2} sr^{-1}μ^{-1}. Vertical lines are individual line brightnesses. Continuous line is simulated HRI instrument spectrum. Totals are indicated on each graph.
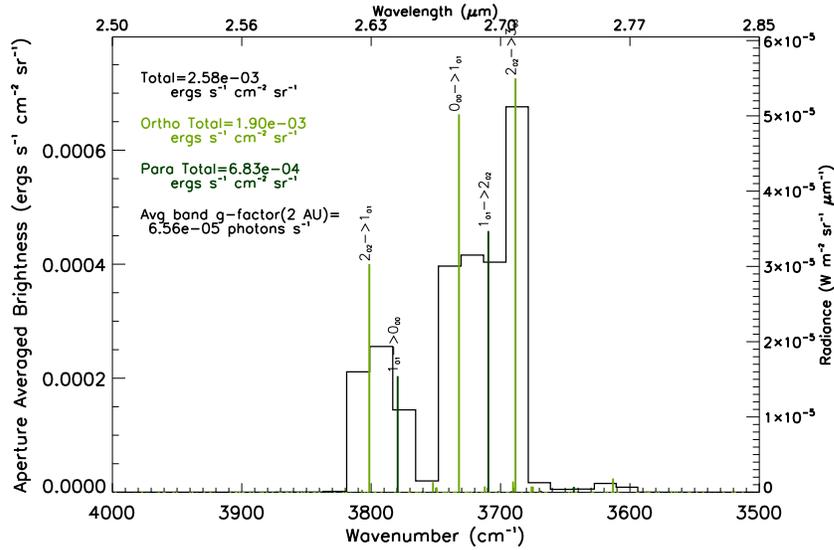
Figure 3.40: 12630 km × 10525 km aperture averaged spectrum for $Q_{H_2O} = 4.6 \times 10^{28}$ s^{-1}. Left side y-axis is aperture averaged brightness in erg s^{-1} cm^{-2} sr^{-1}. Right y-axis is Radiance in W m^{-2} sr$^{-1}\mu^{-1}$. Vertical lines are individual line brightnesses. Continuous line is simulated HRI instrument spectrum. Totals are indicated on each graph.
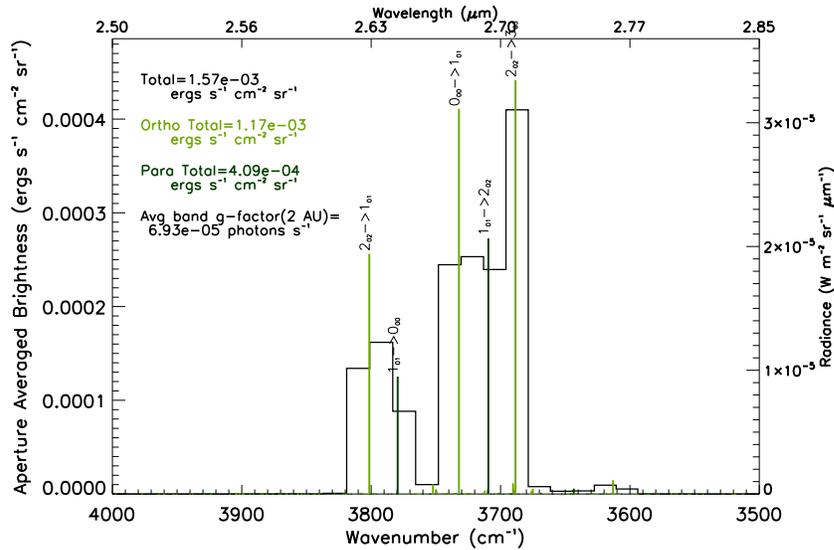
Figure 3.41: 21050 km × 18945 km aperture averaged spectrum for $Q_{H_2O} = 4.6 \times 10^{28}$ s^{-1}. Left side y-axis is aperture averaged brightness in erg s^{-1} cm^{-2} sr^{-1}. Right y-axis is Radiance in W m^{-2} sr$^{-1}\mu^{-1}$. Vertical lines are individual line brightnesses. Continuous line is simulated HRI instrument spectrum. Totals are indicated on each graph.
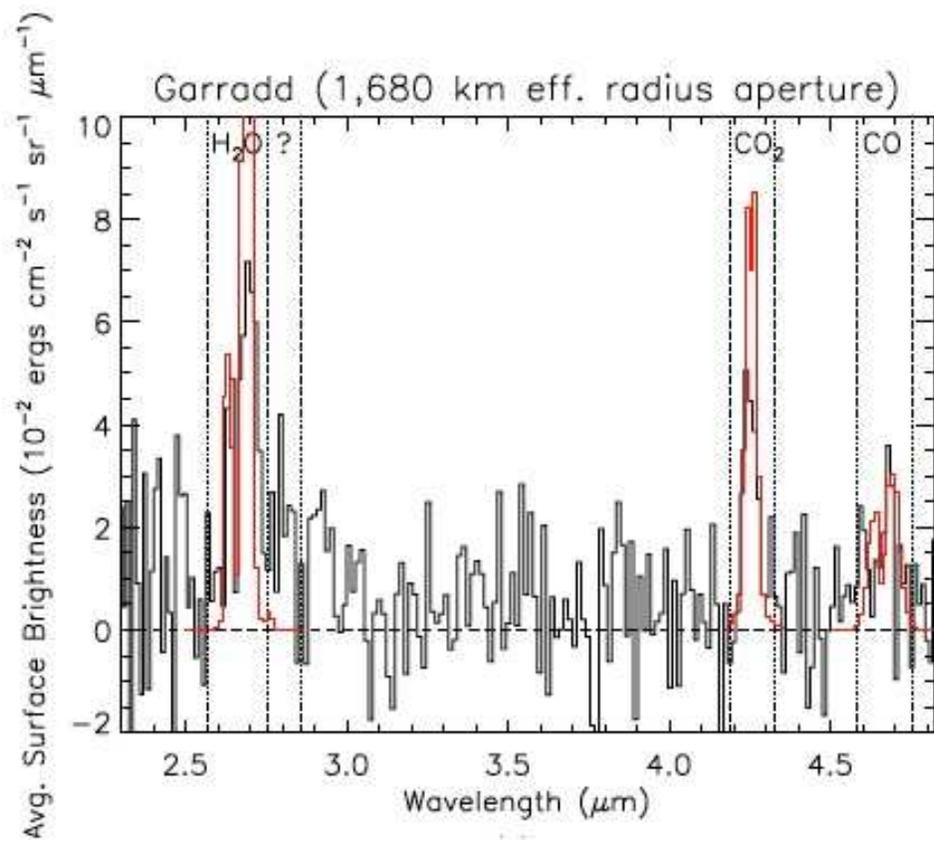
Figure 3.42: Model for all three molecules overplotted (in red) on Garradd small (2105 km × 4210 km) aperture averaged spectrum. From Feaga et al. (2014)
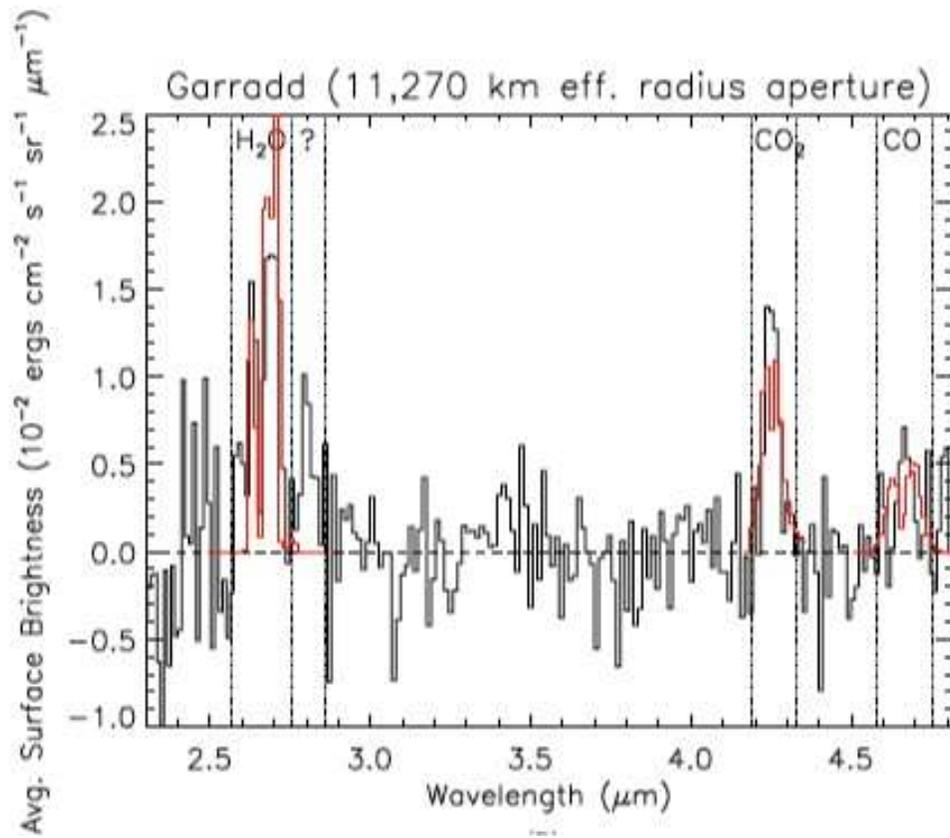
Figure 3.43: Model for all three molecules overplotted (in red) on Garradd large
(18945 km × 21050 km) aperture averaged spectrum. From Feaga et al. (2014)
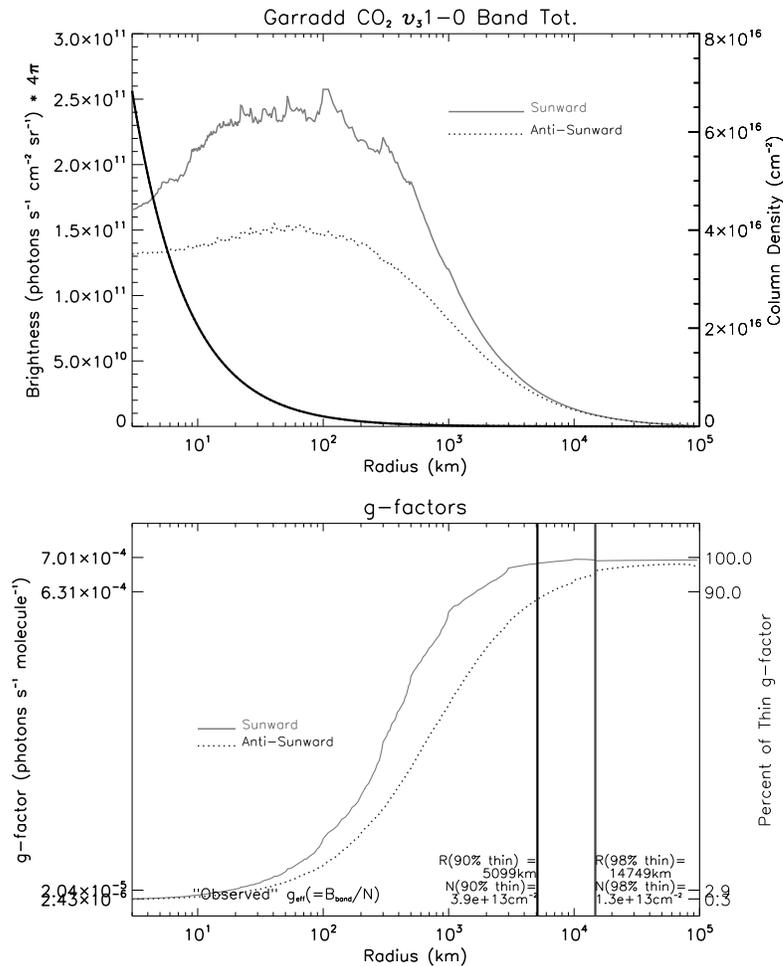
Figure 3.44: Radial profiles for CO_2 for Garradd. Upper frame: Radial profile of band total Brightness (in photons s^{-1} cm^{-2} sr^{-1} vs. R (impact paramater, in km) for Phase angle = 90° and for Sunward and Anti-sunward Azimuthal angles. Column density is included on the left y-axis scale. Lower frame: Effective g-factors. g_{eff}, Brightness over Column density, again plotted with angles corresponding to upper frame. The vertical lines represent the radial distance and column density at which g_{eff} is 90% and 98% of the optically thin value.
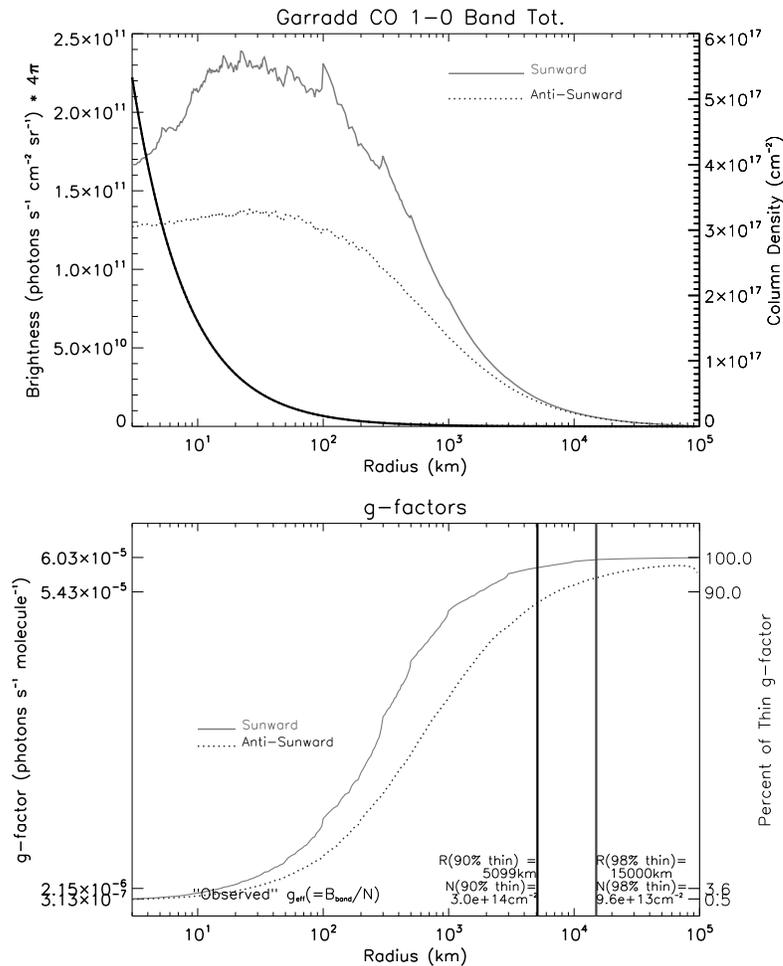
Figure 3.45: Radial profiles for CO for Garradd. Upper frame: Radial profile of band total Brightness (in photons s^{-1} cm^{-2} sr^{-1} vs. R (impact paramater, in km) for Phase angle = 90° and for Sunward and Anti-sunward Azimuthal angles. Column density is included on the left y-axis scale. Lower frame: Effective g-factors. g_{eff}, Brightness over Column density, again plotted with angles corresponding to upper frame. The vertical lines represent the radial distance and column density at which g_{eff} is 90% and 98% of the optically thin value.
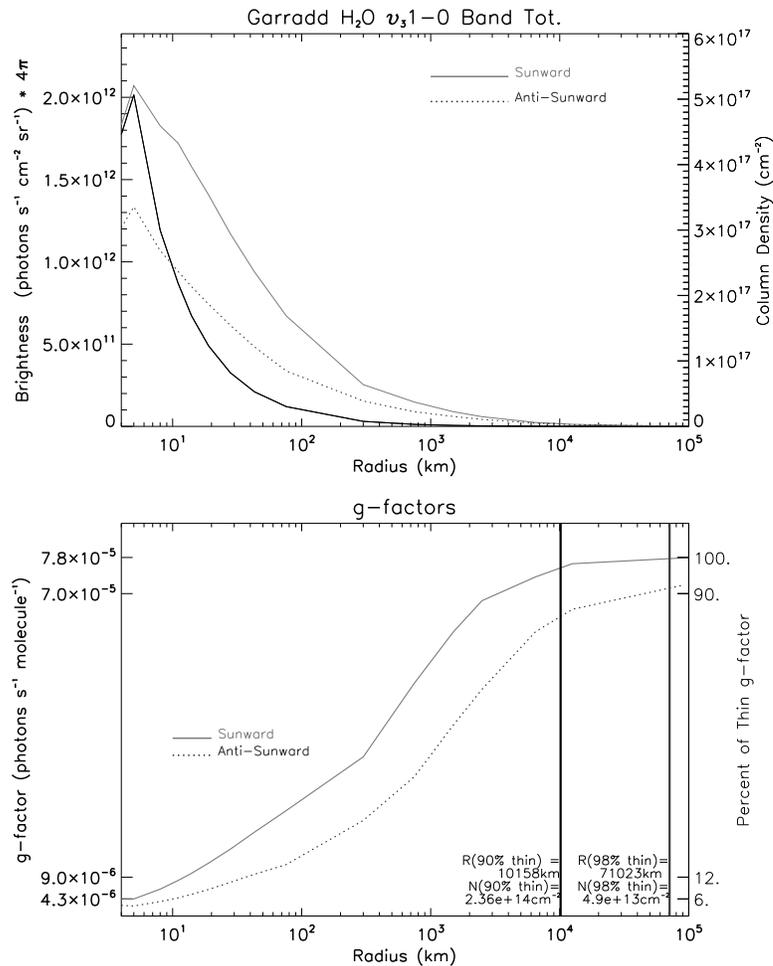
Figure 3.46: Radial profiles for H$_2$O for Garradd. Upper frame: Radial profile of band total Brightness (in photons s^{-1} cm^{-2} sr^{-1} vs. R (impact paramater, in km) for Phase angle = 90° and for Sunward and Anti-sunward Azimuthal angles. Column density is included on the left y-axis scale. Lower frame: Effective g-factors. g_{eff}, Brightness over Column density, again plotted with angles corresponding to upper frame. The vertical lines represent the radial distance and column density at which g_{eff} is 90% and 98% of the optically thin value.

Chapter 4

Model Results with Morphology:

Tempel 1 and Hartley 2

4.1   Tempel 1

4.1.1   The Deep Impact Observations

The observations of comet Tempel 1 made by the successful Deep Impact Mission have been described in great detail in many publications. Here we focus our modeling efforts on those in Feaga et al. (2007a) that have achieved spatially resolved spectra of the ν_3 bands of both H_2O and CO_2 in the coma near the nucleus in unprecedented detail. Carbon monoxide was also detected (see Feaga et al. 2007b), but with poor S/N ratio, and so we are not trying to fit CO here. These observations were made with the HRI-IR spectrometer about ten minutes before the impact on July 4, 2005, when the spacecraft was about 16,800 km from the nucleus. Feaga et al. (2007a) present the data in an array of formats, among them radiance maps of particular emission bands and spectra from specific lines of sight near the nucleus. We have included those here in Figs.4.1 and 4.2. Since publication of Feaga et al. (2007a) the values of absolute radiances observed have been decreased by a factor of two due to the discovery of an error in the calibration pipeline. These are the observations for which our model was originally intended.

4.1.2   Basic Model Parameters

The input parameters which can be adjusted in our model consist of production rates, temperature model, and expansion velocity for each of two regions of the nucleus, the background and the cone. The different temperature models available are either a constant temperature throughout the coma or a radial profile fit to a surface temperature parameter (see Sec. 2.3.1). Two models of collisional cross-sections and excitation are also possible, the "Chin & Weaver" or the "Goldsmith"

(a) H_2O ν_3 band.
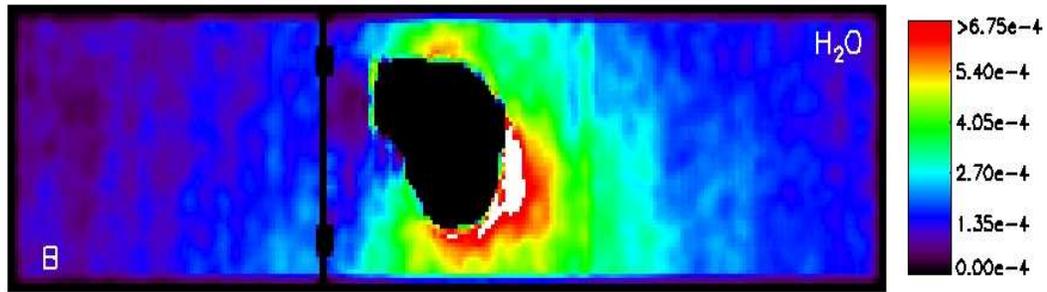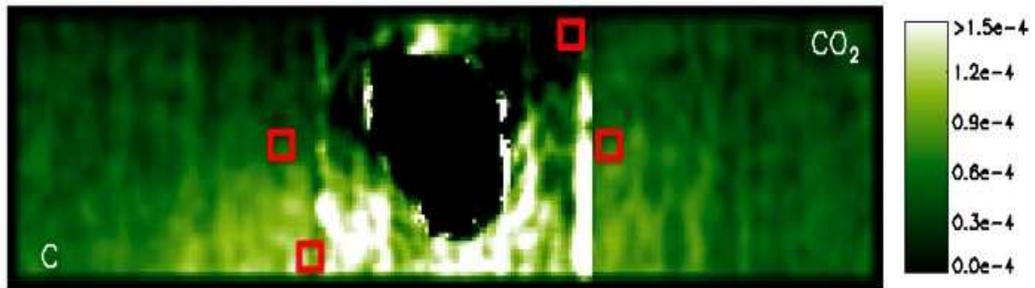
(b) CO_2 ν_3 band.

Figure 4.1: Near nucleus radiance maps of the H_2O and CO_2 ν_3 bands. The field of view is 43×10 km. Radiance values indicated by the color bars are in W m^{-2} sr^{-1}. Red boxes shown on the CO_2 (added here) show the approximate locations of the four line of sight spectra in Fig. 4.2. (The vertical black line in the H_2O and the sharp edge of brightness in the CO_2 are artifacts that show the boundaries of the anti-saturation filter.) From Feaga et al. (2007a).

models (see Sec. 2.2.1). The geometry of the cone, its orientation and opening angle, are also parameters that can be adjusted. These parameters are all separately defined for each species. Varying these parameters, we fit the model to the data with an iterative approach.

Based on consultations with L. Feaga, the initial model parameters used the geometry shown in Figs. 4.3 & 4.4 and a division of the total Q's into the background and cone based on the values in Table 4.1. These were based on a rough "eyeballing" where to locate the single cone for each species in the model. In our initial model, the CO_2 cone's center line is aligned 90° away from sunward and points south (in

136
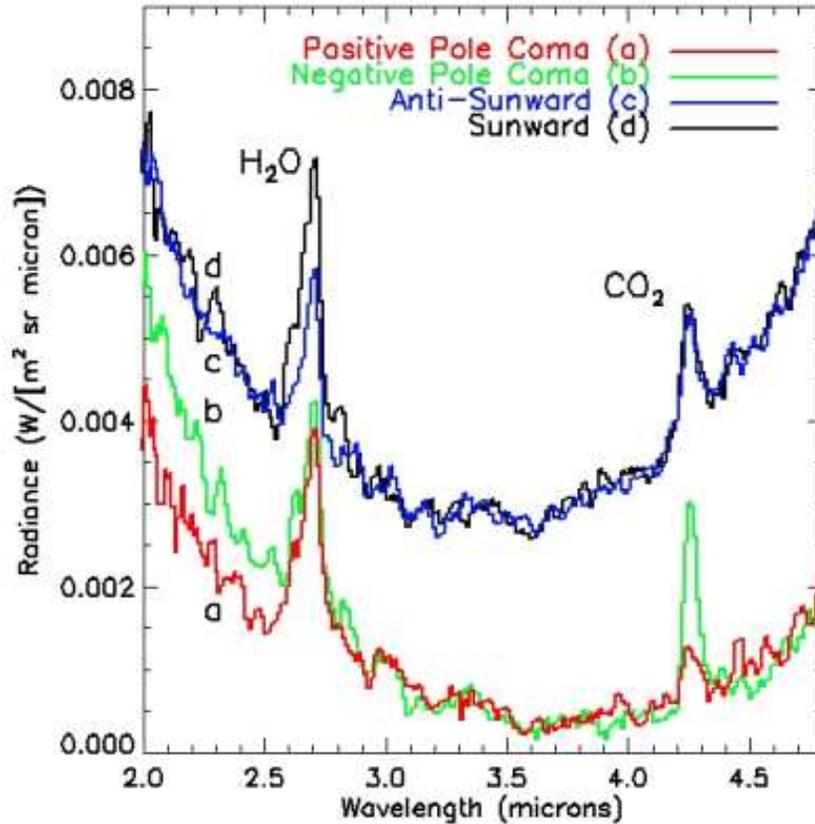
Figure 4.2: Near nucleus spectra along lines of sight at four different points $\sim$7 km from the nucleus. Spectra span from 2.0 - 4.8 μm and include the H_2O and CO_2 ν_3 bands. Radiance values are in W m^{-2} sr$^{-1}\mu$m^{-1}. From Feaga et al. (2007a) *Not corrected* for factor of 2 calibration error. See Fig. 4.7 for corrected spectra.

the image plane). The H_2O cone's center line is aligned 45° south from sunward and points 30° out of the image plane towards the observer, which puts it in the plane containing the Sun. (We have ignored the relatively smaller features on the ecliptic north side of the nucleus as our model can currently only include one cone at a time. Future improvements may add multiple cone capabilities, but such improvements are beyond the scope of the present work.) The opening angle of both cones was $\sim$85°. (See Figs. 4.3 and 4.4.) Note that in our model the nucleus is always spherical, but this can simply be viewed as an approximation of one "lobe" of a not-really-so spherical actual nucleus.

Also see Table 4.1 for various other constant model parameters.

Tempel 1 H$_2$O Model Geometry
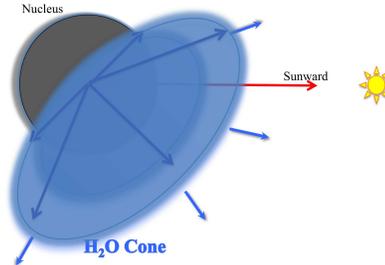
Figure 4.3: *Rough* diagram of the H$_2$O cone used for modeling the observed southern morphology of Tempel 1. The cone's center line is aligned 45° south from sunward and points 30° out of the image plane towards the observer. The opening half-angle of the cone is 85°. (Somewhat broader than in our rough diagram.)

Tempel 1 CO$_2$ Model Geometry
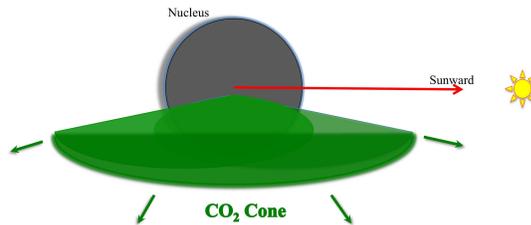
Figure 4.4: *Rough* diagram of the *initial* CO$_2$ cone used for modeling the observed southern morphology feature of Tempel 1. The cone's center line is aligned 90° away from sunward and points to ecliptic south (in the image plane). The opening half-angle of the cone is 85°. (Slightly broader than in our rough diagram.)

Basic Model Parameters used for 9P/Tempel 1	
Mean Nucleus Radius	3 km
V_{exp}	0.5 - 0.8 km s^{-1}
Heliocentric Distance	1.5 AU
H_2O Values	
Ortho:Para Ratio	3:1
Highest Rot. Level, J_{max}	7
Solar flux	$3.9 \times 10^{13}\, photons\, cm^{-2} s^{-1}/cm^{-1}$
σ_{rot}	$2.5 \times 10^{-15}\, cm^2$
CO_2 Values	
Highest Rot. Level, J_{max}	70
Solar flux	$2.8 \times 10^{13}\, photons\, cm^{-2} s^{-1}/cm^{-1}$
σ_{rot}	$3.6 \times 10^{-15}\, cm^2$

Table 4.1: Basic model parameters for modeling Deep Impact observations of comet Tempel 1, for H_2O and CO_2.

4.1.3 Varying the Model Parameters to Fit the Data

We primarily varied production rates and temperatures in the process of fitting the Tempel 1 data. We judged the "closeness" of our model fitting based primarily on matching the observed band brightness, both peak and total, and secondarily on band shape.

The input production rates have the greatest impact on the peak and total brightness of model spectra, as expected. We do see that in most of these cases there is a non-linear relationship between them, implying optical depth effects are involved.

The band shape is primarily controlled by the combination of temperature and density, at least in the inner coma, where those spectra of Tempel 1 that we are modeling were observed. The rotational level population distribution of molecules will be primarily controlled by temperature, if the gas is sufficiently dense to be collisionally dominated, and the shape of the spectra will reflect this (as seen above

in Sec. 3.3.4 and Sec. 3.4.5). In the outer coma, the density is too low for collisions to dominate and the distribution will tend to a fluorescence dominated shape. For CO_2, that shape is very much broader than a collisionally dominated band at typical cometary temperatures. For water it reduces the number of lines to very few. The choice between collisional models can affect the band shape, since the Goldsmith model effectively increases collisional cross-section compared to the Chin & Weaver model. However, unlike what we saw for Garradd, the choice is less crucial, since we are dealing with a region of the coma much closer to the nucleus. On the other hand, having a significantly different distribution for CO_2 in the outer coma than the inner coma may allow more flux to escape from the inner coma since the peak lines in the collisionally dominated inner coma will be less populated and hence less optically thick in a flourescence dominated outer coma, thus reducing self-shielding of the gas.

Production Rates

Two different approaches to calculating "initial guess" model production rate inputs were tried. The first was based on total production rates from Feaga et al. (2007a) ($Q_{H_2O} \sim 4.6 \times 10^{27}$ and $Q_{CO_2} \sim 3.2 \times 10^{26} s^{-1}$). In the second, we used production rate values derived from the column densities listed in Table 3 of Feaga et al. (2007a). The values in that table are (lower limits to) column densities calculated *assuming negligible optical depth* at 7 km distance from the center of the nucleus, in six different directions, four of which correspond to the spectra in Fig. 4.2. Thus if the coma was in fact optically thin at that distance, a model based on these values should easily match the corresponding spectra. Table 4.2 shows those values and the corresponding calculated production rates. (Note that the column densities are taken from Table 3 of Feaga et al. (2007a), *and divided by 2 to correct for a mistake*

140

in the pixel size in the original processing pipeline and correspond to but supersede those published values; see Klaasen et al., 2013.) We chose production rates for the cone and background in our model based on these values. The second method produced considerably closer fitting results for the spectra in Fig. 4.2, which is not surprising, since these inputs were derived from the values at 7 km distance.

Column Density & Production Rates from *Corrected* DI Observations for Tempel 1

Region	$N(CO_2)$	$Q(CO_2)$	$N(H_2O)$	$Q(H_2O)$
Ecliptic North	1.25×10^{15}	1.75×10^{26}	3.45×10^{16}	4.85×10^{27}
Positive Rot. Pole	3.8×10^{14}	5.3×10^{25}	1.4×10^{16}	1.95×10^{27}
Sunward	9.0×10^{14}	1.26×10^{26}	2.0×10^{16}	2.8×10^{27}
Ecliptic South	1.5×10^{15}	2.1×10^{26}	3.55×10^{16}	4.95×10^{27}
Negative Rot. Pole	1.3×10^{15}	1.8×10^{26}	1.45×10^{16}	2.05×10^{27}
Anti-Sunward	7.5×10^{14}	1.15×10^{26}	1.0×10^{16}	1.4×10^{27}

Table 4.2: Column densities and corresponding production rates for different regions near (7 km) the nucleus of comet Tempel 1, for H_2O and CO_2. The column densities are taken from Table 3 of Feaga et al. (2007a) where they were calculated assuming negligible optical depth. *They have been divided by 2 here to correct for a mistake in the pixel size in the original processing pipeline* and are in cm^{-2}. The production rates (in s^{-1}) are calculated from the column densities using $Q = 4v\rho N$ at $\rho = 7$ km with $v = 0.5\ km\ s^{-1}$.

Since we are constrained by the model to use only one production rate for the "background" and one for the "cone", we chose the background CO_2 production rate based on the positive rotational pole column density and we used values for the cone production rate based on the negative rotational pole column density. These are the smallest and greatest of the four CO_2 column densities in Table 4.2. The value for the positive pole is considerably lower than the others that correspond to the background, so this choice was expected to produce model results that would be too low for the other background spectra (sunward and anti-sunward) but would fit the positive pole. This is not surprising as a visual inspection of the positive pole in Fig. 4.1 shows that it is located in a region that is considerably less bright in the

CO_2 band than the other lines of sight.

For the H_2O cone we based the production rate on the sunward and ecliptic south column densities. For the background we used values based on the anti-sunward column density. These values (in conjunction with temperatures discussed in 4.1.3) produced a fairly close fit for the H_2O spectra as shown in Figs. 4.5, 4.7 and 4.9. This implies that the H_2O band is not significantly reduced in brightness due to optical depth. However, individual lines within the band may be optically thick with the energy being pushed into other, thinner lines.

The CO_2 production rate values were varied to fit the data by increasing them from the initial values in Table 4.2 and adjusting temperatures and collisional models. The model was run for CO_2 using a series of model parameter variations as listed in Table 4.3.

This table summarizes a series of models approaching a best-fit by varying production rates (both background and cone), temperatures, collisional models and geometry begining with the initial Model I based directly on the values in Table 4.2 which should have been adequate (at least for the positive pole) if there were no significant optical depth effects.

Multiplying the model production rates to adjust the peak and total values in the spectra did not produce a linear increase in model spectra brightness. This non-linear relation between increase in actual density and increase in emerging flux demonstrated that these spectra are indeed influenced by optical depth effects.

Nevertheless, we should be cautious in that statement; it is possible that other factors are involved, in particular the shadowing by the nucleus in the anti-sunward direction may affect that spectrum. However, to test that we sampled a slightly south of anti-sunward model spectrum, outside the shadow, and it was not significantly different. This lends support to the likelihood of optical depth effects along

Varying/Fitting CO_2 Model Parameters used for 9P/Tempel 1

Model	Q_{bkgd}	T_b	Q_{cone}	T_c	Model Details	Fit?
Data/Observed Values						C$\sim$11, S$\sim$5.8, A$\sim$6, P.Pole$\sim$3
Model I	5.3×10^{25}	200	2.1×10^{26}	100	G	$\lesssim$Pos. pole
Model II	1.6×10^{26}	200	4.2×10^{26}	100	C&W	$\gtrsim$Pos. pole
Model III	1.6×10^{26}	200	4.2×10^{26}	100	G	C,S,AS$\lesssim$3
Model IV	2.2×10^{26}	200	8.4×10^{26}	100	C&W	
Model V	2.2×10^{26}	200	8.4×10^{26}	100	G	C$\sim$3.4, S$\sim$2.9, A$\sim$2.2
Model VI	1.6×10^{26}	200	8.4×10^{26}	100	G, 20° A, θ_o=35°	C$\sim$4.6, S/A$\sim$4.3
Model VII	2.4×10^{26}	100	8.4×10^{26}	55	G, 20° A, θ_o=35°	C$\sim$5.1, S$\sim$5.3, A$\sim$5
Model VIII	2.4×10^{26}	200	8.4×10^{26}	200	G, 20° A, θ_o=35° v_c=1	C$\sim$6, S/A$\sim$5.2
Model IX	2.6×10^{26}	200	4.2×10^{26}	200	G, 20° A, 20° O	C$\sim$5.5, S/A$\sim$5.5
Model X	2.6×10^{26}	300	4.2×10^{26}	300	G, 20° A, 30° O, θ_o=45° v_c=1	C$\sim$6.2, S$\sim$5, A$\sim$4.5
Model XI	2.6×10^{26}	300	4.2×10^{26}	300	G, 20° A, 30° O, θ_o=45° v_c=1 v_b=0.8	C$\sim$6.4, S$\sim$5.4, A$\sim$5.5
Model XII	2.6×10^{26}	200	4.2×10^{26}	200	G, 20° A, 30° O, θ_o=45° v_c=1 v_b=0.8	C$\sim$6.5, S$\sim$5, A$\sim$4.5
Model XIII	2.6×10^{26}	55	4.2×10^{26}	55	G, 20° A, 30° O, θ_o=45° v_c=1	C$\sim$5.8, S$\sim$5.5, A$\sim$4.5
Model XIV	2.6×10^{26}	60	4.2×10^{26}	200	G, 20° A, 30° O, θ_o=45° v_c=1 v_b=0.8	C$\sim$6.2, S$\sim$4.6, A$\sim$5.2
Model XV	2.6×10^{26}	60(c)	4.2×10^{26}	200	G, 20° A, 30° O, θ_o=45° v_c=1 v_b=0.8	C$\sim$6.5, S$\sim$5.3, A$\sim$5.5
Model XVI	2.6×10^{26}	200	8.4×10^{26}	200	G, 20° A, 30° O, θ_o=45° v_c=1 v_b=0.8	C$\sim$7.3, S$\sim$5.4, A$\sim$5.5
Model XVII	2.6×10^{26}	200	1.2×10^{27}	200	G, 20° A, 30° O, θ_o=45° v_c=1 v_b=0.8	C$\sim$7, S$\sim$5.4, A$\sim$5.5
Model XVIII	2.6×10^{26}	200	1.68×10^{27}	200	G, 20° A, 30° O, θ_o=45° v_c=1 v_b=0.8	C$\sim$6.4, S/A$\sim$5.4
Model XIX	2.6×10^{26}	200	1.68×10^{27}	200	G, 20° A, 30° O, θ_o=45° v_c=1 v_b=0.5	C$\sim$6.2, S$\sim$4.6, A$\sim$4.3
Model XX	2.6×10^{26}	55	1.68×10^{27}	55	G, θ_o=5°	C$\sim$6, S/A$\sim$5
Model XXI	2.6×10^{26}	55	1.68×10^{27}	100	G, θ_o=5°	C$\sim$6, S$\sim$4.8, A$\sim$5.3

Table 4.3: A sample of model parameters tested for Tempel 1 CO_2 Model. "Model Details" are indicated as follows: "G" or "C&W" refer to Goldsmith or Chin & Weaver collisional models. Cone centerline direction is indicated by "A"=Anti-sunward, "O"=towards Observer; no angle notation = "initial" direction of ecliptic south in the image plane. θ_o is the cone opening half-angle. v_c is Cone expansion velocity (in km/s) and v_b of the background. Default value for both is 0.5 km/s. "Fit" column refers to quality of the fit with respect to the peak radiance (in 10^{-4} W m^{-2} sr$^{-1}\mu$m^{-1}) of the Cone ("C"), the Sunward ("S") and Anti-sunward ("A") spectra. Models I and II are close to the Positive Pole ($\sim$3) and comparisons of subsequent models with the PP are not listed.

the incident solar radiation being at work as opposed to shadowing by the nucleus. We also explored tilting the cone in the anti-sunward direction, to increase the anti-sunward spectrum as well, this also did not significantly improve the fit.

Models I and II produced best fits for Positive Pole, with I having a peak slightly less than the data and II slightly greater, with Model II minimally better than I. However they fell quite short for other lines of sight. Further Models explored using higher production rates and varying other parameters to produce the best fit.

Temperature and Collisional Models

Water

Using the values taken from Table 4.2 of $1.4 \times 10^{27} s^{-1}$ for the background Q_{H_2O} based on the anti-sunward value and $4.95 \times 10^{27} s^{-1}$ for the cone based on the ecliptic south value, we made adjustments to the model parameters based on temperature. Noting (see Fig. 4.2) that the spectra along the two directions outside the cone, anti-sunward and positive poleward, share a slight thinness and lack of "shoulder" on their shorter wavelength side unlike the two in-cone spectra, we chose to use a lower temperature for the background and a higher one for the cone. The cone also includes the sub-solar point and nearby areas that are most directly receiving solar insolation, and so logically should be significantly warmer. We chose $T_{bkgd} = 200$ K and $T_{cone} = 370$ K, which is somewhat extreme but not significantly higher than the peak T = 363 K in Davidsson et al. (2013) or T $\sim$ 330 K in Groussin et al. (2013). Needless to say, our model using only two temperatures to model the entire surface is extremely oversimplified.

Carbon Dioxide

A narrow band shape was a crucial feature of the CO_2 spectra that our model did not initially reproduce well, as we had learned in the process of adjusting our CO_2 modeling of Garradd.

To model the narrow CO_2 band of Tempel 1 we varied the surface temperature of the CO_2 cone and the background (i.e. non-cone) surface temperature from 290 K to as low as 100 K. However, these changes alone did not greatly affect the breadth of the initial model CO_2 band.

We explored the effects of switching of the collisional cross section calculation from Chin & Weaver's method to Goldsmith's (which had proved crucial in the Garradd modeling). The "Goldsmith" collisional model, in conjunction with varying temperatures, achieved roughly the desired band widths. Once we settled on the Goldsmith collisional model, we again explored the possible effects of varying temperatures. The upper bounds explored were based very roughly on Groussin et al. (2013); we tested the model with surface temperatures as high as $T_{bkgd} = T_{cone} = $ 300 K. We varied T_{bkgd} between 55 and 300 K, but primarily used 200 K for most models. For T_{cone} we likewise explored such a range, but focused more on lower temperatures, notably 55 K, based on the CO_2 cone originating from a surface not near the subsolar point and the background including the subsolar point (albeit, along with most of the night side as well which is likely much colder, so this is again a very gross approximation).

Morphology: Cone Geometry

The geometric model parameters remained fairly unchanged through most of the model fitting process. Only after producing fairly close fits to the data for three out of the four line-of-sight spectra did we then adjust the CO_2 cone geometry to improve the model for the negative pole spectrum, the one line-of-sight including the cone.

The CO_2 cone opening half-angle was varied from $\sim 85°$ to $35°$ (a cone narrower than that did not appear to visually fit the appearance of Fig. 4.1(b)), and its orientation was adjusted to point $\sim 20°$ anti-sunward of ecliptic south (which actually agrees with Farnham et al., 2007 more closely than our initial cone model). Tilting the cone towards the observer (i.e. out of the plane of the image) by various angles was also tested. Variation of these geometric parameters was attempted to explore whether the proportion of background to cone along the line of sight was a significant factor. This would be a reasonable expectation since varying the path length through the cone along the line-of-sight could increase the brightness observed along that line-of-sight. We tried tilting the cone towards the observer to vary that path length by greater than a factor of two. On the other hand, increasing the path length through the background on the observer's side of the cone could decrease any possible attenuation due to optical depth effects outside the cone, thus allowing more emission (from the denser cone) to escape. However the differences between models in to these tilting tests were found to be minimal for these cases.

Other possible geometries that we have not yet attempted may still improve the model fit. It is also possible that the simple geometry of a single solid cone with constant production rate over the base of the cone may not be a sufficiently precise model to produce significantly better fits to the data. (See e.g. Tenishev et al., 2008, Fougere et al., 2013 for modeling of a "cone" with density that varies over

angle.) In particular, it is quite possible that the observed "cone" is actually a spiral produced by a much narrower cone that is being rotated around the negative pole, thus producing something that would be closer to a "hollow" cone. (See Farnham et al. 2007) Models that simulate this possibility in effect were explored (Models XX & XXI). For this we used a much narrower cone, aligned along the plane of the image. While this does not visually appear similar to the data, with respect to optical depth effects on the emerging spectrum it simulates a "conical shell" shape in that the actual volume of cone gas with higher density than the background is closer to a narrower cone that through rotation produces a "conical shell" and the velocities along the observer's line-of-sight vary from the far side to the near side.

Expansion Velocity

Most of our models used a constant expansion velocity of 0.5 km/s, in keeping with the assumed value used in Feaga et al. (2007a) for calculations of production rates from brightness. In several models, we varied V_{exp} of both the cone and the background, as shown in Table 4.3. The best-fit model, Model XVI, used $V_{exp,bkgd}$ = 0.8 km/s and $V_{exp,cone}$ = 1.0 km/s. These changes, in conjunction, contributed a noticeable but not large amount of extra brightness. However, this variation of expansion velocities may point the way to improving model fitting even further, especially for the cone spectrum.

Differential doppler velocities can significantly reduce optical depth. Since our model spectra for the cone seem to be too optically thick, a (preliminary) exploration of the possible effects on optical depth of an acceleration of the gas near the nucleus as opposed to the simple constant expansion velocity (of a simple Haser model) was made. We added to our parameter space two further values, the expansion velocity

at the nucleus' surface and the radial distance at which the constant velocity (our previously defined constant expansion velocity) is reached. These create a "zone" of (constant) acceleration close to the nucleus. Our initial exploration of these parameters has not yet yielded a significantly better fit of the model. Further exploration of these parameters is warranted as we have only recently added this capability to the model and have not thoroughly explored them yet.

4.1.4 Results

The parameter exploration and fitting process arrived at the best-fit model parameters listed in Table 4.4.

The total Q_{H_2O}, calculated by a solid-angle average of cone and background production rates, is $3.2 \times 10^{27} s^{-1}$. This is almost 50% greater than the (corrected, i.e. halved) value from Feaga et al. (2007a) of $2.3 \times 10^{26} s^{-1}$ assuming negligible optically depth.

The H_2O model based on these values produced brightness maps as presented in Fig. 4.5 and the near nucleus line of sight spectra shown in Fig. 4.9. The model spectra can be seen overplotted on the recalibrated data in Fig. 4.7.

The H_2O spectra produced using the model are a fairly good fit to the data. The peak brightness and distribution seen in the brightness map (Fig. 4.5) are in rough but close correspondence to Fig. 4.1. (Note that the units scale in the model is shown in ergs s^{-1} cm^{-2} sr^{-1} so a conversion of 10^{-3} is needed to compare numerically with Fig. 4.1(a) whose units are Watts m^{-2} sr^{-1}. Also note that there will still be a factor of 2 difference due to our correcting for the pixel size error in the original pipeline. Once all that is taken into account, the model's peak brightness of 3×10^{-1} ergs s^{-1} cm^{-2} sr^{-1} is in close agreement with 6.75×10^{-4} Watts m^{-2} sr^{-1}.)

For CO_2, the best-fit model, albeit not excellent, is Model XVI from Table 4.3.

Best-fit Model Parameters used for 9P/Tempel 1	
H_2O Values	
Total Q_{H_2O}	$3.2 \times 10^{27} s^{-1}$
Cone Q_{H_2O}	$4.95 \times 10^{27} s^{-1}$
Background Q_{H_2O}	$1.4 \times 10^{27} s^{-1}$
Cone $T_{surface}$	370 K
Background $T_{surface}$	200 K
Cone V_{exp}	0.5 km s^{-1}
Background V_{exp}	0.5 km s^{-1}
Cone orientation	45° South of sunward, 30° Towards obs.
Cone opening half-angle θ_O	85°
CO_2 Values	
Total Q_{CO_2}	$3.7 \times 10^{26} s^{-1}$
Cone Q_{CO_2}	$8.4 \times 10^{26} s^{-1}$
Background Q_{CO_2}	$2.66 \times 10^{26} s^{-1}$
Cone $T_{surface}$	200 K
Background $T_{surface}$	200 K
Cone V_{exp}	1.0 km s^{-1}
Background V_{exp}	0.8 km s^{-1}
Cone orientation	20° Anti-sun., 30° Towards obs.
Cone opening half-angle θ_O	45°

Table 4.4: Best fit model input parameters for modeling Deep Impact observations of comet Tempel 1, for H_2O and CO_2. "Total Q" refers to the solid angle weighted mean between Cone and Background Q's. (Note that for CO_2 the Positive Pole is better fit by Models I or II than these parameters; see Table 4.3.)

It is a fairly close match to the data for the sunward and anti-sunward spectra, but still falls short in comparison with the negative pole spectrum. The total Q_{CO_2}, calculated by a solid-angle average of cone and background production rates, is $3.7 \times 10^{26} s^{-1}$. This is slightly greater than double the (corrected, i.e. halved) value from Feaga et al. (2007a) of $1.6 \times 10^{26} s^{-1}$ assuming negligible optical depth. This model may still be an underestimate, since we have not yet perfected the fitting of the negative pole/cone model spectrum which is still producing a lower peak brightness than the data. (On the other hand, if improvements to the velocities in the modeling is the key to better fitting spectra, as per Sec. 4.1.3, then the model
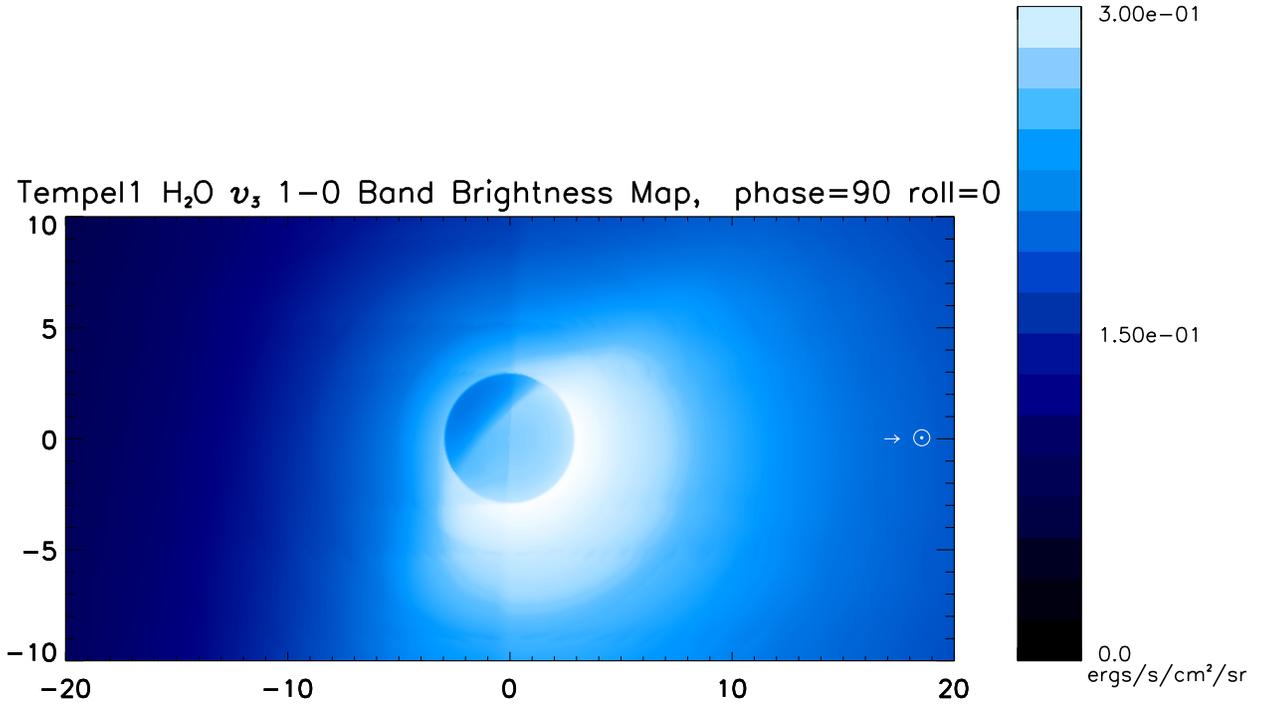
Figure 4.5: Near nucleus radiance map produced from our model of the H$_2$O ν_3 band total of Tempel 1, corresponding to Fig. 4.1(a). Note that the units scale in the model is ergs s^{-1} cm^{-2} sr^{-1} so multiplication by 10^{-3} is needed to compare numerically with Fig. 4.1(a) whose units are Watts m^{-2} sr^{-1}. Also note that there will still be a factor of 2 difference due to our correcting for the pixel size error in the original pipeline.

production rates might be an overestimate.)

However, the positive pole spectrum fits the data better with respect to the peak value (albeit slightly too narrow in width) in Models I and II than in any subsequent iterations, including Model XVI. Therefore, we have included the Model II results plotted over the data in Fig. 4.8, as well as the Model XVI results in Fig. 4.7 which are the best-fit for the other lines of sight. This dichotomy is probably due to the simplicity of our "one cone" model. In fact, if we were to "mix and match" different line-of-sight spectra from models with different parameters the overall quality of our fitting could be improved. This reflects the fact that Tempel 1 appears to have multiple "cone-like" features at various locations and areas of the surface that seem
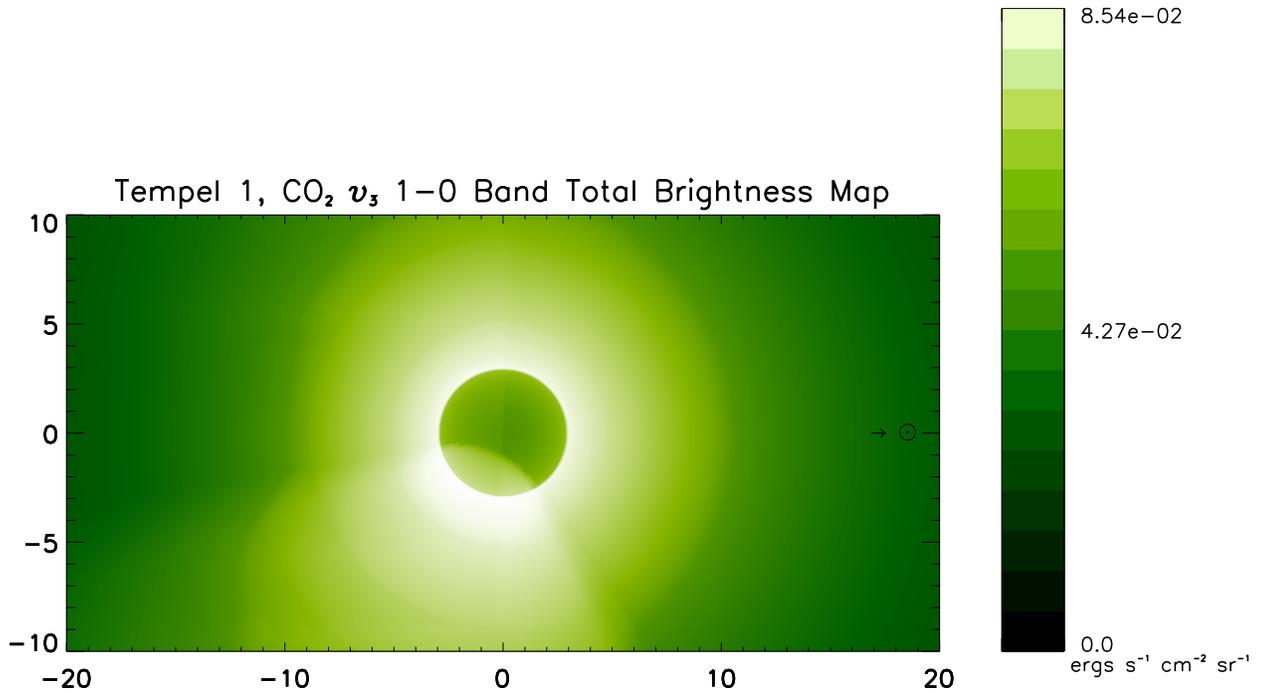
Figure 4.6: Near nucleus radiance map produced from our model of the CO_2 ν_3 band total of Tempel 1, corresponding to Fig. 4.1(b). Note that the units scale in the model is ergs s^{-1} cm^{-2} sr^{-1} so a conversion of 10^{-3} is needed to compare numerically with Fig. 4.1(b) whose units are Watts m^{-2} sr^{-1}. Also note that there will still be a factor of 2 difference due to our correcting for the pixel size error in the original pipeline.

to be devoid of them. A more accurate and/or flexible morphology model would likely produce better results.

It should be noted that the Tempel 1 data have not been reprocessed other than the aforementioned division by 2 since originally published (Feaga et al. 2007a), but subsequent improvements have been made to the original calibration methods (and *were* used for the other comets observed). It is somewhat unclear exactly what effect(s) this recalibration might have on the actual data we are attempting to model. Thus any attempts to better fit the model to the data remain tentative and may require further revision at some time in the future to re-fit recalibrated data when it becomes available.
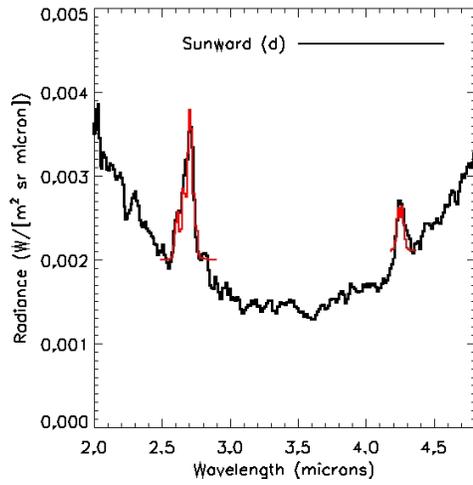
(a) Tempel 1 Sunward line of sight.
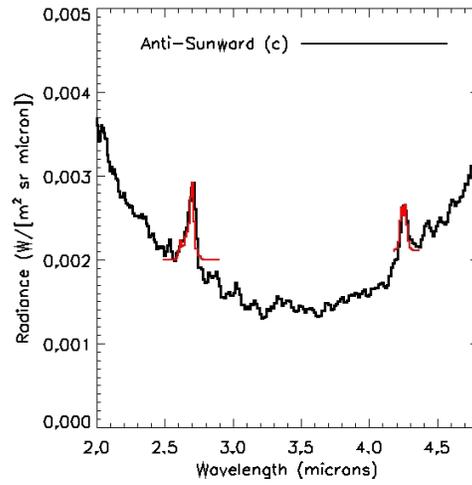
(b) Tempel 1 Anti-Sunward line of sight.
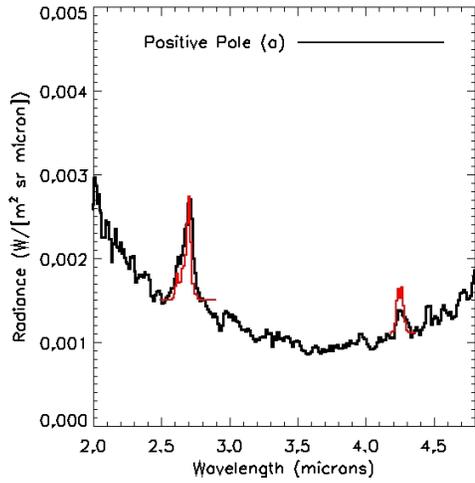
(c) Tempel 1 Positive Pole line of sight.
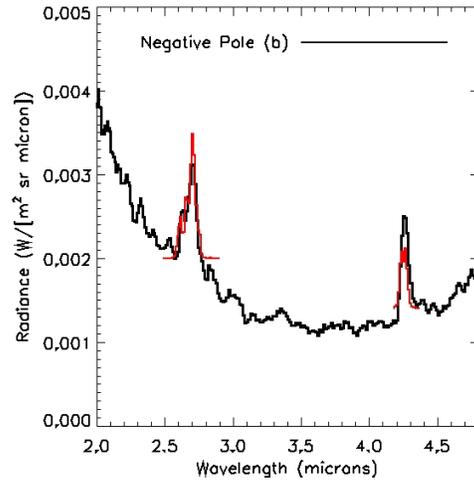
(d) Tempel 1 Negative Pole line of sight.

Figure 4.7: The best-fit Tempel 1 line of sight spectra, 7 km from center of nucleus. Models for H_2O and CO_2 plotted on recalibrated DI data (i.e. divided by 2) from Feaga et al. (2007a). The model results are the same as those in Figs. 4.9 and 4.10.
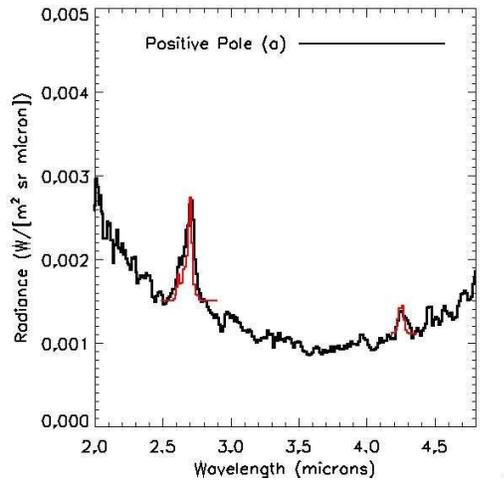
(a) Tempel 1 Positive Pole line of sight.

Figure 4.8: The best-fit for the positive pole CO_2 spectrum Tempel 1 line of sight spectra, 7 km from center of nucleus. Models for H_2O and for CO_2 the positive pole only plotted on recalibrated DI data (i.e. divided by 2) from Feaga et al. (2007a).

4.2   Hartley 2

4.2.1   EPOXI: The Deep Impact Flyby Observations

The Deep Impact Flyby spacecraft observed a second comet when it flew by comet 103/P Hartley 2 as part of the extended mission, named EPOXI. It made observations of Hartley 2 with the HRI spectrometer similar to those described above for Tempel 1. (See A'Hearn et al., 2011.) Closest approach to Hartley 2, at which time the spacecraft was about 694 km from the nucleus, was on Nov. 4, 2010 at a heliocentric distance of 1.064 AU.

A'Hearn et al. (2011) present radiance maps of emission bands for both H_2O and CO_2 (among others) and spectra from two lines of sight near the nucleus taken 7 minutes after closest approach. We have reproduced those here in Figs. 4.11, 4.12, respectively. Carbon monoxide was not detected in the EPOXI spectra of Hartley

(a) Sunward

(b) Anti-Sunward

(c) Positive Pole

(d) Negative Pole
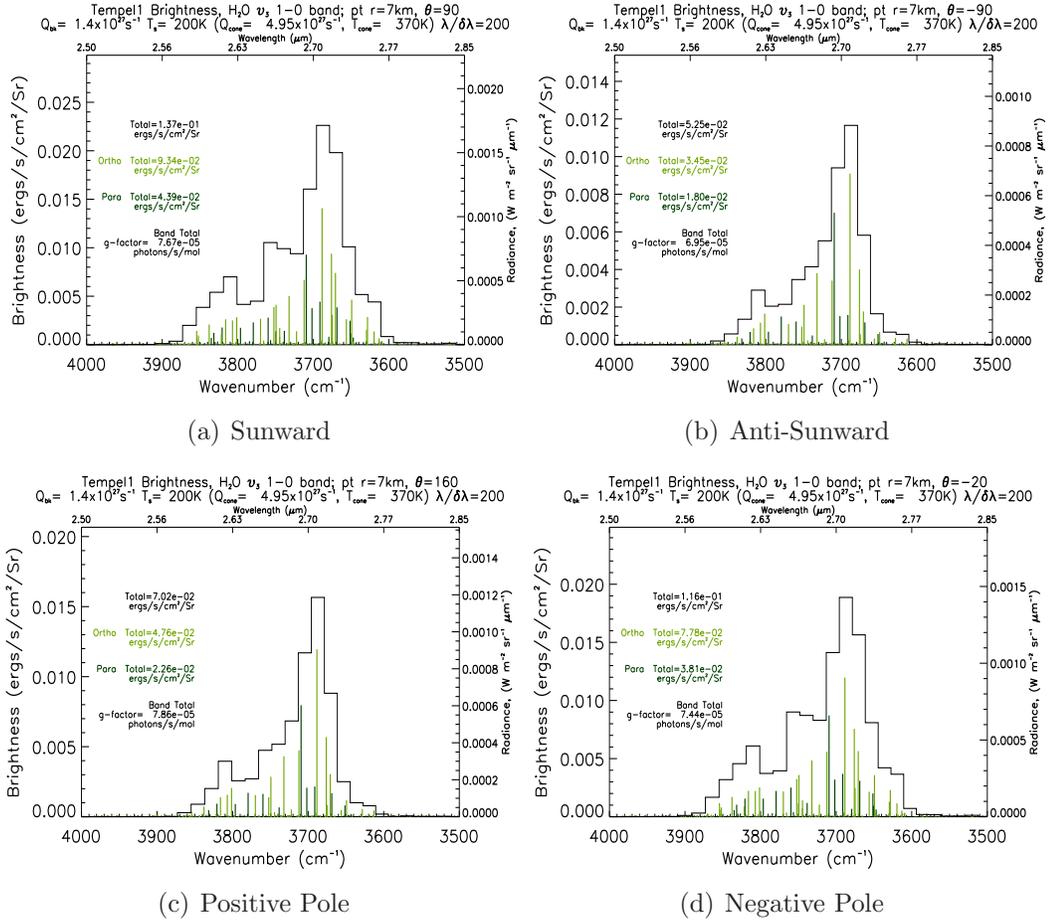
Figure 4.9: Model Tempel 1 H_2O spectra along four lines of sight at 7 km distance from the center of the nucleus, corresponding to those in Fig. 4.7

2 and HST observations indicated that its abundance was only $0.3\pm0.15\%$ that of H_2O (see Weaver et al. 2011). In addition, "box" apertures of 120 km and 600 km size from 55 hours before closest approach were included in the supporting online material (henceforth "SOM"). We have reproduced those here in 4.13.

Since publication, the spectra from Hartley 2 have been recalibrated with improvements to the pipeline and new improved versions of the spectra in Fig. 4.12 are now available. These are shown in Fig. 4.16. There is not a very great difference, except for the shape of the CO_2, now notably lacking double peaks in the CO_2 jet spectrum. The improved spectra of Fig. 4.16 are the ones we ultimately attempted
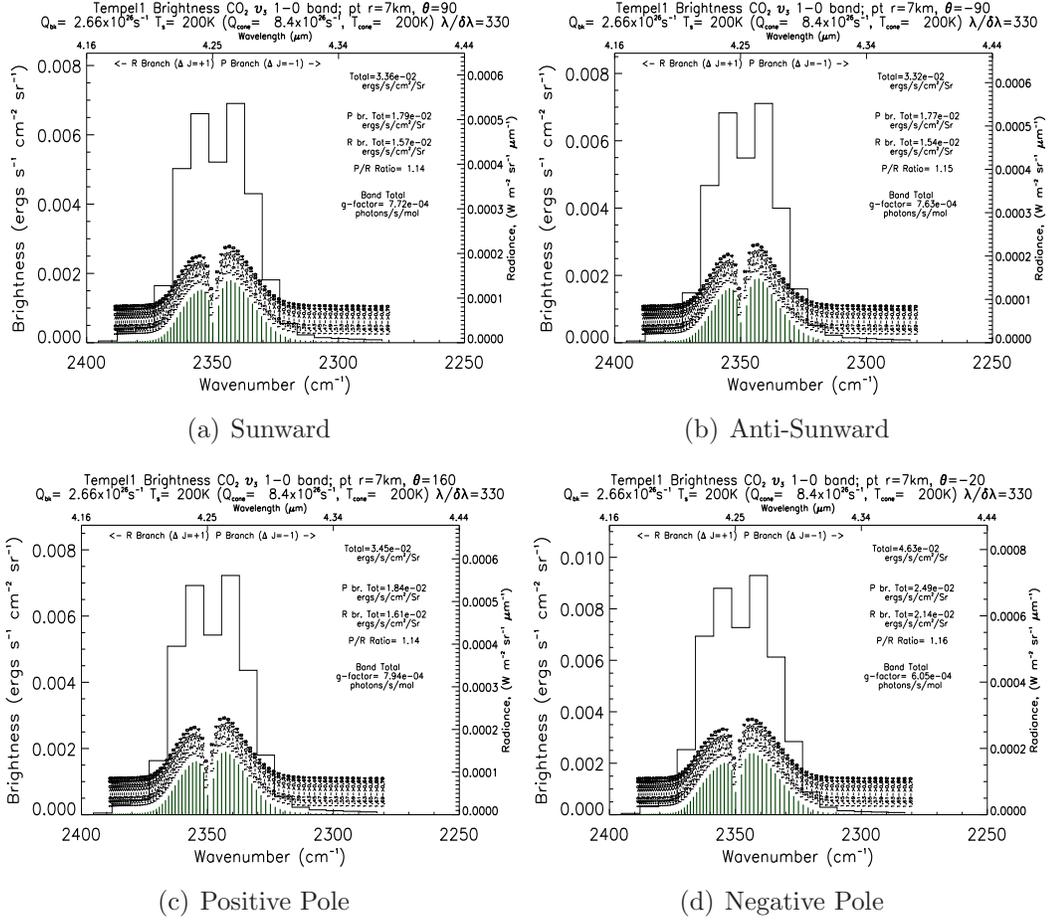
Figure 4.10: Model Tempel 1 CO_2 spectra along four lines of sight at 7 km distance from the center of the nucleus, corresponding to those in Fig. 4.7

to model.

As can be seen clearly in Fig. 4.11, the geometry of the Hartley 2 EPOXI observations is clearly more complex than the previous cases we have dealt with here.

4.2.2 Model Parameters

To model these observations we initially used the geometry shown in Figs. 4.14 & 4.15 and the values in Table 4.5. The CO_2 cone's center line was in the sunward direction (in the image plane) and the opening angle was $\sim 85°$. The H_2O cone's center line is aligned $75°$ north from sunward and points $45°$ into the image plane
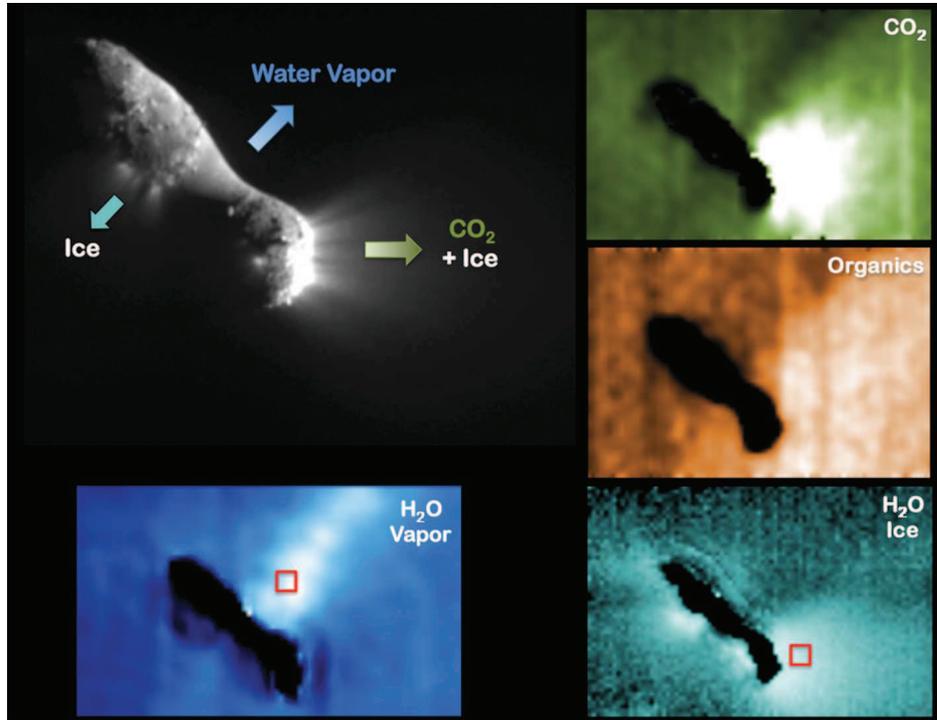
Figure 4.11: Near nucleus radiance maps of the H_2O and CO_2 ν_3 bands and other bands, along with a corresponding MRI image of the nucleus. From A'Hearn, et al. 2011.

away from the observer. The opening angle was $\sim 15°$. Again, in our model the nucleus is always spherical, but this can represent the sunward "lobe" of Hartley 2's very non-spherical actual nucleus.

The total production rates used were those in A'Hearn, et al. 2011. The apportioning between background and cone features were based on a rough 2:1 ratio between cone and background column densities of CO_2, and a rough 9:1 ratio between column densities of H_2O, and "eyeballing" where to locate our cones in the model.
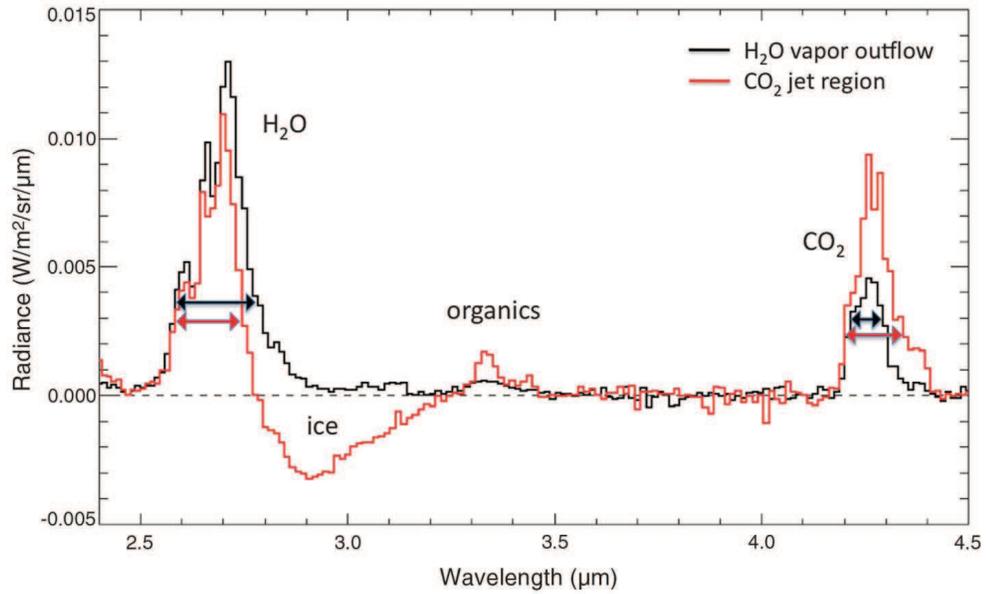
Figure 4.12: Near nucleus spectra sampled in the areas indicated by the red boxes near the nucleus in Fig. 4.11. The continuum has been removed. Radiance values are in W m^{-2} sr^{-1}μm^{-1}. (The arrows are just to show the different band widths for the two regions.) From A'Hearn, et al. 2011.
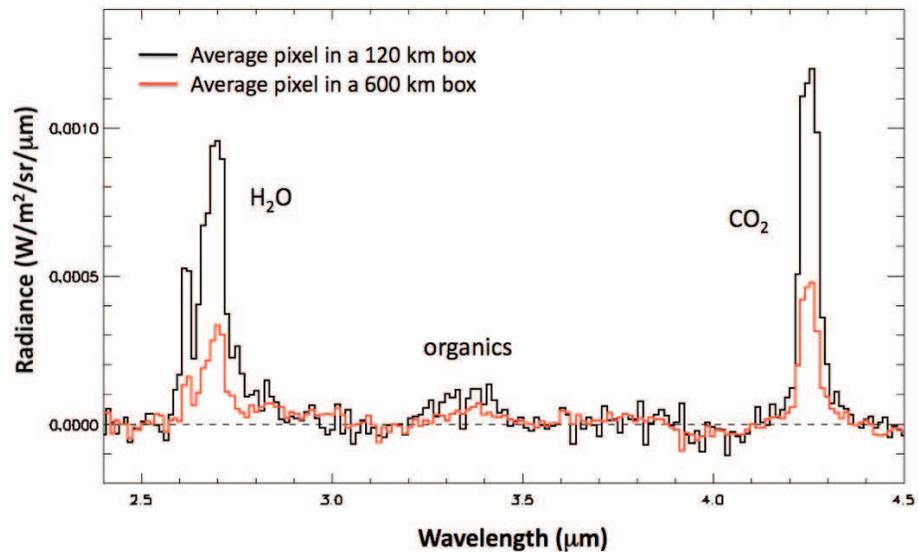
Figure 4.13: Spectra sampled in 120 km and 600 km box apertures centered on the nucleus taken 55 hours before closest approach. The continuum has been removed. Radiance values are in W m^{-2} sr^{-1}μm^{-1}. From A'Hearn, et al. 2011.

157
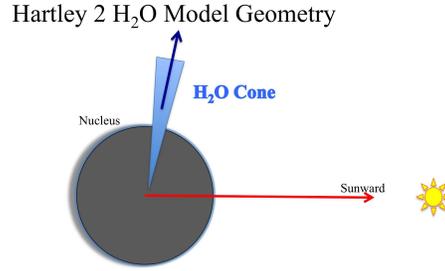
Figure 4.14: *Rough* diagram of the H_2O cone used for modeling the observed northern H_2O morphology feature of Hartley 2. The cone's center line is aligned $\sim$75° north from sunward and points $\sim$45° out of the image plane towards the observer. The opening angle of the cone was initially $\sim$15° (and subsequently changed to $\sim$22°).
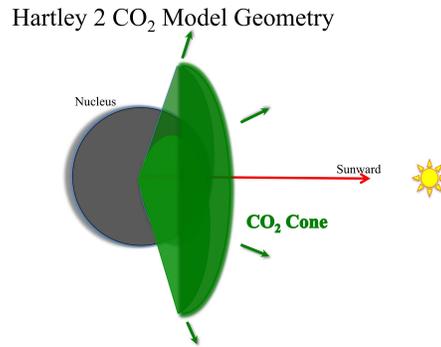
Figure 4.15: *Rough* diagram of the CO_2 cone initially used for modeling the observed sunward CO_2 morphology of Hartley 2. The cone's center line is aligned in the sunward direction. The opening angle of the cone was initially 85° (and later varied cone parameters were tried). (Slightly broader than in our rough diagram.)

4.2.3 Fitting the Model to the Data

Our initial model spectra for CO_2 were not very good when compared to the data (Fig. 4.12). Our initial H_2O fit was a somewhat better match than the CO_2 and after the parameter adjusting and fitting process we arrived at an H_2O model that

Initial Model Parameters used for 103P/Hartley 2

Mean Nucleus Radius	0.5 km
$T_{surface}$	200 K
Q_{H_2O}	$1 \times 10^{28} s^{-1}$
Cone Q_{H_2O}	$9.1 \times 10^{27} s^{-1}$
Background Q_{H_2O}	$0.9 \times 10^{27} s^{-1}$
Ortho:Para Ratio	3:1
Highest Rot. Level, J_{max}	7
Solar flux	$3.9 \times 10^{13} \, photons \, cm^{-2} s^{-1}/cm^{-1}$
σ_{rot}	$2.5 \times 10^{-15} \, cm^2$
Q_{CO_2}	$2 \times 10^{27} s^{-1}$
Cone Q_{CO_2}	$1.82 \times 10^{27} s^{-1}$
Background Q_{CO_2}	$0.18 \times 10^{27} s^{-1}$
Highest Rot. Level, J_{max}	70
Solar flux	$2.8 \times 10^{13} \, photons \, cm^{-2} s^{-1}/cm^{-1}$
σ_{rot}	$3.6 \times 10^{-15} \, cm^2$

Table 4.5: Initial Model input parameters for modeling EPOXI observations of comet Hartley 2, for H_2O and CO_2.

is a pretty close fit to the data.

Production Rates

CO_2 presented familiar difficulties, similar to the ones encountered for other comets we have modeled. The band shape was too broad and showed two peaks much more distinctly than the observations. Our model worked best for the 120 and 600 km box apertures (see Figs. 4.13) included in the SOM. However, the initial model of the coma very close to the nucleus was quite optically thick, and the resulting spectra were too low both in peak and band total brightness. Thus, we explored varying the available model parameters to produce model spectra that would be more optically thin, which was quite difficult.

However, we discarded those early models based on the total production rates derived from the 600 km aperture, particularly for water, as they would not produce

Data and Corresponding Model Inputs Derived from EPOXI Hartley 2 Observations

Region	B(H_2O)	N(H_2O)	Q(H_2O)	B(CO_2)	N(CO_2)	Q(CO_2)
Sunward	1.1×10^{-3}	6.8×10^{16}	1.4×10^{27}	8.1×10^{-4}	8.7×10^{15}	1.8×10^{26}
Waist	1.7×10^{-3}	1.1×10^{17}	2.1×10^{27}	4.1×10^{-4}	4.4×10^{15}	8.8×10^{25}

Table 4.6: Radiance, column densities and corresponding production rates calculated (assuming negligible optical depth) for 2 "boxes"/regions near ($\sim$1-2 km from) the nucleus of comet Hartley 2, for H_2O and CO_2. The radiance values are taken from the SOM of A'Hearn, et al 2011, and are in $Wm^{-2}sr^{-1}$. The column densities (in cm^{-2}) and production rates (in s^{-1}) are calculated from the radiance using N = 4 π B (h c ω)$^{-1}$ r$_h^2$/g (where ω is wavenumber, r$_h$ is heliocentric distance in AU, g is the optically thin 1 AU g-factor, all in appropriate units) and $Q = 4v\rho N$ at $\rho = 1$ km with $v = 0.5 \ km \ s^{-1}$.

as close a fit as the near nucleus observations due to the strong likelihood of an extended source. The presence of large quantities of large icy grains in the coma was well established by the DI observations and it is highly likely that a significant fraction of the water in the large aperture observations was not being emitted as gas directly from the nucleus, but from sublimation from grains farther out in the coma. Both Fougere et al., 2013 and Kelley et al., 2013 estimate that as much as approximately 80% of water emission may be from such extended sources, although Kelley et al.'s estimated percentage is specifically *near* ($\sim$20 km) the nucleus while Fougere et al. suggest that the contribution of an extended source may continue to be more significant for thousands of kilometers from the nucleus. (Alas, our model does not deal with extended sources, as yet, and so we cannot weigh in on the matter.)

We also discovered that the published production rates calculated from the 600 km aperture were too large by a factor of 2, due to a miscalculation related to using aperture *averaged* radiance together with the aperture's *total/maximum* radius for the calculation of Q. When this is corrected and then compared to our calculated values in Table 4.6, the approximate ratio of nucleus to extended source

water production rates is about 1:4, quite close to that of Fougere et al. (2013). Thus, in truth, to model *all* the published DI spectra using our modeling method, would require separate models with different production rates (at the very least): one for the near-nucleus gas spectra and one for larger aperture(s) including sublimation from grains in the coma.

Instead of the 600 km aperture production rates, we proceeded to use values for Q's derived directly from the near nucleus lines of sight. The radiance values in the SOM were used to calculate production rates, shown in Table 4.6.

Water Production Rates

Due to the relative narrowness of the Hartley 2 water cone feature (as compared to the other three cones in these models), we decided to modify the approach to calculating the cone's production rate from that used for the other sources. Instead of using $Q_{cone} = 4v\rho N$ to calculate a Q_{cone} from a given value of N, we treated the cone as *an addition* to the background line of sight over a short distance, and that the *extra* emission along the line of sight due to the cone was the *difference* between the cone and the background values. We integrated the density along the line of sight distance through the cone by itself at $\rho = 1km$ and set that value equal to the *extra* column density in addition to the background column density, from which we calculated $Q_{H_2O_{cone}} = 3.03 \times 10^{27}s^{-1}$. For the background we used the usual calculation, and the value $Q_{bkgd} = 1.4 \times 10^{27}$. (See Table 4.6.)

These initial values, calculated assuming optical thinness, produced spectra with much too low brightnesses to match the data, indicating high optical depths. We adjusted parameters to fit the data values better, using the band total brightnesses (in Table 4.6) and peak radiance values (see Fig. 4.16) as our targets. In this incremental iterative fitting process, we generally changed only one parameter (but

occasionally more) from one iteration to the next. We incrementally increased production rates in subsequent model runs, generally by doubling the input Q's. This did not result in a linear increase (i.e. doubling) of the output brightness, but much smaller incremental increases, as can be seen in Table 4.7. We also varied temperatures, temperature profiles and collisional models for various pairs of values of Q's.
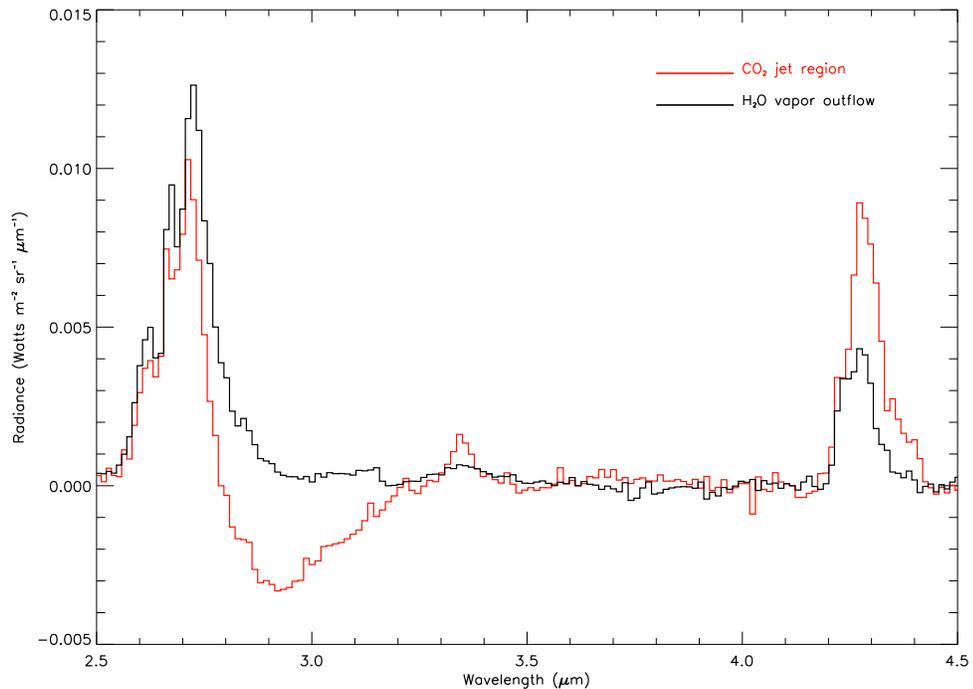
Figure 4.16: Recalibrated Hartley 2 near nucleus spectra corresponding to Fig. 4.12 but produced by the improved data pipeline. The continuum has been removed. Radiance values are in W m^{-2} sr$^{-1}\mu$m^{-1}.

Temperatures and Collisional Models

As with the other comets, our switch to the Goldsmith collisional model made some improvements to the CO_2 band shape, but the band was still broader than the band in the data. Lowering the temperature in conjunction with the newer collision model improved the fit somewhat.

Varying/Fitting Water Model Parameters used for Hartley 2

Model	Input Parameters				Sunwd. Results		Cone Results	
#	Q_{bkgd}	T_b	Q_{cone}	T_c	Peak R	Total B	Peak R	Total B
Data/Observed Values					$\sim 10^{-2}$	1.1×10^{-3}	$\sim 1.2 \times 10^{-2}$	1.7×10^{-3}
I	1.36×10^{27}	120	3.03×10^{27}	200	4.5×10^{-3}	3.9×10^{-4}	5×10^{-3}	5×10^{-4}
II	2.8×10^{27}	120	3.03×10^{27}	200	6×10^{-3}	5.3×10^{-4}	6.3×10^{-3}	6.1×10^{-4}
III	5.6×10^{27}	120	3.03×10^{27}	200	7.25×10^{-3}	6.5×10^{-4}	7.5×10^{-3}	6.95×10^{-4}
IV	5.6×10^{27}	60(c)	3.03×10^{27}	200	8.5×10^{-3}	6.1×10^{-4}	7.1×10^{-3}	8.5×10^{-4}
V	5.6×10^{27}	60(c)	6.06×10^{27}	200	9.2×10^{-3}	6.4×10^{-4}	9.2×10^{-3}	8×10^{-4}
VI	5.6×10^{27}	60(c)	6.06×10^{27}	300	9.2×10^{-3}	6.4×10^{-4}	9.2×10^{-3}	9×10^{-4}
VII	5.6×10^{27}	60(c)	9.09×10^{27}	300	9.2×10^{-3}	6.4×10^{-4}	9×10^{-3}	8.3×10^{-4}
VIII	1×10^{28}	60(c)	1.8×10^{28}	300	1.1×10^{-2}	7.6×10^{-4}	1×10^{-2}	1.2×10^{-3}
IX	1×10^{28}	60(c)	1.8×10^{28}	350	1.1×10^{-2}	7.6×10^{-4}	1×10^{-2}	1.25×10^{-3}
X	1.25×10^{28}	60(c)	1.8×10^{28}	300	1.15×10^{-2}	8.67×10^{-4}	1.1×10^{-2}	1.25×10^{-3}
XI	1×10^{28}	60	1.8×10^{28}	350	6.5×10^{-3}	4.7×10^{-4}	7.5×10^{-3}	1.1×10^{-3}
XII	1.25×10^{28}	60	2.4×10^{28}	300	6.5×10^{-3}	4.7×10^{-4}	8×10^{-3}	1.1×10^{-3}
XIII	1.25×10^{28}	60(c)	2.4×10^{28}	300	1.15×10^{-2}	8.67×10^{-4}	1.1×10^{-2}	1.24×10^{-3}

Table 4.7: Fitting/Variations of parameters: A sampling of production rates and collisional models tested for Hartley 2 H_2O Model. The initial model is based on the Q values in Table 4.6 *assuming negligible optical depth*). "(c)" after a temperature value indicates a constant temperature model used. "R" refers to Radiance "B" to Brightness. Peak Radiance and Band Total are in W m^{-2} sr$^{-1}\mu$m^{-1} and W m^{-2} sr^{-1} respectively. For Peak Radiance, the data values are from Fig. 4.16.

Similarly, using a fairly low temperature for the background temperature in water models also made improvements to the fitting. Reducing the background temperature by half, e.g. from T = 120 K to T = 60 K, while leaving other parameters unchanged, increased the peak brightness of the band (in the sunward spectra) by a factor similar in magnitude to doubling the production rate (while leaving other parameters unchanged, in either case). However, this change also simultaneously decreased the band total brightness. (See e.g. Table 4.7, Models # III and IV.) This is presumably due to the band being more narrow at the colder temperature, with more of the population being in low J levels, so that the lines of peak emission emit more (than those lines do in a warmer distribution) due to their higher populations, but also making a larger number of lower J lines optically thicker than a broader

(warmer) population distribution. Ultimately, combining both a lower T and higher Q proved, not surprisingly, to be more effective than either change individually.

In the water cone ("waist" feature), we found that a considerably higher temperature produced better fitting model spectra. This is not so surprising since this spectrum clearly shows a broader band than the sunward spectrum. The use of a surface temperature of 300-350 K is also quite reasonable based on Groussin et al. (2013). These model temperatures imply support for the idea that the "waist" water feature is produced by water directly leaving the nucleus, hence the best-fit model is one using a temperature profile based on the surface temperature of the nucleus, This is also consistent with private communication from L. Feaga regarding the waist water being highly dependent on the nucleus shape model, solar illumination and nucleus rotation. (In future work, we may attempt to model spectra from the waist at different orientations of nucleus rotation and illumination.) However, the "background" water may be sublimating from icy grains around the nucleus and thus the colder, radially independent temperature model works better for the background.

Geometry

Changes in geometry to make the cone(s) somewhat narrower, primarily for the CO_2 feature, while still within the rough bounds of the observations, were among alternate models tested. A narrower cone, with densities of both the cone and background unaltered, would lead to a given line of sight being comprised more of the lower density background, hence reducing the overall optical depth along the line of sight, and allowing more emission from the cone itself to escape. This was expected to decrease the optical depth for the emerging radiation for the CO_2 sunward spectra. However this alone did not have a dramatic effect.

4.2.4 Results

We have produced brightness maps (see Fig. 4.17) and line of sight spectra near the nucleus (Figs. 4.18 and 4.19 for our best-fit model. After the fitting process described, the H_2O is a fairly close fit to the data but the spectra for CO_2 are not very good matches to the observed data.

Water

The model labeled "Model X" in Table 4.7 is the best fit to the data, based on total band brightness. However, it is a "close call" whether "Model X" is better than "Model IX"; the deciding criterion used is the band total brightness, but in terms of peak brightness, "Model IX" might be a slightly better match.

This is still not a perfect fit. Our best-fit H_2O model produces peak radiance values very close to 0.01 W m^{-2} $sr^{-1}\mu m^{-1}$, for both the sunward and water vapor feature spectra. This is quite close to the data for the sunward spectra ($\gtrsim$0.01 W m^{-2} $sr^{-1}\mu m^{-1}$), but about 20-25% lower than the peak value of the water vapor region ($\sim$0.0125 W m^{-2} $sr^{-1}\mu m^{-1}$).

The band shapes, however, are a less ideal fit to the data. Although the FWHM of the model band is very close to the data, elsewhere the width of the water vapor cone model spectrum is noticeably narrower than the data. Even though the hotter temperature models produce broader spectra, they are still not quite broad enough to match the observed width. This may be due to needing more lines and/or bands included in the model, in particular the inclusion of water "hot bands". The hot bands are particularly likely to improve the model fit for the "shoulder" feature between 2.8-2.9 μm in the H_2O waist spectrum, but might improve the fit elsewhere in our models as well (possibly even for other molecules, such as CO in Garradd).

(a) H$_2$O ν_3 band total

(b) CO$_2$ ν_3 band total
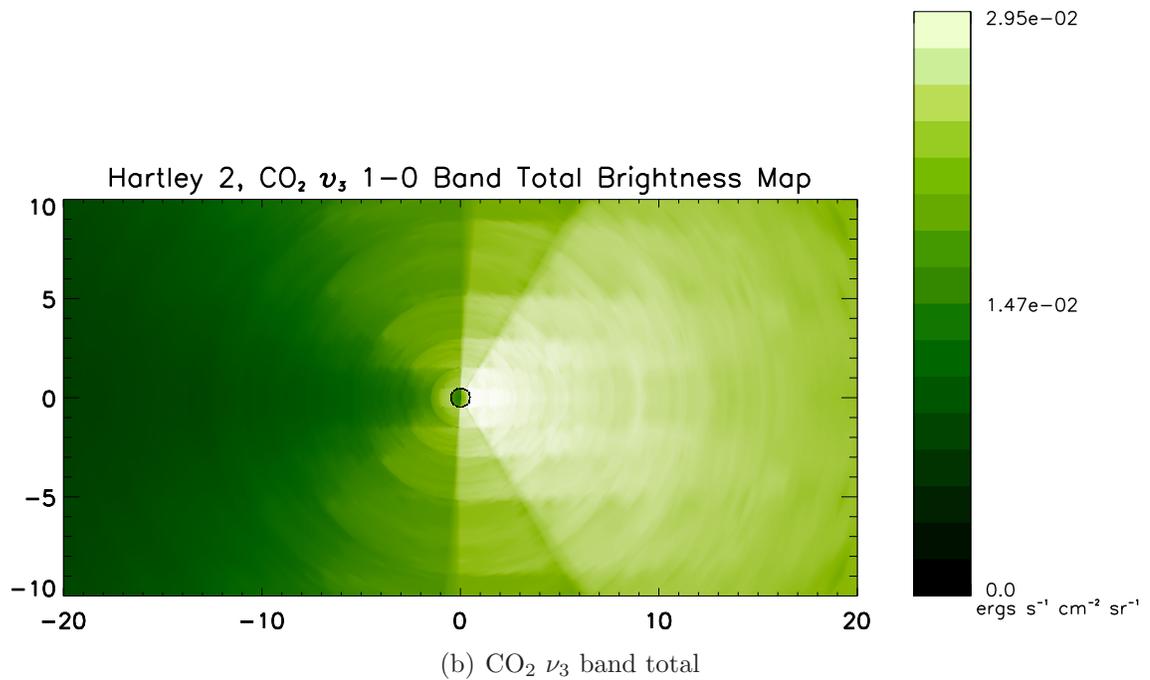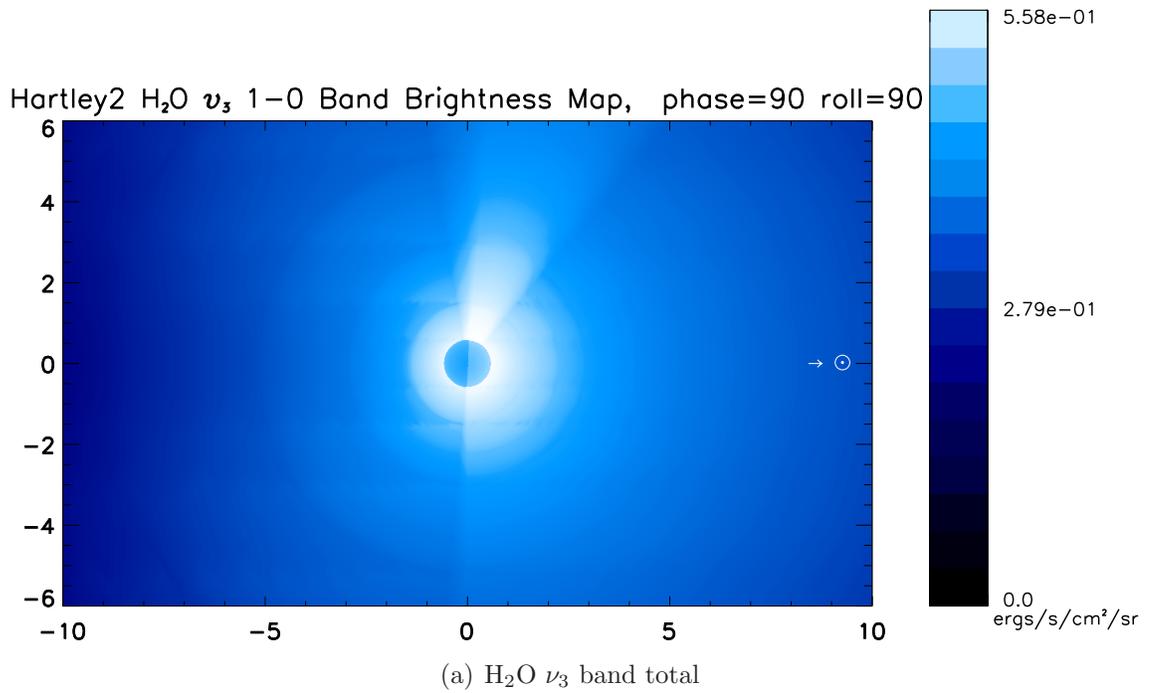
Figure 4.17: Brightness maps of Hartley 2, H$_2$O and CO$_2$ ν_3 band totals based on our best model results and corresponding to those in Fig. 4.11. Brightness is in ergs s^{-1} cm^{-2} sr^{-1}. Note that the spatial scale of the maps is slightly different, as labeled (in km).

For the sunward spectra, although the model's band width is closer to the data, the smaller peaks at shorter wavelengths of the main peak are a considerably less close fit compared to the data than the main peak. Similarly, the band total brightness is too low by a factor of ∼20-30%.

However, the proportion of the brightness totals between the two spectra is quite close to the data. For H_2O, the sunward to waist region ratio of total brightness is ∼0.65 in the data and ∼0.6 in our model.

The implied water production rates seem very high as would the high optical depths. This is discussed below in Sec. 4.3.

Carbon dioxide

Our modeling results for CO_2 for Hartley 2, so far, have been rather mediocre. The largest discrepancy would immediately appear to be a large difference in magnitude of the spectra. The peak values of the CO_2 band being about a factor of 10 or more too low when compared to the data. It should be noted that the respective band shapes, if stretched up to a similar scale as the data are not a terrible fit. (See Fig. 4.20(b).) The ratios between band total brightnesses are likewise not far from the observed values: For CO_2, the ratio is ∼2 for the data and a slightly less close ∼1.4 for the model. Other minor adjustments to band width or shape would presumably be minor compared to the magnitude of the scale factor required.

This has been a persistent problem in modeling Hartley 2, and it seems that it is again due to high optical depths. These may require more computing power and/or time to accurately calculate. (This is due to the size of many Regions being larger than would produce optically thin Regions thus reducing the accuracy of the CEP calculations, which are based on the assumption of uniform conditions throughout a Region. Greater computing power would allow the use of smaller Regions.) A
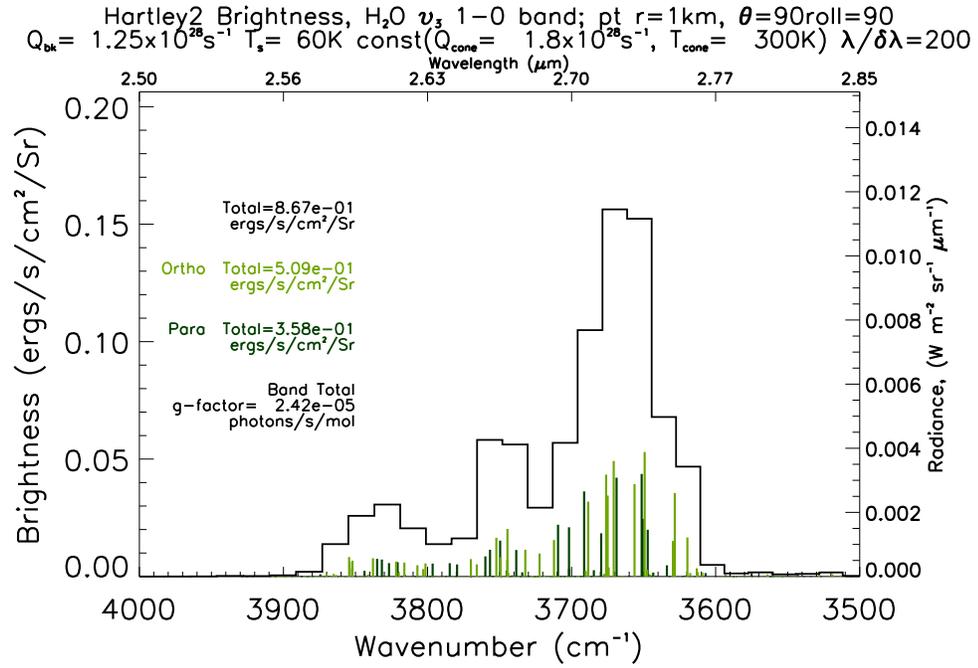
(a) Sunward (on CO_2/ice feature)
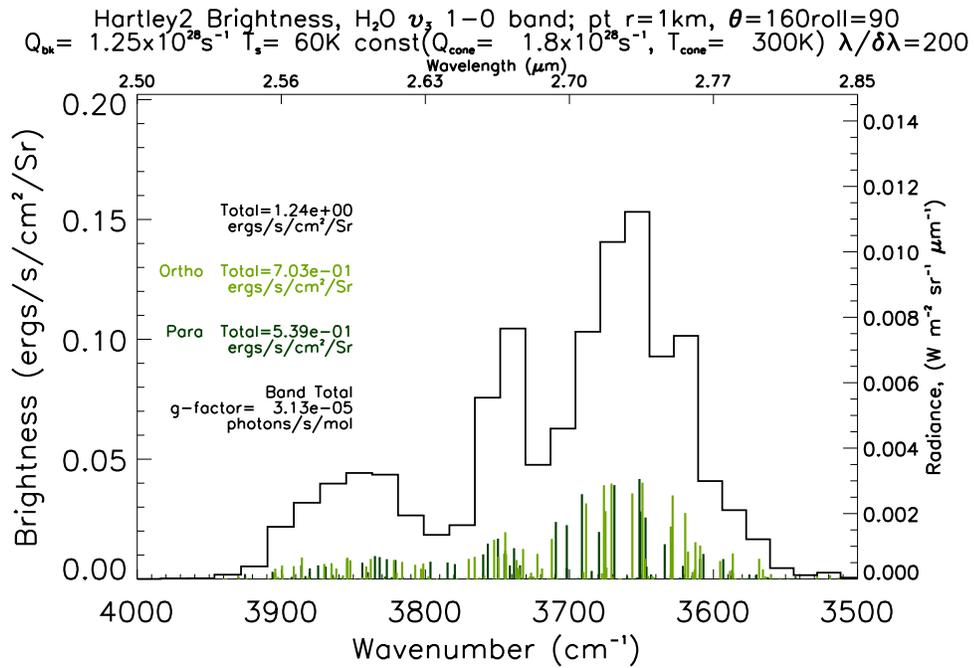
(b) "Waist cone" (on H_2O gas feature)

Figure 4.18: Best-fit Model Hartley 2 H_2O spectra ("Model X" in Table 4.7) along lines of sight at 1 km distance from the center of the nucleus, corresponding to those in Fig. 4.12.
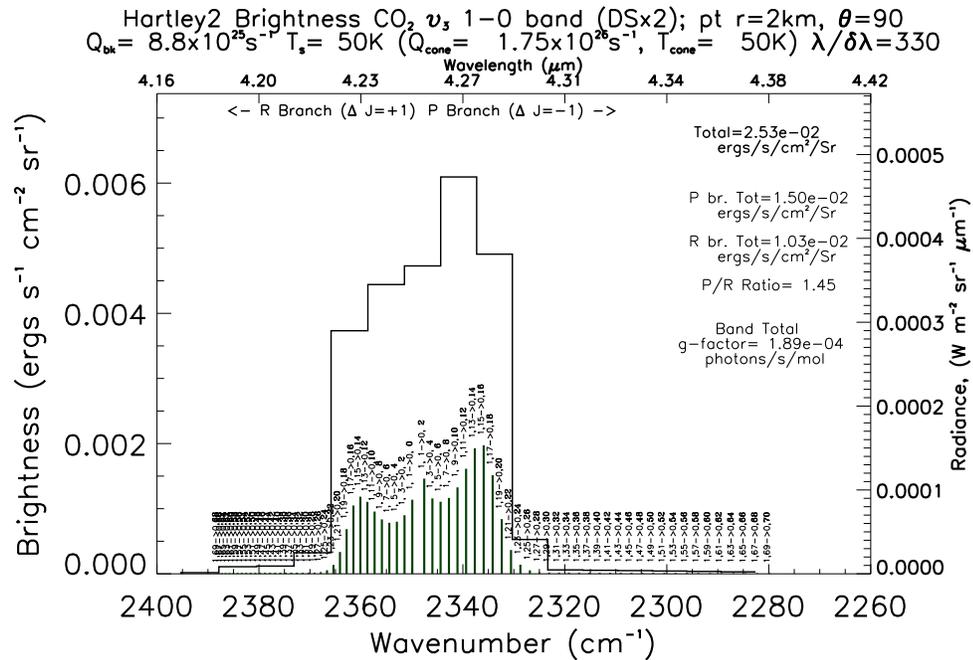
(a) Sunward (on CO_2/ice feature)
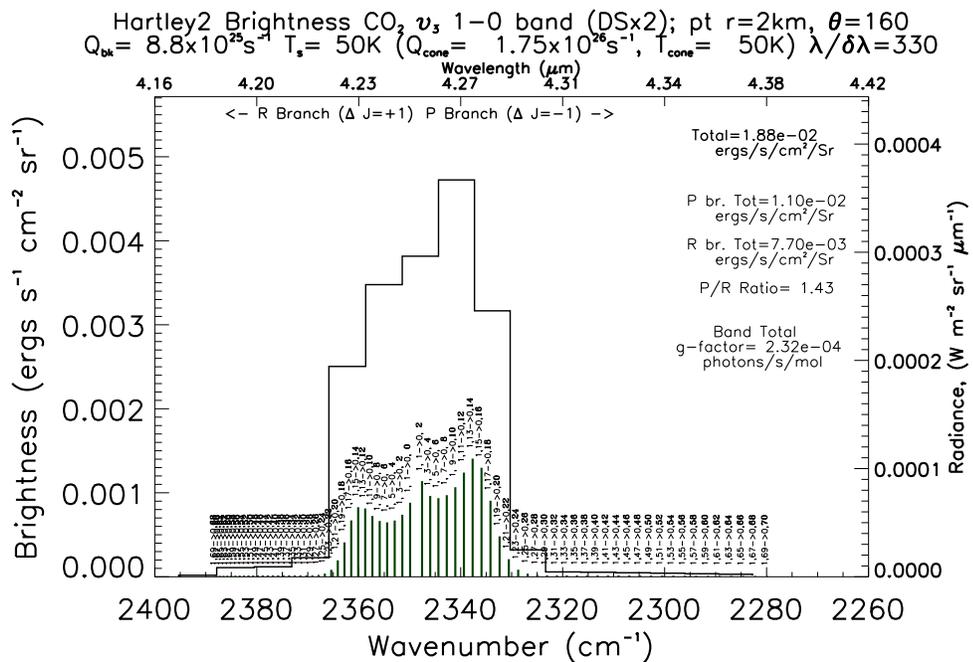
(b) "Waist cone" (on H_2O gas feature)

Figure 4.19: Model Hartley 2 CO_2 spectra along lines of sight at 2 km distance from the center of the nucleus, corresponding to those in Fig. 4.12.
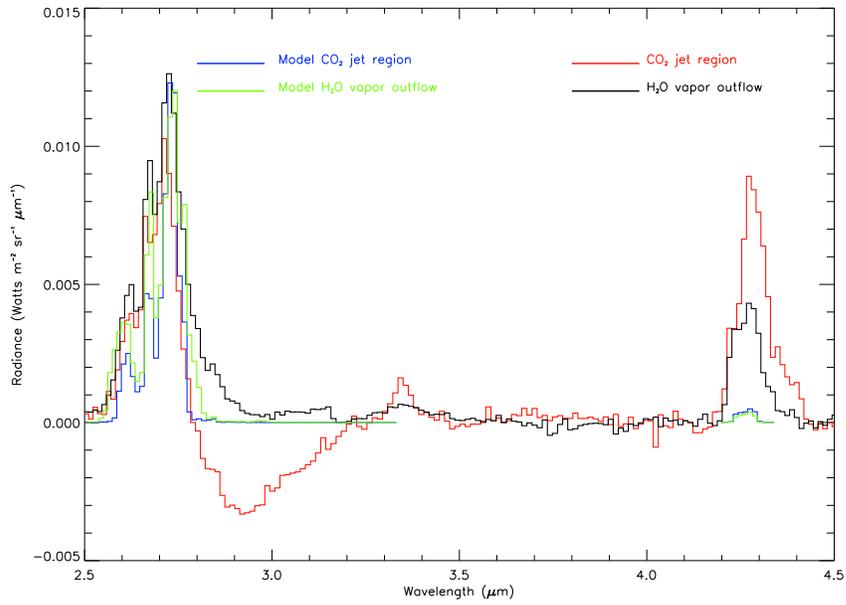
(a) Hartley 2 Model plotted over EPOXI data.
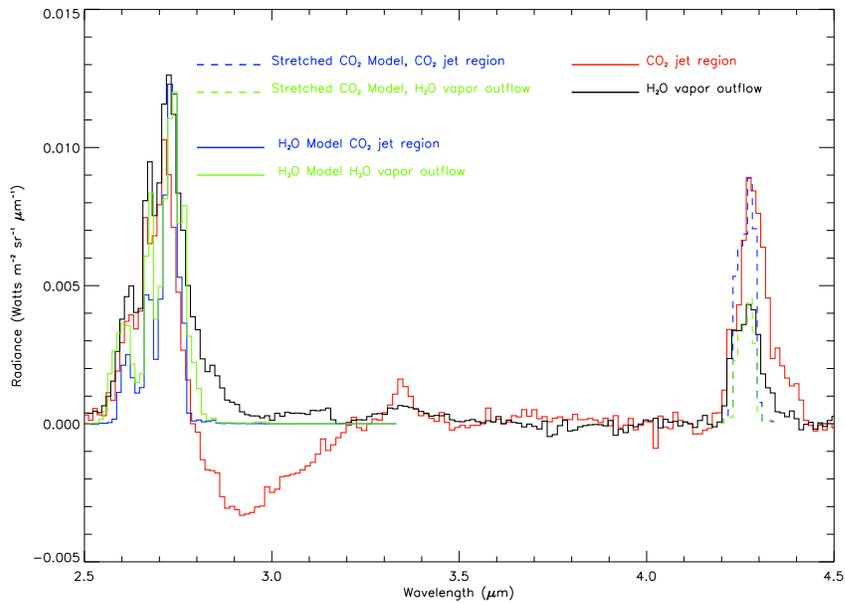
(b) Scaled Hartley 2 Model plotted over EPOXI data.

Figure 4.20: (a) Hartley 2 model spectra overplotted on recalibrated Hartley 2 near nucleus spectra shown in Fig. 4.16. The H_2O model spectra are the best-fit "Model X" in Table 4.7. Spectra span from 2.5 - 4.5 μm and include the H_2O and CO_2 ν_3 bands. The continuum has been removed.
(b) The same but with the CO_2 model values scaled to (approximately) the same magnitude as the data.

170

more accurate modeling of expansion velocities might also reduce the optical depths involved to a computationally manageable level.

4.3 Analysis

Among our four models of near-nucleus spectra, two molecules for each of two comets (CO was not modeled due to poor S/N ratio in Tempel 1 and it was undetected by EPOXI in Hartley 2), the degree of ease and the success of fitting the data with the models vary widely. The easiest to fit were the water spectra of Tempel 1. We arrived at a successful fit quite quickly, almost just by using our first optically thin estimates of production rates. On the other extreme, the Hartley 2 CO_2 has proven the hardest to successfully fit; we still have only poor results for this case. The "in between" cases, the Hartley 2 water spectra and the Tempel 1 carbon dioxide spectra, both ultimately arrived at fairly successful best-fit model parameters after a long process of fitting. Each of these cases indicates something about optical depth effects in general as well as its own specific case.

4.3.1 Water

The H_2O model production rates for Tempel 1 are quite close to the optically thin estimated values based on band total radiances. Note that individual lines within the band may still be optically thick, even if the band as a whole is not.

However, for Hartley 2, the model production rates that produce the best fit to the data are considerably greater than an optically thin estimate. Our model indicates that the ν_3 water band in the Hartley 2 near-nucleus spectra is optically thick, considerably more so than Tempel 1. However, the different cometocentric distances at which the spectra were observed may account for a significant factor in

the degree of thickness. Using a simple Haser model, even for comets with identical production rates (and expansion velocities), the difference in column densities, and hence optical depths, between a line of sight at 7 km versus one at 1 km is clearly a factor of seven. A difference of such size could easily account for one spectrum being optically thin and another optically thick.

Some skepticism is nevertheless in order. Despite the fairly close fit for the spectra at ∼1 km from the nucleus, the same model produces spectra that are *too* bright to match the 120 km or 600 km box aperture spectra in the SOM. In fact, the model production rates for the Hartley 2 near-nucleus water spectra are roughly the same as, or even slightly greater than, those that would be calculated from the 600 km aperture observations with the assumption of optical thinness, even though the model spectra are somewhat optically thick in the 600 km aperture. This seems problematic, since, as mentioned above (see Section 4.2.3) it is very likely that extended sources of emission account for a significant fraction of the total water emission in the larger aperture spectra. Yet even without including such extended sources (which, at present, is beyond the capabilities of the model) the model has produced spectra too bright for the observations. This hints that the model has perhaps neglected some crucial factor that would reduce optical depths considerably and thus over-estimated the optical depth effects and production rates.

One likely possibility is that a more realistic treatment of expansion velocity may be necessary. While we have varied expansion velocity as a model parameter, it remains a constant velocity throughout the coma for any given input value. The simple Haser model using a constant expansion velocity may very well be a poor approximation very near to the nucleus. We should also note that the velocities used in our models (as well as most others) are practically just "ballpark" guesses. Yet when using the Haser model these values are entirely crucial to determining Q's from

column densities or band brightnesses; e.g. a factor of two difference in expansion velocity yields a factor of two difference in production rate. Furthermore, most models of coma expansion agree that there is a (possibly brief) period in which the gas in fact accelerates near the nucleus before reaching a constant velocity. Acceleration of the gas leaving the nucleus could create a significant differential doppler velocity for near-nucleus spectra that would significantly reduce overall optical depths along an observer's near-nucleus line of sight. This would be less significant farther away from the nucleus.

Note that some recent models, (see, e.g. Fougere et al. 2013; Tenishev et al. 2008) have abandoned the simple Haser model and calculate a more detailed model of the acceleration and velocities of the coma. In fact, Fougere et al. (2013), has modeled the same observations of Hartley 2 as we have and with somewhat better fitting results for CO_2 (and more "sensible" Q's for H_2O, although our best-fit band shape looks closer to the data than theirs, or at least as close).

We have made some preliminary initial steps to explore the effects of adding an "acceleration zone" around the nucleus, but have not yet arrived at definitive results to determine how significant it might be. This is a feature to be fully implemented in the model in future work.

Another possible reason for the over-estimation of optical depths may be that we have used a very simple and restricted model of molecular levels for water, a particularly complicated molecule in this respect. Our band shapes for these spectra tend to be narrower than the data, even for higher temperatures, and it stands to reason that more lines should be more excited. This would reduce the band total optical depths produced by the model. In reality, the ν_3 water band cannot be treated entirely separately from other bands that may have transitions leading into it. Also a limit of $J_{max} = 7$ may be too low. This is probably especially true

very near the nucleus, where higher temperatures, densities and velocities may collisionally excite levels that are generally not significant in more distant observations of comets. Furthermore, our collisional model itself is adapted from a considerably simpler molecule (CO) and may contribute significantly to inaccuracy in collisionally dominated regimes.

4.3.2 Carbon dioxide

Carbon dioxide remains the most difficult of the three molecules that we have implemented to successfully model. It has been, historically, the least studied of the three and also the hardest for which to find either earlier models (especially any that include optical depth) or available observations for comparing with a model.

In particular for Hartley 2, but also to some extent for Tempel 1, in particular for the negative pole cone, it seems that our models' optical depths are so high that we have not produced good fitting spectra.

As discussed for water, a very likely culprit is the use of a simple constant velocity Haser model in the region close to the nucleus. As mentioned, Fougere et al. (2013), modeled the same Hartley 2 CO_2 spectra with a more detailed velocity treatment and with somewhat better fitting results than ours. Even so, for the "background" spectra their results are still not a very good fit in band shape, illustrating further the difficulty of CO_2 modeling.

4.4 Conclusions

We see that our model works well in some situations and less well in others. Unfortunately, some of the cases for which the model was specifically intended fall into the latter category, namely spectra that are well resolved in the very near nucleus regions of comae. Improvements planned for the near future, such as further exploration with our models of acceleration near the nucleus, should address some of the cases in which we have seen poor matching between model and data. Also possible is that we have not sufficiently fully explored the range of model input parameters to achieve a "best fit".

It should also be noted that we are attempting to model "moving targets", both literally and figuratively. In particular for Garradd, but also to a lesser extent with Tempel 1 and Hartley 2, the adjustments, corrections and recalibration of the data have been going on simultaneously as we have been attempting to model that data.

Other longer term future improvements could also help to address some of the deficiencies in our model due to our many simplifying assumptions regarding the coma gas expansion, temperature, density and morphology.

Along with the development of the model algorithms and code, we have also come to understand how better to approach the handling of some of the inputs to models. The gas density is perhaps the most important parameter in optical depth effects, and it can be determined by a combination of production rates, expansion velocity and morphology, among other factors. Temperature is also a crucial factor and can have an extreme effect on spectra. A better temperature profile/model, or a correct choice of temperature for such a model, can make all the difference in the appearance of molecular spectral bands.

One useful modeling lesson we have learned is that attempting to use production

rates derived at greater distances from the nucleus as model inputs to model the near nucleus coma is ineffective. In the case of Hartley 2, emission from an extended source dominates the total production rate (for water). Therefore production rates derived from large apertures proved totally inappropriate as the input Q for the model to be able to reproduce the spectra observed 1 km away from the nucleus. This could be a relatively common occurrence in comets, in which case, modeling must be done with care to account for it somehow.

For Tempel 1, this was not so much of a problem overall, since the "global" production rates were calculated from the mean of lines of sight only 20 km from the center. Those values are quite closely in the same range as the ones in Table 4.2 (although at the 20 km distance the azimuthal averaging favors sunward and anti-sunward due to the rectangular shape of the observations). However, even so, choosing production rates for specific cone/background model inputs based on the global values could result in poorly fitting models.

Chapter 5

Epilogue

5.1 Overview

In this research project I have attempted the very difficult task of modeling the spectra of comets' comae, with an emphasis on radiative transfer and optical depth effects. To accomplish this I developed an adaptation of the Coupled Escape Probability method of radiative transfer for asymmetrical spherical situations which is ideally suited to cometary comae.

This focus was motivated by the unprecedented very-near-nucleus infrared spectra acquired by the Deep Impact and EPOXI missions to comets 9P/Tempel 1 and 103P/Hartley 2, respectively, and I have used this method to model those observations. We have also applied our model to comet Garradd, which was also recently observed by the Deep Impact Flyby spacecraft.

5.2 Summary

Using my own asymmetrical spherical adaptation of the Coupled Escape Probability method of radiative transfer, I have implemented a model for three primary volatiles, CO, H_2O and CO_2 that could deal with multiple aspects of radiative transfer and optical depth effects involved in comets. This includes optical depth effects on both the incident solar radiation pumping the coma's fluorescence and on the emergent flux from the coma seen by the observer. Furthermore, the CEP method includes the effects of radiative transfer from one region of the gas to another occurring "in between" the incidence and emergence of radiation.

We have seen and shown that *all* aspects of radiative transfer can play a role in different ways in different cases. None should be ignored or neglected. Neglecting any of them on an a priori basis, as some approximate methods do, is likely to lead

178

to inaccuracy in some cases that will arise, especially in the optically thick regions near comets' nuclei.

5.3 Main Results

5.3.1 Modeling of Theoretical Comets

We have produced models of theoretical comets to explore the effects of varying optical depths on infrared spectra of primary volatiles CO, H_2O and CO_2.

For each of the three primary volatiles studied, we modeled varying production rates and showed the effects of optical depth on band shape for a range of simulated apertures. We also explored how radial profiles of brightness and g-factor vary for these cases, and at what radial distance optical depth effects are or are not significant.

For CO, only for production rates of $\sim 10^{28}$ or greater were the effects of optical depth significant (using our "90% of optically thin" benchmark) at radial distances greater than O(10) km, and for such high Q_{CO} the effects may be significant out to several hundred to $\lesssim O(10^3)$ km.

Similarly, water also shows the effects of optical depth for production rates of $\sim 10^{28}$ or greater out to several hundred km but little effect for lower production rates at distances any greater than O(10) km.

However, for CO_2 only for production rates of $\sim 10^{26}$ are optical depth effects *not* significant at less than 500-1000 km; for higher production rates the effects are quite significant.

Needless to say, for all three molecules, at radial distances on the order of the DI observations of Tempel 1 and Hartley 2, i.e. <O(10) km, the effects of optical depth can be significant for all these production rates.

Modeled Optical Depths: Representative Values

We present here (Table 5.1) some representative values of optical depths from our theoretical models. These values represent the total of the maximum $d\tau$ in each Region along a radial line of sight from the nucleus to the sunward edge of the coma. (Note that the maxima in all Regions do not necessarily occur in the same wavenumber, even within a single case.) Thus these values are an upper bound on optical depth for each case.

Representative Values of Radial Optical Depths

Model	# Shells	# Regions	Max	Max$_{\parallel}$	Mean	Mean$_{\parallel}$
CO, Q=10^{26}	19	379	0.16	0.37	0.02	0.06
CO, Q=10^{27}	19	379	1.71	3.96	0.24	0.59
CO, Q=10^{28}	19	379	17.08	39.33	2.28	5.58
CO_2, Q=10^{26}	15	239	1.57	3.51		
CO_2, Q=10^{27}	15	239	16.20	35.93		
CO_2, Q=10^{28}	15	239	154.25	338.39		
ortho H_2O, Q=10^{26}	16	271	0.19	0.42		
ortho H_2O, Q=10^{27}	16	271	1.40	3.04		
ortho H_2O, Q=10^{28}	16	271	11.40	24.61		
para H_2O, Q=10^{26}	16	271	0.08	0.17		
para H_2O, Q=10^{27}	16	271	0.61	1.29		
para H_2O, Q=10^{28}	16	271	4.66	9.89		

Table 5.1: Modeled upper bound optical depth values along the direct radial sun-to-nucleus line of sight and an "almost diameter" parallel to that line of sight one Region removed from the center (i.e. off-nucleus). Maximum (and for CO mean) values for the whole line of sight . Maximum value is the sum of Regions' maximal $d\tau$ values along the line of sight, even though they are not all for the same wavenumber. The number of shells and Regions used in the models is also shown for each case. (Note that for a case with no cone morphology, the number of Regions is (N^2+N-1) where N is the number of shells, including a shell of 0 radius.)

We also present a "tangential" value: a parallel line of sight through the column

of Regions adjacent to the nucleus. This line of sight is *almost* equal in length to the diameter of the coma and is an effective "proxy" for the diameter. For CO, we have also calculated the total for those Regions of the mean values across all wavenumbers for the same two lines of sight .

5.3.2 Modeling of Actual DI Observations

With respect to actual comets, the model has proven fairly successful. It has successfully modeled all three relevant species in observations of comet Garradd and provided useful understanding and constraints on the interpretation of the Garradd spectra. Our model gives credence to the highly enriched CO to H_2O ratio ($\sim$60%) of production rates at 2 AU post-perihelion of Feaga et al. (2014) while aiding in the placement of those values in a consistent context with other observations (as per Feaga et al. 2014).

For Tempel 1, the original target of this study, the model has been partially successful, effectively modeling the water spectra observed by Deep Impact, and having mixed success with CO_2, a molecule that is both difficult to observe and difficult to model, being only observable from space. We have confirmed that optical depth effects do play some role in the observed spectra, especially for CO_2.

Hartley 2, a hyper-active comet whose activity seems to be driven mostly by CO_2, has consequently proven even more difficult to model, in large part due to the high optical depths involved. We have nevertheless managed to make some semi-successful models for the EPOXI spectra. The model has fit the EPOXI H_2O spectra fairly well. I plan to continue to work on improving these models.

5.3.3 General Insights from the Modeling

Based on our work modeling these comets, we may draw some generally useful insights. The much greater difficulty involved in modeling and interpreting cometary spectra from the very-near-nucleus regions of the coma than much larger apertures points to several problematic issues that have generally been glossed over with approximations in the past.

Obviously, the most significant factor that makes modeling of the near-nucleus regions different from "larger aperture" models is the importance of the complex morphology. As we have seen, in particular for the carbon dioxide in Tempel 1, a simple morphology (i.e. our "one cone" model) was insufficient to model all the various lines of sight around the nucleus accurately. We were forced to use results for at least one spectrum (the positive pole) as the best fit for that line of sight which did not agree with the best fit model for the spectra of the other lines of sight.

A more nuanced approach to expansion velocity must be a major factor in understanding such spectra. Most calculations of production rates use a Haser model based on a constant velocity, often one that is assumed to be a "typical value". This has often been a matter of necessity, since precise measurements of V_{exp} are not usually available. However, in the near-nucleus regions it is a poor approximation and can lead to significant errors. The direct proportion of production rate to expansion velocity used in a Haser model, for a given column density, will obviously cause an error in production rate of the same factor as any error in velocity. Furthermore, the fact that the gas is accelerating simply indicates that production rates calculated at different radial distances assuming a Haser model will produce different production rates, *at least* one of which will be inaccurate.

In addition to that, the use of a constant velocity in a radiative transfer model will lead to overly optically thick spectra. Notwithstanding the complex morphology itself, our results show that differences in velocity along a line of sight are strongly implied, for both the emergent and incident solar radiation. Without such velocity differences the emission could not escape the coma to produce the brightness values in the spectra observed. In the near-nucleus regions of both Tempel 1 and Hartley 2 the volatiles observed in different morphological features and/or radial distances must be moving with different velocities relative to each other. Since this is true along radial lines of sight, there must also be acceleration involved. Similarly, without velocity differences reducing optical depths, the innermost regions of the coma would not experience sufficient excitation by incident solar radiation to produce the spectra observed and modeled.

Different temperatures as well as velocities are needed to model each of the volatiles with their respective different morphological features around the nuclei of both Tempel 1 and Hartley 2. This points to the activity and release mechanisms being driven by different processes in different features, even for a given molecule or a given comet.

With respect to optical depth effects, in both comets, Tempel 1 and Hartley 2, CO_2 is thicker than H_2O, even though water is more abundant. This is simply due to the Einstein coefficients and the molecular structure of the molecules.

5.4   Future Work

We have attempted the daunting overarching goal of accounting for all the possible optical depth effects in a coma, without ignoring any, or using approximate methods of radiative transfer.

This work has shown that such a method is possible. However, practical limitations due to realistically available computing power have forced the use of many approximations in the implementation and limited the degree of granularity in our coma model. This is, of course, a problem that may solve itself with the passage time alone: advances in computing power will likely be readily available, although adapting to parallel architectures may be needed to take fullest advantage of that computing power. However, a more appealingly pro-active approach can also improve the model's accuracy with improvements to the algorithms developed and used in this work.

Several known and important aspects of the model also require improvement, such as the need for a more thorough treatment of doppler shifts.

Many other factors affect coma spectra besides radiative transfer. In as much as optical depth effects were our primary focus, we have necessarily simplified many other important aspects including temperature, velocity and density profiles, nucleus shape models and morphology. Other future improvements should include using more realistic shape and morphology models; not everything is a simple cone! More complicated and realistic velocity, temperature and density profiles should also ideally be used. There are also other processes at play in the coma, such as extended sources, electron collisions and more. These may have a significant effect in some cases as well. Perhaps in the future our radiative focused model can be combined with more accurate models that focus on coma gas properties.

Last, but not least, the addition of more molecules and more bands of these molecules to the model would greatly increase its utility, and probably its accuracy as well.

We also hope that with further improvements our model can be adapted to other astronomical phenomena of interest, in particular exoplanets and circumstellar disks.

5.5　Concluding Remarks

The future of cometary spectroscopy is bright, but it may also be optically thick. Opportunities and the need for modeling such as we have done in this research will abound.

Unfortunately, the Deep Impact Flyby spacecraft is no longer operating and the unique opportunity that it provided (in particular for CO_2) to observe some very important and unusually active comets is now lost.

The Rosetta Mission will be arriving at its target, comet 67P/Churyumov-Gerasimenko, next year. When it does, many more near-nucleus spectra will be forthcoming, which will require optical depth modeling for accurate interpretations.

Not many years farther on, there will be other IR space observatories, such as JWST, which will be able to observe IR spectra similar to these, both of comets and other targets, such as exoplanet atmospheres, for example. Those observations will also need modeling.

All these future endeavors will provide spectra like the ones we've modeled here, and more! The need for accurate modeling, especially of near nucleus spectra, or of highly active and optically thick comae will certainly be growing in the future.

Appendix A

A.1 The Coma Integration Technique and Software

This section of this appendix describes the "gory details" of computer functions and code modules. The C and C++ programs described in this section are sufficient to reproduce Chin and Weaver (1984) work. Other "modules" of the software are discussed in more detail below.

The linear equations defining the coma integration (Eq. (2.1) and (2.6)) are solved for n_J^v with LU decomposition with back substitution, using the **ludcmp** and **lubksb** routines from Press et al. (1992).

The numerical integration of Eq. (2.1) is done using methods from Press et al. (1992) which are able to solve "stiff" systems of equations (where the orders of magnitude of coefficients differ greatly, as is the case here where rate constants even for the ambient coma conditions range from $\sim 10^2 s^{-1}$ to $\sim 10^{-8} s^{-1}$.) We use their function **stifbs**, and associated other functions (**odeint, simpr, pzextr**) which implement an algorithm using a semi-implicit discretization discovered by Bader and Deuflhard (1983), similar to the Stoer and Bulirsch (1983) method (which does not work well for stiff problems.) Press et al. (1992) claim that this method

is at least as effective (if not more so, depending on the size of the problem) as the Gear method used by Chin and Weaver (1984). These are all used in conjunction with our own C/C++ code, **Integrator.cpp** (and other smaller modules of code), which include functions to calculate the A, B and C coefficients, the density and temperature (as a function of radial distance and surface temperature), gas velocity and other required functions.

The values of the integration, all the n_J^v's of Eq. (2.1) for each step of the integration passing an integral number of seconds, are saved in an output file.

Our integration module (a C++ class), **Integrator**, produces a coma output file each time it is run. We can and do produce many of these files, each with different initial integration conditions (varying T_{init}, Q and V_{gas}).

A.2 CEP Algorithm Implementation & Technical Details

We have coded the CEP algorithm described in Chapter 2 in the C++ language, using numerous functions from Press et al. (1992) primarily to implement numerical integration of functions (with **odeint** and **stifbs** and associated functions) and solution of N-dimensional non-linear matrices with Newton's Method (using **newt**, etc.). The bulk of the coding, which implements the radiative transfer algorithm in spherical geometry is our own.

A major practical limitation of our algorithm is the matrix size; since Newton's method requires (repeated) $O(N^3)$ matrix solving operations (which for which **newt** uses the brute force **ludcmp** and **lubksb**), the algorithm can get prohibitively slow for large matrices. For example, on an Intel Core2 Quad computer (with CPU speed of 2.4GHz) running Scientific LINUX 6.2 (Carbon), when N $\gtrsim$ 10,000-15,000,

a solution may take one or more days. For greater sizes, even a week. The matrix size equals the number of molecular levels used times the number of regions. The molecule (and band/s) being modeled determines the first value, with the latter value demanding to be increased with greater optical depths and production rates. Depending on the species of interest, the maximum practical production rates we can currently manage are of $O(10^{28})$. One simple workaround is to use a more powerful computer. To make more effective use of modern multi-core architectures, development of parallel algorithms would be quite beneficial. Algorithms for solving sparse matrices faster than the above functions can also be used, and we have begun to explore these options.

Among others, we have created C++ classes for diatomic and triatomic molecules. The object oriented programming style of C++ lends itself ideally to being able to switch molecules easily. The diatomic molecule classes (currently implemented for CO and SiO) calculate energies and Einstein coefficients based on constants (taken primarily from Krupenie, 1966, for CO) that are included in the code. The triatomic class, which can actually be used for other polyatomic molecules as well (or the aforementioned diatomic molecules themselves, for that matter), must be provided with energies and coefficients from some outside source in formatted input files. We used the HITRAN database (see Rothman et al. 1998) to supply these values for CO_2 and H_2O. This approach has the versatility to handle many other molecules with a minimal effort of "data massaging" to get the data into the proper format.

Although designed specifically with comets in mind, our code is versatile enough to be used in other spherical radiative transfer problems as well. Input files describe all the required and optional parameters for a specific comet model or other problem, including molecule of interest, size of nucleus and radial shells, production rate,

morphology (if any), incident radiation, etc.

The C++ code outputs a file containing a point-by-point line-by-line spectral mapping, as described above, for one or more specified viewing orientations. This data can then be presented in multiple formats as described above. We have implemented this data presentation portion of the model using IDL code which we have developed specifically for the purpose.

Appendix B

B.1 Background & Operation

B.1.1 Background: Development

To better explain the code, I will provide a bit of background.

This research began as my second year project. Then it involved only CO and only integration of the coma without any optical depth or radiative transfer calculations at all. All the code was written in C, and used several functions from the edition of Press et al. (1992) that was available at that time.

Not long thereafter, the project was expanded to include a strong focus on radiative transfer. As the project grew in scope, more molecules were added and it was decided to use the spherical geometry instead of plane parallel. These led to a natural switch in coding to use C++ for the greater modularity offered by object oriented programming (e.g. to build code that was configurable to "swap" in different molecules.)

Since then, the code was developed in C++, and now, the majority of the code is mostly in C++. However, some older C functions still remain in use. Press et al. (1992) functions are still used (as opposed to the more recent C++ based edition) but many have been incorporated into C++ classes of our own, as described below.

The output from the C/C++ code, each time it is run, is essentially one or more (if multiple maps are produced) very large text files of numbers. Then visually comprehensible outputs are produced from the text files using various IDL programs, most of which essentially create spectra using various forms of the IDL **plot** function or brightness maps using the **contour** function.

B.1.2   Running the Code

The most up-to-date version(s) of the code simply runs with one command line parameter: the name of an input/comet definition file. For example:

./comet ExampleComet.CO2.Q28.txt

or

./comet Tempel1.CO2.cone.txt

Depending on the parameters provided in such a file, a user can run either the Integrator alone, or CEP alone (using files containing previously integrated results) or both parts of the process.

Running the code from start to finish will produce an integration file (or two, if using a cone as well) a saved populations file (which stores the populations of all Regions after the CEP calculations), and a point-by-point spectral map output file. Likewise, running only part of the process will produce one or more of these files. Several non-essential informational files (logs of sorts) are also produced along the way. It is also possible to rerun the output mapping based on previous results (with or without CEP actually having been run, using a stored populations file.)

Plotting the Output

The main IDL programs that read integration files and produce plots from their output data are listed and described in brief below. These produce most of the graphical results in this work. Note that there are two forms of each program, one for water and one for the other molecules, due to the essential difference of needing to combine both ortho and para water data into one output at this point in the process.

boxAperture.idl / boxApertureH2O.idl : Produces an aperture averaged spectrum over a nucleus-centered rectangular aperture.

ptSpectra.idl / ptSpectraH2O.idl : Produces a spectrum at a specific point (i.e. from a single line of sight).

fluxMapPlot.idl / h2oFluxMapPlot.idl : Produces a band-integrated brightness map for a specified field of view.

fluxVsR.idl / H2OfluxVsR.idl : Produce radial profiles of band-integrated brightness and g-factor over a range of cometocentric distance (usually from the nucleus to the edge of the coma).

branchRatio.idl and **prRatio.idl** were used to produce the plots examining the P/R ratio for CO.

B.1.3 Comet Definition Files

The structure of these "Comet Definition" text files is a list of simple key-value pairs, separated by spaces and with an equal sign between the key and the value, one per line. (However, a "single" parameter value *can be* an array of multiple values, separated by commas.) The order of parameters in the files is mostly irrelevant, *unless* a parameter is repeated, in which case the latter value "wins".

Comments can be inserted in the files using a "#" as the "comment character", either at the begining of a line or after the values (thus "commenting out" the rest of the text on the line).

The following is a list of parameters (in boldfaced font), divided into required and optional categories: (In this description, *not in the actual files* each key is followed by a colon, and a description. Explanatory remarks have been interspersed below in italics. Examples follow below.)

Required Parameters

Note that "Required" in this context does not mean 100% of cases will need *all* of these parameters. Some are required only for given molecules, etc., but are required to run and not fail catastrophically *in those cases.* Also, many have default values, that fulfil the "requirement".

CometName: A single word name, e.g. "Hypothetical" or "Tempel1"

CometSuffix: An abbreviation that is appended to many files created in the process, e.g. "CO2.Q28" or "T1.orthoH2O.cone"

Radius: of the comet nucleus, in cm

Molecule: Your choice of "CO", "CO2", "H2O" or "SiO"

The following 2 parameters are filename required only for "Triatomic" molecules - i.e. any but CO or SiO - they provide the energy levels and transition data which has been taken from Rothman et al. (1998) and "massaged" into the form required by the code.

LvlsFile: e.g. "J70.lvls.CO2.wEnergy.txt"

LinesFile: e.g. "J70.linesCO2.txt"

Integrate: "true" or "false", i.e. yes/no whether to do a (new) coma integration from scratch. (The CEP algorithm can be run on the results of a previously saved

integration.)

IntegrationOutfile: A base name (to which the suffix above is appended) of output file to store integration results; only relevant if above "integrate" = true

IntegrationFile: Name of integration results file (from a previous run) to be read in for CEP calculation. (If NOT integrating from scratch, as above.)

Tsurf: Temperature of gas at surface of comet, in degrees K, of course

Q: Production rate of the species being modeled, in molecules/s of GIVEN species; total AS IF produced uniformly over whole nucleus surface

Q_H2O: Production rate of the dominant collisional species (or sum of more than one), in molecules/s; total AS IF produced uniformly over whole nucleus surface. Usually just the sum of ortho and para water Qs.

V: Gas expansion velocity, in cm/s

CEP: "true" or "false"; whether or not to do a CEP calculation

Radii: Array of shell/cylinder/Region boundary radii, in cm. The first value must be 0, the second, the radius of the nucleus, and the last the maximum extent of the coma. e.g. "0.0, 3.0e5, 5.2e5, 9.0e5, 12e5, 16e5, 22e5, 33e5, 52e5, 100e5, 500e5, 2000e5, 100000e5"

Typically, for a spherically symmetric coma, with no cone, the size of the array of radii is between 15-18. For cases including a cone, 10-12 is typical. These sizes are determined mostly by computational complexity and the memory and speed of the computer being used.

AddingDivisions: "true" or "false"; whether or NOT to auto-divide shells further, safer to set to false

These two parameters are for determining the density of points in output flux maps.

DeltaR: Number of radial points between shell boundaries (as per radii above); typically 20; default is 10.0, if none provided

DeltaTheta: Number of points into which a circle is divided at each radial distance (as per radii above); typically 36; default is 18.0, if none provided

The following four parameters determine the number and the viewing angle(s) of flux out brightness map. The default viewing angle is from the +x axis direction, as in Fig. 2.17. Angles are in radians. The angles can be arrays, with the "NumMaps" telling how many elements the arrays contain (they must match in number.)

NumMaps: A whole number

Theta: If used alone, rotates around z axis; default = 0.0

Phi: If used alone, rotates around x axis (essentially, rotating the image plane around its center); default = 0.0

Psi: If used alone, rotates around y axis; equivalent to phase angle, but "0" is phase=90; default = 0.0

PlaneParallel: "false"; *Deprecated; Should definitely default to false for running Spherical CEP.*

UsePrevResults: "true" or "false"; to do or not to do a calculation; if not, use population values saved from before to produce output maps

PrevResultsPopFile: Name of saved populations file; this is only relevant if prev value is true. e.g. "pops.out.CO.Q27"

MapOutputFileDir: Directory into which output map file (which is HUGE!) will be saved; typically "/tmp"

MapOutputFileBaseName: Base name of output map file that will be saved; default is "testMapFile"

Nucleus: "true" or "false"; is there a nucleus? (Use "true"! It was just experimental.)

NucleusRegions: Array of Regions "blacked out" by the nucleus (above line) listed in form of "[0,0]", which is the default case (one central region only); example for NON-default case: "NucleusRegions = [0,0] [0,-1] [0,-2]"

Optional Parameters

These two parameters define the name and type of solar flux input file; the following are the defaults

SolarFluxFile: Use "day0144.dat" (just a file with solar radiance per wavelength that Mike A'Hearn pointed me to...)

SolarFluxFileType: "dat"

HelioDistAU: Heliocentric distance of the comet, in AU; default = 1.0

SCdistance: Spacecraft distance to center of comet; default = maximum radius in radii above

CollisionalModel: Controls which type of collisional model to use; "Goldsmith" or "ChinWeaver"; the default is "ChinWeaver"

ConstantTemp: "true" or "false"

Temp: Value of the constant T above, in degrees K

Cone parameters, if included (if "Cone" value is false, all others will be ignored.)

Cone: "true" or "false"

ConeTheta: Angle from $+z$/sunward axis of cone centerline

ConePhi: Rotation angle of cone centerline around $+z$ axis

ThetaOpen: Half-opening angle of cone

The following cone integration parameters repeat the integration parameters above for the cone if one is included.

IntegrateCone: "true" or "false"

ConeIntegrationOutfile

ConeIntergationFile

ConeTsurf

ConeQ

ConeQ_H2O

ConeV

Example Files

Below are three examples of Comet Definition Files, as actually used for several model runs; one for para-H_2O in a hypothetical comet, one for CO in comet Garradd and one for CO_2 in Tempel 1. (Note that these files have been only minimally edited for presentation and that they contain *some* irrelevant notes and/or commented out attempted values.)

ExampleComet.paraH2O.Q26.txt

This file is a sample of a "Comet Definition File" to be used with
Spherical CEP (& Integrator).
It defines/sets most of the parameters that can/must be used
when running the code.
Format: the file follows a key/value format:
key/param name = *value/s*

CometName = Hypoth # NB: NO SPACES ALLOWED
CometSuffix = paraH2O.Q26 # hypothetical comet, example...

Radius = 3e5 # in cm
Molecule = H2O # your choice of CO, CO2, H2O or SiO
# these 2 files are needed for "Triatomic" molecules - i.e. any but CO or SiO
LvlsFile = ../unifiedMolecules/para.v3.lvls.wtd.energyOrder.J7
LinesFile = ../unifiedMolecules/para.v3.rotl.combind.lines.J7
# solar flux input file
SolarFluxFile = day0144.dat
SolarFluxFileType = dat
Integrate = true
IntegrationOutfile = coma
Tsurf = 200 # in degrees K, of course
Q = 0.25e26 # NB: Q for PARA should be fraction of Q_H2O (total)
Q_H2O = 1e26 # molecules/s of collision dominating species
V = 8e4 # in cm/s
IntegrationFile = coma.paraH2O.Q26 # name of integration results file to be
read in for CEP calc. (if NOT integrating from scratch, above)
CEP = true
# Array of shell/cylinder/Region radii - in cm!!!
Radii = 0.0, 3.0e5, 5.2e5, 9.0e5, 12e5, 16e5, 22e5, 33e5, 52e5, 100e5,
500e5, 1000e5, 2000e5, 3000e5, 5000e5, 18000e5, 100000e5
# viewing angle(s) of flux out brightness map
# run the gamut of phase angles:
NumMaps = 5
Theta = 0.0, 0.0, 0.0, 0.0, 0.0
Phi = 0.0, 0.0, 0.0, 0.0, 0.0
Psi = 0.0, -1.5708, 1.5708, -0.785, 0.785
PlaneParallel = false
UsePrevResults = false # DO a CEP/RT calculation "from scratch"
MapOutputFileDir = /tmp
MapOutputFileBaseName = testMapFile
Nucleus = true
NucleusRegions = [0,0]
# Cone params, if included
Cone = false

Garradd.CO.nocone.txt
CometName = Garradd # NB: NO SPACES ALLOWED
CometSuffix = CO.Garradd.T40K.newest
Radius = 3e5 # in cm
Molecule = CO # your choice of CO, CO2, H2O or SiO
# solar flux input file
SolarFluxFile = day0144.dat
SolarFluxFileType = dat
HelioDistAU = 2.0
Integrate = true # yes/no to do a (new) coma integration from scratch
IntegrationOutfile = coma # name of output file to store integration
IntegrationFile = coma.CO.Garradd.nu # integration results (if NOT integrating)
Tsurf = 100 # in degrees K, of course
# ... and then reduced by 5% to try and get better fit 09/17/13
Q = 3.04e28 # molecules/s; total AS IF produced uniformly over whole nucleus surface
# ... and then CORRECTED!! 9/17/13
$Q_H2O = 4.6e28 \# molecules/s of H2O$
V = 5e4 # in cm/s
Temp = 40
ConstantTemp = true
CEP = true
# Array of shell/cylinder/Region radii
Radii = 0.0, 3.0e5, 5.2e5, 9.0e5, 12e5, 16e5, 22e5, 33e5, 52e5, 100e5, 300e5,
500e5, 1000e5, 3000e5, 10000e5, 15000e5, 100000e5
# to NOT auto-divide shells further, set to false
AddingDivisions = false
# for determining density of points in output maps
DeltaR = 20.0 # default is 10.0, if none provided
DeltaTheta = 36.0 # default is 18.0, if none provided
# viewing angle(s) of flux out brightness map
NumMaps = 1
Theta = 0.0
Phi = 0.0
Psi = 0.0
PlaneParallel = false
UsePrevResults = false # DO a CEP/RT calculation "from scratch"
MapOutputFileDir = /tmp
MapOutputFileBaseName = testMapFile
Nucleus = true
NucleusRegions = [0,0]
# Cone params, if included
Cone = false

Tempel1.CO2.cone.tilt3.txt
This file is a sample of a "Comet Definition File" to be used with
Format: the file follows a key/value format:
key/param name = $value/s$
The default is one value. If multiple values are allowed for a given param,
use blanks to separate values
# Lines begining with a "#" character (such as these) or blank lines are ignored.
# Any portion of a line following a "#" is also ignored.
# In other words, "#" is the "comment/comment out" character.
# these are Essential Params
CometName = Tempel1 # NB: NO SPACES ALLOWED
CometSuffix = Temp1.CO2.cone.tilt3g30Ts200v.8vc1Qc8.4 # re-run "best" ?
model? w/Vb=0.8 # 10/17-18/13
Radius = 3e5 # in cm
Molecule = CO2 # your choice of CO, CO2, H2O or SiO
# these 2 files are needed for "Triatomic" molecules - i.e. any but CO or SiO
LvlsFile = ../unifiedMolecules/J70.lvls.CO2.wEnergy.txt
LinesFile = ../unifiedMolecules/J70.linesCO2.txt
# solar flux input file
SolarFluxFile = day0144.dat
SolarFluxFileType = dat
HelioDistAU = 1.5
Integrate = true # yes/no to do a (new) coma integration from scratch
IntegrationOutfile = coma.CO2
IntegrationFile = coma.CO2.Temp1.CO2.cone.tilt3
Tsurf = 200 # in degrees K, of course
# 7/31/13 & now increased that by 50%...
Q = 2.66e26 #
Q_H2O = 2e27 # 6/20/13: NOW w/Q's from 1/2 of LOS N's in article;
bkgd. from Pos. Pole
V = 8e4 # in cm/s
CollisionalModel = Goldsmith # added 6/16/13

CEP = true
# Array of shell/cylinder/Region radii
Radii = 0.0, 3.0e5, 5.2e5, 9.0e5, 12e5, 16e5, 22e5, 33e5, 52e5, 100e5, 100000e5
# to NOT auto-divide shells further, set to false
###AddingDivisions = false
# for determining density of points in output maps
DeltaR = 20.0 # default is 10.0, if none provided
DeltaTheta = 72.0 # default is 18.0, if none provided
# viewing angle(s) of flux out brightness map
NumMaps = 1
Theta = 0.0
#Phi = -1.57079632679 # 0.0 works OK, but tried cone rot by phi instead...
Phi = 0.0
Psi = 0.0
# these are some defaults for running (Spherical) CEP...
PlaneParallel = false
UsePrevResults = false # DO a CEP/RT calculation "from scratch"
MapOutputFileDir = /tmp
MapOutputFileBaseName = testMapFile
Nucleus = true
NucleusRegions = [0,0]
# Cone params, if included
Cone = true
ConeTheta = 1.91986 ### tilted antisunward 20 deg past Ecl. S.
ConePhi = 1.04716 # tilted 30 from Ec. S. toward obs.
ThetaOpen = 0.785398 # 45 degrees
IntegrateCone = true
ConeIntegrationFile = coma.cone.Temp1.CO2.cone.tilt3
ConeIntegrationOutfile = coma.cone
ConeTsurf = 200 # in degrees K, of course
# really the best-fit!!!
# 10/17-8/13 & doubled it again
ConeQ = 8.4e26 #6/20/13: w/Q's from 1/2 LOS N's in article; cone from Ecl. S.
# 10/18/13 & doubled it again - which was TOO Thick!
#ConeQ = 1.68e27 # 6/20/13: NOW w/Q's from 1/2 of LOS N's in
article - cone from Ecl. S.
10/20/13 & tried in between again - which was TOO Thick!
#ConeQ = 1.2e27 # 6/20/13: NOW w/Q's from 1/2 of LOS N's in
article - cone from Ecl. S.
6/24/13 - new values; corrected=1/2'd from published; Q_bk from Anti-S.
N value, Q_cone from Ec.S. value
ConeQ_H2O = 4.95e27
ConeV = 10e4 # in cm/s

Appendix C

C.1 Code

This appendix contains a high-level description of code, classes, functions, etc. It is not a thorough documentation, or even a listing of all functions/methods; only some of the ones more important to a high-level understanding of the implementation of the algorithms in our code.

C.1.1 "Plain old" C Functions

The following is a list of C functions used/adapted from Press et al. (1992):

nrutil.c & nrutil.h

lubksb.c & ludcmp.c

pzextr.c

snrm.c

asolve.c & atimes.c

locate.c

qtrap.c

trapzd.c

expint.c

expInt.c - An alternate exponential integral function converted from a FOR-TRAN function given to me by J. P. Harrington.

NRfuncs.h - A .h file containing a "wrapper" that is just a compiler directive needed to compile pure C functions (above) together with C++.

The following is a list of Press et al. (1992) functions that I converted to C++ methods to be included as part of my own C++ classes, primarily the Integrator or CEP Classes (see below):

fdjac.cpp

newt.cpp

odeint.cpp

simpr.cpp

stifbs.cpp

linbcg.cpp

lnsrch.cpp

fmin.cpp

These files are simple lists of constants:

UniversalConsts.h

franck-condon.h

Functions used in calculating CEP values (as per Elitzur and Asensio Ramos 2006) α, β and γ, written by me in C, are contained in these:

alphaShape.c & alphaShape.h

These are the C++ classes that implement the plane parallel CEP algorithm:

CEP

Integrator

Molecule.hpp, Diatomic, Triatomic, CO, SiO

Level

Transition

Population

Flux

Zone

In addition to those, the following are the classes that implement the Spherical CEP algorithm:

Comet

SphericalCEP

Region, SubRegion

Point

Cone.hpp

Line, IntegrationLine, FluxOutIntegrationLine

FluxOutMap

Classes listed on the same line above are related by inheritance. (So are CEP and SphericalCEP and Zone, Region and SubRegion, but they were listed separately in their plane parallel or spherical lists above.) Each of these classes has both a .cpp file and a .hpp, except where indicated otherwise by the inclusion of the suffix above.

C.1.2   C++ Class Descriptions

The following are C++ classes described in brief; a selection of the most important properties and methods are listed. (All classes obviously have more methods and properties, e.g. one or more constructors, destructors, printing/debugging functionality, etc.) Figures C.1 and C.2 show a class hierarchy, although many of the classes are unrelated by inheritance.

Figure C.3 shows a relational diagram of classes involved in the implementation of spherical CEP, which primarily shows which classes "hold" one or more instances
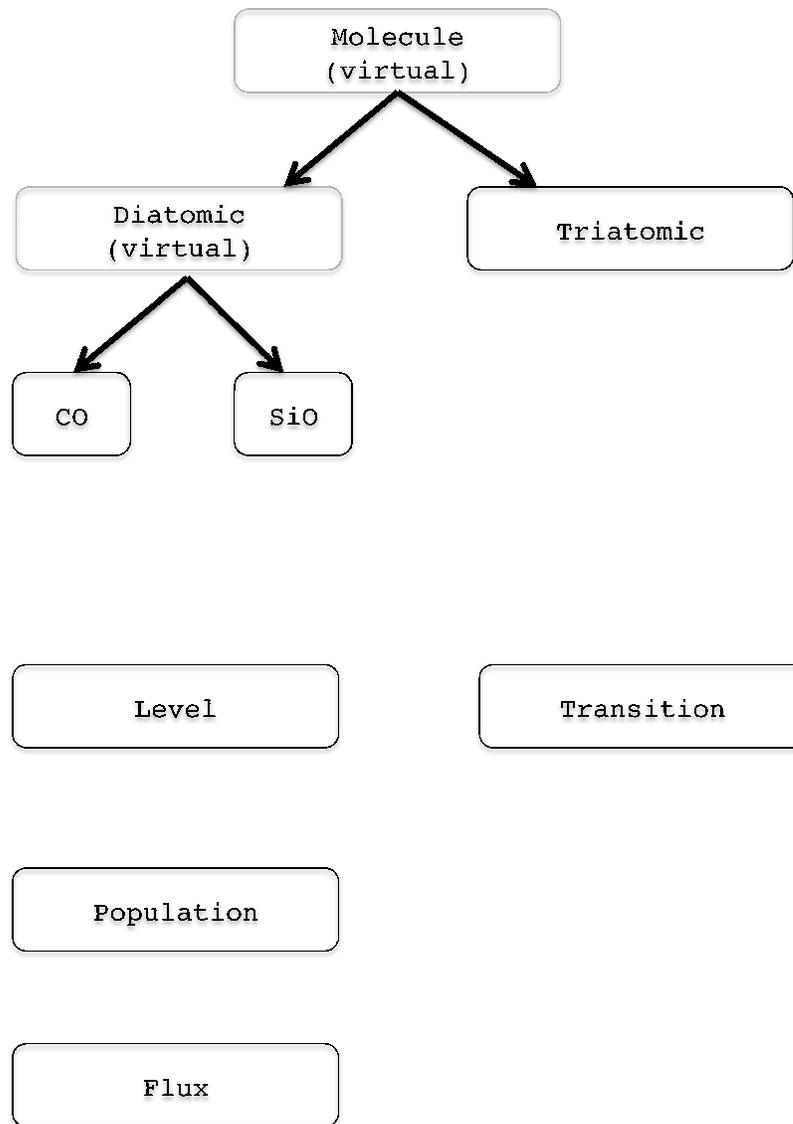
Figure C.1: Diagram of C++ Class hierarchy used in implementing the algorithms described.

of other classes. A simplified version of Figure C.3 is also included for a case without a morphological cone and the attendant SubRegions, second Integrator and Cone classes.
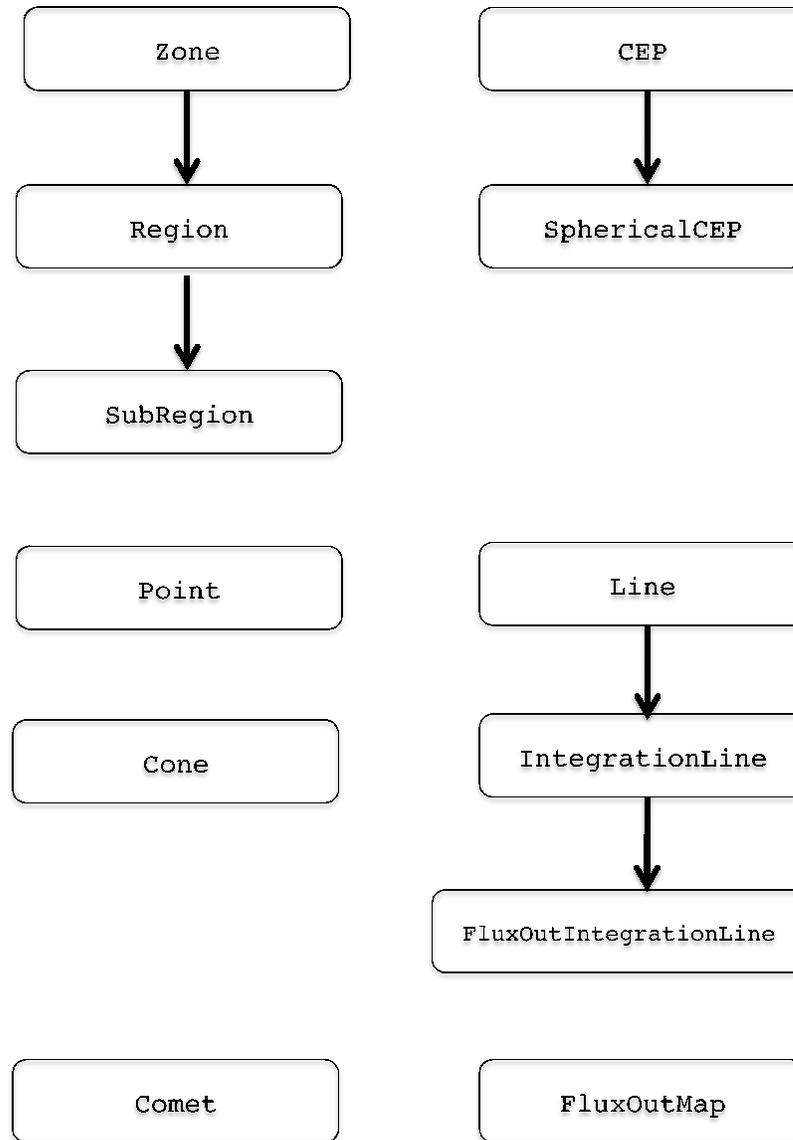
Figure C.2: Diagram of C++ Class hierarchy used in implementing the algorithms described. (Continued from Fig. C.1)

Implementation Details

In this section, I provide a brief very high level description: major classes and class hierarchy and how they implement the algorithms described above.

Several classes implement the basic data of the molecules we have modeled. These form a class hierarchy with the abstract class **Molecule** as the base class. Inheriting from that are the **Diatomic** and **Triatomic** classes. The **Diatomic** class is also abstract and is fully realized in either the **CO** or **SiO** classes which provide the necessary molecular values, which are completely specific to those molecules. The **Triatomic** class, on the other hand, is completely general, and can contain data for any molecule (or band) taken from a molecular lines database (e.g. Rothman et al. 1998). They are used here for the water and carbon-dioxide molecules, but could be used for others as well.

These molecule classes store a list of **Levels** a list of **Transitions**. The **Transition** class uses two instances of the **Level** class, for the initial and final energy levels of the transition. It also holds the relevant coefficients for the transition. The **Level** class stores the energy level and associated quantum numbers of a specific molecular energy level. The **Population** class stores the fractional populations of each **Level** in a **Molecule**. There are also functions that iterate through the lists of **Transitions** (or wavenumbers), calling a function passed as a parameter on each **Transition**. These iterators accomplish a great deal of the calculations related to a given transition or wavenumber, including calculating τ, the source functions, transition rates, etc.

The **Integrator** class implements an improved version of the original integration done in my second year project. It is spread over several modules, most of which are adapted C++ versions of functions (**odeint**, **simpr** and **stifbs**) from Press et al. (1992).

The **Zone** class encapsulates a single Zone in the original plane parallel formulation of **CEP**. A **Zone** contains information on the species/molecule, density (& H_2O density), temperature, its **Population**, and other properties of a CEP zone.

It includes mappings of values by wavenumber for Je (mean intensity), $d\tau$, P (net radiative bracket) and the source function, as well as functions that calculate these quantities.

The **Region** class inherits the properties of the **Zone** class (and re-implements some of them for spherical geometry). In addition, it includes necessary geometric data such as the cylinders and shells to identify the **Region**, and the boundaries of the **Region**.

Each **Region** also includes a list of **IntegrationLines** which connect to the intensity in other **Regions** to calculate the net radiative bracket in the Spherical CEP algorithm. A **Region** has iteration functions to iterate over this list and call relevant functions on each relevant line (generally used in conjunction with the wavenumber iterating functions of a molecule).

A **SubRegion** is a sub-class inheriting from **Region**, and comprises a portion of a **Region** with the more narrow constraints of a **Cone** geometry. Every **SubRegion** belongs to a "parent **Region**" of which it is a geometric subset. Its other properties may differ from those of its parent **Region**.

Several classes encapsulating relevant geometry are used. The **Point** class is a simple point in 3D space. The **Line** is likewise a line in 3D space with functions to calculate intersection points with spheres, cylinders, planes and cones. The **IntegrationLine** inherits from the simple **Line** and implements the lines along which integration from one region to another are done to calculate the net radiative bracket. The **FluxOutIntegrationLine** inherits from that and implements the line of sight integration of intensity out of the coma. There is also a **Cone** class to encapsulate the necessary geometry for implementing morphological cones.

The **CEP** class is our implementation of the original plane parallel **CEP** method. It holds a list of **Zones**, and uses the algorithm described to produce spectra inte-

grated over angle one the top and bottom of a "slab". The actual matrix solving is done using modified versions of Press et al. (1992): the **newt** function that implements Newton's method and the **fdjac** function that is used by **newt** to build the jacobian matrix by a finite differencing. **fdjac** calls a user-defined function called **vecfunc**, which calculates one row (i.e. a vector) of the derivatives comprising the jacobian using the finite differnce approach after changing one value by a small amount. In our code, this requires "tweaking" all the associated properties affected by the change in a single population level in one **Region**. The **CEP** class uses iteration functions to iterate over all the affected values, and "tweak" them (i.e. recalculate them after a minor change) using functions such as **tweakTaus**, **tweakBrackets**, etc. Since this is a very cumbersome process, we have also implemented "book-keeping" lists and corresponding iteration functions to only iterate and re-calculate the relevant values, i.e. ones that are affected. This greatly speeds up the **fdjac** matrix building process. After building the matrix, it is solved using **ludcmp** and **lubksub**, as part of the **newt** function.

The **SphericalCEP** class has the same properties as the **CEP** base class, with all the geometry-related functionality added to it. It contains a list of **Regions** (and **SubRegions**, as called for) and to build the matrix with **fdjac**, in the process calculating the net radiative bracket, it iterates over them, each of which iterates over its list of **IntegrationLines**, for each wavenumber. Once the matrix is built, the same solving functions used for the plane parallel **CEP** are used to calculation the molecular populations.

However, once the matrix solution is completed, the **SphericalCEP** object creates one or more **FluxOutMaps** based on the populations calculated for each region. A **FluxOutMap** essentially contains a large list of **FluxOutIntegrationLines** that form a 2D mapping from the observer's point of view (specified

by viewing angles in the creation of a **FluxOutMap**).
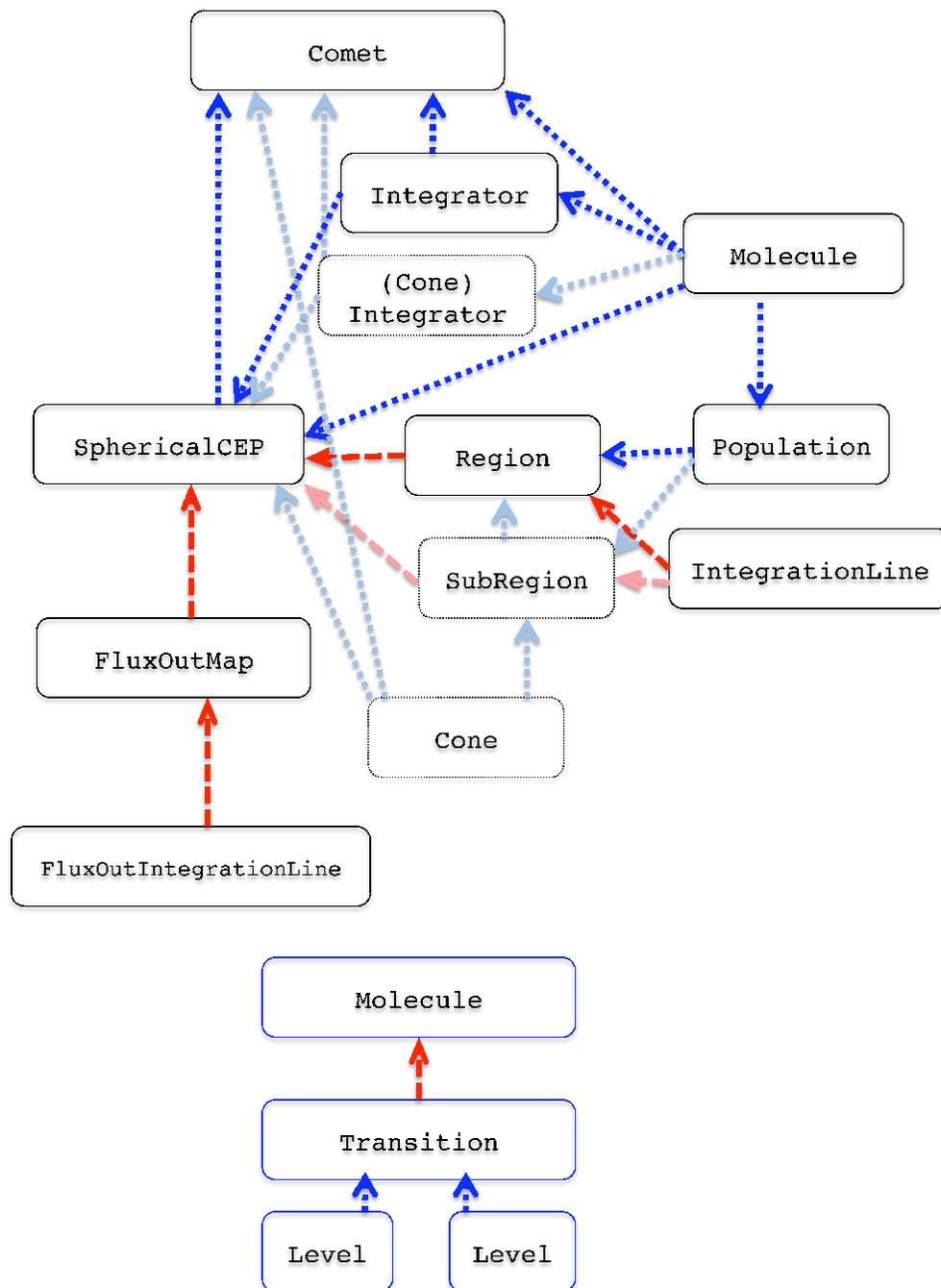
Figure C.3: Diagram of C++ Class relationships used in implementing the algorithms described. Arrows indicate a "member of" relationship (in the direction of the arrow; e.g. an instance of a Comet possesses an instance of an Integrator). Blue arrows represent a one-to-one relation and red arrows a many-to-one (e.g. a Molecule possesses many Levels and Transitions). The "greyed out" classes and relationships are only active in a case where there is a Cone and attendant SubRegions.
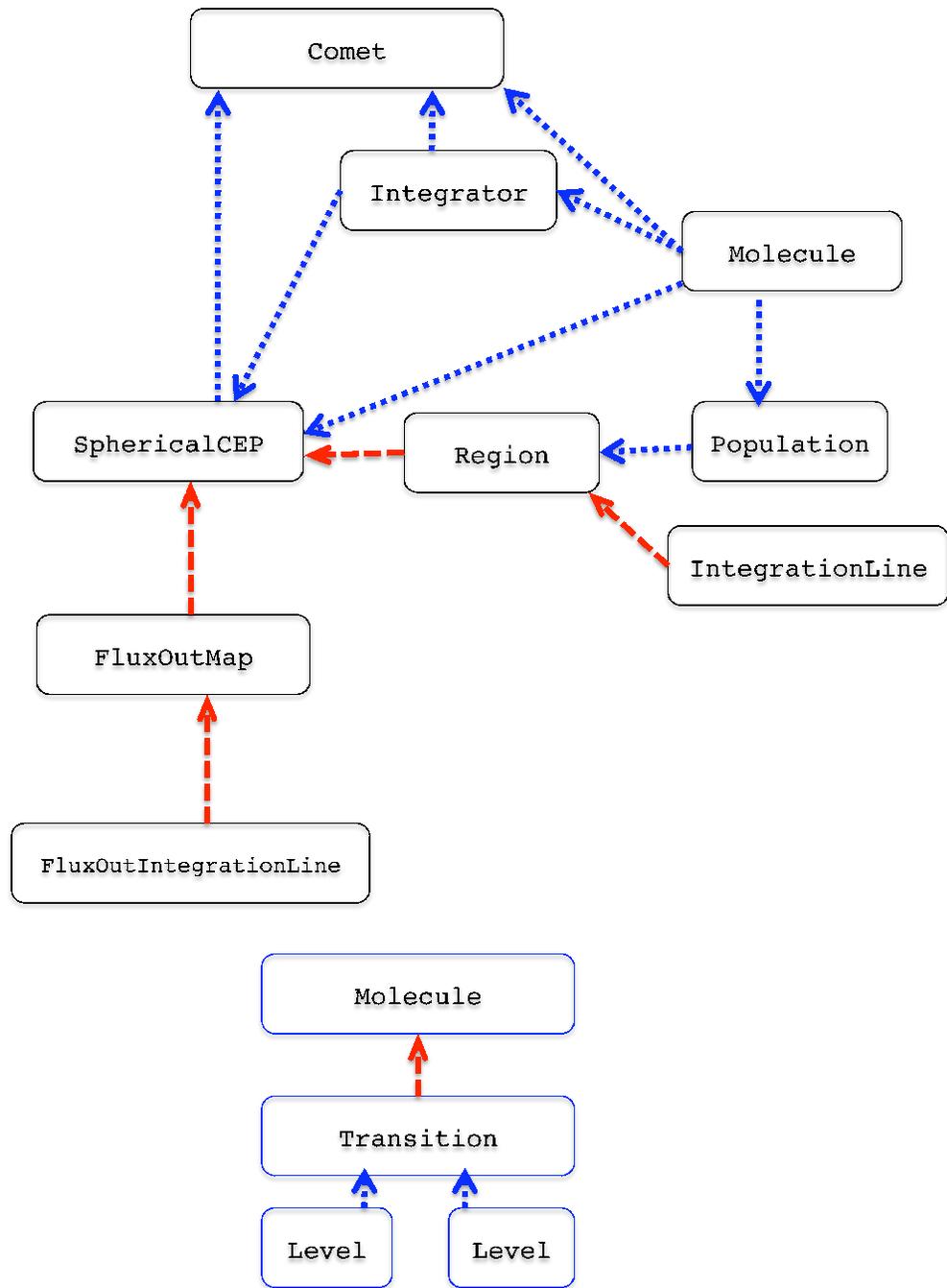
Figure C.4: Same as Fig. C.3, but shown for the simpler case without the classes used for a case with morphology.

Bibliography

A'Hearn, M. F., Belton, M. J. S., Crockett, C. J., Farnham, T. L., Feaga, L., Groussin, O., Mastrodemos, N., Owen, W. M., Sunshine, J. M., and Deep Impact Team (2005a). Natural Outbursts by Comet Tempel 1. In *American Astronomical Society Meeting Abstracts*, volume 37 of *Bulletin of the American Astronomical Society*, page 189.01.

A'Hearn, M. F., Belton, M. J. S., Delamere, A., and Blume, W. H. (2005b). Deep Impact: A Large-Scale Active Experiment on a Cometary Nucleus. *Space Sci. Rev.*, 117:1–21.

A'Hearn, M. F., Belton, M. J. S., Delamere, W. A., Feaga, L. M., Hampton, D., Kissel, J., Klaasen, K. P., McFadden, L. A., Meech, K. J., Melosh, H. J., Schultz, P. H., Sunshine, J. M., Thomas, P. C., Veverka, J., Wellnitz, D. D., Yeomans, D. K., Besse, S., Bodewits, D., Bowling, T. J., Carcich, B. T., Collins, S. M., Farnham, T. L., Groussin, O., Hermalyn, B., Kelley, M. S., Kelley, M. S., Li, J.-Y., Lindler, D. J., Lisse, C. M., McLaughlin, S. A., Merlin, F., Protopapa, S., Richardson, J. E., and Williams, J. L. (2011). EPOXI at Comet Hartley 2. *Science*, 332:1396–1400.

A'Hearn, M. F., Belton, M. J. S., Delamere, W. A., Kissel, J., Klaasen, K. P., McFadden, L. A., Meech, K. J., Melosh, H. J., Schultz, P. H., Sunshine, J. M., Thomas, P. C., Veverka, J., Yeomans, D. K., Baca, M. W., Busko, I., Crockett,

C. J., Collins, S. M., Desnoyer, M., Eberhardy, C. A., Ernst, C. M., Farnham, T. L., Feaga, L., Groussin, O., Hampton, D., Ipatov, S. I., Li, J.-Y., Lindler, D., Lisse, C. M., Mastrodemos, N., Owen, W. M., Richardson, J. E., Wellnitz, D. D., and White, R. L. (2005c). Deep Impact: Excavating Comet Tempel 1. *Science*, 310:258–264.

A'Hearn, M. F., Feaga, L. M., Keller, H. U., Kawakita, H., Hampton, D. L., Kissel, J., Klaasen, K. P., McFadden, L. A., Meech, K. J., Schultz, P. H., Sunshine, J. M., Thomas, P. C., Veverka, J., Yeomans, D. K., Besse, S., Bodewits, D., Farnham, T. L., Groussin, O., Kelley, M. S., Lisse, C. M., Merlin, F., Protopapa, S., and Wellnitz, D. D. (2012). Cometary Volatiles and the Origin of Comets. *ApJ*, 758:29.

A'Hearn, M. F., Millis, R. L., Schleicher, D. G., Osip, D. J., and Birch, P. V. (1995). The ensemble properties of comets: Results from narrowband photometry of 85 comets, 1976-1992. *Icarus*, 118:223–270.

Asensio Ramos, A., Ceccarelli, C., and Elitzur, M. (2007). H{2}D$^+$ line emission in Proto-Planetary Disks. *A&A*, 471:187–192.

Bader, G. and Deuflhard, P. (1983). *Numerische Methematik*, 41:373–398.

Belton, M. J. S., Thomas, P., Veverka, J., Schultz, P., A'Hearn, M. F., Feaga, L., Farnham, T., Groussin, O., Li, J.-Y., Lisse, C., McFadden, L., Sunshine, J., Meech, K. J., Delamere, W. A., and Kissel, J. (2007). The internal structure of Jupiter family cometary nuclei from Deep Impact observations: The talps or layered pile model. *Icarus*, 187:332–344.

Bockelee-Morvan, D. (1987). A model for the excitation of water in comets. *A&A*, 181:169–181.

Bockelée-Morvan, D., Boissier, J., Biver, N., and Crovisier, J. (2010). No compelling evidence of distributed production of CO in Comet C/1995 O1 (Hale-Bopp) from

millimeter interferometric data and a re-analysis of near-IR lines. *Icarus*, 210:898–915.

Bockelee-Morvan, D. and Crovisier, J. (1987a). The 2.7-micron water band of comet P/Halley - Interpretation of observations by an excitation model. *A&A*, 187:425–430.

Bockelee-Morvan, D. and Crovisier, J. (1987b). The role of water in the thermal balance of the coma. In Rolfe, E. J. and Battrick, B., editors, *Diversity and Similarity of Comets*, volume 278 of *ESA Special Publication*, pages 235–240.

Chin, G. and Weaver, H. A. (1984). Vibrational and rotational excitation of CO in comets Nonequilibrium calculations. *ApJ*, 285:858–869.

Combes, M., Moroz, V. I., Crifo, J. F., Lamarre, J. M., Charra, J., Sanko, N. F., Soufflot, A., Bibring, J. P., Cazes, S., Coron, N., Crovisier, J., Emerich, C., Encrenaz, T., Gispert, R., Grigoryev, A. V., Guyot, G., Krasnopolsky, V. A., Nikolsky, Y. V., and Rocard, F. (1986). Infrared sounding of comet Halley from VEGA 1. *Nature*, 321:266–268.

Combi, M. R. (1989). The outflow speed of the coma of Halley's comet. *Icarus*, 81:41–50.

Combi, M. R. (1996). Time-Dependent Gas Kinetics in Tenuous Planetary Atmospheres: The Cometary Coma. *Icarus*, 123:207–226.

Crovisier, J. (1984a). The water molecule in comets - Fluorescence mechanisms and thermodynamics of the inner coma. *A&A*, 130:361–372.

Crovisier, J. (1984b). The Water Molecule in Comets: Fluorescence Mechanisms and Thermodynamics of the Inner Coma. *A&A*, 135:197.

Crovisier, J. (1987). Rotational and vibrational synthetic spectra of linear parent molecules in comets. *A&AS*, 68:223–258.

Crovisier, J. (1989). The photodissociation of water in cometary atmospheres. *A&A*,

213:459–464.

Crovisier, J. (1994). Photodestruction rates for cometary parent molecules. *J. Geophys. Res.*, 99:3777–3781.

Crovisier, J. and Encrenaz, T. (1983). Infrared fluorescence of molecules in comets - The general synthetic spectrum. *A&A*, 126:170–182.

Crovisier, J. and Le Bourlot, J. (1983). Infrared and microwave fluorescence of carbon monoxide in comets. *A&A*, 123:61–66.

Davidsson, B. J. R., Gutiérrez, P. J., Groussin, O., AHearn, M. F., Farnham, T., Feaga, L. M., Kelley, M. S., Klaasen, K. P., Merlin, F., Protopapa, S., Rickman, H., Sunshine, J. M., and Thomas, P. C. (2013). Thermal inertia and surface roughness of Comet 9P/Tempel 1. *Icarus*, 224:154–171.

Dello Russo, N., Mumma, M. J., DiSanti, M. A., Magee-Sauer, K., Novak, R., and Rettig, T. W. (2000). Water Production and Release in Comet C/1995 O1 Hale-Bopp. *Icarus*, 143:324–337.

Disanti, M. A., Mumma, M. J., Dello Russo, N., and Magee-Sauer, K. (2001). Carbon Monoxide Production and Excitation in Comet C/1995 O1 (Hale-Bopp): Isolation of Native and Distributed CO Sources. *Icarus*, 153:361–390.

Disanti, M. A., Mumma, M. J., Dello Russo, N., Magee-Sauer, K., Novak, R., and Rettig, T. W. (1999). Identification of two sources of carbon monoxide in comet Hale-Bopp. *Nature*, 399:662–665.

Donati, G. B. (1864). Schreiben des Herrn Prof. Donati an den Herausgeber. *Astron. Nachr.*, 62:375.

Duncan, M., Quinn, T., and Tremaine, S. (1988). The origin of short-period comets. *ApJ*, 328:L69–L73.

Edgeworth, K. E. (1949). The origin and evolution of the Solar System. *MNRAS*, 109:600–609.

Elitzur, M. and Asensio Ramos, A. (2006). A new exact method for line radiative transfer. *MNRAS*, 365:779–791.

Elitzur, M., Asensio Ramos, A., and Ceccarelli, C. (2012). Rotating discs and non-kinematic double peaks. *MNRAS*, 422:1394–1402.

Farnham, T., Bodewits, D., A'Hearn, M. F., and Feaga, L. M. (2012). Deep Impact MRI Observations Of Comet Garradd (C/2009 P1). In *AAS/Division for Planetary Sciences Meeting Abstracts*, volume 44 of *AAS/Division for Planetary Sciences Meeting Abstracts*, page 506.05.

Farnham, T. L., Besse, S., Feaga, L. M., Sunshine, J. M., A'Hearn, M. F., Lindler, D., Bodewits, D., Lisse, C. M., Belton, M. J. S., and Dixi Team (2011). Jet Activity in Comet 103P/Hartley 2 as Observed by the Deep Impact Spacecraft. In *Lunar and Planetary Institute Science Conference Abstracts*, volume 42 of *Lunar and Planetary Inst. Technical Report*, page 2160.

Farnham, T. L., Wellnitz, D. D., Hampton, D. L., Li, J.-Y., Sunshine, J. M., Groussin, O., McFadden, L. A., Crockett, C. J., A'Hearn, M. F., Belton, M. J. S., Schultz, P., and Lisse, C. M. (2007). Dust coma morphology in the Deep Impact images of Comet 9P/Tempel 1. *Icarus*, 187:26–40.

Feaga, L. M., A'Hearn, M., Farnham, T., Bodewits, D., Sunshine, J. M., Gersch, A., Protopapa, S., Yang, B., Drahus, M., and Schleicher, D. G. (2014). Uncorrelated Volatile Behavior During the 2011 Apparition of C/2009 P1 Garradd. *AJ*, 147.

Feaga, L. M., A'Hearn, M., Farnham, T., Gersch, A., Bodewits, D., and Klaasen, K. (2012). A Study of C/2009 P1 Garradd's Dominant Volatiles as Observed by the Deep Impact HRI-IR Spectrometer. In *AAS/Division for Planetary Sciences Meeting Abstracts*, volume 44 of *AAS/Division for Planetary Sciences Meeting Abstracts*, page 313.08.

Feaga, L. M., A'Hearn, M. F., Sunshine, J. M., Groussin, O., and Farnham, T. L.

(2007a). Asymmetries in the distribution of H_2O and CO_2 in the inner coma of Comet 9P/Tempel 1 as observed by Deep Impact. *Icarus*, 191:134–145.

Feaga, L. M. and Deep Impact Science Team (2005). Composition of the ambient coma of Comet 9P/Tempel 1. In *American Astronomical Society Meeting Abstracts*, volume 37 of *Bulletin of the American Astronomical Society*, page 189.02.

Feaga, L. M., Groussin, O., Sunshine, J., and A'Hearn, M. F. (2007b). Comparison of 9P/Tempel 1's IR Spectra from Deep Impact with Synthetic Models. In *AAS/Division for Planetary Sciences Meeting Abstracts #39*, volume 39 of *Bulletin of the American Astronomical Society*, page 450.

Feaga, L. M., Sunshine, J. M., Groussin, O., Besse, S., Protopapa, S., Merlin, F., Farnham, T. L., A'Hearn, M. F., and Dixi Science Team (2011). Heterogeneity of Comet 103P/Hartley 2's Gaseous Coma. In *Lunar and Planetary Institute Science Conference Abstracts*, volume 42 of *Lunar and Planetary Inst. Technical Report*, page 2461.

Fernandez, J. A. and Ip, W.-H. (1983). On the time evolution of the cometary influx in the region of the terrestrial planets. , 54:377–387.

Festou, M. C., Keller, H. U., and Weaver, H. A. (2004). A brief conceptual history of cometary science. In Festou, M. C., Keller, H. U., and Weaver, H. A., editors, *Comets II*, pages 3–16. University of Arizona Press, 2004.

Fougere, N., Combi, M. R., Rubin, M., and Tenishev, V. (2013). Modeling the heterogeneous ice and gas coma of Comet 103P/Hartley 2. *Icarus*, 225:688–702.

Goldsmith, P. F. (1972). Collisional Excitation of Carbon Monoxide in Interstellar Clouds. *ApJ*, 176:597.

Gomes, R., Levison, H. F., Tsiganis, K., and Morbidelli, A. (2005). Origin of the cataclysmic Late Heavy Bombardment period of the terrestrial planets. *Nature*, 435:466–469.

Gomes, R. S. (2003). The origin of the Kuiper Belt high-inclination population. *Icarus*, 161:404–418.

Gomes, R. S., Morbidelli, A., and Levison, H. F. (2004). Planetary migration in a planetesimal disk: why did Neptune stop at 30 AU? *Icarus*, 170:492–507.

Groussin, O., A'Hearn, M. F., Li, J.-Y., Thomas, P. C., Sunshine, J. M., Lisse, C. M., Meech, K. J., Farnham, T. L., Feaga, L. M., and Delamere, W. A. (2007). Surface temperature of the nucleus of Comet 9P/Tempel 1. *Icarus*, 187:16–25.

Groussin, O., Sunshine, J. M., Feaga, L. M., Jorda, L., Thomas, P. C., Li, J.-Y., A'Hearn, M. F., Belton, M. J. S., Besse, S., Carcich, B., Farnham, T. L., Hampton, D., Klaasen, K., Lisse, C., Merlin, F., and Protopapa, S. (2013). The temperature, thermal inertia, roughness and color of the nuclei of Comets 103P/Hartley 2 and 9P/Tempel 1. *Icarus*, 222:580–594.

Hamid, S. E.-D. and Whipple, F. L. (1953). On the motions of 64 long-period comets. *AJ*, 58:100.

Hampton, D. L., Baer, J. W., Huisjen, M. A., Varner, C. C., Delamere, A., Wellnitz, D. D., A'Hearn, M. F., and Klaasen, K. P. (2005). An Overview of the Instrument Suite for the Deep Impact Mission. *Space Sci. Rev.*, 117:43–93.

Haser, L. (1957). Distribution d'intensite dans la tete d'une comete. *Bulletin de la Societe Royale des Sciences de Liege*, 43:740–750.

Hermalyn, B., Farnham, T. L., Collins, S. M., Kelley, M. S., A'Hearn, M. F., Bodewits, D., Carcich, B., Lindler, D. J., Lisse, C., Meech, K., Schultz, P. H., and Thomas, P. C. (2013). The detection, localization, and dynamics of large icy particles surrounding Comet 103P/Hartley 2. *Icarus*, 222:625–633.

Herzberg, G. (1950). *Molecular spectra and molecular structure. Vol.1: Spectra of diatomic molecules.* New York: Van Nostrand Reinhold, 1950, 2nd ed.

Herzberg, G. (1971). *The spectra and structures of simple free radicals. an intro-*

duction to molecular spectroscopy. The George Fisher Baker Non-Resident Lectureship in Chemistry at Cornell University, Ithaca: Cornell University Press, 1971.

Hollas, J. M. (2004). *Modern Spectroscopy.* Wiley, 2004, 4th ed.

Huebner, W. F., Keady, J. J., and Lyon, S. P. (1992). Solar photo rates for planetary atmospheres and atmospheric pollutants. *Ap&SS*, 195:1–289.

Huggins, W. (1868). Further Observations on the Spectra of Some of the Stars and Nebulae, with an Attempt to Determine Therefrom Whether These Bodies are Moving towards or from the Earth, Also Observations on the Spectra of the Sun and of Comet II., 1868. *Royal Society of London Philosophical Transactions Series I*, 158:529–564.

Kelley, M. S., Lindler, D. J., Bodewits, D., A'Hearn, M. F., Lisse, C. M., Kolokolova, L., Kissel, J., and Hermalyn, B. (2013). A distribution of large particles in the coma of Comet 103P/Hartley 2. *Icarus*, 222:634–652.

Kim, S.-J. (1996). The Swings Effects of the A-X System and v" = 1-0 Band of CO. *Journal of Korean Astronomical Society*, 29:223–243.

Klaasen, K. P., A'Hearn, M., Besse, S., Bodewits, D., Carcich, B., Farnham, T., Feaga, L., Groussin, O., Hampton, D., Huisjen, M., Kelley, M. S., McLaughlin, S., Merlin, F., Protopapa, S., Sunshine, J., Thomas, P., and Wellnitz, D. (2013). EPOXI instrument calibration. *Icarus*, 225:643–680.

Krupenie, P. (1966). *The Band Spectrum of Carbon Monoxide.* Washington, D.C.: U.S. Dept. of Commerce, National Bureau of Standards.

Kuiper, G. P. (1951). On the Origin of the Solar System. *Proceedings of the National Academy of Science*, 37:1–14.

Labs, D. and Neckel, H. (1968). The Radiation of the Solar Photosphere from 2000 Å to 100 μm. *ZAp*, 69:1.

Levison, H. F. (1996). Comet Taxonomy. In Rettig, T. and Hahn, J. M., editors, *Completing the Inventory of the Solar System*, volume 107 of *Astronomical Society of the Pacific Conference Series*, pages 173–191.

Levison, H. F., Dones, L., and Duncan, M. J. (2001). The Origin of Halley-Type Comets: Probing the Inner Oort Cloud. *AJ*, 121:2253–2267.

Levison, H. F. and Duncan, M. J. (1997). From the Kuiper Belt to Jupiter-Family Comets: The Spatial Distribution of Ecliptic Comets. *Icarus*, 127:13–32.

Levison, H. F., Morbidelli, A., Van Laerhoven, C., Gomes, R., and Tsiganis, K. (2008). Origin of the structure of the Kuiper belt during a dynamical instability in the orbits of Uranus and Neptune. *Icarus*, 196:258–273.

Litvak, M. M. and Kuiper, E. N. R. (1982). Cometary NH - Ultraviolet and submillimeter emission. *ApJ*, 253:622–633.

Marconi, M. L. and Mendis, D. A. (1982). The photochemical heating of the cometary atmosphere. *ApJ*, 260:386–394.

Marconi, M. L. and Mendis, D. A. (1983). The atmosphere of a dirty-clathrate cometary nucleus - A two-phase, multifluid model. *ApJ*, 273:381–396.

Meech, K. J., A'Hearn, M. F., Adams, J. A., Bacci, P., Bai, J., Barrera, L., Battelino, M., Bauer, J. M., Becklin, E., Bhatt, B., Biver, N., Bockelée-Morvan, D., Bodewits, D., Böhnhardt, H., Boissier, J., Bonev, B. P., Borghini, W., Brucato, J. R., Bryssinck, E., Buie, M. W., Canovas, H., Castellano, D., Charnley, S. B., Chen, W. P., Chiang, P., Choi, Y.-J., Christian, D. J., Chuang, Y.-L., Cochran, A. L., Colom, P., Combi, M. R., Coulson, I. M., Crovisier, J., Dello Russo, N., Dennerl, K., DeWahl, K., DiSanti, M. A., Facchini, M., Farnham, T. L., Fernández, Y., Florén, H. G., Frisk, U., Fujiyoshi, T., Furusho, R., Fuse, T., Galli, G., García-Hernández, D. A., Gersch, A., Getu, Z., Gibb, E. L., Gillon, M., Guido, E., Guillermo, R. A., Hadamcik, E., Hainaut, O., Hammel, H. B., Harker, D. E.,

Harmon, J. K., Harris, W. M., Hartogh, P., Hashimoto, M., Häusler, B., Herter, T., Hjalmarson, A., Holland, S. T., Honda, M., Hosseini, S., Howell, E. S., Howes, N., Hsieh, H. H., Hsiao, H.-Y., Hutsemékers, D., Immler, S. M., Jackson, W. M., Jeffers, S. V., Jehin, E., Jones, T. J., Ovelar, M. d. J., Kaluna, H. M., Karlsson, T., Kawakita, H., Keane, J. V., Keller, L. D., Kelley, M. S., Kinoshita, D., Kiselev, N. N., Kleyna, J., Knight, M. M., Kobayashi, H., Kobulnicky, H. A., Kolokolova, L., Kreiny, M., Kuan, Y.-J., Küppers, M., Lacruz, J. M., Landsman, W. B., Lara, L. M., Lecacheux, A., Levasseur-Regourd, A. C., Li, B., Licandro, J., Ligustri, R., Lin, Z.-Y., Lippi, M., Lis, D. C., Lisse, C. M., Lovell, A. J., Lowry, S. C., Lu, H., Lundin, S., Magee-Sauer, K., Magain, P., Manfroid, J., Mazzotta Epifani, E., McKay, A., Melita, M. D., Mikuz, H., Milam, S. N., Milani, G., Min, M., Moreno, R., Mueller, B. E. A., Mumma, M. J., Nicolini, M., Nolan, M. C., Nordh, H. L., Nowajewski, P. B., Odin Team, Ootsubo, T., Paganini, L., Perrella, C., Pittichová, J., Prosperi, E., Radeva, Y. L., Reach, W. T., Remijan, A. J., Rengel, M., Riesen, T. E., Rodenhuis, M., Rodríguez, D. P., Russell, R. W., Sahu, D. K., Samarasinha, N. H., Sánchez Caso, A., Sandqvist, A., Sarid, G., Sato, M., Schleicher, D. G., Schwieterman, E. W., Sen, A. K., Shenoy, D., Shi, J.-C., Shinnaka, Y., Skvarc, J., Snodgrass, C., Sitko, M. L., Sonnett, S., Sosseini, S., Sostero, G., Sugita, S., Swinyard, B. M., Szutowicz, S., Takato, N., Tanga, P., Taylor, P. A., Tozzi, G.-P., Trabatti, R., Trigo-Rodríguez, J. M., Tubiana, C., de Val-Borro, M., Vacca, W., Vandenbussche, B., Vaubaillion, J., Velichko, F. P., Velichko, S. F., Vervack, Jr., R. J., Vidal-Nunez, M. J., Villanueva, G. L., Vinante, C., Vincent, J.-B., Wang, M., Wasserman, L. H., Watanabe, J., Weaver, H. A., Weissman, P. R., Wolk, S., Wooden, D. H., Woodward, C. E., Yamaguchi, M., Yamashita, T., Yanamandra-Fischer, P. A., Yang, B., Yao, J.-S., Yeomans, D. K., Zenn, T., Zhao, H., and Ziffer, J. E. (2011). EPOXI: Comet 103P/Hartley 2 Observations

from a Worldwide Campaign. *ApJ*, 734:L1.

Morgenthaler, J. P., Harris, W. M., Combi, M. R., Feldman, P. D., and Weaver, H. A. (2011). GALEX FUV Observations of Comet C/2004 Q2 (MACHHOLZ): The Ionization Lifetime of Carbon. *ApJ*, 726:8.

Moroz, V. I., Combes, M., Bibring, J. P., Coron, N., Crovisier, J., Encrenaz, T., Crifo, J. F., Sanko, N., Grigoryev, A. V., Bockelee-Morvan, D., Gispert, R., Nikolsky, Y. V., Emerich, C., Lamarre, J. M., Rocard, F., Krasnopolsky, V. A., and Owen, T. (1987). Detection of Parent Molecules in Comet p/ Halley from the IKS VEGA Experiment. *A&A*, 187:513.

Mumma, M. J. and Charnley, S. B. (2011). The Chemical Composition of CometsEmerging Taxonomies and Natal Heritage. *ARA&A*, 49:471–524.

Mumma, M. J., DiSanti, M. A., Magee-Sauer, K., Bonev, B. P., Villanueva, G. L., Kawakita, H., Dello Russo, N., Gibb, E. L., Blake, G. A., Lyke, J. E., Campbell, R. D., Aycock, J., Conrad, A., and Hill, G. M. (2005). Parent Volatiles in Comet 9P/Tempel 1: Before and After Impact. *Science*, 310:270–274.

Mumma, M. J., McLean, I. S., DiSanti, M. A., Larkin, J. E., Dello Russo, N., Magee-Sauer, K., Becklin, E. E., Bida, T., Chaffee, F., Conrad, A. R., Figer, D. F., Gilbert, A. M., Graham, J. R., Levenson, N. A., Novak, R. E., Reuter, D. C., Teplitz, H. I., Wilcox, M. K., and Xu, L.-H. (2001). A Survey of Organic Volatile Species in Comet C/1999 H1 (Lee) Using NIRSPEC at the Keck Observatory. *ApJ*, 546:1183–1193.

Mumma, M. J., Weaver, H. A., Larson, H. P., Williams, M., and Davis, D. S. (1986). Detection of water vapor in Halley's comet. *Science*, 232:1523–1528.

Oort, J. H. (1950). The structure of the cloud of comets surrounding the Solar System and a hypothesis concerning its origin. *Bull. Astron. Inst. Netherlands*, 11:91–110.

Ootsubo, T., Kawakita, H., Hamada, S., Kobayashi, H., Yamaguchi, M., Usui, F., Nakagawa, T., Ueno, M., Ishiguro, M., Sekiguchi, T., Watanabe, J.-i., Sakon, I., Shimonishi, T., and Onaka, T. (2012). AKARI Near-infrared Spectroscopic Survey for CO_2 in 18 Comets. *ApJ*, 752:15.

Ootsubo, T., Usui, F., Kawakita, H., Ishiguro, M., Furusho, R., Hasegawa, S., Ueno, M., Watanabe, J.-i., Sekiguchi, T., Wada, T., Ohyama, Y., Oyabu, S., Matsuhara, H., Onaka, T., Nakagawa, T., and Murakami, H. (2010). Detection of Parent H_2O and CO_2 Molecules in the 2.5-5 μm Spectrum of Comet C/2007 N3 (Lulin) Observed with AKARI. *ApJ*, 717:L66–L70.

Paganini, L., Mumma, M. J., Villanueva, G. L., DiSanti, M. A., Bonev, B. P., Lippi, M., and Boehnhardt, H. (2012). Erratum: "The Chemical Composition of CO-rich Comet C/2009 P1 (Garradd) at R $_h$ = 2.4 and 2.0 AU before Perihelion" ¡A href="/abs/2012ApJ...748L..13P"¿(2012, ApJ, 748, L13)¡/A¿. *ApJ*, 756:L42.

Press, W. H., Teukolsky, S. A., Vetterling, W. T., and Flannery, B. P. (1992). *Numerical recipes in C. The art of scientific computing*. Cambridge: University Press, —c1992, 2nd ed.

Quinn, T., Tremaine, S., and Duncan, M. (1990). Planetary perturbations and the origins of short-period comets. *ApJ*, 355:667–679.

Rothman, L. S., Rinsland, C. P., Goldman, A., Massie, S. T., Edwards, D. P., Flaud, J.-M., Perrin, A., Camy-Peyret, C., Dana, V., Mandin, J-Y., Schroeder, J., McCann, A., Gamache, R. R., Wattson, R. B., Yoshino, K., Chance, K., Jucks, K., Brown, L. R., Nemtchinov, V., and Varanasi, P. (1998). The HITRAN Molecular Spectroscopic Database and HAWKS (HITRAN Atmospheric Workstation): 1996 Edition. *J. Quant. Spec. Radiat. Transf.*, 60:665–710.

Rybicki, G. B. and Lightman, A. P. (1986). *Radiative Processes in Astrophysics*. Wiley-VCH, 1986.

Sahai, R. and Wannier, P. G. (1985). CO 4.6 micron emission lines from the IRC +10216 inner envelope. *ApJ*, 299:424–442.

Schleicher, D. G. (1983). *The fluorescence of cometary OH and CN*. PhD thesis, Maryland Univ., College Park.

Schwarzschild, K. and Kron, E. (1911). On the Distribution of Brightness in the Tail of Halley's Comet. *ApJ*, 34:342.

Sinding, E. (1937). Zur Bestimmung der ursprünglichen Gestalt parabelnaher Kometenbahnen. *Astronomische Nachrichten*, 261:457.

Stoer, J. and Bulirsch, R. (1983). *Introduction to Numerical Analysis*. New York: Springer-Verlag.

Stroemgren, E. (1947). The short-periodic comets and the hypothesis of their capture by the major planets. *Publikationer og mindre Meddeler fra Kobenhavns Observatorium*, 144:1–11.

Strömgren, E. (1914). Über den Ursprung der Kometen mit wesentlicher Unterstützung des Mag. Johannes Braae. *Publikationer og mindre Meddeler fra Kobenhavns Observatorium*, 19:1–62.

Sunshine, J. M., A'Hearn, M. F., Groussin, O., Li, J.-Y., Belton, M. J. S., Delamere, W. A., Kissel, J., Klaasen, K. P., McFadden, L. A., Meech, K. J., Melosh, H. J., Schultz, P. H., Thomas, P. C., Veverka, J., Yeomans, D. K., Busko, I. C., Desnoyer, M., Farnham, T. L., Feaga, L. M., Hampton, D. L., Lindler, D. J., Lisse, C. M., and Wellnitz, D. D. (2006). Exposed Water Ice Deposits on the Surface of Comet 9P/Tempel 1. *Science*, 311:1453–1455.

Sunshine, J. M., A'Hearn, M. F., Schultz, P. H., Groussin, O., Feaga, L., and Deep Impact Science Team (2005). The Spatial and Temporal Distribution of Ice Excavated by the Deep Impact Experiment on the Comet 9/P Tempel 1. In *American Astronomical Society Meeting Abstracts*, volume 37 of *Bulletin of the*

American Astronomical Society, page 189.09.

Sunshine, J. M., Groussin, O., Schultz, P. H., A'Hearn, M. F., Feaga, L. M., Farnham, T. L., and Klaasen, K. P. (2007). The distribution of water ice in the interior of Comet Tempel 1. *Icarus*, 190:284–294.

Swamy, K. S. K. (1997). *Physics of comets*. Singapore: World Scientific Publication, 1997.

Tenishev, V., Combi, M., and Davidsson, B. (2008). A Global Kinetic Model for Cometary Comae: The Evolution of the Coma of the Rosetta Target Comet Churyumov-Gerasimenko throughout the Mission. *ApJ*, 685:659–677.

Tsiganis, K., Gomes, R., Morbidelli, A., and Levison, H. F. (2005). Origin of the orbital architecture of the giant planets of the Solar System. *Nature*, 435:459–461.

van Woerkom, A. J. J. (1948). On the origin of comets. *Bull. Astron. Inst. Netherlands*, 10:445–472.

Villanueva, G. L., Mumma, M. J., Bonev, B. P., Novak, R. E., Barber, R. J., and Disanti, M. A. (2012a). Water in planetary and cometary atmospheres: H_2O/HDO transmittance and fluorescence models. *J. Quant. Spec. Radiat. Transf.*, 113:202–220.

Villanueva, G. L., Mumma, M. J., DiSanti, M. A., Bonev, B. P., Paganini, L., and Blake, G. A. (2012b). A multi-instrument study of Comet C/2009 P1 (Garradd) at 2.1 AU (pre-perihelion) from the Sun. *Icarus*, 220:291–295.

Weaver, H. A., Feldman, P. D., A'Hearn, M. F., Dello Russo, N., and Stern, S. A. (2011). The Carbon Monoxide Abundance in Comet 103P/Hartley 2 During the EPOXI Flyby. *ApJ*, 734:L5.

Weaver, H. A. and Mumma, M. J. (1984). Infrared molecular emissions from comets. *ApJ*, 276:782–797.

Whipple, F. L. (1950). A comet model. I. The acceleration of Comet Encke. *ApJ*,

111:375–394.

Whipple, F. L. (1951). A Comet Model. II. Physical Relations for Comets and Meteors. *ApJ*, 113:464.

Whipple, F. L. (1963). On the Structure of the Cometary Nucleus. In Kuiper, G. P. and Middlehurst, B. M., editors, *The Moon Meteorites and Comets*, page 639. Chicago: University of Chicago Press, 1963.

Xie, X. and Mumma, M. J. (1992). The effect of electron collisions on rotational populations of cometary water. *ApJ*, 386:720–728.

Yeomans, D. K. (1991). *Comets. A chronological history of observation, science, myth, and folklore.* New York: Wiley, 1991.

Yun, Y. J., Park, Y.-S., and Lee, S. H. (2009). Application of the coupled escape probability method to spherical clouds. *A&A*, 507:1785–1791.

Zakharov, V., Bockelée-Morvan, D., Biver, N., Crovisier, J., and Lecacheux, A. (2007). Radiative transfer simulation of water rotational excitation in comets. Comparison of the Monte Carlo and escape probability methods. *A&A*, 473:303–310.